Characterisation of Radiation Damage in Nuclear Graphite at the Nanoscale

Helen Mary Freeman

School of Chemical and Process Engineering

University of Leeds

Submitted in accordance with the requirements for the degree of

Doctor of Philosophy

May 2016

The candidate confirms that the work submitted is her own, except where work which has formed part of jointly authored publications has been included. The contribution of the candidate and the other authors to this work has been explicitly indicated below. The candidate confirms that appropriate credit has been given within the thesis where reference has been made to the work of others.

Chapter 6 was published in Carbon
Mironov, B.E., Freeman, H.M., Brown, A.P., Hage, F.S., Scott, A.J., Westwood, A.V.K., Da Costa, J.-P., Weisbecker, P., Brydson, R.M.D. (2015). Electron irradiation of nuclear graphite studied by transmission electron microscopy and electron energy loss spectroscopy. Carbon, 83, 106117. doi:10.1016/j.carbon.2014.11.019
The candidate wrote the paper and carried out all experimental work and data analysis (TEM image analysis and EELS analysis). Wrote majority of paper. (Mironov, Hage, and Brown helped with EELS experimental and analysis work, Scott, Westwood and Brydson provided technical advice, Da Costa and Weisbecker helped with TEM image analysis. Mironov and Brydson were involved with writing).

Chapter 9 was published in Carbon
Freeman, H.M., Jones, A.N., Ward, M.B., Hage, F. S., Tzelepi, N., Ramasse, Q.M., Scott, A.J., Brydson, R.M.D., (2016). On the nature of cracks and voids in nuclear graphite. Carbon, 103, 45-55. doi:10.1016/j.carbon.2016.03.011
The candidate wrote the paper and carried out experimental work of EELS and some EFTEM and all data analysis. (Jones and Ward did experimental TEM, EDX, some EFTEM and TEM, Hage and Ramasse assisted in EELS experiments and analysis, Tzelepi, Scott, and Brydson provided technical advice).

Acknowledgements

I would firstly like to thank my academic and industrial supervisors, Rik Brydson, Andrew Scott, and Nassia Tzelepi for their supervision and scientific guidance throughout my PhD. In particular I would like to thank Rik for proof reading this thesis in detail. I would also like to thank Mike Ward, Andy Brown, and Nicole Hondow for continual training on the transmission electron microscopes at the University of Leeds and their excellent company and encouragement, it made my time at Leeds a lot more enjoyable.

Collaboration with the following people was a great pleasure and provided valuable insight into a wide range of techniques: Brindusa Mironov on electron irradiation and beam convergence studies; Jean-Marc Leyssale, Jean-Pierre da Costa, and the late Patrick Weisbecker of the PyroMaN research group at the University of Bordeaux for developing TEM analysis software and assisting in sample preparation; Anne Campbell at Oak Ridge National Laboratory for provision of diffraction pattern analysis software GAAP; Fred Hage at SuperSTEM for helping with efficient analysis of EELS spectra; Pratibha Gai for facilitating a host of stable in situ TEM experiments at the University of York; and all those involved with the FunGraph research consortium. Thank you to the funders of this project, the National Nuclear Laboratory and EPSRC (grant EP/J502042/1).

I would also like to thank my family and Dan Starkey for putting up with my PhD wobbles, encouraging me throughout. Running over lunch breaks with Jaiyana Bux, Jess Shiels, Omar Matar, Mike Ward, and Andy Brown provided much needed breaks from writing and time to vent about life, work, and everything in between!

Abstract

Graphite is a key component in many of the UK's civil nuclear reactors whose lifetime is heavily dependent on the physical and chemical performance of the graphite. Exposure to neutron radiation at high temperatures (∼350°C) induces complex structural changes over many length scales. This thesis focuses on the nanoscale, an area where a lack of understanding leaves a variety of contentious issues.

Transmission electron microscopy (TEM), electron diffraction, and electron energy loss spectroscopy (EELS) were the three main experimental techniques used to study a range of virgin, electron irradiated, and neutron irradiated graphites. Information gained from energy filtered TEM, X-ray diffraction, and Raman was also used to complement these techniques. In situ electron irradiation experiments were conducted at a range of temperatures to better understand the collective effect of thermal annealing and radiation damage.

TEM lattice images were quantified using software provided by the PyroMaN research group to extract information about fringe length and tortuosity as a function of radiation damage. A 3D atomistic modelling technique was also applied to micrographs to produce 3D models of electron irradiated graphite. Electron irradiation resulted in the breaking and bending of basal planes and the fragmentation of crystallites. Analysis of electron diffraction patterns showed a ∼10% increase in d-spacing and polycrystallisation following electron irradiation.

Low and core loss EEL spectra were collected during in situ electron irradiation which were fitted to extract information about specimen

density, planar and non-planar sp^2 content, and bond length. Irradiated specimens exhibited a reduced planar sp^2 content which was thought to be attributed to the introduction of non-hexagonal rings and inter-planar defects. The reduction in planar sp^2 bonded carbon was replaced by non-planar sp^2 bonded carbon. Bond lengths were also seen to increase due to an increase in peripheral dangling bonds at crystallite boundaries.

This quantitative analysis methodology was then applied to neutron irradiated specimens to analyse the bulk material and also material found within microcracks, the latter which could have a significant effect on irradiation-induced dimensional change.

Abbreviations

Å	Angstrom (10^{-10}m)
A_b	TEM beam area
α	Convergence semi angle
B	Magnetic field
BF	Bright Field
BEPO	British Experimental Pile 'O'
β	TEM collection semi angle
β_{eff}	TEM effective collection angle
β_m	TEM magic angle
c	Speed of light (3 x 10^8 m s^{-1}) (Young & Freedman, 2007)
C2	Condenser 2 current within the TEM
C_c	Chromatic aberration
C_s	Spherical aberration
CCD	Charge Coupled Device
CLP	Core Loss Peak
CTE	Coefficient of Thermal Expansion
CTF	Contrast Transfer Function
D	Dose
DF	Dark Field
dpa	Displacements per atom
DV	Di-Vacancy
Δf	Defocus
E	Energy
e	Electronic charge (1.6 x 10^{-19} C) (Young & Freedman, 2007)
E_a	CTF envelope function due to spatial coherence
E_c	CTF envelope function due to chromatic aberration
E_dt	Displacement threshold energy
E_{fi}	Interstitial formation energy
ELNES	Energy Loss Near Edge Structure
E_{MSR}	EELS MSR peak energy
E_p	EELS bulk plasmon peak energy
eV	Electron volts

EDX	Energy Dispersive X-ray
EELS	Electron Energy Loss Spectroscopy
EFTEM	Energy Filtered TEM
EXELFS	Extended Electron Energy Loss Fine Structure
ε	TEM emulsion setting
ε_0	Permittivity of free space
FEG	Field Emission Gun
FFT	Fast Fourier Transform
FWHM	Full Width at Half Maximum
FLM	Florescence Light Micrograph
GAAP	Graphite Anisotropy Analysis Programme
h	Planck's constant (6.6261 10^{-34} m^2 kg s^{-1}) (Young & Freedman, 2007)
HAADF	High Angular Annular Dark Field
HOPG	Highly Ordered Pyrolytic Graphite
HRTEM	High Resolution TEM
I	TEM beam current
IGAR	Image Guided Atomic Reconstruction
I_R	Residual intensity of Gaussian peaks in core loss EEL spectrum to measure non-planar sp^2 content
J	Electron fluence
kV	Kilovolts
k_B	Boltzmann's constant
k	Spatial frequency
L_{cam}	TEM camera length
λ	Wavelength
L2	Fringe length
m_0	Electron rest mass (9.11×10^{31} kg) (Young & Freedman, 2007)
mA	Milliamps
MAADF	Medium Angular Annular Dark Field
mrad	Milliradians
MSR	Multiple Scattering Resonance
MTR	Materials Test Reactor
MV	Megavolts
N	Noise
N_e	Valence electron density
p	Momentum
Pa	Pascals
PD	Photodiode
PGA	Pile Grade A

PKA	Primary Knock-on Atom
PLM	Polarised Light Micrograph
R	TEM Resolution
R'	Aberration corrected TEM resolution
r_A	TEM aperture size
R_{MSR}	Radius of the 2nd scattering shell in graphite's 001 plane
RDF	Radial Distribution Function
SAED	Selected Area Electron Diffraction
SEM	Scanning Electron Microscope
SKA	Secondary Knock-on Atom
STEM	Scanning TEM
SV	Single Vacancy
σ_d	Displacement cross-section
TEM	Transmission Electron Microscope
T(k)	CTF oscillating function due to defocus
t_e	Exposure time
θ_b	Bragg angle
τ	Tortuosity
υ	Defect migration frequency
v	Velocity
XRD	X-Ray Diffraction
ZLP	Zero Loss Peak

Contents

List of Figures

List of Tables

Chapter 1

Introduction

1.1 Why nuclear graphite

The UK has been harnessing electrical power from nuclear fission for nearly 60 years. The 16 reactors which are currently in operation produce up to 9.4 GW of electricity, contributing to approximately 18% of the UK's electricity mix. These reactors are nearing the end of their lifetime, and by 2023 it is expected that all but two (Sizewell B and Dungeness B) of the reactors will be closed. A new fleet of fission reactors are currently being built which are expected to contribute 16 GW of electricity by 2030. There are concerns surrounding the predicted 'energy gap' the UK might face later this decade where the closure of old reactors and opening of new reactors is not balanced. To address this problem, the UK nuclear industry is looking into extending the lifetime of current reactors, with public safety at the forefront of its concerns.

To extend the lifetime of a nuclear reactor, firstly the components must be considered. The four basic components of a nuclear reactor are: fuel rods or pellets for fission energy, control rods to regulate the fission reaction, a moderator material to limit the energies of fission neutrons, and a coolant to extract heat from the core and deliver it to the turbines for electricity production. There are two ways to sustain a nuclear fission chain reaction for continuous and controlled power output from a nuclear reactor: using a neutron moderator to slow the high energy fission neutrons (0.1 MeV to tens of MeV) to the thermal energy range (0.001 eV - 1.0 eV) so they are more likely to be captured by fissionable uranium-235, or by enriching fuel so there is a higher-than-natural proportion of

uranium-235 relative to uranium-238 (Haag, 2005; Lewis, 2008). The amount of uranium-235 found in mined natural uranium is 0.7% which can be enriched to around 4-5% for power reactors and 20% for research reactors.

When a fast neutron collides with a nucleus in the moderator, following fission, some of its energy is transferred. After several collisions, enough energy has been transferred to slow the neutron to the thermal energy range. In order to slow down fast neutrons in as few collisions as possible, the moderator material must have a suitably low thermal neutron absorption cross section and a high scattering cross section (Baker, 1970; Lamarsh & Baratta, 2001; Lewis, 2008). This is best achieved with materials of low atomic weight such as carbon, in the form of graphite, or water, both H_2O and D_2O (Lewis, 2008). Although graphite has poorer moderating properties than D_2O, it is physically and chemically stable (the most stable of the eight allotropes of carbon under standard conditions) and so remains solid up to very high temperatures which is structurally beneficial. Other favourable properties include: a low thermal neutron absorption cross section, a high scattering cross section, high thermal conductivity, a low thermal expansion coefficient, and resistivity to thermal shock. By slowing down the energies of fast neutrons with a moderator there is no need for high levels of fuel enrichment which can be be a lengthy and expensive process.

Over 80% of the UK's current nuclear reactors are graphite-moderated, of which there are two main designs: the Advanced Gas Cooled Reactor (AGR) and the Magnox reactor (DECC, 2014). In addition to moderating the energies of neutrons in the fission process, the graphite core provides structural support, accommodates the fuel and control rods, and allows for coolant flow (figure 1.1). The graphite blocks are subject to high levels of neutron irradiation resulting in chemical and physical property changes, which in turn affect neighbouring reactor components; one of the main concerns being that dimensional change of the graphite might hinder the insertion of control rods which would affect the safe running of the reactor. The lifetime of such reactors is therefore primarily limited by the performance of the irreplaceable graphite within the working reactor, so an accurate measure of its condition is essential for economic success and plant safety. To apply for life extension, the owners of the reactors are required by the Office for Nuclear Regulation to conduct 10-year safety reviews. EdF owns 14 of

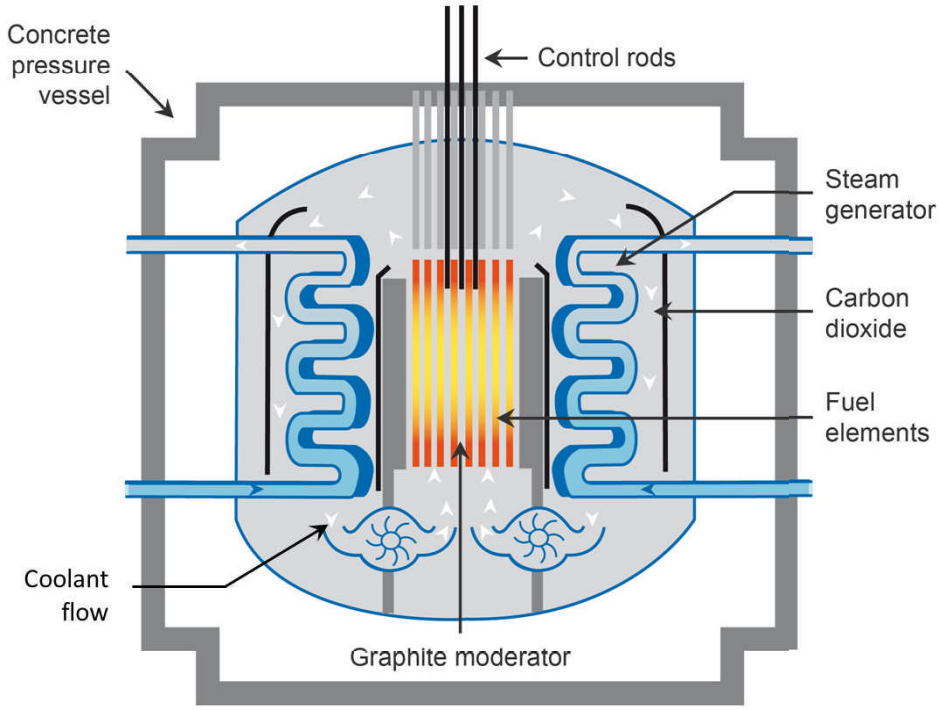

Figure 1.1: Schematic of a typical advanced gas-cooled graphite-moderated nuclear reactor (World Nuclear Association, 2015).

the UK's 16 reactors and has successfully extended the lifetime of many of their plants, averaging 7 years of extra operation per reactor.

1.2 Manufacturing of nuclear graphite

It is largely the manufacturing process which determines the properties of nuclear grade graphite; thus each batch can be designed for specific needs (Baker, 1970). Nuclear graphite is a synthetic material produced from pitch and petroleum coke particles, with a high degree of crystallinity following thermal treatment at high temperatures over a number of stages (figure 1.2) (Nightingale, 1962). The first stage involves the removal of volatile hydro-carbons by calcination of raw petroleum coke at temperatures around 1000°C to 1300°C. The coke-based filler is then milled to produce particles (of several hundred μm in diameter) and filler flour (of tens of μm in diameter) (Baker, 1970). Coal tar pitch, also known as binder, is added and the mixture, cooled, and undergoes extrusion. During this

extrusion process, the filler particles become aligned according to the direction of extrusion, where the long dimension of the particles are aligned with the direction of extrusion. The extruded material is then subject to graphitizing temperatures of around 3000°C in order to achieve polycrystallinity through crystal growth, diffusion, and annealing. The concentration of impurities is reduced at these

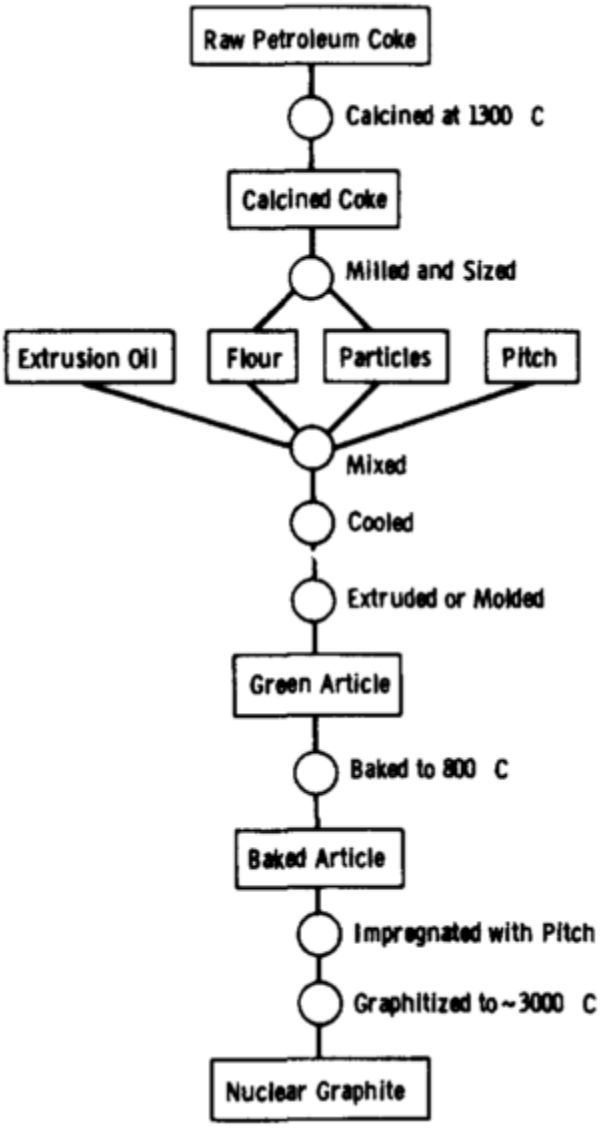

Figure 1.2: Flow diagram illustrating each stage and the materials involved in the nuclear graphite manufacturing process (Baker, 1970).

high temperatures. Impurities commonly found in nuclear graphite (e.g. H, B, N, Cl, Ti, V, Gd) can hinder moderating performance due to their high neutron absorption cross sections; however small percentages of certain impurities, such as boron, enable graphite to be used as both a moderator and neutron absorber for the shielding component of a nuclear reactor (Baker, 1970). The combination of raw material variability and variability within each manufacturing stage results in a wide variety of nuclear graphite grades and quality (Haag, 2005).

Despite these variations, all nuclear graphite finished products exhibit similar features: a majority of filler particles, a minority of binder phase, and also voids. Voids arise during multiple stages in the manufacturing process and continue to change during reactor operation due to temperature and neutron flux gradients, the anisotropy of the coefficient of thermal expansion (CTE) of graphite, internal stresses beyond the elastic limit of graphite crystals, as well as radiolytic oxidation. Both the filler and binder phases have potentially inter- and intra- structural porosity ranging from Mrozowski cracks in and between crystallites (50 nm - 10 μm) to micro- and macro-pores around domains and particles (figure 1.3) (Wen *et al.*, 2008).

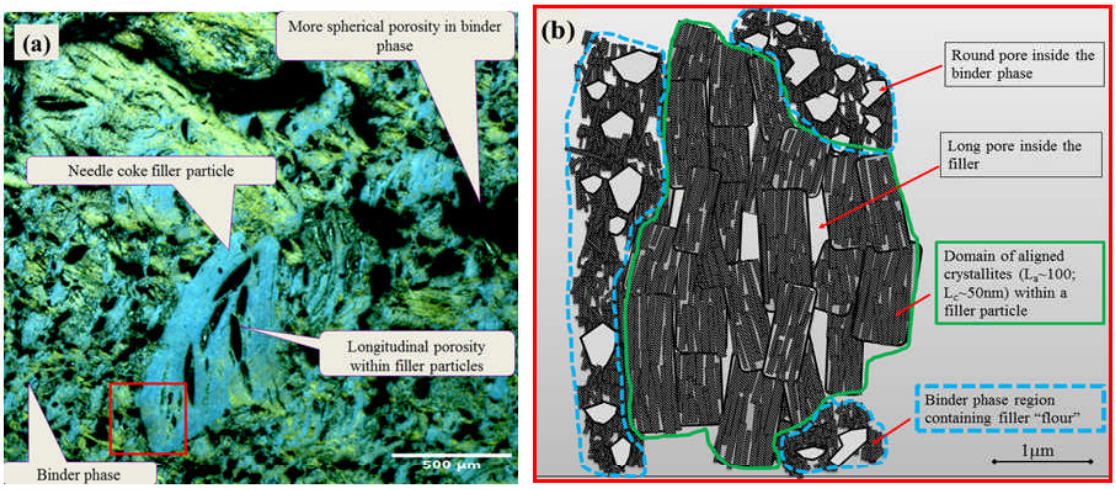

Figure 1.3: (a) Polarised light micrograph of pile grade A (PGA) nuclear graphite showing the main constitutive elements, with the outlined area in red corresponding to (b), a schematic of short range features within the filler particle (outlined in green) and binder phase (outlined in blue).

1.3 Research questions and approach

For over 70 years, a considerable body of evidence has been assembled to understand the behaviour of irradiated graphite (Bollmann & Hennig, 1964; Hennig, 1962; Mrozowski, 1954; Nightingale, 1962; Reynolds, W.N.; Thrower, 1963). The effects of radiation damage on the bulk have been thoroughly investigated and theoretical models based on empirical evidence of induced structural changes have been derived (Delannay *et al.*, 2014; Heggie *et al.*, 2011). Although this has allowed property changes in the irradiated bulk to be partly understood and accounted for in current and future graphite moderated reactor designs, the precise mechanisms of such processes at the nanoscale still remain uncertain. Revisiting the structure of nuclear graphite following irradiation is timely as there has been a considerable progress in the identification of new forms of carbon allotropes and graphite-based nanostructures such as fullerenes (C_{60}, C_{70}, and carbon nanotubes) and graphene (Boehm, 1997; Geim, 2015; Monthioux & Kuznetsov, 2006). The increased understanding of the graphitization process is also of interest as it is a critical stage in the manufacturing process and, in terms of structural change, is effectively the opposite of irradiation damage (Harris, 1997, 2012; Telling *et al.*, 2003).

There are four key research questions for this thesis:

1. How does (electron and neutron) radiation affect graphite at the nanoscale, what role does flux and temperature play, and how can theoretical calculations be used to better understand these phenomena?
2. What is the best way to measure these changes?
3. Is it possible to simulate a reactor environment using electrons?
4. Does the material behave uniformly; are there structural differences between the behaviour of material in the bulk, within cracks, and at grain boundaries?

I have attempted to address these research questions by thoroughly reviewing the existing literature and performing a series of experiments using largely tranmission electron microscopy (TEM) and electron energy loss spectroscopy

(EELS) to resolve gaps in understanding. A variety of virgin and neutron/electron irradiated nuclear graphites were studied by TEM and EELS. Collaboration with the PyroMaN research group at the University of Bordeaux and Frederik Hage at SuperSTEM laboratory led to the development of a methodology for (nano)structural analysis of irradiated graphites. The TEM reactor environment simulation required several in situ experiments exposing specimens to varying operating voltages, electron fluxes, and temperatures. In addition, these experiments provided a controlled environment for the development of imaging and spectral analysis techniques. Analysis of the material within different areas of an irradiated sample was performed using the collected knowledge from the aforementioned research. This provided particularly novel results with full characterization of the material within and surrounding a crack within neutron-irradiated graphite.

This thesis will begin by providing background information regarding the structure of graphite over several length scales and discussing a variety of physical and chemical property changes resulting from radiation exposure. The literature review will then give an overview of the current understanding of radiation damage in nuclear graphite, with particular focus on the properties measured and experimental techniques used in this thesis. The theory, advantages and limitations of the chosen techniques will be discussed in chapter 4 along with a discussion of the various analysis methods. These chapters will provide the reader with the required information to then appreciate the relevance and rigour of the results chapters (chapters 5 to 9). Finally the outcomes of all the results chapters will be discussed and future research areas will be proposed.

Chapter 2

Background

There are two main processes which affect the material properties of nuclear graphite during reactor operation: neutron irradiation and radiolytic oxidation. The extent of damage will depend on the received radiation dose and the temperature at which the reactor is operated. Of the material properties discussed, strength, Young's modulus, and thermal conductivity are affected by both processes. In this thesis, only the former damaging process (irradiation) will be investigated. This section begins by introducing graphite and discussing the effects of radiation damage, then outlines the bulk material properties of different graphite types: single and poly-crystalline graphite, virgin nuclear graphite, and irradiated nuclear graphite. This will enable the reader to appreciate the effect of irradiation damage in nuclear graphite over a range of length scales.

2.1 Introduction to graphite

Graphite has a unique layered structure in which the carbon atoms in each plane are arranged in a regular hexagonal crystal lattice as illustrated in figure 2.1. A single lattice layer, also referred to as a basal plane, is called graphene.

Lattices can be characterised by their symmetrical properties; a unit cell is the simplest form of this symmetry and by being translated and repeated in three dimensions will form the crystal structure. The alternate layering of planes is described as AB, the interlayer spacing is 0.34 nm. The in-plane hexagonal atomic arrangement has a C-C bond length of 0.14 nm.

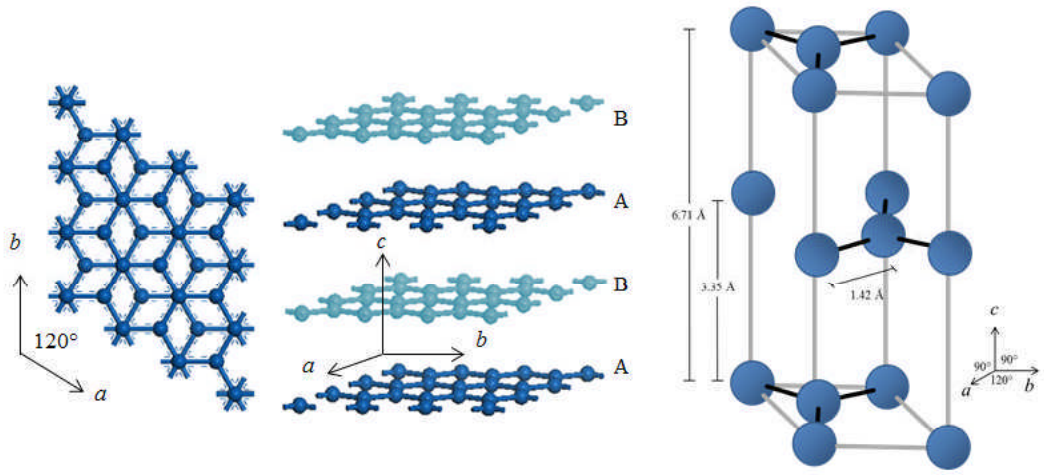

Figure 2.1: Layered structure of graphite from two view points and its unit cell.

Bonding

The atomic covalent bonding within the crystal lattice of graphite is strong, however the van der Waals force between layers is weak making graphite anisotropic in behaviour (Ohr *et al.*, 1972; Telling *et al.*, 2003). This means the material is naturally lubricating and the planes can easily slide over one another.

Each carbon atom has four unpaired electrons which can bond to neighbouring carbon atoms (figure 2.2). Three of these electrons will covalently bond to neighbouring carbon atoms within the crystal lattice. These are known as sp^2 bonds and are trigonal planar (i.e. they lie in a plane at 120° to one another). Two neighbouring in-plane carbon atoms with overlapping sp^2 bonds will form a covalent chemical σ bond. The fourth unpaired electron of the carbon atom forms a delocalised π bond across the planar sheets (figure 2.2). Two neighbouring in-plane carbon atoms with overlapping delocalised electron orbitals will form a covalent chemical π bond. It is this fourth unpaired electron which results in weak inter-planar bonding, self-lubrication, and electrical conductivity.

The electrons within the $a-b$ crystal plane are fairly mobile, however mobility between planes along c is low. Graphite therefore has metallic properties (i.e. good electrical and thermal conductance) in the $a-b$ plane and non-metallic in the c plane (Baker, 1970). Graphite is also insoluble in water as the forces between water and graphite are always less than the strong covalent bonds within

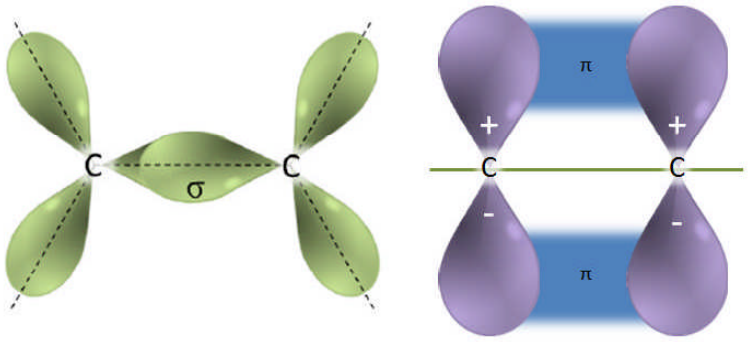

Figure 2.2: Schematic of the hybridization of carbon atoms to form σ and π bonds.

the crystal lattice (Nightingale, 1962). During exposure to radiation, the rearrangement of the atomic structure will affect this bonding system. The various techniques used to detect such changes will be further discussed in the literature review.

2.1.1 Radiation damage to the nanostructure

During reactor operation, the graphite structure is bombarded with high energy neutrons of several MeV. When a neutron collides with a carbon atom momentum and energy transfer, ΔE, occurs, the level of which depends upon the mass ratio between the target atom and the incident particle. The atomic displacement rate, measured in displacements per atom (dpa), is dependent on the energy of this incident particle, E_i. For neutrons, equation 2.1 suggests that in an elastic head on collision with a carbon atom (i.e. collision angle is 0°), where A = 12, the transfer of energy from the neutron to the carbon atom is $0.28\mathrm{E}_i$ (Haag, 2005).

$$\Delta E = \frac{4A}{(A+1)^2} E_i \tag{2.1}$$

It is generally understood that cascades of atomic displacements are the most common route for large scale structural disturbances. Models have been developed to calculate the number of atoms involved in cascade events resulting from different incident neutron energies (Christie *et al.*, 2015; Nordlund *et al.*, 1996; Smith, 1990). The first displaced atom is referred to as the primary knock on atom (PKA) which travels through the lattice and, if the energy is high enough

(Equation 2.1), it can displace further atoms. These then behave as secondary knock on atoms (SKA) and continue to cause atomic displacements until the energy has been dissipated throughout the structure (figure 2.3).

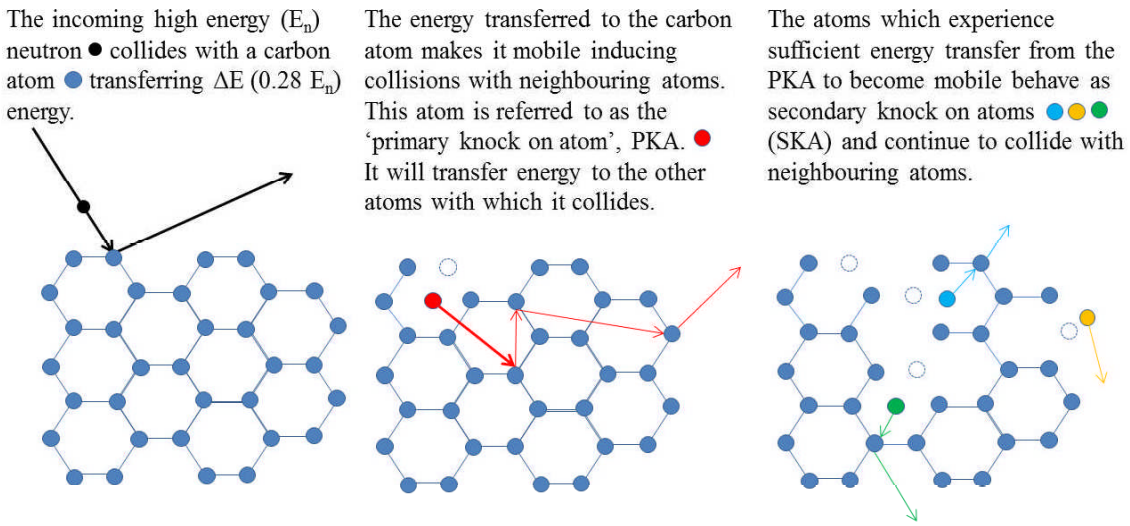

Figure 2.3: Illustration of the effect of a high energy neutron on the atomic lattice.

It is important to note the decrease in energy with collisions. From equation 2.1 above, the transfer of energy of the neutron following the first collision will be 0.28 of the first collision's energy, which is only 0.08 of the original neutron energy. These low energies make it uncommon to have a large series of knock on atoms; however the original collision can displace a large number of atoms alone. Graphite bombarded by high energy neutrons has a dpa of several thousand (Haag, 2005). In some cases, where the target lattice is already unstable, the collision cascade can induce a shock wave whereby distant material is damaged (Krasheninnikov & Nordlund, 2010).

Simulation of neutron radiation in a TEM

To imitate safely the behaviour of neutron radiation damage in the laboratory, ion or electron radiation can be used. It is therefore essential to be aware of the differences and similarities between ion, electron, and neutron irradiation and take these into account when analysing results. Although the ion/electron will

be rapidly neutralised by capturing electrons from the carbon atoms, they will continue to be described as an ion for the sake of particle differentiation.

When comparing electron to neutron radiation, the mass difference should be considered; the mass of a neutron is around 2000 more than an electron, which explains why the energy transfer from neutrons is much more than from electrons. According to calculations by Thrower & Mayer (1978) a 1 MeV neutron and electron produce an average of 500 and 1.6 atomic displacements respectively.

Electron excitation can also cause radiation damage to a material. The total stopping power of the incident particle can be described as the sum of the nuclear stopping power and the electron stopping power (Krasheninnikov & Nordlund, 2010). The nuclear stopping power accounts for the elastic collision between the incident particle and the carbon atom and the electron stopping power involves the slowing down of the incident particle due to collisions between the incident particle and the bound electrons in the carbon atom. As the latter collision is inelastic it is possible for the electrons in either the carbon atom or the incident particle to become excited. This can only occur with charged particles thus is not present in nuclear reactors where neutrons are the incident particle. The main factor influencing the level of damage from electron stopping is the electronic structure of the target. In graphite the excitation of delocalised electrons reduces the conversion of excitation energy to thermal energy thus reducing the level of kinetic energy of the carbon atoms. In such systems, nuclear stopping is dominant.

Higher TEM electron energies allow for thicker specimen examination and simulated radiation damage but increase the risk of unwanted specimen damage during the examination of neutron irradiated specimens. On using TEM to observe atomic defects in neutron irradiated graphite it is important to ensure the atomic displacement threshold energy is not exceeded as this would further distort the lattice structure giving misleading results. The displacement threshold energy is the minimum amount of energy required by the incident particle to displace at least one atom to an interstitial position or for it to completely leave the system (Krasheninnikov & Nordlund, 2010). If the damage threshold, E_{DT}, for a material is known, equation 2.2 can be used to calculate an appropriate, non-damaging, TEM accelerating voltage.

$$E_{DT} = \frac{4m_e}{m_C} E_{TEM} \tag{2.2}$$

where E_{TEM} is the energy of the electron beam, and m_e and m_C are the masses of the electron and carbon atom respectively (Krasheninnikov & Nordlund, 2010). Only a fraction of the electron beam energy is transferred to the carbon atom ($4m_e/m_C = 1.8 \times 10^{-4}$), a figure significantly lower than the 0.28 transferred due to neutron bombardment (as established in equation 2.1). If the damage threshold energy for carbon atoms in graphite is taken to be 15 eV (Krasheninnikov & Nordlund, 2010), the TEM operating voltage should therefore be lower than 82 kV to prevent sample damage in neutron irradiated samples (Banhart *et al.*, 2011; Krasheninnikov & Nordlund, 2010).

When imitating neutron radiation damage with a field electron gun in a TEM, it is also important to account for the higher electron dose rate of electrons to neutrons in a nuclear reactor (by about 10^4) and the reduced cascade damage from electrons due to their lower mass (El-Barbary *et al.*, 2006). Electron irradiation results in point defect damage whereas the higher mass of neutron irradiation causes cascade damage. The wide spacing of graphite's lattice planes results in low density collision cascades and the low neutron doses (10^{-7} dpa s^{-1}) and high temperatures (450°C) in a nuclear reactor allows cascade damage to partly anneal between cascade events (Karthik *et al.*, 2011). The net effect of this is point defect damage in neutron irradiated nuclear graphite which is comparable to relatively high dose (10^{-4} to 10^{-3} dpa s^{-1}) electron beam induced damage (Karthik *et al.*, 2011; Koike & Pedraza, 1992).

2.1.2 Point defects and dislocations

Atoms within the crystal structure have well defined crystallographic positions however during exposure to radiation these may alter. Point defects are concerned with single atomic sites and defects involving larger numbers of atoms are usually described as line defects (dislocations) or plane defects (grain boundaries/stacking faults). Many defects occur and/or anneal over extremely short timescales (picoseconds), but those which do not can migrate to form larger line or plane defects (Krasheninnikov & Nordlund, 2010). Understanding radiation

induced changes in atomic structure and bonding is important for the interpretation of EEL spectra and TEM lattice images.

Point defects

During neutron irradiation in the graphite core, relatively high energy neutrons collide with carbon atoms which can be displaced from their lattice positions. This phenomenon is referred to as the Wigner effect and results in a vacancy and interstitial pair (Frenkel pair). Although the atomic structure has changed, the density of the system does not as both volume and mass are conserved.

An interstitial atom is one which has been knocked out of its perfect lattice point and relocates to a non-atomic lattice point outside of the basal plane. Interstitials do not occur within the hexagonal lattice as the energy required to do so is considerably higher than an inter-planar location and would cause intense localised strain (Banhart, 1999). Locating between planes is therefore energetically favoured. The interstitial formation energy, E_{fi}, has been thoroughly investigated both theoretically and experimentally however the values in both cases vary somewhat. Formation energies can be difficult to accurately calculate due to the energy of the defect super cell being of the order 10^3 times higher than the formation energy. Thus the super cell energy must be accurate to about five significant figures (Li *et al.*, 2005).

There are two contradicting models to describe the behaviour of the atomic structure when the interstitial moves in between lattice layers. The Kelly and Latham models differ with respect to dimensional change and atomic bonding (Kelly, 1971; Latham *et al.*, 2008). However, it is generally agreed that single or multi-interstitials can be integrated with an extra plane leading to a localised curvature of existing planes (Banhart *et al.*, 2011).

In 1971, Kelly derived a model to investigate the interaction between interstitials and their neighbouring planes. The findings of the model were compared to experimental data and it was concluded that inter-planar interstitials did not form covalent bonds with the neighbouring basal planes. When concentrating on the dimensional changes in graphite following neutron irradiation, Kelly proposed two kinds of interstitial behaviour: interstitial cluster growth by capturing single

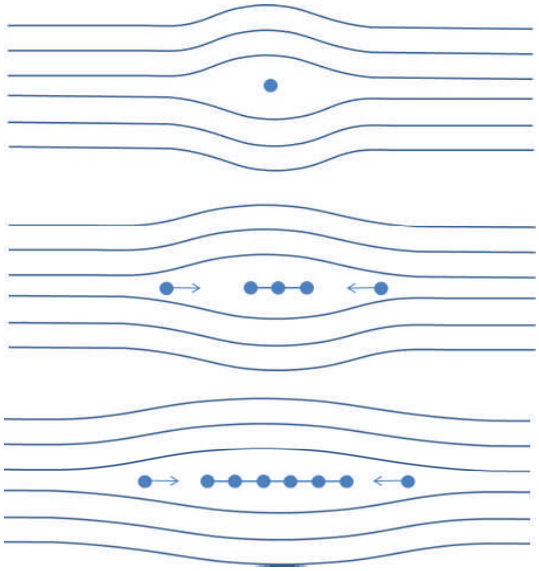

Figure 2.4: Kelly model (Kelly, 1971).

interstitials; and interstitial cluster growth to a stable size of 4 ± 2 atoms wide (which is regularly broken up by radiation to maintain such a size). At small doses where the stable clusters are not regularly broken up, the interstitials form small linear groups between the defect planes as illustrated in figure 2.4. According to Kelly's experimental results, highly ordered pyrolytic graphite expanded in the c direction at relatively low neutron doses of $5 - 10 \times 10^{20}$ neutrons cm^{-2} ($0.6 - 1.2$ dpa) and contracted in the a direction at temperatures between 150°C and 700°C. The c direction expansion agrees with the loops of interstitials accumulating between basal planes. The a plane contraction is accounted for by the migration of vacancies to crystal boundaries at temperatures above which vacancies become mobile. Experimental results also revealed a constant change in total volume. Kelly's explanation for such behaviour was based upon the combination of interstitial loop growth and vacancy cluster collapse parallel to the basal planes. This proposal showed a quite good agreement with experimental data (Kelly, 1981). These complex dimensional changes are thought to be reversed by thermal annealing but will be exaggerated under further radiation (Metcalfe & Payne, 2008).

In recent years, a new model has been developed based on the inter-planar interstitial forming covalent bonds with its neighbouring planes to cause defor-

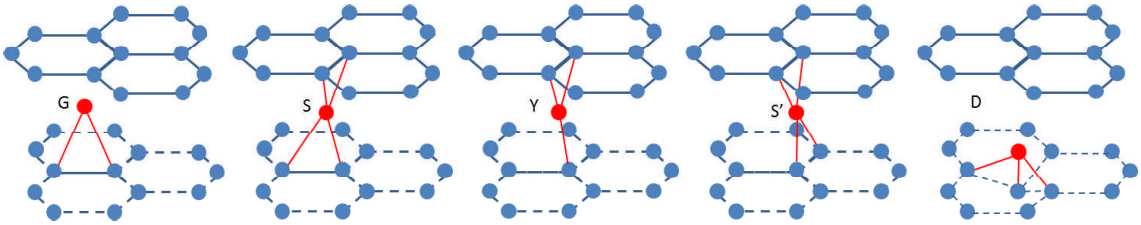

Figure 2.5: (Left to right) Schematic of the grafted (G), spiro (S), y-lid (Y), migrated-spiro (S'), and dumbbell (D) interstitial arrangements. Adapted from (Gulans *et al.*, 2011; Ma, 2007; Telling *et al.*, 2003).

mation in the opposite direction. It has been proposed by Latham *et al.* (2008); Telling *et al.* (2003); Teobaldi *et al.* (2010) that there are four arrangements which the extra atom can take: grafted; spiro; dumbbell; and y-lid saddle point with a stability dependent on their formation energy. The most basic arrangement is the grafted-interstitial (figure 2.5G) which bonds with two atoms in one of the neighbouring planes to form a triangle like shape. An interstitial which forms bonds with four atoms, (two atoms in the layers both above and below) is referred to as a spiro-interstitial (figure 2.5S). This has been found to be the most stable interstitial configuration (Gulans *et al.*, 2011; Li *et al.*, 2005; Ma, 2007; Teobaldi *et al.*, 2010). A slight alteration to the grafted-interstitial is the dumbbell-interstitial (figure 2.5D) whereby the orientation of the triangle tilts to allow an extra bond to be formed between the interstitial and another atom in the same plane. It is the least stable of all the interstitials (Gulans *et al.*, 2011; Teobaldi *et al.*, 2010). Note the position of the interstitial atoms with respect to its neighbouring planes; none of the interstitial positions match up to either the A or B layers, thus introducing a new layer positioning; C. The theoretical formation energies vary between each interstitial configuration and are dependent on the exact method of calculation but are generally between 5.5 eV and 7.5 eV (Gulans *et al.*, 2011; Latham *et al.*, 2008; Li *et al.*, 2005; Ma, 2007; Teobaldi *et al.*, 2010).

When the system experiences basal sheer the spiro-interstitial becomes mobile, and can traverse through the lattice structure in the a direction by breaking and reforming bonds. The new position of the spiro is noted S' and is made possible by the y-lid (figure 2.5Y) bonding arrangement. The energy threshold at which

the spiro-interstitial can migrate is yet to be fully understood as the migration route and end position can vary. Several calculated figures have been proposed for all possible migration routes ranging from 0.1 eV to 2.12 eV (Gulans *et al.*, 2011; Ma, 2007; Mitchell & Taylor, 1965; Telling *et al.*, 2003; Thrower & Mayer, 1978; Zhang *et al.*, 2010). An increased number of bonds will induce localised basal plane curvature as illustrated in figure 2.6 (Li *et al.*, 2005).

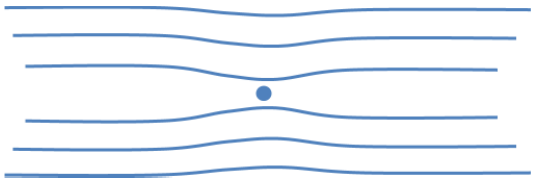

Figure 2.6: Latham model

Latham *et al.* (2008) proposed that the initial migration of single interstitials leads to the formation of strongly bound di-interstitials which are essentially immobile up to very high temperatures and result in dimensional change inconsistent with the measured values (Banhart *et al.*, 2011; Latham *et al.*, 2008). This theory contradicts the behaviour of interstitials in the Wigner effect where the accumulation of interstitials leads to areas of high energy density (Mitchell & Taylor, 1965). There are multiple types of di-interstitial configurations, each having a slightly different binding energy, ranging from 1.3 eV for the double split interstitial defect and 2.78 eV for the grafted interlayer bridge defect (Latham *et al.*, 2008).

Vacancies are formed due to an atom moving from its lattice point, resulting in an empty lattice point. The rate of migration of a vacancy increases exponentially with temperature (Hull & Bacon, 2011). On the formation of a single vacancy (SV), three bonds are left without a carbon atom; these bonds undergo a process known as Jahn-Teller distortion which involves the saturation of two of the three missing bonds leaving the final one to attach to its nearest neighbour resulting in a pentagon and a nonagon as illustrated in figure 2.7.

The strength of the crystal structure prevents the surrounding atoms totally collapsing into the vacancy site however a certain degree of 'relaxation' is experienced (Hull & Bacon, 2011), the extent of which depends on the atomic spacing

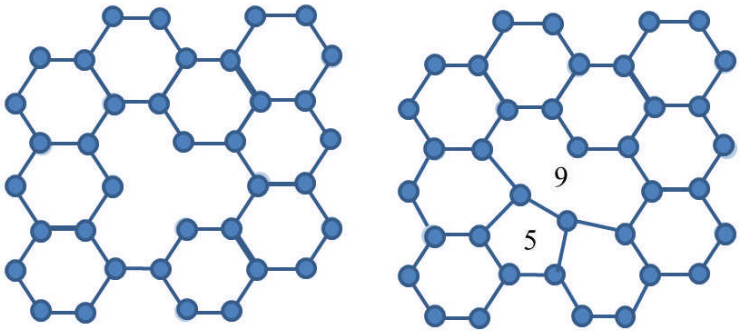

Figure 2.7: Relaxation of atoms around a SV (5-9)

within the lattice and the size of the atoms in the system. The process of relaxation has been found to reduce the formation energy thus increasing stability: "This (5-9) configuration has a relatively high formation energy due to the increased local density of states at the Fermi energy which is spatially localized on the dangling bonds" (Banhart *et al.*, 2011).

Di-vacancies (DV) occur when either two vacancies migrate together or when two neighbouring atoms are removed at the same time. The four dangling bonds join to form two new bonds. DV structures (as illustrated in figure 2.8(a)) have been seen in graphene (Banhart *et al.*, 2011; Gass *et al.*, 2008). This structure relaxes from four hexagons in perfect graphite to two pentagons and an octagon, and is referred to as the DV (5-8-5), illustrated in figure 2.8(c). The formation energy of a di-vacancy is comparable to that of the single vacancy defect however as there are two missing atoms in the di-vacancy configuration; the energy per missing atom is lower, making it more thermodynamically stable. This results in the di-vacancy having a higher migration energy than the single vacancy (Banhart *et al.*, 2011).

The stability of an interlayer di-vacancy means that it can stimulate vacancy aggregation, extending the interlayer defect by an increase in interlayer bonding from dangling bonds. This gradual extension results in a structure whereby two neighbouring planes are linked by a continuous plane (figure 2.9). Trevethan *et al.* (2013) demonstrated that extended interlayer defects can occur in graphite via aggregation of vacancy point defects and are stable to high temperatures (>1000°C).

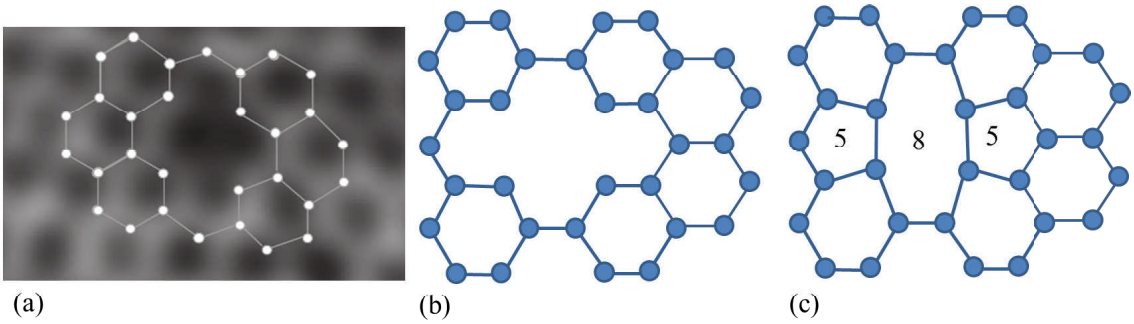

Figure 2.8: (a) HRTEM image showing a DV in graphene (Gass *et al.*, 2008). (b) Schematic of the DV. (c) Relaxation of atoms around a DV to produce a DV (5-8-5).

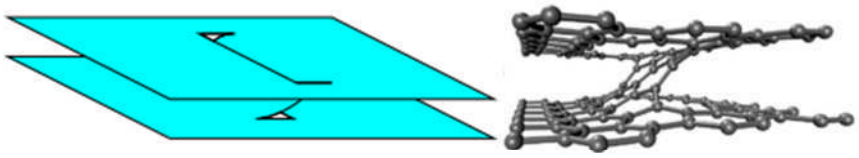

Figure 2.9: Schematic (left) and example of the atomic arrangement (right) of an extended inter-planar defect in graphite (Trevethan *et al.*, 2013).

To conserve charge within the lattice, vacancies must be with an interstitial (Frenkel pair). The combination of mobile interstitials and vacancies results in significant multi-dimensional changes for polycrystalline graphite. For crystalline materials such as HOPG there is expansion in the c direction, due to new lattice planes forming from interstitial clusters, and contraction in the a direction, due to vacancies migrating to grain boundaries (Haag, 2005; Karthik *et al.*, 2011). However slow moving interstitials and vacancies are more likely to recombine as a Frenkel pair and annihilate. Large crystal sizes are thus less likely to experience permanent radiation damage explaining the need for high temperature graphitization during nuclear graphite manufacture (Haag, 2005). A Stone-Wales (SW) defect involves the movement of atoms within the lattice to form pentagons, hexagons, heptagons and/or octagons. No atoms are gained or lost, but bonds are broken and reformed.

Line defects

Understanding the behaviour of point defects provides the building blocks for understanding larger dislocation structures. As interstitials and vacancies migrate they coalesce, bind together, and lower their energy becoming less mobile. The behaviour of such clusters has been investigated since the mid-1960s by Reynolds and Thrower (1965) and is still of great interest today (Banhart *et al.*, 2011; Krasheninnikov & Nordlund, 2010). Clusters of interstitals can vary in size from di-interstitals involving only two defect atoms to multiple interstital clusters of a few nanometers in width (Telling *et al.*, 2003). Larger clusters of interstitials are refered to as dislocations and are generally associated with linear lattice faults. The main types are edge, screw, and dislocation loops.

Edge (basal) dislocation

The shear stress on the graphite core can result in lattice dislocations. For a finite number of notional planes, shear stress can result in lattices splitting causing an edge, or basal, dislocation.

For the infinite case, as assumed in graphite, a half plane may become stationary between full planes with a different layering position, C. The base of the half lattice is noted as $\perp$ (figure 2.10). Theoretical work of Ewels *et al.* (2003) has proposed that the bridging defects illustrated in figure 2.5 are likely to be associated with the creation of an edge dislocation due to the spontaneous shear force generated (Ewels *et al.*, 2003; Latham *et al.*, 2008). Understanding the movement of such dislocations is essential for predicting the structural behaviour of the material over time. The movement of planar dislocations through a structure is referred to as glide which is best described pictorially in figure 2.11. As the extra half plane of atoms moves, bonds are constantly broken and reformed. Dislocation glide allows for a reasonable level of plasticity within the structure.

Screw dislocation

In a screw dislocation, the movement of the defect is perpendicular to the direction of applied shear stress. The result is a break in the structure where the planes experiencing the shear stress move away from one another as illustrated in

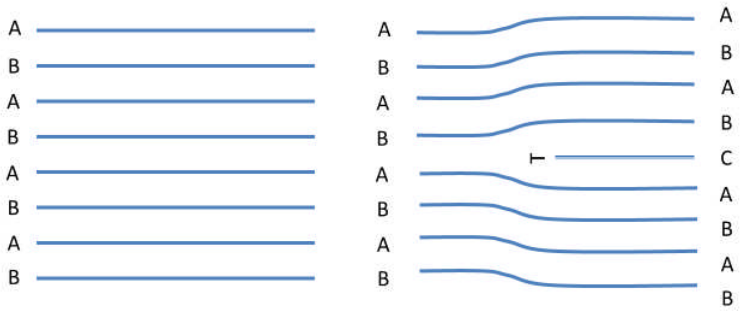

Figure 2.10: Edge or basal dislocation for AB stacked graphite. A new plane of stacking position C is introduced

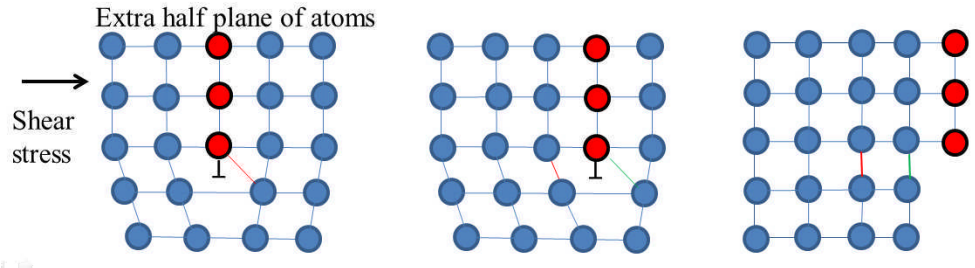

Figure 2.11: Dislocation glide

figure 2.12. The spiralling movement of this dislocation means that it is sometimes referred to as a helix. Eventually a helical path will appear (Hull & Bacon, 2011). The net plastic deformation of the edge and screw dislocation is in fact the same even though the edge dislocation moves parallel to the direction of shear stress and the shear dislocation moves perpendicular. As these dislocations progress and interact they begin to hinder the movement of neighbouring dislocations which results in increased levels of embrittlement (Crouse, 2011; Wirth, 2007).

Dislocation loops

There are two types of dislocation loops: those formed by vacancies and those by interstitials. When vacancies accumulate and collapse under stress they form vacancy loops, resulting in a direction contraction. Interstitial loops form between basal planes and result in c direction expansion. Dislocation loops are mobile along the grain boundaries and can change size with the absorption and emission of defects. Large prismatic dislocation loops impede dislocation glide,

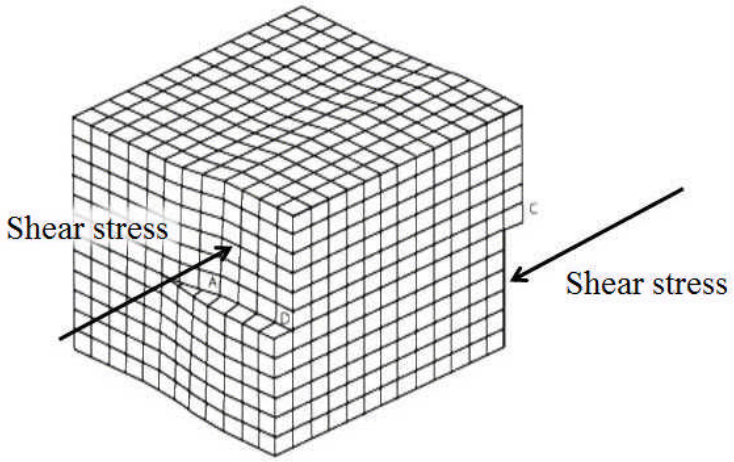

Figure 2.12: Screw dislocation (Crouse, 2011)

weakening the structure (Fitzgerald & Yao, 2009). It is therefore thought that both vacancy and interstitial dislocation loops contribute the most damage with increased embrittlement and dimensional change (Telling *et al.*, 2003; Wirth, 2007).

Novel theory, ruck and tuck

A new theory for the behaviour of graphitic planes following irradiation was proposed by Heggie *et al.* in 2011. According to this model, when planes of different length are inter-connected at two points with the single interstitials described in figure 2.5, localised buckling can occur (as it is energetically favourable for the long section to compress and buckle, rather than the shorter sheets stretching).

It is estimated that around one third of the super cell energy is contained in these buckles (where a super cell is defined as a cell containing multiple original unit cells; e.g. once a 3x3x3 unit cell configuration is achieved, the super cell is made a single unit cell by removing the symmetry to enable the substitution of atoms or the creation of vacancies). At temperatures below 250°C the calculated dimensional changes were 63% *c*-axis expansion and 5% *a*-axis contraction the latter of which agrees well with experimental data (Kelly *et al.*, 2000; Shtrombakh *et al.*, 1995). When temperatures rise above 250°C the interlayer spacing is consistently 0.34 nm (from X-ray diffraction (XRD) measurements), yet expan-

sion in the c-axis continues. This is explained by the 'ruck and tuck' of planes. The loss of the single interstitial inter-planar connectors means that the edge dislocations are free to interact and the 'pile up' of dislocations results in an accumulation of matter which is bent and folded (ruck and tuck) as illustrated in figure 2.13. This theory explains the large energy release that occurs below the defect migration temperature ($\sim$ 300°C), with Frenkel pair recombination and the disappearance of single interstitial inter-planar connectors. It also addresses the large dimensional changes, which dislocation loops struggle to explain. Note that many models and theories used to understand the dimensional changes of neutron irradiated graphite are based on crystalline as opposed to polycrystalline graphite. Polycrystalline graphite has a much more complex structure, thus more complex modelling is required involving embryonic voids of vacancies at grain boundaries and changes in material strength (Haag, 2005).

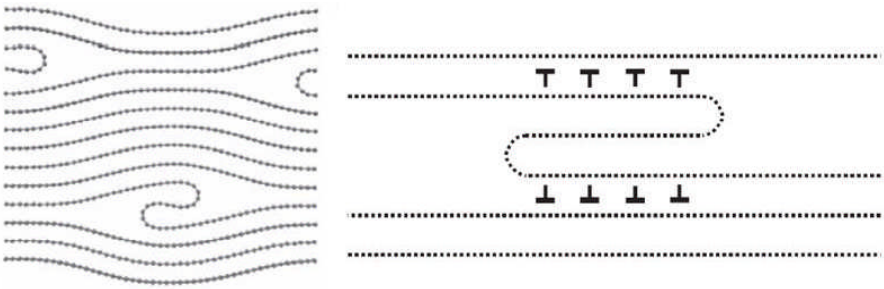

Figure 2.13: 'Ruck and tuck' dislocation (Heggie *et al.*, 2011)

2.1.3 Microstructure

Nuclear graphite consists of a coke-based filler, a binder matrix containing small filler particles (flour), and voids. The voids are in the form of gas-escape pores and cracks of varying dimension accounting for ~20% of the total volume. Nuclear graphite is polycrystalline and is often imparted with a preferred orientation via extrusion which assumes the filler crystallites are aligned with their c axes perpendicular to the extrusion direction. The border in which two crystal orientations or domains meet is referred to as a grain, or domain, boundary. The energies at domain/grain boundaries are more than those between single crystals; boundaries which meet their neighbour's edge at an imperfect angle result

in small voids as illustrated in figure 2.14, where larger voids result in higher energies. Under neutron radiation, it is common for the crystals to become fragmented. Reduction in crystal sizes (from XRD coherence lengths) are as high as 70% for HOPG, but are generally between 35% and 50% for nuclear grade graphites (Gallego *et al.*, 2006, 2013; Mironov, 2015; Zhou *et al.*, 2014). The removal of volatiles during the manufacturing process produces gas-escape pores which are open and do not accommodate thermal expansion due to their larger dimension (Yan *et al.*, 2014); however they do affect properties such as strength, thermal conductivity and Young's modulus, particularly under radiolytic oxidation during reactor operation (Sutton & Howard, 1962).

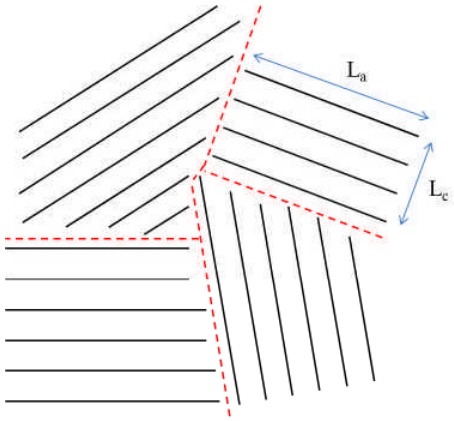

Figure 2.14: Grain boundaries in polycrystalline graphite.

During almost every step in the high temperature graphitization process associated with the manufacture of nuclear graphite and also during reactor operation, cracks arise due to a number of factors. Firstly, as a result of gradients in both temperature (during manufacture and operation) and neutron flux (during operation) and, secondly, as a result of the anisotropy of the coefficient of thermal expansion (CTE) in crystallites and the consequent generation of internal stresses beyond the elastic limit of graphite crystals (Delannay *et al.*, 2014; Hacker *et al.*, 2000; Mrozowski, 1954). The internal stresses act on both the carbon bonds between crystallites and on the van der Waals forces between basal planes; to relieve this stress cracks form, more usually between the weaker bound basal planes. Since the CTE is higher in the crystallographic c direction ($\sim$20-40 x 10^{-6} K^{-1} compared to $<$1.5 x 10^{-6} K^{-1} in the a direction), lenticular cleavage

cracks between basal planes, known as Mrozowski cracks, are observed to form lying approximately perpendicular to the crystallographic c direction as a result of anisotropic contraction following post-graphitization cooling during manufacture (Hacker *et al.*, 2000; Mrozowski, 1954; Sutton & Howard, 1962). With increasing dose during reactor operation, the rate of contraction or shrinkage of graphite components in the a-axis direction reduces, and eventually the graphite starts to experience net expansion; the critical point at which this reversal occurs is known as "turnaround" which can vary with operating temperature (Hall *et al.*, 2006). Mrozowski cracks lead to turnaround as they provide accommodation for the initial expansion in the c-axis direction up to a point. When Mrozowski cracks become closed, then net expansion occurs (Hacker *et al.*, 2000; Wen *et al.*, 2008).

Microcracks can be classified into two categories: intra and inter-granular, where the former are found within crystallites and lie perpendicular to the crystallographic c direction (e.g. Mrozowski cracks (Mrozowski, 1954; Sutton & Howard, 1962)). The latter lie between crystallites at grain boundaries with, in principal no specific orientation with respect to neighbouring basal planes, unless crystallites are aligned into domains as a result of mesophase development. Within thermally anisotropic filler particles, (closed) calcination cracks form due to volumetric shrinkage during the 1300°C calcination stage in the manufacturing process (Hacker *et al.*, 2000).

2.2 Bulk properties

2.2.1 Thermal conductivity

Thermal conductivity is the measure of a material's ability to transfer heat. Heat is transferred predominantly by phonons; the thermal conductivity is therefore dependent on the phonon mean free path and velocity.

Graphite Properties

Single Crystal	In a single crystal, the thermal conductivity is higher in the a-axis by a factor of 10^5 due to strong covalent bonds (Sun *et al.*, 2009). Experimental and theoretical calculations have found the thermal conductivity to vary between 1660 - 1900 $\mathrm{Wm}^{-1}K^{-1}$ at 25°C in the a-axis and to be ∼0.013 $\mathrm{Wm}^{-1}K^{-1}$ at 25°C in the c-axis (Holland *et al.*, 1966; Klemens & Pedraza, 1994; Null *et al.*, 1972; Sun *et al.*, 2009). The thermal conductivity has also been found to decrease with increasing temperature and when the grain size in the $a-b$ plane is less than 2 μm in size (Klemens & Pedraza, 1994; Sun *et al.*, 2009).
Virgin nuclear grade	The net thermal conductivity of nuclear graphite is relatively high and generally ranges from ∼60 to 170 $\mathrm{Wm}^{-1}K^{-1}$ at 25°C (Baker, 1970; Burchell *et al.*, 2000; Matsuo, 1980). The main factor to influence thermal conductivity in nuclear graphite is porosity. Heat transfer across pores is lower to that across graphite and will involve convection, conduction and radiation thus increasing the number of variables on which thermal conductivity depends (Matsuo, 1980).
Irradiated nuclear grade	The heat produced during a nuclear reaction is efficiently dissipated due to the high thermal conductivity of graphite and the fact that heat is carried out of the reactor system via the coolant fluid (Lewis, 2008). When the phonon mean free path and velocity are hindered by atomic defects due to neutron irradiation, the thermal conductivity will decrease (Baker, 1970; Haag, 2005). Although slight decreases in thermal conductivity due to neutron irradiation can be accommodated, significant reductions must be avoided to prevent a reduction in system safety (Burchell *et al.*, 2000). If insufficient heat is carried away from the core, the fuel can overheat resulting in the release of radiation (Haag, 2005). Thermal conductivity also decreases with increased weight loss, i.e. decreased density, due to thermal oxidation (Matsuo, 1980). Thermal annealing has been found to partially recover the change in thermal conductivity (to around 30% the virgin value following 1200°C annealing) (Ishiyama *et al.*, 2008; Maruyama & Harayama, 1992).

2.2.2 Young's modulus

Graphite is able to retain many of its mechanical properties at very high temperatures due the strong covalent bonds, high thermal conductivity and low coefficient

of thermal expansion (Burchell *et al.*, 2000; Haag, 2005). At very high temperatures, the strength of graphite increases, maximising at ∼2500°C, and even at temperatures over 1500°C it's strength exceeds that of many other materials. The melting point is 3977°C at 103 atm (Baker, 1970). The Young's modulus is a ratio of stress to strain used to measure the stiffness of a material; a high Young's modulus material is stiffer than that with a low value.

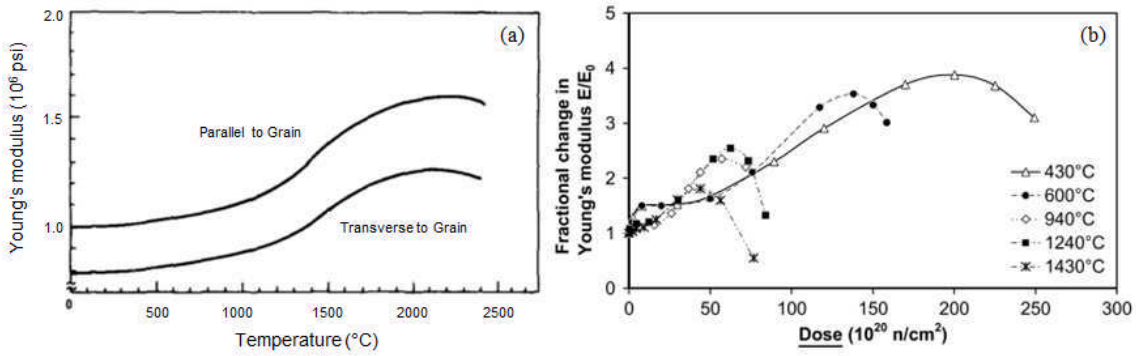

Figure 2.15: (a) Difference in Young's modulus with temperature in two directions: parallel to grain and transverse to grain (Baker, 1970). (b) Change in Young's modulus as a function of neutron dose for Gilsocarbon nuclear grade graphite (Hall *et al.*, 2006).

Graphite	**Properties**
Single Crystal	Graphite is stiffer in the a direction than the c due to strong covalent bonding and in high vacuum conditions, the stiffness has been observed to increase by 30% due to an increase in inter-crystallite cohesion via strong valency forces (Baker, 1970; Deacon & Goodman, 1958; Rowe, 1960).
Virgin nuclear grade	The stiffness of nuclear graphite can be engineered and depends on crystal orientation, density, and manufacturing procedures. Minimising the levels of adsorbed gases during the manufacturing process significantly stiffens the material (Rowe, 1960; Smith *et al.*, 1964). At room temperature, the average Young's modulus is slightly anisotropic; between 5 and 10 GPa parallel to the grain, and 4 to 8 GPa transverse to the grain (figure 2.15(a)) (Baker, 1970).

Irradiated nuclear grade	In 1970, Baker stated that the Young's modulus for graphite increases with temperature, however Haag's study in 2005 stated that any changes in temperature have little effect on the modulus; it is the neutron flux which dominates the variation. At high fluxes, the modulus will increase and tighten the structure. However embryonic void production during c direction expansion and a direction contraction eventually results in a net decrease in the Young's modulus (Haag, 2005). At low doses, the Young's modulus increases (usually 2-3 times that of the original value (Hall *et al.*, 2006; Ishiyama *et al.*, 2008; Shtrombakh *et al.*, 1995)). With increasing neutron irradiation, the rate of increase of the Young's modulus reduces until a certain dose threshold where the Young's modulus begins to decrease, sometimes to values below the original. The threshold of this change in behaviour becomes lower for higher operating temperatures, as displayed in figure 2.15(b).

2.2.3 Electrical resistivity

Electrical resistivity is a measure of how resistant a material is to an electrical current. As well as giving information about the electrical flow within a material, the resistivity also gives information about the level of crystallinity. The eddy-current technique is the most common method used to measure electrical resistivity (Kennedy, 1990; Young & Freedman, 2007).

Graphite	**Properties**
Single Crystal	The value of resistivity can be used as an indicator of crystallinity; anisotropic pyrolytic carbons for example exhibit much higher values of electrical resistivity in the a direction to the c direction by an order of $\sim 10^3$ due to the poor conductivity between widely spaced basal planes (Baker, 1970; Haag, 2005).
Virgin nuclear grade	Virgin graphite has a net electrical resistivity of 7 to 15 $\Omega\mu$m at room temperature (Baker, 1970; Haag, 2005). Values of electrical resistivity vary with respect to extrusion direction from the manufacturing process; values are nearly double that in the parallel direction compared to the transverse direction. The calcination and graphitization temperatures during manufacture can also affect electrical resistivity due to their influence on the ultimate crystallinity on the final product.

Irradiated nuclear grade

During neutron radiation the electrical resistivity increases in the *a* direction (due to defects encouraging electron scattering which disrupts bonds within the basal plane) and decreases in the *c* direction (due to extra coupling between layers) (Heggie *et al.*, 2011; Telling *et al.*, 2003). However, even at low neutron fluxes the net electrical resistivity of graphite increases significantly (figure 2.16) (Baker, 1970). Despite this, a saturation level is rapidly reached where the changes thereafter are extremely slow (Haag, 2005). Changes in electrical resistivity due to neutron irradiation do not usually differ between graphite grades or operating temperatures.

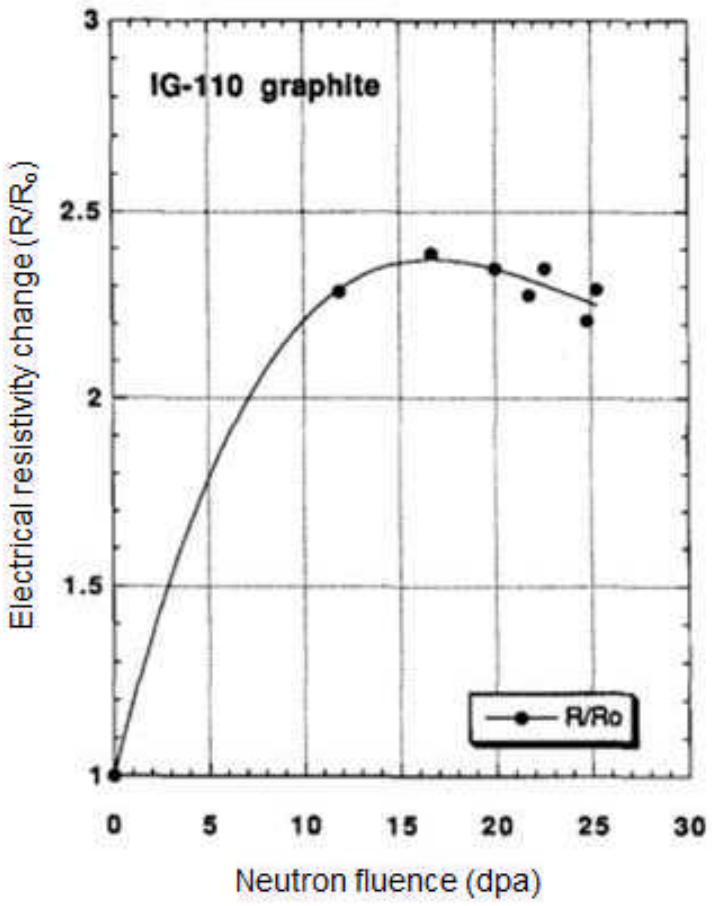

Figure 2.16: Change in electrical resistivity as a function of neutron dose for IG-110 graphite (Ishiyama *et al.*, 2008).

2.2.4 Coefficient of thermal expansion

Thermal expansion involves a change in linear dimension or volume as a result of a change in temperature. Thermomechanical analysis is used to measure the initial dimensions of the sample and record the finite changes experienced following a change in temperature.

Graphite	**Properties**
Single Crystal	Due to the layered structure of graphite, the coefficient of thermal expansion (CTE) is different for the crystallographic a (<1.5 $\times 10^{-6}$ K^{-1}) and c (∼20-40 $\times 10^{-6}$ K^{-1}) directions. During heating, expansion is more notable in the c direction. This anisotropy is due to the layered structure of graphite; the relatively large spacing of planes and weak van der Waals forces compared to the in-plane tightly covalently bonded structure. At low temperatures (<150°C), the stronger in-plane bonding can result in a negative CTE leading to contraction in the a direction.
Virgin nuclear grade	Due to high levels of porosity in nuclear graphite, the CTE is relatively low compared to the single crystal structure (Haag, 2005). Since the CTE is higher in the crystallographic c direction (∼20–40 $\times 10^{-6}$ °C^{-1} compared to <1.5 $\times 10^{-6}$ °C^{-1} in the a direction) lenticular cleavage cracks (known as Mrozowski cracks) are observed to form approximately perpendicular to the c direction. This is a result of greater contraction in the c direction following cooling during the manufacturing process (Baker, 1970; Burchell *et al.*, 2000; Mrozowski, 1954; Nightingale, 1962; Sutton & Howard, 1962).

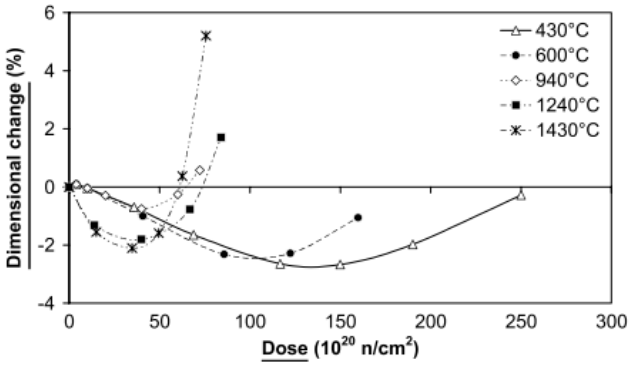

Figure 2.17: Dimensional change as a function of neutron dose for Gilsocarbon (Hall *et al.*, 2006).

Irradiated nuclear grade

The pores and cracks within nuclear graphite are able to accommodate some of the localised crystallite expansion during fast neutron irradiation. With increasing dose during reactor operation, the rate of contraction or shrinkage reduces and eventually the graphite starts to expand; the point at which this reversal occurs is known as turnaround and can vary with operating temperature and dose (Hall *et al.*, 2006). Figure 2.17 shows that for lower temperatures, turnaround occurs at higher neutron irradiation doses and vice versa; however beyond 1200°C turnaround remains at approximately 30×10^{20} neutrons cm^{-2}. The closure and generation of cracks influences the net expansion of the extruded component, but it is the closure of cleavage cracks which primarily influences the change in bulk CTE during neutron irradiation (increasing CTE with crack closure) (Baker, 1970; Sutton & Howard, 1962). Dimensional change is often more discreet in the bulk than in a single crystal due to the accommodation of expansion in the *c* direction in pores, Mrozowski cracks, and microcracks (Hacker *et al.*, 2000; Kelly *et al.*, 1966a; Wen *et al.*, 2008).

2.2.5 Irradiation induced creep

During irradiation, materials exhibit creep to lessen the increased stress levels from dimensional change which could lead to fracture. Creep involves material deformation at high temperature when subject to a constant load. In graphite, point defects created during neutron radiation are able to migrate through the lattice and enable the irradiation creep mechanism. There are three types of creep: permanent set creep; transient creep; and steady state creep. The former two behave proportionally to elastic strain whereas the latter is thought to be proportional to the total stress and neutron dose (Neighbour & Hacker, 2005; Simmons, 1965). Creep can be measured by analysing the change in the ratio of creep strain to elastic strain as a function of fast neutron fluence (Neighbour & Hacker, 2005). It is time dependent and varies with density, crystal orientation, and manufacturing process and can affect a variety of chemical and physical properties. Experimental evidence suggests that creep increases linearly with dose but does not vary significantly with respect to the temperatures experienced in a graphite moderated nuclear reactor (300 - 600°C) (Baker, 1970; Haag, 2005).

Chapter 3

Literature Review

When comparing the length scales to assess the structure of graphite four major constituents will be discussed: filler/binder phases, sometimes referred to as particles or grains; domains of aligned crystallites within these phases; single crystallites within the domains; and localised dislocations in and between the basal planes. The various techniques used for assessing the structure at different length scales and the benefits and limitations of each will be discussed throughout.

3.1 Nanostructure

3.1.1 TEM

High resolution TEM (HRTEM), selected area electron diffraction (SAED), and dark field imaging are commonly used to investigate the arrangement of basal planes and their atoms following the manufacturing process and to observe structural changes arising from irradiation.

The spacing of SAED (002) diffraction spots is related to the average d-spacing via Bragg's law ($n\lambda = 2dsin\theta$) (Muto & Tanabe, 1997). It is easily and accurately determined by examining the intensity profile in the diffraction pattern and measuring the peak to peak spacing. The opening angle of the (002) spots is related to the level of disorder, where narrow spots imply perfect graphite, sharp rings imply polycrystalline graphite, and diffuse halos imply an amorphous structure.

The effect of irradiation on cleaved flakes of graphite single crystals was the subject of several significant publications in the 1960s (Baker & Kelly, 1965;

Reynolds, W.N.; Thrower, 1965; Thrower, 1964, 1967). It was found that interstitial dislocation loops formed at irradiation temperatures below 650°C interrupting the AB stacking sequence. This suggests interstitials are mobile below 650°C and are able to aggregate to form larger interstitial structures. At temperatures above 650°C, smaller vacancy loops were observed in neighbouring planes as shown in figure 3.1 (Thrower, 1964, 1967). Irradiation experiments at 650°C and of 0.5 $\times$ 10^{20} neutrons cm^{-2} showed that the smaller dislocation loops were joined by dislocation lines (Reynolds, W.N.; Thrower, 1965).

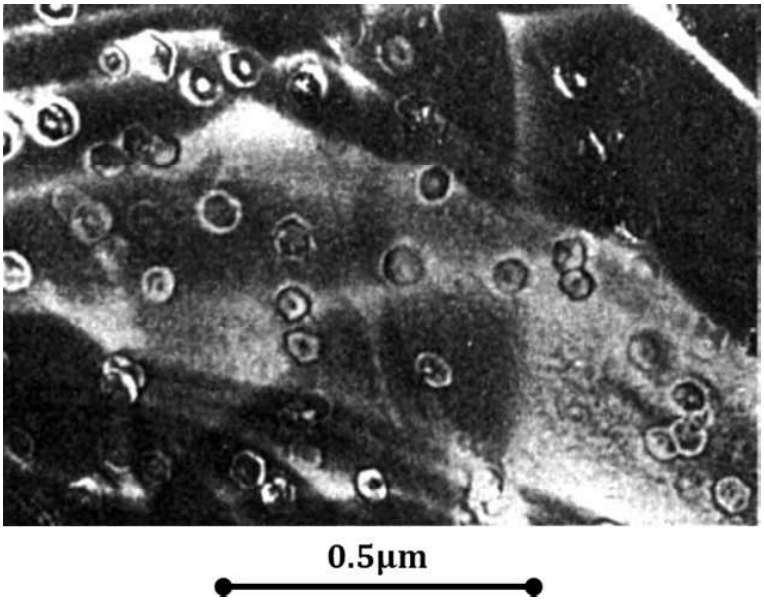

Figure 3.1: Dark field TEM image of dislocation loops in cleaved graphite single crystals, neutron irradiated at 900°C to 1.85 $\times$ 10^{20} neutrons cm^{-2} (Thrower, 1967).

Muto & Tanabe (1997) investigated the effect of 200 kV electron irradiation on highly graphitized carbon fibre. Both lattice images and SAED patterns were collected. The spacing of planes was measured directly from the micrographs, from the spacing of (002) diffraction spots in the SAED pattern, and from the spacing of (002) spots in fast Fourier transforms (FFTs) of micrographs. Results from the latter two were compared. SAED data showed a homogeneous increase in d-spacing of 11% following 2500 seconds of beam exposure (2.5 x 10^{22} electrons cm^{-2}) after which no significant changes were observed. Calculations of d-spacing from the FFTs showed a more rapid expansion (figure 3.2). The diffraction spots

remained radially sharp, implying homogeneous expansion. The saturation of expansion in the c-axis following irradiation contradicts the findings of Kushita & Hojou (1991) and Niwase & Tanabe (1993) who studied H and He radiation damage in graphite, reporting near amorphous structures through the development of diffuse rings in electron diffractions patterns. Results also contradict the findings of Iwata (1985); Kelly (1981); Maeta *et al.* (1975) who proposed c-axis expansion was attributed to the inter-planar accumulation of interstitials and the formation of dislocation loops, rather than an increase in *d*-spacing.

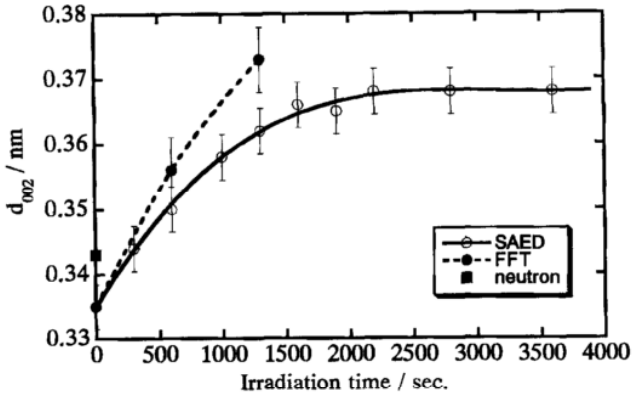

Figure 3.2: Change in d-spacing as measured by SAED and FFT. For comparison, the black square shows lattice spacing of neutron irradiated carbon fibre (1.9 x 10^{24} neutrons m^{-2} (Muto & Tanabe, 1997).

Following experiments at room temperature, Muto & Tanabe (1999) repeated similar experiments at high temperatures under higher electron energies using TEM, SAED, and EELS on cleaved graphite thin foils and highly graphitized carbon fibres. Lattice images of carbon fibre under a 1 MV electron beam (fluence not reported) at 400°C showed slight disruption to the basal planes but not to the same extent as at room temperature and under a 200 kV beam (figure 3.3).

After 1 hour of 200 kV electron beam exposure, SAED patterns (along [001]) at the the two temperatures showed significant differences: irradiation at room temperature resulted in diffuse rings whereas irradiation at 400°C gave sharp rings (figure 3.4). TEM images and SAED patterns (along [100]) also provided evidence for temperature-dependent structural changes. Inspection of the edge of the specimen revealed surfaces became undulated after 1 hour of electron beam

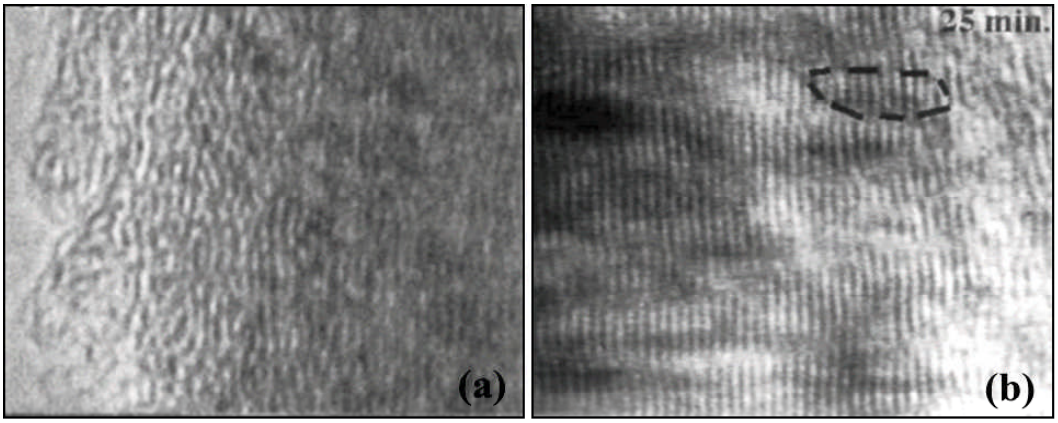

Figure 3.3: Comparison of electron irradiation at different temperatures and electron energies. (a) TEM micrograph of carbon fibre irradiated for 21 minutes under a 200 kV electron beam at room temperature (Muto & Tanabe, 1997) (b)TEM micrograph of carbon fibre irradiated for 25 minutes under a 1 MV electron beam at 400°C (Muto & Tanabe, 1999).

exposure at 400°C, suggesting the migration of interstitials to the surface, however the SAED patterns showed no change in d-spacing indicating that irradiation above 400°C does not alter the graphite structure locally. Lattice images were also collected at 400°C; after 25 minutes of electron irradiation under a 1 MV beam (required due to specimen thickness), bending and/or breaking of the lattice fringes were observed as well as fragmentation of crystallites. Analysis of these images provided further evidence for the retention of d-spacing. A temperature threshold was determined by considering a critical dose (defined as the dose at which the [001] diffraction pattern turned into diffuse rings). In this study the temperature threshold, where the effects of thermal annealing surpass the effects of ion-irradiation damage, was calculated to be 125°C. EEL spectra were collected for pre-irradiated specimens, after 1.6 hours of beam exposure at room temperature, and after 8 hours of beam exposure at 400°C. Although not quantitatively analysed, the spectra from the pre-irradiated specimens and specimens exposed to high temperatures showed little difference indicating that the hexagonal structure within basal planes was maintained following electron irradiation at 400°C. In contrast, the spectrum from room temperature electron irradiation exhibited significant changes in the π^* and σ^* peaks which was suggested to be

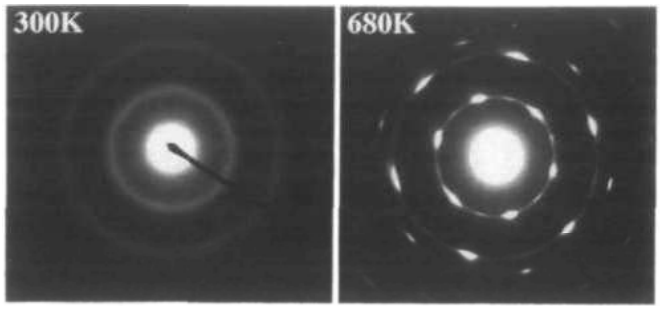

Figure 3.4: "Electron diffraction patterns along [001] of graphite electron-irradiated at 20°C for 1 hour and at 400°C for 4 hours" (Muto & Tanabe, 1999).

related to the formation of non-hexagonal atomic rings. It was proposed that the damaging process at 400°C was polycrystallization. The fragmented crystals were measured to be of the order of a few nanometres in diameter, and the undulating basal planes were thought to accommodate the inter-crystal strains. The defects which were observed to occur at 400°C were thought to exist between these fragmented crystallites.

Burden & Hutchison (1996) exposed specimens of "KS10" grade graphite particles (highly graphitized carbon with a particle size of 10 μm) to a 400 kV electron beam (10^{19} electrons $cm^{-2}s^{-1}$) at room temperature and also at 500°C. At room temperature crystalline particles deteriorated to amorphous spheres of up to 50 nm in diameter. However at 500°C the structural stability was significantly improved so that the specimen could be exposed for much longer (1200 s) without the formation of disordered carbonaceous spheres. It was suggested this was due to thermal energy providing the ability to resist and repair damage simultaneously.

Nakai *et al.* (1991) investigated the effect of electron irradiation (0.1-1.0 MV) on HOPG at a range of temperatures, from -160°C to 200°C. TEM images and SAED patterns along [001], and EEL spectra were collected. The fluence threshold for so called amorphization was measured for each temperature, where amorphization was recognised as diffuse rings in a [001] SAED pattern. For fluxes of $\sim 10^{19}$ electrons $cm^{-2}s^{-1}$ the fluence threshold gradually increased with increasing temperature, and increased significantly above 150°C (figure 3.5). There were no significant variations between different fluxes, suggesting that radiation damage is not flux dependent.

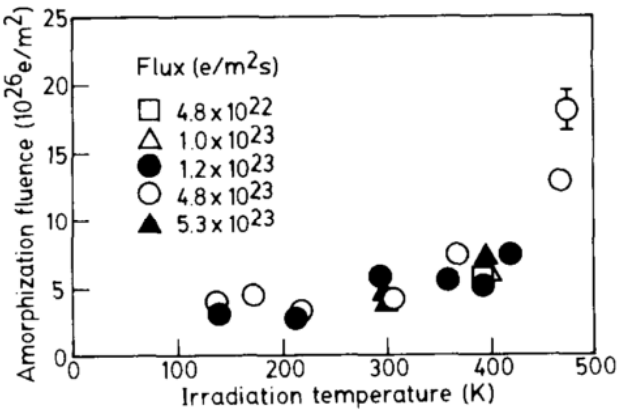

Figure 3.5: "Irradiation temperature dependence of the amorphization fluence under various 1 MV electron fluxes" (Nakai *et al.*, 1991).

The effects of 200 kV electron irradiation and its influence on the closure of cracks in nuclear grade graphite (NBG-18) was studied by Karthik *et al.* (2011) in real-time. Noised filtered lattice images (via notch-pass filtering of fast Fourier transforms) were used to aid the identification of irradiation induced structures leading to "unprecedented clarity" of vacancy and interstitial loops, and resulting dislocations in the processed images. After 2.5 $\times$ 10^{22} electrons cm^{-2} what was thought to be a dislocation dipole was identified. The average d-spacing was observed to change by 13% and was calculated from the Fourier transforms. Based on the work of Muto & Tanabe (1997) and figure 3.2 it would be reasonable to suppose this is a slight over estimate. Noise filtering a series of images during electron beam exposure allowed the movement of specific dislocations to be tracked. Karthik *et al.* used such a method to follow the formation of a dislocation dipole via vacancy loops (figure 3.6(a-d)). Although figure 3.6 appears to show a clear change in structure it must be noted that noise filtering not only removes noise from the image but potentially blocks other structural information from higher angle scattered electrons. Furthermore, irradiation induced changes in the thickness, the effective defocus of the specimen, and graphitic nature of the specimen (which affects contrast) must be accounted for, making TEM image interpretation of disordered material a delicate task, to be conducted with caution.

A similar study was published by Karthik *et al.* (2015) investigating the ef-

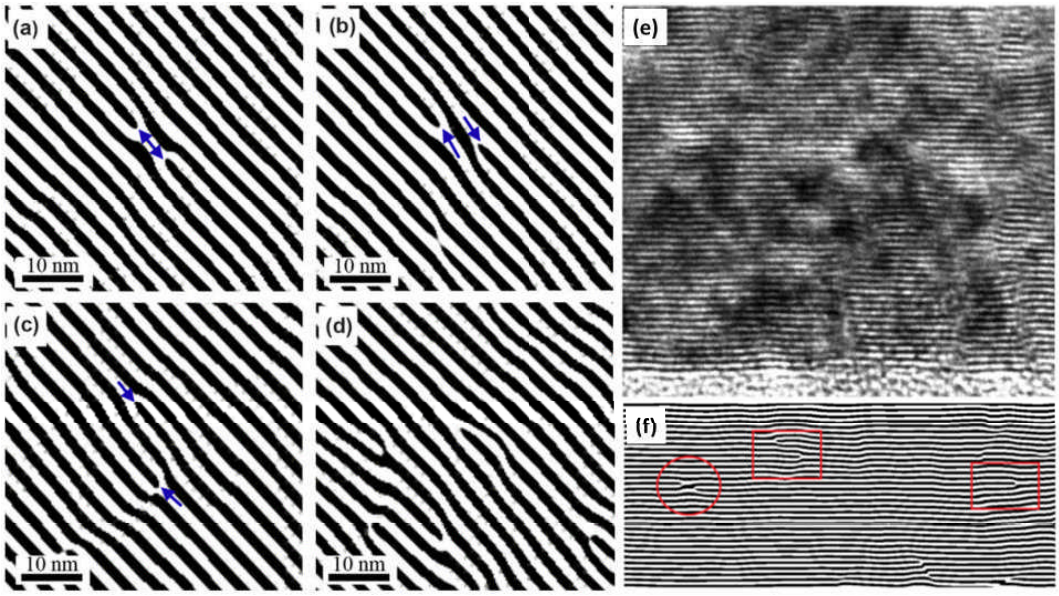

Figure 3.6: "Noise filtered HRTEM images showing the formation of dislocation dipoles via vacancy loops (a) shows the nucleation of a vacancy loop (~0.25 dpa) dissociating itself into a set of dislocations as shown in (b) with the incomplete planes marked with arrows, (c) shows the growth of the incomplete planes via positive climb and (d) shows the accumulation of several dislocations at higher irradiation doses resulting in disordering of the graphite lattice. Distance between two black fringes corresponds to (002) inter-planar spacing (~0.36 nm)." (Karthik *et al.*, 2011). "(e) High resolution TEM image of a filler particle in NBG-18 graphite irradiated to 6.78 dpa showing the presence of defects in the lattice. (f) Is a noise filtered image of a section of (e) showing the presence of dislocations. Distance between two black fringes corresponds to (002) inter-planar spacing (~0.37 nm)." (Karthik *et al.*, 2015).

fects of neutron irradiation on the micro and nanostructure. TEM lattice images (collected at 200 kV) of NBG-18 and IG-110 graphite specimens irradiated to 6.78 dpa at 678°C provided evidence for intense nanostructural damage through the fragmentation and bending of basal planes, however the retention of (002) spots in SAED patterns showed that the layered structure was preserved. Noise filtering of lattice images was used to highlight extended interlayer defects and prismatic dislocations, similar to those found from electron irradiation (figure 3.6) (Karthik *et al.*, 2011). Neutron irradiated specimens appeared to exhibit less significant damage than electron irradiation, even for what are considered

high doses of >6.7 dpa. It is assumed the largely retained structure is due to the higher irradiation temperatures (∼678°C) which allows point defects to migrate and thermally anneal. Images and SAED patterns were not analysed to quantify the degree of damage at each dose.

Neutron irradiated HOPG was studied in the TEM by Asthana *et al.* (2005) to extract information about the irradiation induced structural disorder. Specimens were irradiated at 60°C to doses of 3.2 x 10^{20} neutrons m^{-2}. Observation of TEM lattice images showed breaking and bending of basal planes. Broadening of SAED spots was observed for irradiated specimens and the increase in (002) d-spacing was observed to increase to 0.381 nm, 10% more than unirradiated HOPG measurement. Intensity profiles across lattice images were also used to determine average d-spacing; results from this technique also gave an irradiated d-spacing value of 0.38 nm, although this time this is 12% more than the unirradiated HOPG measurement. Measurements of the d-spacing from the FFTs of micrographs were also made. This technique gave a slightly larger value of 0.41 nm. This is consistent with the findings of Muto & Tanabe (1997) (figure 3.2) that calculations of d-spacing from Fourier transforms give a slightly higher value than SAED analysis. No further image analysis was performed in this study.

Nuclear-grade ATR-2E graphite was irradiated by Tsai *et al.* (2013) with 3 MeV C^{2+} ions at 500-800°C. TEM lattice images (at 200 kV) and FFTs of micrographs were collected after 0.6 dpa, 3 dpa, and 10 dpa of ion irradiation, and were used to measure changes in the atomic and crystalline structure. TEM lattice images showed a fragmented nanotexture with a wavy morphology and planar defects. The change in d-spacing was measured from FFTs which showed that after 10 dpa at 600°C, the spacing of basal panes expanded from 0.336 nm to 0.396 nm (18%). The largest strain in the c-axis was experienced at 600°C; at 500°C, 700°C, and 800°C the d-spacing increased by 13.5%, 16.1%, and 13.6% respectively. It was proposed that 600°C is the temperature threshold which defines the point at which the effects of thermal annealing surpass the effects of ion-irradiation damage. This is a higher temperature threshold than that proposed by Muto & Tanabe (1999) (125°C).

In situ ion irradiation of graphite has also been studied by Hinks *et al.* (2014). Single crystal HOPG was subject to 60 keV Xe^{+} ions at room temperature and

imaged in situ using TEM (at 80 kV), and ex situ TEM (at 300 kV). Images were captured perpendicular to the basal planes. At fluences above $\sim 3 \times 10^{12}$ ions cm^2 structural changes were observed as a result of mechanical stress. The damage profile was seen to vary with specimen depth and hence resulted in differing degrees of a-axis contraction. This was thought to create the observed dislocations and kink band networks inducing a polycrystalline structure and localised doming.

Takeuchi *et al.* (1997) used FFTs of lattice images to calculate the radial distribution function (RDF) in HOPG as a function of electron fluence. Each peak in the RDF relates to the i^{th} nearest neighbour. The 3^{rd} peak experienced a negative shift with dose indicating a decrease in the 3^{rd} nearest neighbour distance and a buckling of basal planes as observed in TEM images of Karthik *et al.* (2011); Muto & Tanabe (1997); and Muto & Tanabe (1999) and in agreement with the idea that non six-membered rings are introduced to the structure as a result of radiation damage. The 4^{th} peak experienced a positive shift suggesting the interlayer spacing of planes increases with irradiation ($\sim$5% after 10^{23} electrons cm^{-2}).

The measurement of the opening angle in an SAED can be ambiguous as it depends on what the data analyst considers to be the edge of a diffraction spot (see figure 3.7). To address this problem, Campbell *et al.* developed an SAED analysis software program where the radial intensity around the (002) ring is plotted and the FWHM of the two peaks (representing the two (002) spots) is measured (figure 3.8). This automated approach was verified against X-ray diffraction data; the program can also determine *d*-spacing as per the method described above, has open access and has been named GAAP (Graphite Anisotropy Analysis Program). Its application to the SAED patterns collected for this thesis will be further discussed in Chapter 6.

3.1.2 TEM image analysis

The most common approach to assess the structure from a TEM lattice image is to count the number of planes and dislocations before and after irradiation (Karthik *et al.*, 2011; Muto & Tanabe, 1997). This can have high error margins, as what might be assumed to be a dislocation may be a change in phase contrast

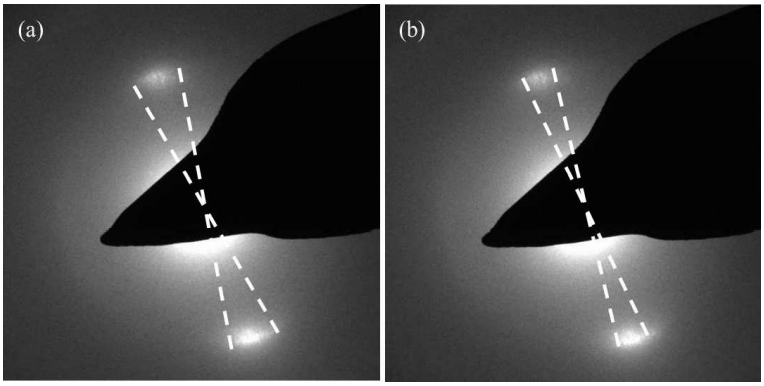

Figure 3.7: Two of the same SAED pattern demonstrating different interpretations of the opening angle.

or specimen thickness (the issues associated with TEM image interpretation is discussed in more detail in section 4.2). It can also be time consuming if many micrographs are to be analysed.

In an attempt to understand changes in lattice images following electron irradiation, Muto & Tanabe (1997) used multislice TEM image simulations (along [100]) incorporating interstitial clusters. The secondary contrast effects from small clusters influencing the translational symmetry of the local crystal structure were investigated. A variety of interstitial clusters and loops were inserted between planes, and the surrounding lattice was relaxed. It was found that the change in contrast and d-spacing is dependent on the loop size: those larger than half the sample thickness were visible in TEM image simulations, whereas a loop which is much less than half the sample thickness, the effect on the surrounding lattice is unobservable. Since image simulation did not reveal structures comparable to direct TEM observations it was concluded that loops were not the sole reason behind the lattice dilation observed experimentally by Muto & Tanabe (1997). The change in bonding, the development of three dimensional structural changes, and the introduction of non-hexagonal atomic rings were also suggested to be contributing factors.

In 1989 Parent & Zucker focused on developing an algorithm to distinguish between merged curved lines in a range of images. The algorithm directly detects curves and was applied to the arrangement of blood vessels in the brain, fingerprint identification and detecting logging roads in forests. To improve this

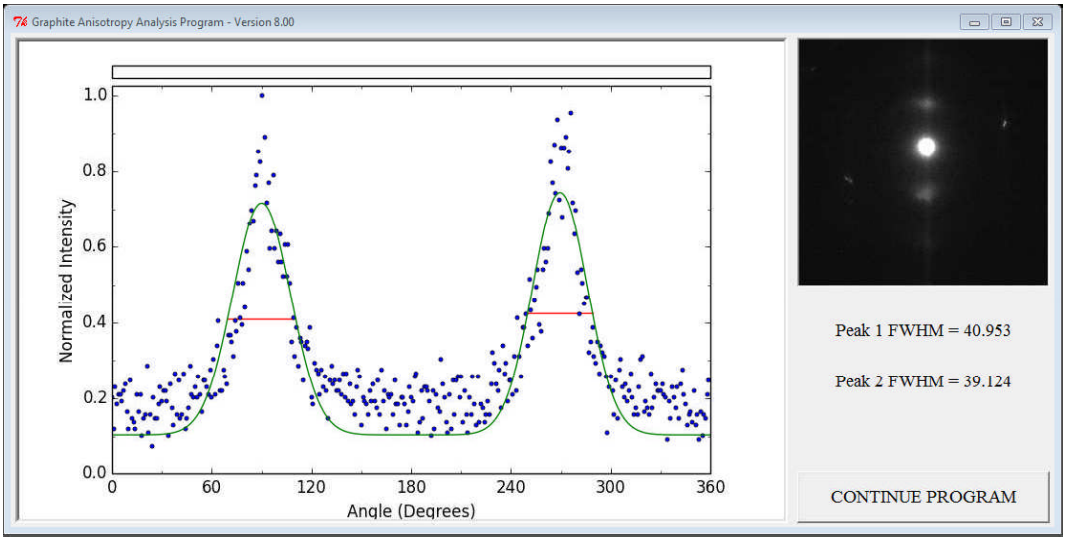

Figure 3.8: Application of GAAP to an SAED pattern of highly ordered pyrolyitc graphite (HOPG) showing the normalised intensity around the (0 0 1) ring vs. the azimuthal angle. Gaussian curves (green) are fitted over the data points (blue) and the FWHM of each peak is calculated from the red line.

technique, Donahue & Rokhlin (1993) developed an algorithm which was able to determine the components of a curve, tangential direction and curvature, without directly extracting the entire curve structure. It was also used to identify finger prints and quantify the structure of porous membranes. By 2000 a research group at the University of Bordeaux working on pyrocarbons developed a TEM-specific lattice fringe image analysis algorithm to fully automate the process; making it objective, quantitative, and more efficient. The 'directional texture characterization' software is capable of applying a grey scale threshold to record the pixels which represent basal planes in order to measure their length and tortuosity (curvature) (DaCosta *et al.*, 2000). The algorithm was first applied to basic structures such as those illustrated in 2.14 and then to filtered TEM images of a carbon-carbon composite. An orientation mapping system has since been developed to complement fringe detection data and examine lattice fringe orientation fields without detecting single lattice planes (DaCosta *et al.*, 2014).

3.1.3 3D atomistic models

To complement the 2D TEM lattice image analysis software of DaCosta *et al.* (2000), a 3D atomistic modelling procedure based on the statistical and constrained reconstruction of HRTEM images was developed by Leyssale *et al.* (2009). The details of this technique are discussed in section 4.2.2. The image guided atomistic reconstruction (IGAR) technique is capable of determining the number of non-hexagonal rings and measures sp^2 and sp^3 content. Figure 3.9 shows how this data is displayed; six membered rings are coloured in blue and non six membered rings in orange. Coloured display allows defects to be easily identified.

Application of the IGAR technique to 16 planes of 'as prepared' (AP) and 17 planes of heat-treated (HT) rough laminar pyrocarbons showed that the AP pyrocarbon had an sp^2 content of $\sim$ 97.3%, sp^3 content of $\sim$ 2.2%, and the proportion of non-hexagonal rings was 12%. For HT pyrocarbons, the sp^2 content was calculated to be $\sim$ 99%, sp^3 content was $\sim$ 0.8%, and the proportion of non-hexagonal rings was 11% (Leyssale *et al.*, 2012). It is believed that the proportion of non-hexagonal rings counted by IGAR is too high and work is in progress to correct this by reducing the quench rates (of the simulated annealing) and introducing H atoms to the system.

There have also been studies which examine the change in atomic structure during a graphitization series, in which the stages of structural change can be considered to be a reversal of radiation damage. Powles *et al.* (2009) performed molecular-dynamics simulations on highly disordered amorphous carbon precursors to determine the change in sp^2 content during heat treatment. A low density 4096-atom amorphous carbon precursor was effectively heat treated for 200 ps to 3225°C and 3725°C. The pre heat-treated structure was calculated to contain 36% sp, 58% sp^2, and 6% sp^3 bonded atoms. Depending on the periodic boundary conditions (0D to 3D), different structures were formed. All structures saw an increase in sp^2 but each differed with respect to the curvature of the formed planes. Nevertheless, all structures experienced a near-complete sp^2 transformation after 200 ps of heat treatment. It was concluded there were two contributing factors that led to "collective organisation": the original geometry of the atoms, and the original density of the system (Powles *et al.*, 2009).

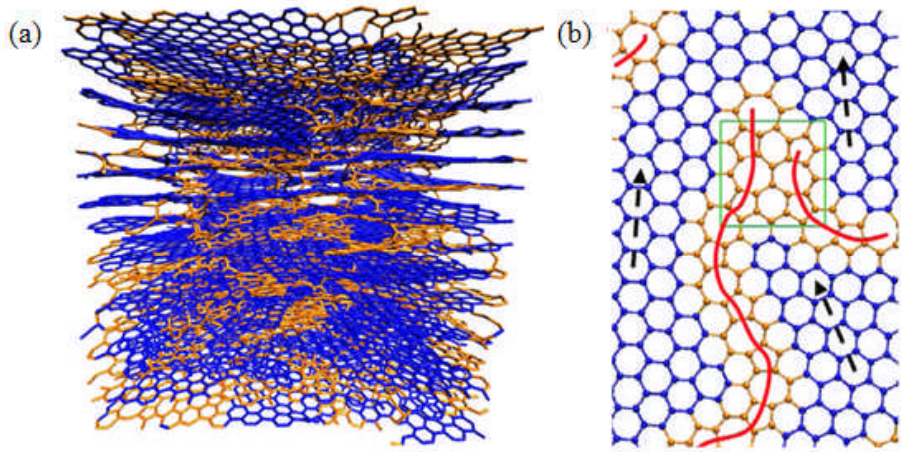

Figure 3.9: Demonstration of the IGAR 3D modelling process to a rough laminar pyrocarbon. (a) "Snapshot of the 16 fringes AP PyC model. Bonds between carbon atoms belonging to pure hexagonal domains are shown with blue sticks. Other bonds are shown with orange sticks.", (b) "Snapshots of some carbon sheets; orientations of some hexagonal domains are indicated by dashed black arrows and a $C_5^2C_6^3C_7^2$ defect is highlighted by a green rectangle." (Leyssale *et al.*, 2012).

3.1.4 Electron energy loss spectroscopy

Many papers reporting radiation damage by TEM investigation also use EELS to substantiate findings. When EELS of graphite is performed, there are usually two to five main areas of interest depending on the rigour of the investigation or the information required. In the low loss region, the position of the $(\pi + \sigma)$ plasmon peak (around 25 eV) gives information about valence electron density and the presence of the π plasmon indicates the presence of a layered structure and delocalised π bonding. In the core loss region, the relative intensities of the π^* and σ^* peaks at the carbon K-edge are related to the sp^2 content or graphitic nature of the specimen, the position of the multiple scattering resonance (MSR) peak (around 325 eV) can be used to calculate in-plane bond lengths, and the residual Gaussian in the trough between the π^* and σ^* peaks is related to fullerene (or non-planar sp^2) content (Daniels *et al.*, 2007; Egerton, 2009; Karthik *et al.*, 2011; Mironov *et al.*, 2015; Takeuchi *et al.*, 1997).

To validate TEM observations in the Karthik *et al.* (2011) paper, EEL spectra were collected for different electron irradiation exposures (figure 3.10). The low

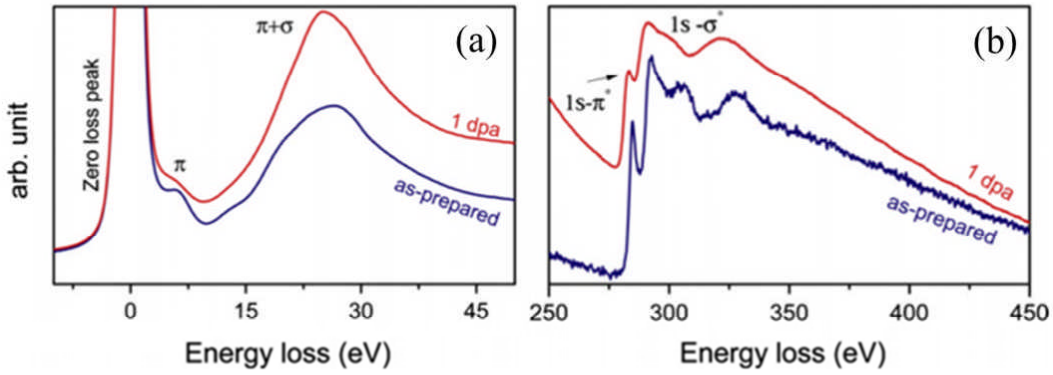

Figure 3.10: (a) Low and (b) core loss EEL spectra of nuclear graphite (NBG-18) before and after 1 dpa of irradiation (Karthik *et al.*, 2011).

loss region was examined to measure changes in the positions of the $(\pi + \sigma)$ and π plasmon peaks. After 1 dpa the $(\pi + \sigma)$ plasmon experienced a negative shift in energy of 1.9 eV indicating a 16% reduction in the valence electron density and subsequent increase in volume, as hypothesized. The stability of the π plasmon suggested the retention of the characteristic layered structure in graphite. The π^* and σ^* peaks in the core loss were also qualitatively analysed, the main observation being a loss in the fine structure of the σ^* tail which was assumed to be due to a deterioration in long range periodicity in the a direction due to reduction in the number of six-membered rings. It was also proposed that interstitial induced buckling of basal planes might lead to the creation of bucky onions. Although this has been observed in graphene, Karthik *et al.* (2011) find there is reason to believe there is a reduced chance in graphite due to the energetic constraints of neighbouring planes. No further quantitative analysis was performed on the EEL spectra collected by Karthik *et al.* (2011).

Takeuchi *et al.* (1997) also used EELS to complement TEM observations of electron irradiation by examining the plasmon peaks in the low loss region and the extended energy loss fine structure. As with Karthik *et al.*, a negative shift in the $(\pi + \sigma)$ plasmon position was observed (3 eV following 1 dpa) indicating a reduction in valence electron density due to an increase in volume in the c-direction and/or a reduction in the number of six-membered rings. The stability of the π plasmon suggests the retention of the characteristic layered structure in

graphite. At higher energies, the π^* and σ^* peaks at the carbon K-edge were not investigated.

As a response to the limited standard analysis of carbon K-edge π^* and σ^* peaks, Bernier *et al.* (2008); Daniels *et al.* (2007); Zhang *et al.* (2011) published a variety of progressive methodologies to optimize the quantification of sp^2 carbon. Prior to this work, there were two methods commonly applied to the π^* and σ^* peaks to extract sp^2 data. The first assumes no overlap between π^* and σ^* where a 'two window method' is used, with windows either centrally positioned over each peak or set with relation to the edge onset (∼282.5 eV) (Berger *et al.*, 1988; Bruley *et al.*, 1995). The second accounts for slight π^* and σ^* overlap and is referred to as the three Gaussian method where three fits are applied to the π^* peak at 285 eV, σ^* peak at 292 eV, and a residual at 288 eV (Bernier *et al.*, 2008; Díaz *et al.*, 2001). The two lower energy peaks are associated with the π^* content and the higher energy peak with the σ^*. Bernier *et al.* (2008) showed that the large number of variables associated with the three Gaussian method (FWHM, position, and intensity of each fit) gives a high level of uncertainty when calculating sp^2 content, particularly when trying to calculate a trend for a graphitization or radiation damage series of spectra. The suggested method was therefore based on the two window method with both windows positioned relative to the edge onset. The fitting function was constrained to density-of-unoccupied-states calculations with an upper energy limit. A satisfying fit was achieved for spectra from a wide variety of specimens, microscope resolutions, and data treatments with variations in sp^2 content to be as low as 4%. Daniels *et al.* (2007) also used a two window method, specifically investigating the effect of hydrogen content in a graphitic EELS core loss spectrum, whereas Zhang *et al.* (2011) developed the three Gaussian method to better understand discrepancies in sp^2 content data arising from the presence of strained sp^2 or curved layers.

The application of these techniques was published by Daniels *et al.* (2007) who studied a heat-treatment graphitization series of a petroleum pitch. Core loss EELS analysis showed pre heat-treated carbon to exhibit an sp^2 content of ∼55%, which increased to 100% after being heated to 2725°C. These results are in agreement with the molecular dynamics simulations performed by Powles *et al.* (2009) who found a low density amorphous carbon structure to have an sp^2

content of ∼58%, which increased to nearly 100% after being heated to 3225°C in 200 ps (discussed on page 44). In addition, the change in position of the multiple scattering resonance peak was studied. It was found that heat-treatment to 1725°C and beyond reduced the bond length from 1.435 to 1.420 Å. The low loss EEL spectra were also analysed; particularly the plasmon energy (associated with specimen density). Heat-treatment to 1725°C and above showed an increase in the plasmon energy from 22.7 eV to values associated with highly graphitized carbon (∼26 eV). These results are in agreement with findings of Fink *et al.* (1983, 1984); Leder & Suddeth (1960).

Information about specimen density, π bonding, and crystallinity in carbon materials can be extracted from the low loss EEL spectrum. Fink *et al.* (1984) analysed the low loss spectra from hard hydrogenated amorphous carbon film by using an 8 eV integration window over the π plasmon and a 40 eV window over the bulk plasmon (both with an onset of 0 eV). The ratio of the two integration areas was then normalised with respect to single crystal graphite. However, this method resulted in a considerable error of ± 30 % due to overlap of the two plasmon peaks. In an attempt to increase accuracy, Daniels et al. (2007) removed the zero loss peak (ZLP) and deconvolved the spectrum using the Fourier log method to remove the effects of plural inelastic scattering. A smaller integration window of 4 eV was used for the π plasmon peak and a larger integration window of 60 eV was used for the bulk plasmon peak so to include the majority of the inelastic intensity. Both integrations were performed with an onset of 4.5 eV. As with Fink *et al.*, comparisons were made by the ratio of the two integrations which were normalised with respect to single crystal graphite. A reduced error of ± 10 % was achieved with suspected sources of error originating from orientation effects due to the inability of satisfying the magic angle criterion at small scattering angles (see section 5.2 for a detailed discussion surrounding the calibration of the microscope to satisfy the magic angle).

3.2 Crystalline structure

Muto & Tanabe (1999) performed TEM and EELS on carbon fibre under a 1 MV electron beam at 400°C. On investigation of TEM images, SAED patterns,

and spectra, it was found that above this temperature, the structure consisted of fragmented graphite crystallites of a few nm in size, whose hexagonal structure within basal planes was maintained. The two most common techniques for measuring the crystalline structure are XRD and Raman.

3.2.1 X-ray diffraction

To measure the arrangement and size of crystallites within the microstructure, low magnification TEM. SAED with larger selected area apertures, and XRD is used. Imperfections are visible in XRD analysis through the increased width and occasional disappearance of peaks with respect to those observed for single crystal graphite. The integrity of the characteristic AB stacking sequence can be determined along with crystal sizes (coherence lengths L_a and L_c) and the d-spacing of basal planes (indirectly leading to dimensional change) (Bacon & Warren, 1956; Zheng *et al.*, 2014; Zhou *et al.*, 2014).

A typical XRD pattern is presented and labelled in figure 3.11 where the spacing of (002) planes is determined from the position of the (00l) reflected peaks through Bragg's law ($n\lambda = 2dsin\theta$) and the coherence lengths L_c and L_a through the full width half maximum (FWHM) of the (002) and (100) peaks respectively. XRD has been performed on a wide range of unirradiated and irradiated nuclear graphites where it has been reported that as the d-spacing increases, the increase in disorder is evident through the reduction in coherence lengths, L_c and L_a (indicating a smaller crystal size) (Zhou *et al.*, 2014). In general pre-irradiation coherence lengths range from 10 to 60 nm depending on coke source and manufacture processes, where L_c is nearly always larger than L_a due to the anisotropic nature of crystals (Hagos *et al.*, 2010; Zheng *et al.*, 2014; Zhou *et al.*, 2014).

Irradiation studies of HOPG at Oak Ridge National Laboratory by Gallego *et al.* (2013) showed a significant reduction in crystallite size with increasing dose. Neutron irradiation was conducted at ∼600°C to doses between 1.5 and 7 dpa. Analysis of the (110) and (002) peaks in XRD patterns provides crystallite size parameters L_a and L_c respectively. It was shown that large crystallites were found in virgin HOPG, of dimension 550 Å(L_a) × 700 Å(L_c). After 3-7 dpa of

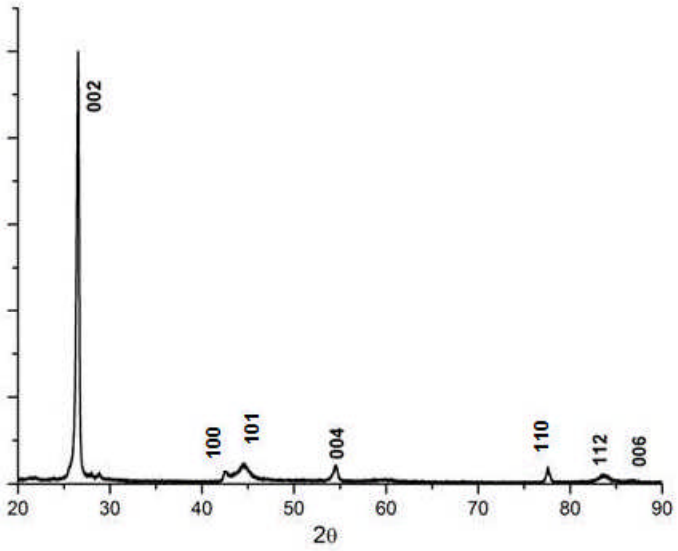

Figure 3.11: Typical XRD spectrum for virgin graphite, PCEA grade (courtesy of B. E. Mironov).

neutron irradiation, crystallite fragmentation resulted in a 60% (L_a) and 70% (L_c) reduction in crystallite size.

This was also found to be the case for nuclear grade graphites (PCEA and PCIB) by Mironov (2015). Neutron irradiation was conducted at ∼350-670°C to doses between 1.5 and 6.8 dpa and the XRD (110) and (002) peaks were analysed. Virgin specimens exhibited crystal sizes of ∼400 Å(L_a) × 230 Å(L_c) which reduced by 35% (in both L_a and L_c) for low dose, low temperature exposures and by 50% (in both L_a and L_c) for high dose, high temperature exposures (Mironov, 2015).

3.2.2 Raman spectroscopy

Raman is a spectroscopic technique which is widely used to measure the changes in L_a before and after irradiation and gives information about the level of disorder within the lattice. The two main peaks are known as the D (∼1350 cm^{-1}) and G (∼1583 cm^{-1}) bands; the former appears regardless of the type of defect and the G band is seen in all poly-aromatic hydrocarbons. It is the ratio of the two bands' intensities that gives information about the crystallite size, L_a, which can

then be compared to XRD measurements. The extent of disorder is also evident through the position and FWHM of the G band.

In 1970, Tuinstra and Koenig proposed that the I_D/I_G ratio was proportional to L_a^2 or $1/L_a$ depending on the material (i.e. amorphous or crystalline respectively) (figure 3.12). There has since been no general agreement about this relationship however two groups have emerged; one believes XRD should be the prominent tool to acquire information about crystallite size due to the high number of parameters which affect the D band intensity (Cuesta *et al.*, 1998), the other believes a correction factor (related to the energy of the Raman laser) can be applied to the I_D/I_G-L_a relationship making it a reliable technique (Knight & White, 1989; Pimenta *et al.*, 2007).

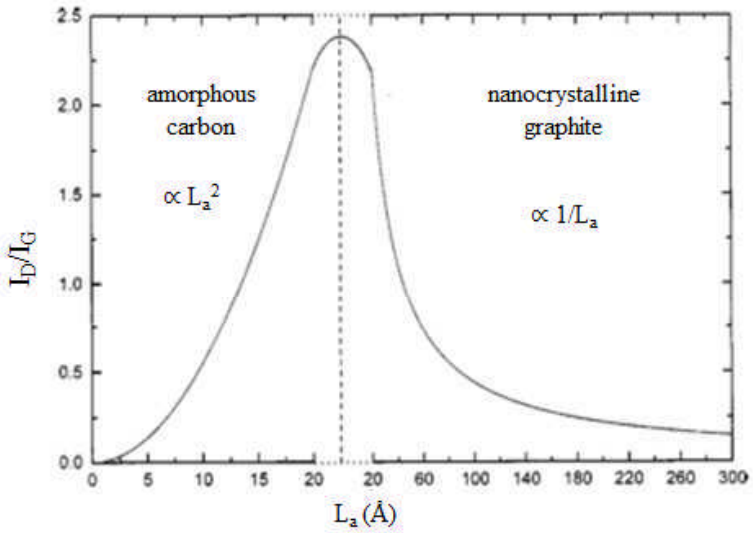

Figure 3.12: "Variation of the I_D/I_G ratio with L_a. The broad transition between the two regimes is indicated." (Ferrari & Robertson, 2000)

(Kwiecinska *et al.*, 2010) performed Raman spectroscopy on a range of carbonaceous materials of varying order and crystal size to understand their crystallographic structure, structural evolution, and graphitization. Analysis of the width of the G peak showed that samples of similar crystallographic properties were distinguishable through their degree of graphitization; where a decrease in peak width is associated to an increased degree of graphitization.

HOPG irradiated by D^+ and He^+ ions by Niwase & Tanabe (1993) became amorphized at a critical dose, which increased with increasing temperature. Through analysis of the relationship between the width of the G peak and the I_D/I_G ratio, Niwase & Tanabe (1993) identified three stages of damage: firstly, the accumulation of defects within the basal plane; second the introduction of basal plane fragmentation and turbulence; and finally amorphization.

3.3 Microstructure

Monitoring the changes in porosity and crack volume during manufacture and operation is important as several physical and chemical property changes occur as a result. The most significant effects are seen in the Young's modulus and thermal conductivity; both reduce by more than half for 30% porosity when compared to completely non-porous control specimens (Berre *et al.*, 2006; Matsuo, 1980).

Light microscopy on reactor and materials test reactor (MTR) samples is performed in order to get a qualitative view of the microstructure of different grades of nuclear graphite, and to measure microstructural changes following irradiation and oxidation. Optical microscopy (bright field (BF), polarised light (PLM) and fluorescence light (FLM)) and low magnification scanning electron microscopy (SEM) is used to measure the shape and size of filler and binder phases and the size and distribution of pores. Sample preparation for such techniques involves mechanical polishing to produce a scratch free surface. Silicon carbide is a commonly used grinding paper; samples are then polished with diamond pastes and washed with water/ethanol to remove the remaining material. For FLM, samples are generally impregnated under vacuum with a fluorescent resin which has a low enough viscosity to flow into open pores. Open and closed porosity are therefore best represented in fluorescence and bright field micrographs respectively as presented in figure 3.13. PLMs highlight areas of aligned crystallites and provide information about the distribution and shape of binder and filler phases. Particle sizes vary from $\sim$20 μm to 1.6 mm and porosity can occupy up to 25% of the material. These pores vary in size, from 20 Å to 300 Å in size and can be in the form of narrow cracks (usually found in the filler phase) to near-spherical pores (usually found in the binder phase) (see figure 3.13) (Hagos *et al.*, 2010;

Kane *et al.*, 2011; Nightingale, 1962). Graphites with smaller particles tend to have more isotropic properties and increased strength compared to large particle grades (Hagos *et al.*, 2010). The structure and size distribution of pores is closely related to the interfaces between the imperfectly packed binder and filler phases; according to Nightingale (1962) longer crystals give smaller pore volumes.

The degree of anisotropy in the crystals is translated through to the microstructure. Hagos *et al.* (2010) collected a series of PLMs of Pile Grade A (PGA), NBG-10, and NBG-18 graphites which showed PGA to have large regions of crystal alignment, with large and elongated pores and aligned coke particles, whereas the NGB-10 and NBG-18 specimens showed a more isotropic structure with smaller regions of crystal alignment and smaller pores (figure 3.14).

Kane *et al.* (2011) used BF light microscopy to investigate the shape of filler and binder phases. The circularity of the filler in nuclear graphite grades IG-110, PGX, NBG-18, and PCEA depended on the coke's ability to align the graphite crystallites during the manufacturing process; petroleum based cokes produce elongated filler particles due to their anisotropy arising from highly aligned crystallites (e.g. PGX, IG110, PCEA). Pitch based cokes are the opposite, where the poor alignment and subsequent isotropy gives circular, or onion-like, structures (e.g.NBG-18) (Kane *et al.*, 2011). Such structures are visible (and highlighted with coloured circles) in figure 3.13(b).

A range of microcrack sizes from less than ∼5 nm to 200 nm in width and up to 10 μm in length have been reported (Hacker *et al.*, 2000; Mrozowski, 1954; Sutton & Howard, 1962; Wen *et al.*, 2008). The nature of material within a crack depends on the graphite grade; it has been proposed that microcracks in Pile Grade A, Gilsocarbon, baked carbon (Wen *et al.*, 2008), and highly ordered pyrolytic graphite (HOPG) (Hinks *et al.*, 2012; Wen *et al.*, 2008) contain low density disordered carbon. However limited research has been carried out to characterise this material in both virgin and irradiated graphite which could better the understanding of the mechanisms involved in crack expansion and contraction (Hinks *et al.*, 2012; Sutton & Howard, 1962) and hence their influence on macroscopic properties such as CTE and elastic modulus during reactor operation.

Delannay *et al.* (2014) used crystal plasticity finite element modelling to predict irradiation-induced dimensional change and variations in CTE at a variety

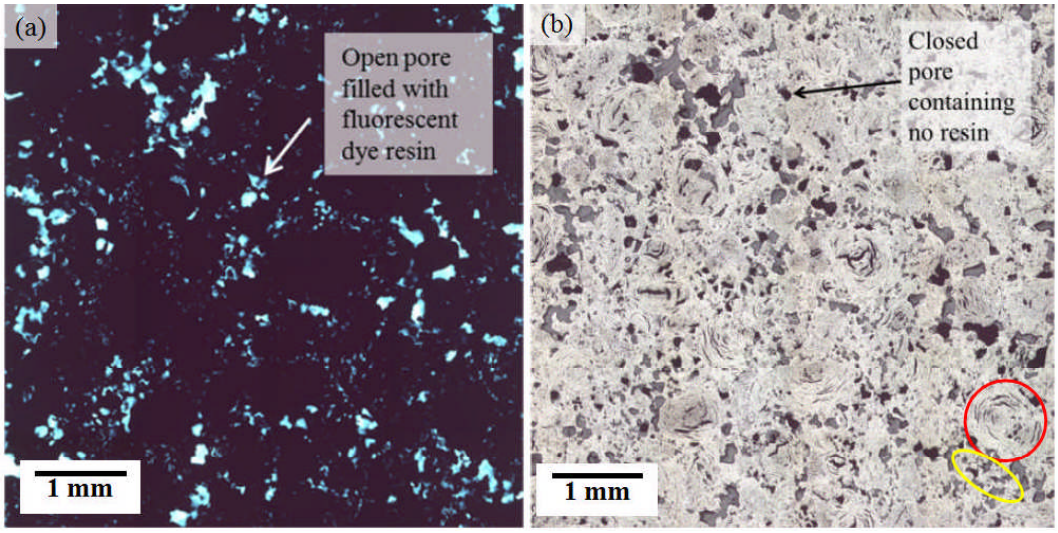

Figure 3.13: Fluorescence (a) and bright field (b) micrographs of the same area highlighting open and closed porosity respectively. The blue areas in the fluorescence micrograph show the fluorescent resin in open pores, and the dark areas in the optical micrograph represent closed pores. In the (b) regions of filler (red) and binder (yellow) are highlighted.

of reactor temperatures. Predictions were in agreement with experimental data showing bulk material shrinkage with irradiation and turnaround after crack closure; all cracks in this model were empty. Work is currently in progress to extend this model to 3D (Delannay *et al.*, 2014).

The investigation of a variety of microcracks in virgin nuclear graphite and HOPG has been undertaken by Wen *et al.* (2008) who showed the presence of lenticular cracks of up to 10 μm long and up to 100 nm wide in PGA nuclear graphite; a fine structure of smaller cracks was also observed with crack lengths down to 10 nm. Both empty and filled microcracks were identified in virgin and electron irradiated material; cracks in the latter were suggested to contain low density, amorphous material. Via a comparison of TEM samples produced by both ion beam thinning and microtome sectioning techniques, it was confirmed that this amorphous material observed within the cracks was not a result of TEM sample preparation. In situ heating of samples to 800°C under a 200 kV electron beam showed a gradual closure of cracks along the *c*-axis. Electron beam exposure without in situ heating also caused cracks to close; after 15 minutes a 60 nm crack was observed to reduce in width to 6 nm, and in some areas to close completely.

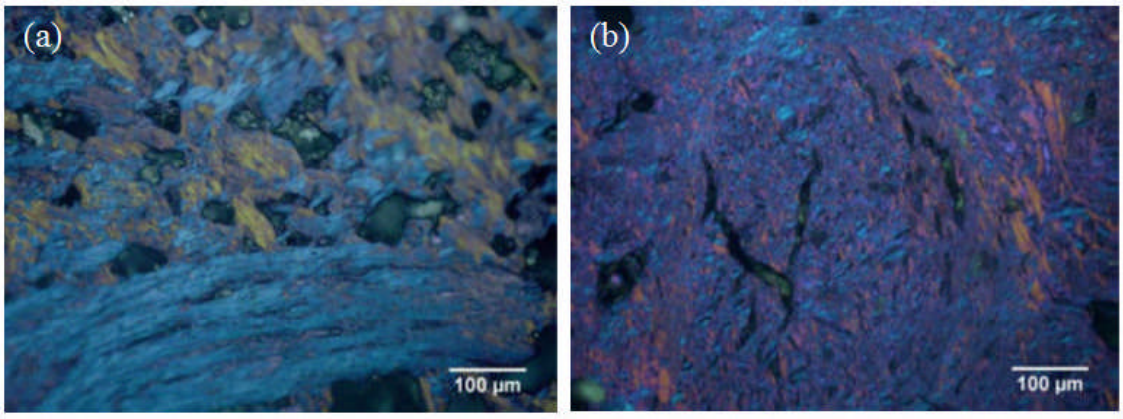

Figure 3.14: Polarised light optical micrographs of (a) PGA and (b) NBG-18 (Hagos *et al.*, 2010).

Neutron irradiated nuclear graphite was also investigated by Karthik *et al.* (2015), who used TEM to observe changes in microcracks and the nanostructure. In both filler and binder phases of NBG-18 and IG-110 graphites irradiated to 1.42 dpa and 1.91 dpa respectively there was no significant change in the size distribution of microcracks compared to virgin specimens. The absence of microcracks in specimens irradiated to ∼6.7 dpa at ∼670°C was attributed to the closure of pre-existing microcracks from significant irradiation-induced *c*-axis swelling. Open microcracks within filler particles in all specimens appeared to contain amorphous carbon but no further analysis on this material was performed.

Cracks have been observed to close when exposed to high temperature or radiation doses; Wen *et al.* (2008) saw cracks in PGA graphite close after heating to 800°C and close after electron irradiation at room temperature, Karthik *et al.* (2015) saw cracks in NBG-18 and IG-110 close after exposure to 6.7 dpa of neutron irradiation at 670°C (but not for specimens exposure to 1.9 dpa at 450°C), and Hinks *et al.* (2012) saw cracks narrow in ion irradiated HOPG exposed to >400°C.

3.4 Summary

In carrying out this literature search, some knowledge gaps and contentious issues have been identified. There has been a wide range of research into the effects of electron and ion irradiation at a variety of operating voltages and temperatures

(Burden & Hutchison, 1996; Hinks *et al.*, 2014; Karthik *et al.*, 2011; Koike & Pedraza, 1992; Muto & Tanabe, 1997; Nakai *et al.*, 1991; Tsai *et al.*, 2013; Wen *et al.*, 2008), however there are still studies which use potentially damaging TEM operating voltages when imaging and characterising neutron irradiated graphites (Karthik *et al.*, 2015; Tanabe *et al.*, 1990; Tsai *et al.*, 2013). To better understand the effect of electron-irradiation, a series of experiments have been performed at various operating voltages, the results of which can be found in chapters 5 and 6. The effect of in situ irradiation temperature on the nano-structure is also unclear, with different studies citing differing migration energies and temperature thresholds for damage to occur (Banhart *et al.*, 2011; El-Barbary *et al.*, 2003; Latham *et al.*, 2013; Li *et al.*, 2005; Muto & Tanabe, 1997; Telling & Heggie, 2007; Thrower & Mayer, 1978; Trevethan *et al.*, 2013). It has also been found that techniques for quantifying radiation damage through TEM micrographs, SAED patterns, and EEL spectra can be inconsistent and must therefore be conducted with caution. A new and thorough radiation damage analysis methodology is tested on electron irradiated specimens in chapter 6 and applied to in situ heated and electron-irradiated specimens in 7, and neutron irradiated specimens in chapter 8. Having established that cracks play a significant role in dimensional change (Chi & Kim, 2008; Delannay *et al.*, 2014; Hinks *et al.*, 2012; Kane *et al.*, 2011; Shtrombakh *et al.*, 1995; Wen *et al.*, 2008), it is of interest exactly what these cracks consist of. Recent studies have shown them to contain amorphous carbon (Karthik *et al.*, 2015; Wen *et al.*, 2008), but little characterization of the in-crack material has been performed. Chapter 9 attempts to characterize the material within cracks in neutron irradiated graphite which would have significant implications for the development of microstructural models to allow the understanding and prediction of radiation-induced dimensional and property changes in nuclear graphite.

Chapter 4

Experimental Theory and Data Analysis

This chapter will introduce the experimental and data analysis techniques used in this PhD and discuss how they have been used to extract material properties. The theory of each technique and the associated parameters used will be also be covered.

4.1 Transmission electron microscopy

To observe or simulate the effects of irradiation, TEM can be used. The first conventional TEM was assembled and successfully used in 1931 and made commercially available by 1939. The small de Broglie wavelength of electrons gives a much higher resolution than visible light microscopes and allows imaging down to the atomic scale (Å). In a TEM a beam of electrons is directed through a thin specimen and an objective lens collects the scattered rays arising as a result of the electron-specimen interaction. This forms a magnified real space image which is subsequently magnified by additional lenses. The final image of the specimen is projected onto an imaging screen or CCD. As well as creating an image of the specimen, the electron beam can also induce atomic damage, depending on the operating voltage and fluence rate. Recent advances in TEM enable point defects to be created with atomistic selectivity (Banhart *et al.*, 2011).

To maximise the mean free path of the electrons it is essential for the column of the TEM to be in vacuum. Standard TEM columns have a pressure of the

order 0.1 mPa and are equipped with a collection of pumps and airlocks to allow the column to be regularly and efficiently evacuated between specimen insertions.

4.1.1 Electron source

In the early 1900s it was proposed that electrons had a dual nature; that is they behave simultaneously as both a particle and a wave where the latter component makes them comparable to electromagnetic radiation. The equation for determining the wavelength, λ, of a particle was proposed by de Broglie in 1924 (Williams & Carter, 1996):

$$\lambda = \frac{h}{p} \tag{4.1}$$

where h is Planck's constant and p the momentum of the particle. However in the case of electrons within a TEM, the relativistic velocities result in a slight alteration to equation 4.1:

$$\lambda_e = \frac{h}{p}\sqrt{1 - \frac{v^2}{c^2}} = \frac{h}{m_0 v}\sqrt{1 - \frac{v^2}{c^2}} = \frac{h}{\sqrt{2m_0 E - \left(1 + \frac{E}{2m_0 c^2}\right)}} \tag{4.2}$$

where m_0, v and E are the rest mass, velocity, and energy of an accelerated electron respectively, and c is the speed of light (Williams & Carter, 1996).

In a TEM the electron source creates a fine beam of electrons which are emitted into the vacuum column at relativistic energies. There are two main categories of electron source: a field emission gun (FEG) in which a fine needle filament is subject to a strong electric field in an ultra-high vacuum in order to extract electrons; a thermionic electron gun can also be used, where a filament made of a material with a low work function (usually lanthanum hexaboride, LaB_6, but more traditionally tungsten) is heated and emits electrons which are accelerated towards an anode (Berger *et al.*, 1988; Williams & Carter, 1996).

4.1.2 Lenses

Although the lenses of the TEM behave in the same way as those in a visible light microscope, they rely on changes in electromagnetic fields rather than re-

fractive indices. Since electrons are charged, their path of travel is altered by an electromagnetic field following Fleming's left hand rule so changing the current flowing through the electromagnetic lens will control the focal length of the lens. In general, electromagnetic lenses can be compared to convex glass lenses used in visible light microscopy (Berger *et al.*, 1988). Each lens consists of a single or several rotational symmetric coils which can be arranged in a variety of ways: the quadrupole lens uses four coils arranged in a square to converge the beam; whereas a hexapole lens uses six coils. As illustrated in figure 4.1 there are three main lens groups: the condenser lenses, the objective lens, and the projector lens. There are also lenses in-between these groups; the diffraction lens and the intermediate lens. The condenser lenses are used to demagnify and converge the beam emitted from the electron gun, focus the it onto the specimen and control the illuminated area. The objective lens then collects the beams diffracted from the specimen to create a magnified inverted image (the initial image). The ratio of the distance between the objective lens and the image, and the objective lens and the specimen determines the magnification of the image (Williams & Carter, 1996; Zhang *et al.*, 2011). The diffraction and intermediate lenses are positioned below the objective lens and both lenses magnify and invert the image created by the objective lens to produce a secondary image. However the diffraction lens is focused on the back focal plane of the objective lens and the intermediate lens is focused on the image created by the objective lens. Whichever lens is used determines the image type displayed on the screen, either a diffraction pattern or a real space image. Finally, a set of projector lenses are used to magnify the secondary image onto the imaging device, such as a fluorescent screen, camera, or photographic film.

4.1.3 Lens aberrations

Optics of any kind, whether with photons or electrons, experiences some form of aberration resulting in an imperfect image. In the TEM, there are two main aberrations to be accounted for: spherical and chromatic. Spherical aberration (C_s) occurs when the rays passing through a lens converge at different points. Rays further from the optical axis focus sooner than those closer to the optical

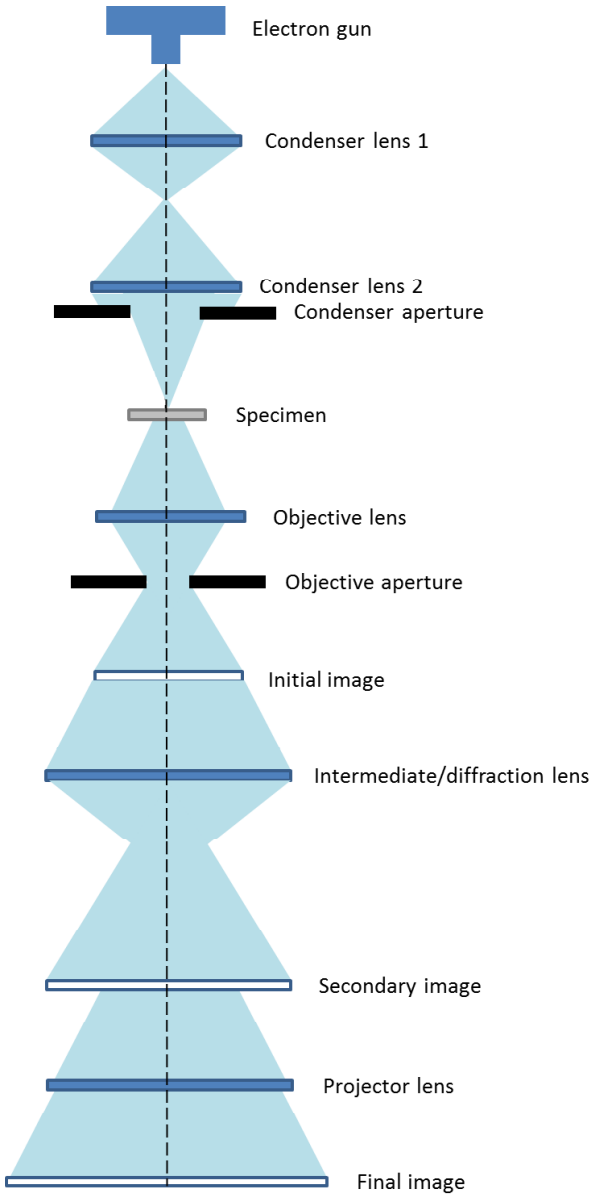

Figure 4.1: Electron beam schematic within a conventional TEM.

axis. Chromatic aberration (C_c) occurs when rays of different wavelengths focus at different points on the optical axis. Both spherical and chromatic aberration distort the image. The aberrations experienced in a TEM are reduced by using a number of auxiliary objective electromagnetic lenses, or aberration correctors (Jouffrey *et al.*, 2004). Although the resolution of the TEM can be limited by these aberrations, the magnification at which many TEMs are operated means that corrections to C_s and C_c have little effect. The merits of aberration correction are also dependent on specimen thickness. Only very thin areas benefit from C_s correction, whereas thicker areas benefit from C_c correction (Williams & Carter, 1996).

4.1.4 Apertures

Apertures are metallic masks which are used to block the high angular diffracted rays. They decrease beam intensity and can reduce the inclusion of wide angle rays in image formation. They can be fixed or mobile; in general the condenser aperture is fixed and determines the fraction of the beam which interacts with the specimen. In some cases, microscopes have a collection of different sized apertures to allow for varying levels of beam exclusion.

Apertures are used in the back focal plane of the objective lens to selectively block information from the diffraction pattern used to create the image. The aperture can be moved to allow either the central undiffracted electrons to form a bright field (BF) image or the first order diffracted electrons to form a dark field image. In the former, vacuum appears as white, whereas in the latter, it is black.

4.1.5 Diffraction

Electron diffraction in the TEM is a valuable tool when characterising the crystal structure of a material. For ordered graphite, the regular arrangement of planes behave like slits and diffract electron waves into a line of bright spots perpendicular to the direction of the planes. The spacing and angular spread of these spots provide information on plane spacing and atomic order respectively. Spots which are closer together imply an increase in the spacing of planes and spots which

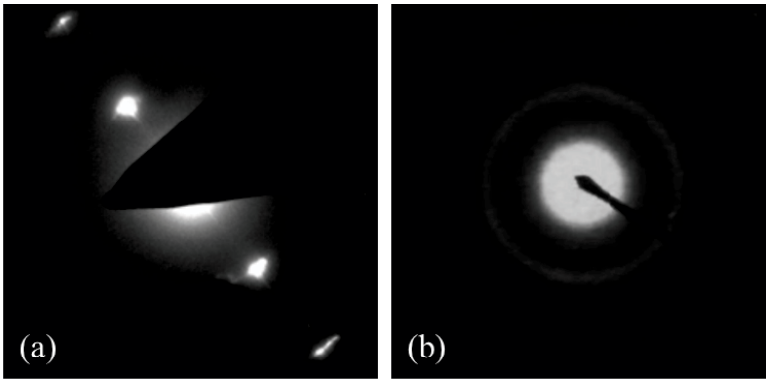

Figure 4.2: SAED patterns for (a) HOPG and (b) amorphous carbon (Muto & Tanabe (1999)).

arc imply the beginnings of polycrystallisation. A totally amorphous carbon will produce a diffraction pattern of concentric halos (figure 4.2).

4.1.6 Scanning TEM

Scanning TEM, or STEM, involves a highly focused electron beam which scans over the specimen in a raster like manner. In a similar way to TEM, STEM measures the transmitted electrons; however it also measures other signals such as secondary electrons, scattered beam electrons, characteristic X-rays, and electron energy loss. These additional signals cannot be spatially correlated in a conventional TEM, leading to an increased spatial resolution for STEM imaging. To perform STEM imaging, transmission detectors can be added to an SEM or scanning coils can be added to a TEM. However the highest quality results are obtained from dedicated STEM instruments, a schematic of which is shown in figure 4.3.

Bright field (BF) imaging in STEM includes the unscattered or low angle scattered electrons (of several milliradians) and provides information about the crystallographic nature of the specimen through phase contrast imaging (the interference of multiple diffracted beams of differing phase). One of the main advantages of using BF STEM is the ability to image thicker samples. Since there is no lens below the specimen, there is an absence of the defocusing effect from

electrons passing through the specimen and losing energy with respect to specimen thickness. BF STEM is therefore capable of imaging specimens of several μm thick at 200 kV.

High angle annular dark field (HAADF) imaging in STEM includes elastically Rutherford scattered electrons which have passed very close to the atomic nuclei in the specimen. The high angle of the detector is usually around 70-200 milliradians which means no Bragg diffracted electrons are collected. HAADF imaging can provide mass-thickness contrast or atomic number contrast images with atomic resolution (defined by the probe diameter).

STEM is also capable of secondary electron imaging which allows surface features to be examined however such a technique has not been used for this PhD and will therefore not be discussed further.

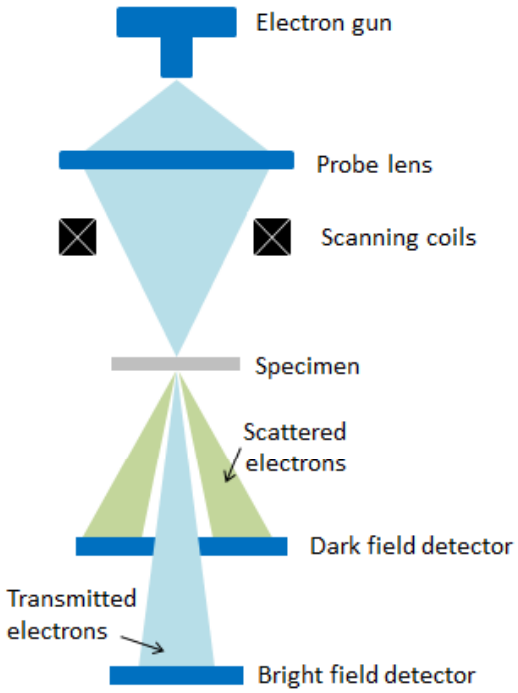

Figure 4.3: Electron beam schematic for a STEM instrument.

4.2 Image interpretation

Contrast in a conventional TEM image can be a result of mass thickness contrast, diffraction contrast, and phase contrast. It is essential to understand the differences between each, and the techniques available to accurately interpret images. The contribution of each contrast mechanism changes with magnification; at low to medium magnification, mass thickness and diffraction contrast are most prominent, and at higher magnification, phase contrast is most prominent.

For uniformly thick specimens, mass contrast shows areas of heavy atoms darker than areas containing lighter atoms since they scatter more electrons to high angles which are blocked by the physical limitations of the bore of the microscope column. If the specimen is of the same atomic composition, thickness contrast shows thicker areas darker than thinner areas since thicker areas result in increased high angle scattering. Diffraction contrast shows changes in intensity due to diffraction over a specimen. The intensity of a feature is a result of variations in the intensity of diffracted beams due to non-uniform specimen thickness or changing diffraction conditions. Diffraction contrast is usually more dominant than mass thickness contrast and may be enhanced by use of an objective aperture. In bright field imaging the objective aperture selects only the undiffracted beam to form the image. Strongly diffracting areas then appear dark. In dark field imaging the objective aperture selects a particular diffracted beam and provides a reverse contrast image. Phase contrast is observed at higher magnifications and offers better spatial resolution and occurs when more than one diffracted beam contributes to an image allowing for the imaging of atomic columns. A large part of structural information is contained within the phase of an electron wave however the TEM only records the intensity, or amplitude. On passing through the specimen, the attractive positive atomic potential changes the phase of the electron waves. The interaction of electron waves of different phase will affect the overall intensity, thereby allowing phase-related structural information to be detected. This appears as an interference pattern whose spacings are related to the lattice spacings associated with the particular diffracted beams included. Understanding the contrast transfer function allows for the optimization of phase contrast.

An alternative imaging technique is energy filtered TEM (EFTEM) which can remove inelastic scattering from images (zero loss filtering) or image with specific energies of inelastically scattered electrons. EFTEM imaging is discussed in more detail in section 4.3.3.

4.2.1 Contrast transfer function

As discussed previously, the high resolution in a TEM is achieved by the small de Broglie wavelength of the electron beam. Using Equation 4.2 the de Broglie wavelength can be calculated for various operating voltages which correspond to the microscope's potential resolution.

Accelerating voltage (kV)	Relativistic de Broglie wavelength, λ_e (pm)
100	3.70
200	2.51
300	1.97

Table 4.1: De Broglie wavelengths at various operating voltages

These resolutions are much smaller than the diameter of atoms but the achievable resolution is in fact worse than that stated due to imperfections or aberrations in the electron lenses; a more accurate TEM resolution limit (R') takes into account the spherical aberration constant of the objective lens (C_s) which can be expressed as

$$R' = 0.66 C_s^{0.25} \lambda_e^{0.75} \tag{4.3}$$

which gives value of R' = 2.45 Å for the TEMs at the University of Leeds which were used for the majority of experiments detailed in this thesis (accelerating voltage = 200 kV and C_s = 1.2 mm) (Scherzer, 1949).

As well as high resolution, it is essential to have contrast within the image. The Rose criterion for visibility states that the difference in intensity of the feature of interest (I_f) and the background (I_b) must be more than 5 times the level of noise (N) which, for Poisson statistics, is the square root of the number of counts detected (equation 4.4) (Williams & Carter, 1996).

$$I_f - I_b > 5N \tag{4.4}$$

A more advanced consideration of contrast regards the 'contrast transfer function' (CTF) which describes the change in the phase of the exit wave due to objective lens aberrations. For non-corrected TEMs with a fixed C_s, a through focal series must be performed to optimize the CTF and determine the best possible defocus to use when imaging (Scherzer, 1949). During a focal series, features in the image can undergo contrast or phase reversal as illustrated in figure 4.4. The phase reversal is also dependent on sample thickness (figure 4.5) so care must be taken to create specimens of even thickness while imaging them at a calculated defocus.

The CTF is a mathematical function which tracks these changes in phase (and hence contrast) during a focal series. It is largely affected by the defocus but also the astigmatism, electron wavelength, chromatic aberration, and spatial coherence of the electron beam (Mindell & Grigorieff, 2003; Williams & Carter, 1996). The former two result in phase reversal which is represented graphically

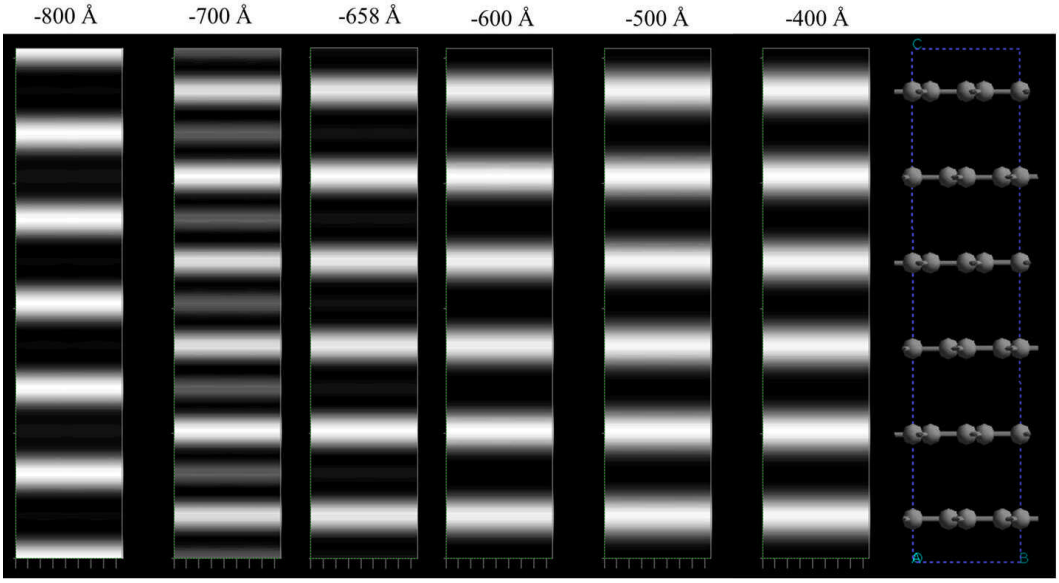

Figure 4.4: Through focal series of 60 nm thick [100] oriented graphite from -800 Å to -400 Å. (200 kV operating voltage). The right hand image shows the atomic model for comparison. Each cell is 20.40 Å high and 4.26 Å wide.

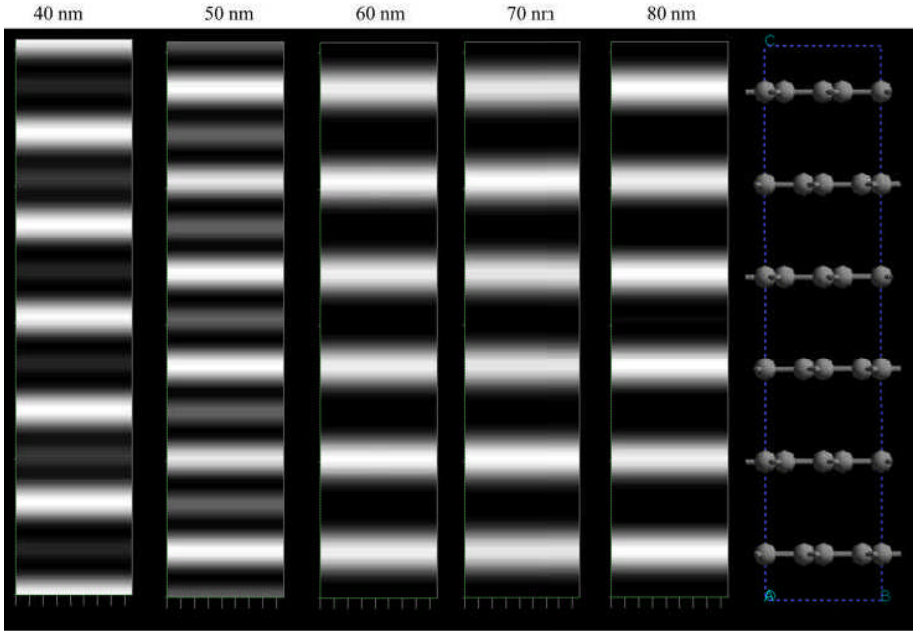

Figure 4.5: Contrast at -600 Å defocus in varying thickness of [100] oriented graphite from 40 nm to 80 nm. (200 kV operating voltage). The right hand image shows the atomic model for comparison. Each cell is 20.04 Å high and 4.26 Å wide.

as an oscillating wave and mathematically as $T(k)$ (equation 4.6). The latter two give the oscillation an attenuating envelope (Mindell & Grigorieff, 2003). This is mathematically described in equation 4.5 and equation 4.6 and illustrated in figure 4.6.

$$CTF = T(k)E_cE_a \tag{4.5}$$

$$T(k) = sin\chi = sin\left(\pi\Delta f\lambda_e k^2 + \frac{\pi}{2}C_s\lambda_e^3 k^4\right) \tag{4.6}$$

where E_c and E_a represent the envelope contribution from chromatic aberration and spatial coherence respectively,$sin\chi$ is the phase induced by the lens, Δf is the defocus, λ_e is the electron beam wavelength, and k is the spatial frequency.

When $sin\chi$ is negative, atoms appear dark and vice versa. The point resolution of the microscope at each defocus can also be determined from a CTF plot by taking the spatial frequency at which the CTF function crosses zero for

the first time (Tromp & Schramm, 2013). A CTF which fluctuates closely about zero would result in a low contrast image. Optimum imaging can be achieved when the base of the first trough is relatively flat around a spatial frequency corresponding to the size of the feature of interest meaning slight size changes in the feature will not experience a change in contrast. For example, when observing the (002) lattice fringes in graphite, a spatial frequency of 0.29 $Å^{-1}$ corresponds to the 3.4 Å atomic spacing. At a defocus of -600 Å, the CTF intensity is at a negative maximum of around -0.9 with a fairly flat bottomed trough (figure 4.7(b)). Figure 4.7 illustrates how the shape of the CTF changes with defocus, and highlights the spatial frequencies corresponding to atomic spacing in the 002 (3.4 Å) and 001 (2.46 Å) directions.

At -500 Å and -700 Å defocus the negative intensity of the CTF is lower than at -600 Å but the troughs are relatively sharp. At -800 Å defocus the spatial frequency corresponding to 3.4 Å becomes positive implying a phase reversal, similar to those observed in figure 4.4. To some extent the observation of atoms along [001] is limited by the CTF as the intensity of the spatial frequency corresponding to the spacing of atoms within the basal plane (2.46 Å) is consistently relatively low. In some cases (figure 4.7 (a) and (d)) the spatial frequency at 2.46 Å is beyond the resolvable limit.

To calculate the best possible defocus more accurately, Scherzer optimized the CTF by balancing the effects of spherical aberration (C_s) against the defocus (Δf) (equation 4.7) (Scherzer, 1949)).

$$\Delta f_{Sch} = -1.2(C_s \lambda_e)^{0.5} \tag{4.7}$$

which gives a defocus value of -658 Å (assuming C_s = 1.2 mm and λ_e = 2.51 pm). If the CTF is plotted for such a defocus, it can be seen that the negative (normalised) intensity for 3.4 Å lattice spacing is $\sim$ 0.73 (figure 4.8) which provides sufficiently significant contrast to observe the fringes in graphite.

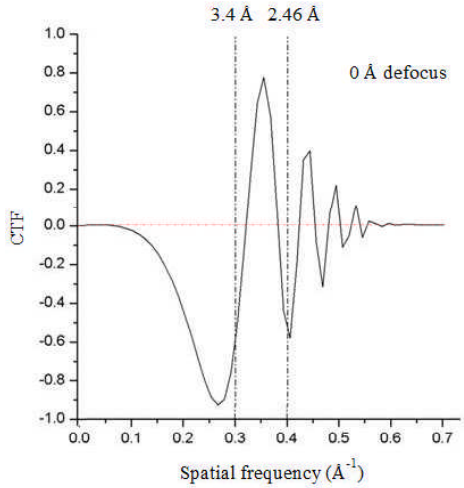

Figure 4.6: Typical CTF illustrating an oscillating wave dampened by an envelope attenuating towards high spatial frequencies. Input parameters: 200 kV operating voltage, 1.2 mm spherical aberration coefficient, 0 Å defocus.

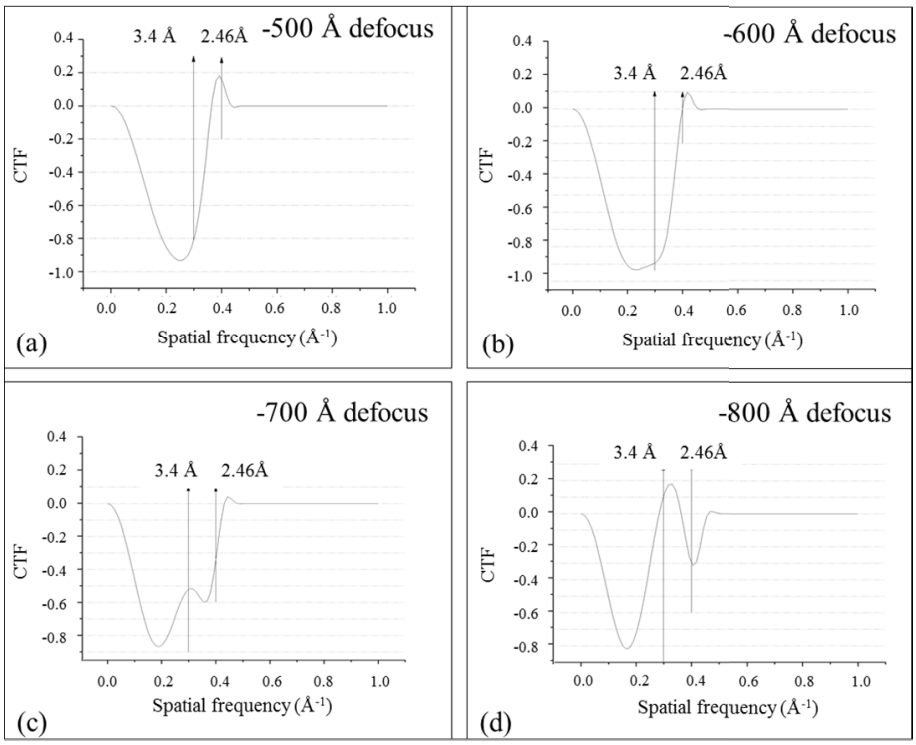

Figure 4.7: Change in CTF with defocus at (a) 500 Å, (b) 600 Å, (c) 700 Å, and (d) 800 Å using simulation software Cerius2. Input parameters: 200 kV operating voltage, 1.2 mm spherical aberration coefficient.

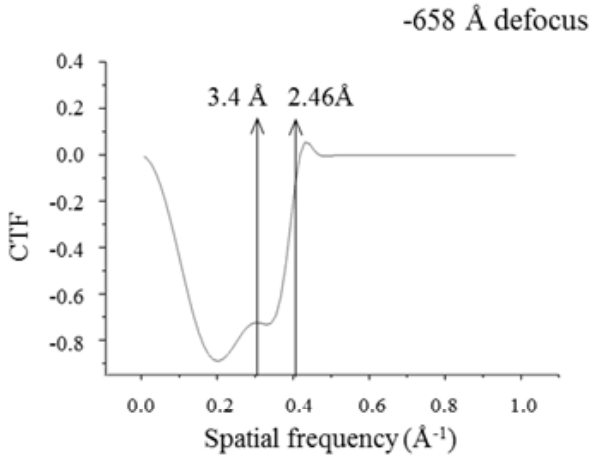

Figure 4.8: CTF plot of the Scherzer defocus. Input parameters: 200 kV operating voltage, 1.2 mm spherical aberration coefficient, -658 Å defocus.

4.2.2 Quantitative image analysis

Transmission electron micrograph analysis

TEM micrographs of irradiated graphite have been analysed using image analysis software provided by the PyroMaN research group, to quantify the change in atomic arrangement following radiation exposure (Raynal *et al.*, 2010). Based on analysis of (002) lattice fringes, the software provides information on fringe length, tortuosity, and orientation using Fourier transform filtering and a level curve tracking algorithm (DaCosta *et al.*, 2015, 2000). Fourier transform filtering is used to reduce levels of unwanted noise in a TEM image to increase the visibility of structural differences. Masks are applied to the (002) spots in a Fourier transform of a micrograph and then the inverse Fourier transform is extracted (see figure 4.9). However noise filtering not only removes noise from the image but potentially blocks other structural information from higher angle scattered electrons. The Fourier transform filtering stage must therefore be finely tuned to ensure valuable structural information is not lost. The same mask as in figure 4.9(c) was applied to a micrograph of amorphous carbon; the resultant micrograph still represented amorphous carbon and not lattice planes, proving that this masking technique does not create images of false structures. To allow for the extraction of radial or angular intensity profiles in the PyroMaN software

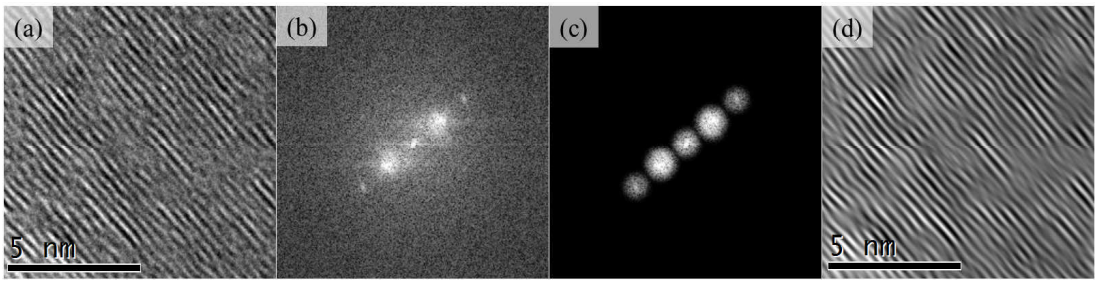

Figure 4.9: Demonstration of FT filtering to and image of electron irradiated HOPG. (a) raw TEM image, (b) FT of the image, (c) masked FT, (d) FT filtered TEM image.

analysis, the power spectrum is remapped onto polar coordinates. The Fourier transform (FT) radial profile (averaged within an estimate of the span of the (002) arcs) is fitted using a Gaussian model to calculate the opening angle of the (002) spots and the d-spacing. The opening angle is considered to be a measure of the degree of twist, or disorientation, of the basal planes. The level curve tracking algorithm is applied to the Fourier transform filtered image to calculate the length and tortuosity of each fringe detected. Although the algorithm detects fringes even if they exceed the image boundaries, they cannot be included when performing measurements since the true length and tortuosity is not known. The detection of fringes in a lattice image of electron irradiated graphite is shown in figure 4.10(c).

Orientation maps of these micrographs show localised changes in the misorientation of neighbouring planes where red indicates no relative change, yellow/green indicates a clockwise misorientation, and purple/blue indicates an anticlockwise misorientation (figure 4.10(d)). A second-order (pairwise) statistical analysis of the orientation maps provides information about the relative orientation of neighbouring fringes, providing additional insights into the nano structure including estimates of coherence lengths parallel and perpendicular to the fringes, together with the mean misorientation of the fringes at larger distances. An example of the application of this software to TEM images of electron irradiated graphite is displayed in figure 4.10.

Three dimensional models from two dimensional micrographs

To better visualise imperfect carbon structures and to add quantitative data to qualitative HRTEM images, 3D atomistic models have also been derived. In collaboration with the 2D HRTEM image analysis work of DaCosta *et al.* (2000) (discussed in section 3.1 and above), Leyssale *et al.* (2009) created a new 3D image synthesis technique based on image guided atomistic reconstruction (IGAR). IGAR has a multi step approach:

1. First, a HRTEM image is subject to a band-pass filter to remove low-frequency (background gradients) and high-frequency (noise) artefacts (figure 4.11(a)).
2. A 2D statistical analysis of this micrograph is then performed to describe the relationship between two neighbouring pixels.
3. These 2D statistics are then extended to a collection of 3D target statistics to describe the relationship between two voxels.
4. A cube of set dimension, filled with randomly arranged carbon atoms is subject to two interaction potentials (V_{REBO} and V_{HRTEM}) which simulates annealing (a "slow" temperature quench using either molecular dynamics or Monte Carlo calculations), and the calculated 3D statistics and standard parameters (such as specimen density, interlayer spacing, and C-C bond length limit of 1.3 $\mathring{A}$) are then applied to the structure. This makes the carbon atoms rearrange themselves based on the lowest energy structure for a given nanotexture. The result is a synthesised 3D TEM-like image (4.11(b)).
5. The atomic model is then simulated iteratively assuming an orthotropic statistical distribution (4.11(c)).
6. TEM images of the 3D models are then simulated using the multislice simulation approach as implemented in the NCEMSS software package (Kilaas, 1987). These simulated TEM images undergo the same 2D statistical treatment as the experimental TEM images to verify that they are statistically equivalent.

The reconstructed atomistic model gives information about the nanotexture by calculating the proportion of sp^2 and sp^3 bonded carbon, and the number of

six-membered rings which can then be compared with EELS data (Farbos *et al.*, 2014; Leyssale *et al.*, 2009, 2012). The atoms are labelled C1 to C6. C1, C2, C4 are carbon atoms with 1, 2 or 4 neighbours, and C3 are defect 3-fold carbon atoms. C6 are hexagonal 3-fold atoms whose nearest neighbours are sp^2 atoms (i.e. C6 (planar sp^2) or C3 (non-planar sp^2)). Application of this technique to electron irradiated specimens can be found in chapter 6. A detailed description of the multi step approach for IGAR can be found in Leyssale *et al.* (2012) (not for the faint hearted...).

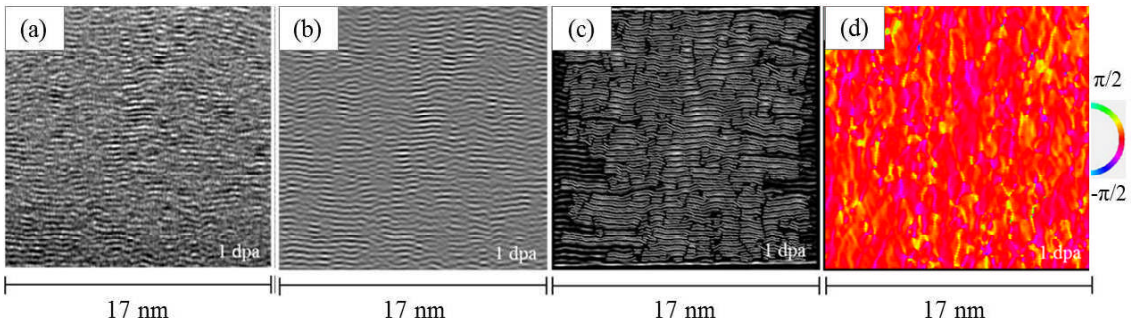

Figure 4.10: Application of the PyroMaN TEM 2D image analysis software to electron irradiated graphite to determine fringe length, tortuosity, and orientation.

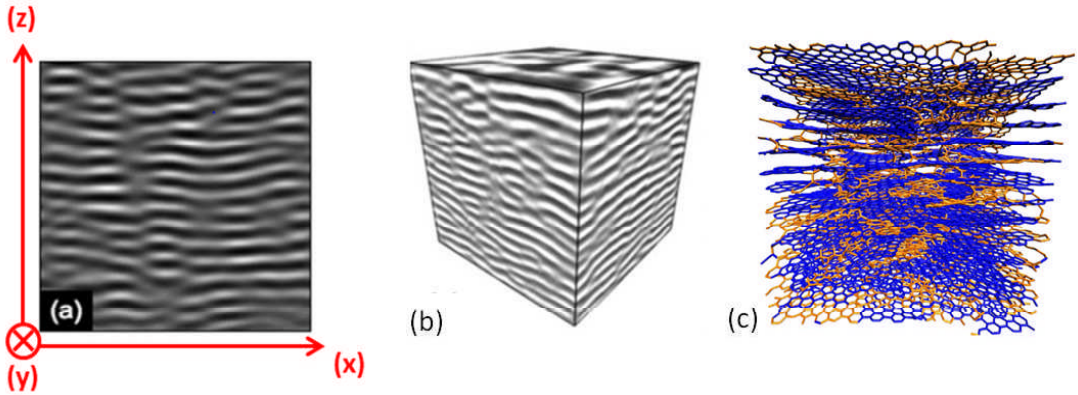

Figure 4.11: Steps of the IGAR 3D modelling process. (a) shows the filtered HRTEM, (b) shows the 3D HRTEM-like reconstructions of (a), and (c) shows the reconstructed atomistic models where blue represents six-membered rings and orange represents non-six-membered rings (Leyssale *et al.*, 2009).

SAED analysis

Diffraction patterns were also recorded together with micrographs where the spacing of (002) spots were measured using intensity profiles in Digital Micrograph. The arcing of the diffraction spots was also measured to assess the misalignment of layers induced during electron irradiation. To extract this information the SAED patterns were intensity normalised and the full width at half maximum (FWHM) of each diffraction arc was measured using the 'Graphite Anisotropy Analysis Program' (GAAP) provided by A. Campbell at the University of Michigan (Campbell *et al.*, 2013). GAAP measures the intensity around a ring at the (002) radius. Gaussian curves are fitted to the intensity plots and the FWHM determined. Figure 4.12 shows an example of GAAP applied to an SAED pattern of electron irradiated graphite. This technique was used in chapter 6 to assess the effect of electron irradiation to PGA graphite.

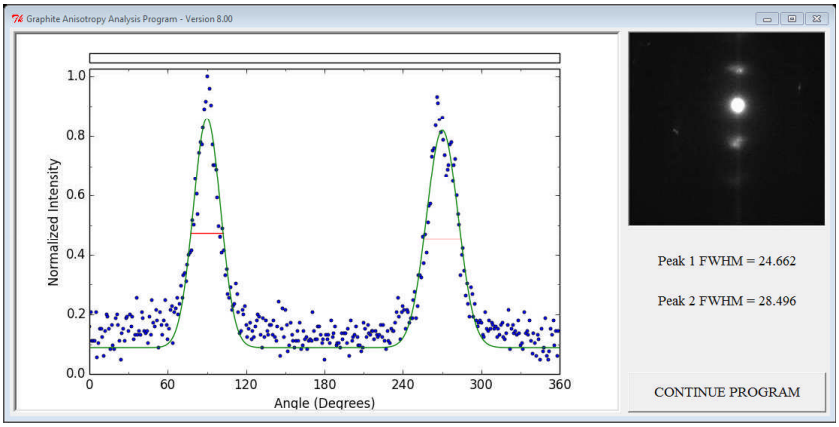

Figure 4.12: Application of the Graphite Anisotropy Analysis Program to electron irradiated graphite to determine spacing and annular spread of SAED (002) spots.

4.3 Electron energy loss spectroscopy

EELS measures the energy loss of electrons passing through a specimen due to a series of inelastic scattering events with electrons associated with atoms and atomistic bonding in the specimen. This interaction results in the transfer of a small amount of energy to the electrons causing excitation. By measuring

the energy loss experienced by the electron beam, information can be obtained regarding the solid state and atomic nature of the specimen.

During inelastic scattering events of sufficient energy, carbon '1s' electrons become excited and move to unoccupied states beyond the Fermi level. Due to the conservation of energy, the incident electron loses the same amount of energy and is scattered. The unstable ionized carbon atom will then undergo de-excitation where the excited electron makes a transition back to a core hole and releases energy in the form of electromagnetic radiation or kinetic energy (i.e. an Auger electron) (Egerton, 2011; Williams & Carter, 1996). It is these excitations which lead to electron energy losses and the characteristic shape of the EEL spectrum.

4.3.1 Instrumentation

EELS instrumentation is located below the viewing screen of a TEM. It comprises of entrance apertures, a magnetic prism (which is used to bend the path of the electrons), a drift tube, and a detector (figure 4.13). The degree of deflection the electron experiences from the magnetic field ($\mathbf{B}$) depends on its energy loss; the higher the energy loss, the high the degree of deflection. A spectrum is thus formed on the dispersion plane which is recorded using a scintillator and a two dimensional charge coupled device (CCD) or one dimensional photodiode (PD) array (Williams & Carter, 1996).

An EEL spectrometer records the kinetic energy of transmitted electrons, producing a spectrum of the number of electrons (or electron intensity) as a function of their energy loss. The magnetic prism not only separates electrons of differing energy loss but also acts as a lens to focus electrons experiencing the same energy loss, but travelling on/off axis. The detector system (scintillator plus CCD or PD) collects the resulting spectrum on the dispersion plane.

4.3.2 Data presentation of EEL spectra

The EEL spectrum can be split into two regions: the low loss and the core loss as illustrated in figure 4.14.

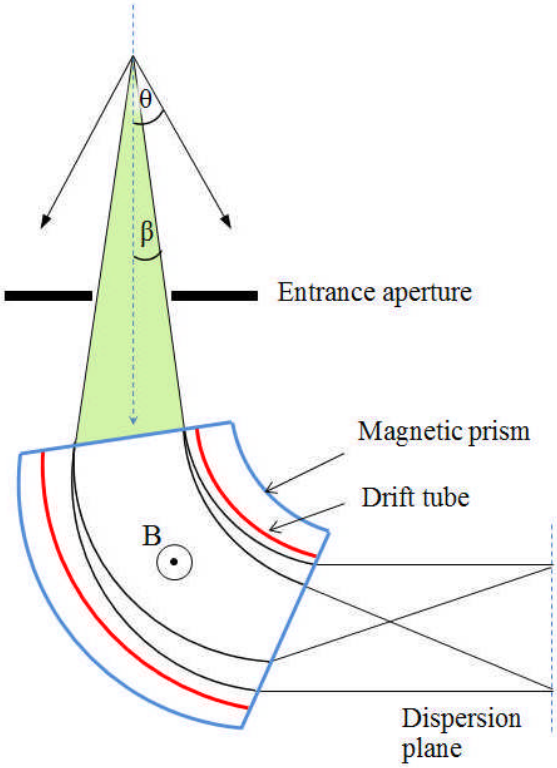

Figure 4.13: Schematic of EELS instrumentation.

Due to the high amounts of energy required for core shell excitation compared to plasmon excitation, the ionization cross-section is small resulting in a low intensity in the core loss region. The core loss edges are superimposed onto a decaying background from plasmon excitations which must be removed before analysis is performed.

EELS has been used to analyse a variety of carbonaceous materials for many years from investigating the p_z, and $p_{x,y}$ projected fine structure in crystalline graphite (Batson, 1993) to measuring the change in sp^2 content during a graphitization series (Daniels *et al.*, 2007). EELS has also been used to examine a range of carbon fullerenes (Henrard *et al.*, 1999) and both amorphous and diamond-like carbon films (Papworth *et al.*, 2000). The findings of these studies are discussed in chapter 3.

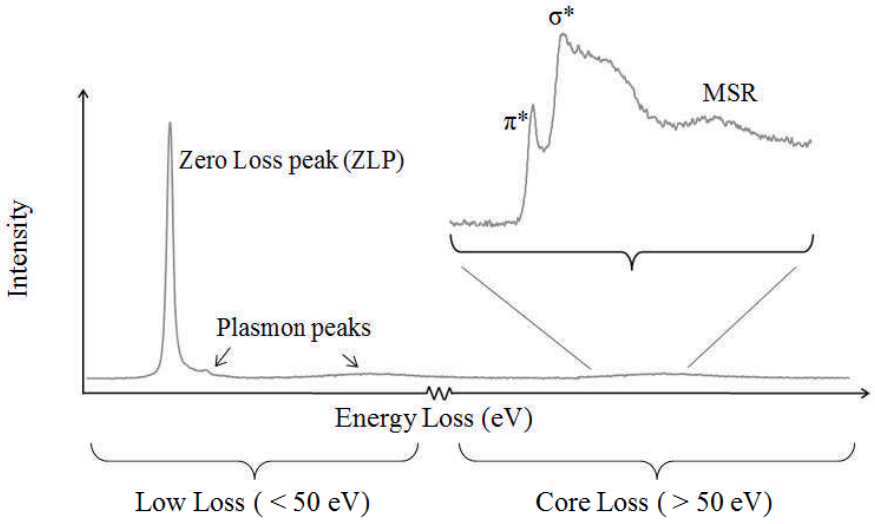

Figure 4.14: A typical EELS spectrum for graphite, highlighting features of importance.

Low loss region

The low loss region generally lies below 50 eV and contains the zero loss peak (ZLP) interband transitions, and plasmon peaks. The ZLP represents the electrons which have passed straight through the specimen, or those which have been elastically or quasi-elastically scattered, retaining the initial beam energy or losing less than the resolvable limit (Egerton, 2011). The plasmon peaks occur due to the excitation of delocalised orbital electrons, providing information about the electrons which have interacted with the conduction/valence bands influencing the electronic and solid state properties of a material. The valence electrons can be excited by three means: intra/interband transitions, plasmon excitation, and Compton scattering. In the former process the electron is excited to an empty state within the same band (intraband transition) or to a higher neighbouring band (interband transition), both of which are above the Fermi level. Plasmon excitation involves the excitation of an oscillating gas or plasma of electrons in the valence or conduction band. The effects of Compton scattering, due to single electron excitation by electron-electron collisions, usually go undetected as the scattering angle is often beyond the collection aperture. Although the plasmon

peak is affected by the bonding within the specimen it's position is not necessarily characteristic of the material being investigated (Brydson, 1991; Reimer *et al.*, 1992).

The resolution of the spectrum is defined by the electron source and can be determined from the full width half maximum (FWHM) of the ZLP. At an operating voltage of 100 keV a tungsten electron source provides a low resolution of 3 eV, a LaB6 electron source provides 1.5 eV, and the Schottky and cold field emission guns (FEGs) provide 0.7 eV and 0.3 eV resolution respectively (Williams & Carter (1996) table 5.1). At standard operating conditions of 200 kV, the resolution is slightly lower than these quoted values, however it can be improved by under saturating the filament, or increasing the gun extraction voltage.

There are three features of interest in the low loss region of a graphitic EEL spectrum: the zero loss peak, π plasmon peak, and bulk plasmon peak (figure 4.15). For thin samples, the zero loss peak has the highest intensity and can be approximated as a Gaussian centred at 0 eV. The next peak is called the π plasmon which occurs around 6.5 eV and provides evidence for the existence of sp^2 bonding; there is also evidence here for the existence of interband transitions between the π and π^* orbitals ($\pi \rightarrow \pi^*$). The third peak in the low loss region is called the bulk plasmon ($\pi + \sigma$) which represents the excitation of a plasma of all the valence electrons (not just the π valence electrons), hence the wider energy spread. This peak can be used to extract information about the density of the specimen and quantify the degree of graphitic character (Daniels *et al.*, 2007).

Since π bonding is characteristic of sp^2 bonding in hybridized carbon, the peaks associated with π plasmon or $\pi \rightarrow \pi^*$ transitions can be analysed to determine the sp^2 content within the specimen. In the low loss region, the two plasmon peaks, π and ($\pi + \sigma$), can be integrated and normalised with respect to perfect graphite to achieve this.

The bulk plasmon peak energy (E_p) is related to the density of the valence electron gas (N_e) by

$$E_p = \frac{h}{2\pi}\left(\frac{N_e e^2}{m_0 \varepsilon_0}\right)^{0.5} \tag{4.8}$$

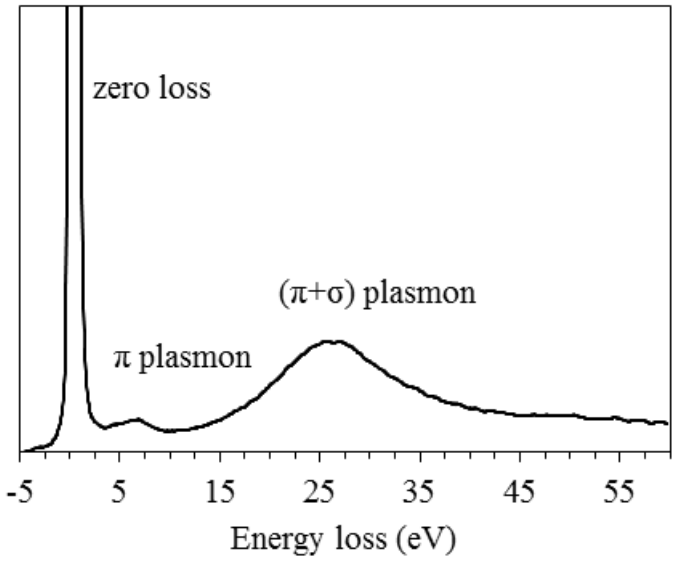

Figure 4.15: Low loss region in a graphite EEL spectrum.

where h is Planck's constant, e is the electron charge, m_0 is the electron mass, and ε_0 is the permittivity of free space (assuming a free electron system) (Williams & Carter, 2009, eq. 38:6). The electron density is directly proportional to the bulk density of the specimen so it can be assumed the energy of the bulk plasmon peak is proportional to the square root of the specimen density (Leder & Suddeth, 1960).

To automatically extract this information from low loss spectra, Hyperspy was used to fit Gaussians to the two plasmon peaks (de la Peña *et al.*, 2015). A fitting of a typical low loss spectrum using Gaussian peaks is shown in figure 4.16; the following constraints were used:

- π plasmon Gaussian centred at ~6.25 eV (with a constraint on the FWHM: 0.25 eV $\leqslant$ FWHM $\leqslant$ 6 eV);
- $(\pi + \sigma)$ plasmon Gaussian centred at ~25 eV (10 eV $\leqslant$ FWHM $\leqslant$ 17 eV).

Core loss region

The core loss region of the spectrum extends from 50 eV to several thousand eV and contains information about the fine structure of the specimen due to

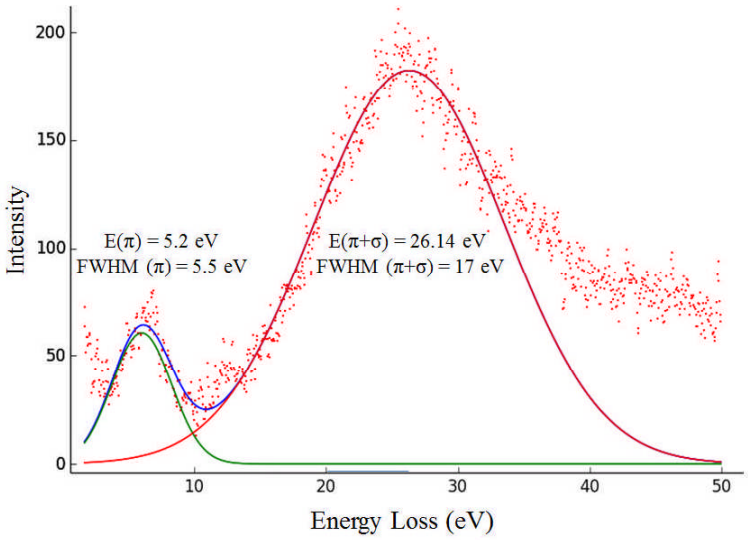

Figure 4.16: Gaussian fits (green and red) over raw (red dotted) low loss EELS data using HyperSpy. The energy position and FWHM of the peaks are shown.

atomic electron excitation from localised orbitals to unoccupied anti-bonding like states above the Fermi level. The transitions observed follow the dipole selection rule. The core loss region therefore gives an insight into the atomic nature of the specimen (Brydson, 1991). The transition of inner shell electrons to unoccupied states generates a series of characteristic edges which are named with respect to the standard spectroscopic notation assigned to electron transitions between orbitals (Williams & Carter, 1996, p.1419). The structure contained in the region 50 eV from the ionization onset peak is known as the Electron Energy Loss Near Edge Structure (ELNES). At these energies an excited electron has a larger range of unoccupied states to choose from resulting in a jagged decay tail (Reimer *et al.*, 1992; Williams & Carter, 1996). The ELNES contains specific information about the phase, local bonding, and density of unoccupied states in the specimen. However care must be taken when analysing such features as with increased energy comes decreased resolution due to solid state broadening mechanisms, such as core hole lifetime broadening (which can override the resolution limit of the electron source) (Brydson *et al.*, 2002).

In graphite the excitation of a carbon 1s electron to an unoccupied σ^* (p) antibonding electron state generates a σ^* peak in the carbon K-edge and the

transitions of inner shell electrons to the unoccupied π^* antibonding electron states generates the peak prior to the carbon K-edge, around 285 eV (figure 4.17). The fine structure and its decaying tail is known as an edge. The σ^* and π^* peaks therefore verify the presence of an sp^2 electronic configuration in the specimen. Conversely, for diamond a lack of π bonding means the EELS spectrum has no π^* peak indicating an sp^3 configuration, and for amorphous carbon structures both the π^* and σ^* peaks are less distinct. The carbon K-edge, observed in the EELS spectra of all carbon allotropes has a 'saw-tooth' profile where the spectrum increases suddenly at the ionization energy and tails off by E^{-r}, where $3 \leq r \leq 4$, towards the background signal (Reimer *et al.*, 1992). The consistency in bond length can be deduced from the intensity and definition of the π^* and σ^* peaks, where a higher intensity and definition suggest an increased bond length consistency (Daniels *et al.*, 2007). The third feature in figure 4.17, labelled MSR, represents the 'multiple scattering resonance' peak whose presence reflects the long range order of the specimen, in particular the radius of the second nearest neighbour shell.

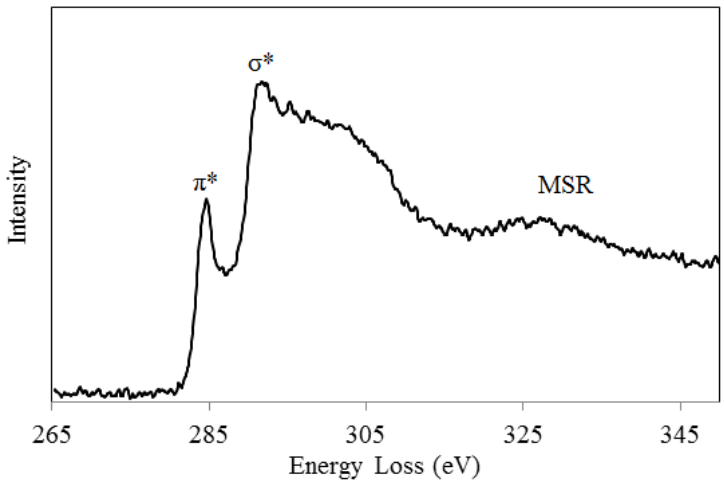

Figure 4.17: Core loss region in a graphite EELS spectrum

Beyond the ELNES region is the Extended Energy-Loss Fine Structure (EXELFS) which spans over several 100 eV. It is a result of diffraction effects when an excited electron wave is reflected by the atoms adjacent to the ionized atom.

Constructive and destructive interference of the reflected wave will increase or decrease the ionisation probability respectively. Analysis of this region can give an indication of atomic spacing (Brydson, 1991; Diaz *et al.*, 2007; Reimer *et al.*, 1992; Williams & Carter, 1996). This has not been employed in the current work.

Planar sp^2 content

A comparison of the two principal peaks in the core loss ELNES region provides information regarding the proportion of planar sp^2 bonded carbon. The simple two window method involves the integration of the area under the π^* peak (I_{π^*}) and a 20 eV integration window including both the π^* and σ^* peaks ($I_{\pi^*+\sigma^*}$) as illustrated in figure 4.18.

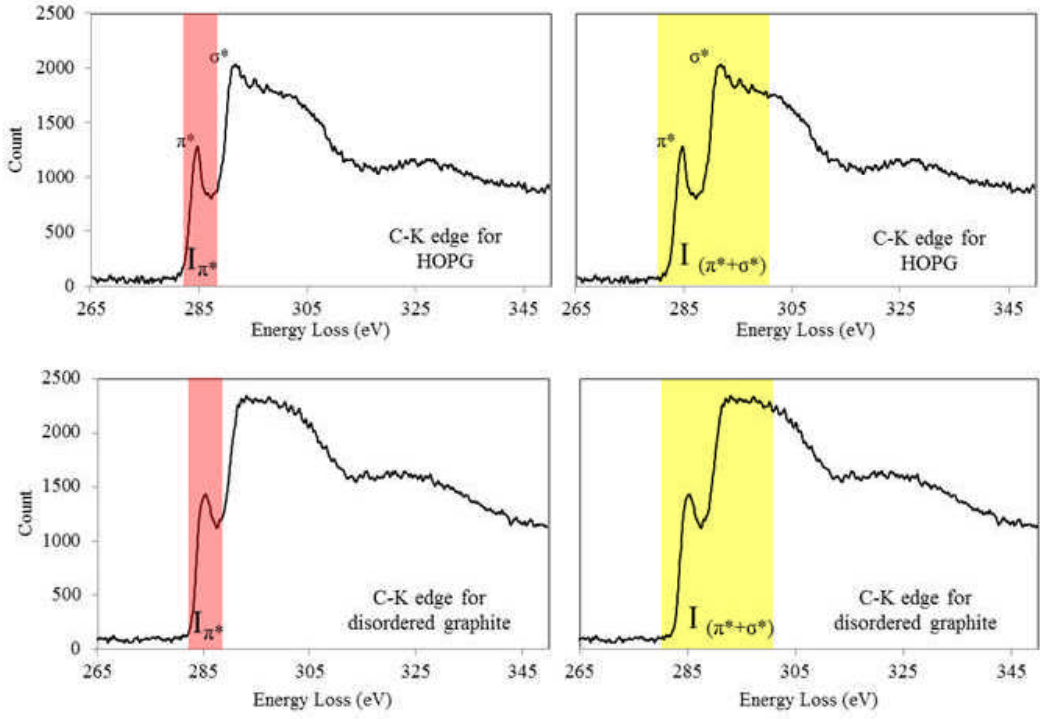

Figure 4.18: Integration windows to extract sp^2 bonding information.

A ratio between these two areas relative to that for perfect graphite (or HOPG) gives an indication of the sp^2 content in the specimen by

$$Planar sp^2 content \propto \frac{\left(\frac{I_{\pi^*}}{I_{\pi^*+\sigma^*}}\right)_{specimen}}{\left(\frac{I_{\pi^*}}{I_{\pi^*+\sigma^*}}\right)_{HOPG}} \tag{4.9}$$

where the integration windows (I) are illustrated in figure 4.18 (Zhang *et al.*, 2011). This method was first successfully used by Berger and McKenzie (1988) who used a 5 eV and 20 eV integration window over the π^* and (π^* and σ^*) peaks respectively (both from an onset of 282.5 eV). An error of ± 1 % was quoted however effects of π^* and σ^* overlap were not considered. In 1994, Bruley et al. presented a series of experiments making changes to the two integration windows to examine the sensitivity of data to the window width. In order to decrease the source of error due to π^* and σ^* overlap, Daniels *et al.* (2007) investigated the effect of using a much smaller integration window of 1 eV for the π^* peak setting the onset to 284.5 eV. Although this produced more reasonable data, the small window was thought to introduce new, unknown errors.

To characterise the ratio of planar sp^2 bonded carbon to total carbon in this work, an improved automated fitting routine for the carbon K-edge was achieved by inclusion of two additional Gaussian curves to the method proposed by Zhang *et al.* (2011). This new method employed five Gaussian peaks (figure 4.19 (a)): G1 centred at ~285 eV for the C=C π^* component; G4 ~292 eV, the C-C σ^* component and G5 ~300 eV, the C=C σ^* component. The additional Gaussians were positioned under the residual peak (~286-288 eV) described in Zhang's method as of uncertain origin: either from the presence of additional heterospecies (e.g. O or H) or the presence of a non-planar sp^2-bonded (fullerene-like) carbon component, as is the case here.

Gaussians were fitted in HyperSpy using the following constraints:

- G1 centred at 284.5 eV (0.25 eV $\leq$ FHWM $\leq$ 2 eV);
- G4 centred at 291.75 eV (2.1 eV $\leq$ FHWM $\leq$ 3.0 eV);
- G5 centred at 297.75 eV (11.2 eV $\leq$ FHWM $\leq$ 13.1 eV).

When fitting the extra two Gaussians (G2 and G3), the script fixed the FWHM and the centre of G1, G4 and G5 along with the area of G4 and G5, but allowed

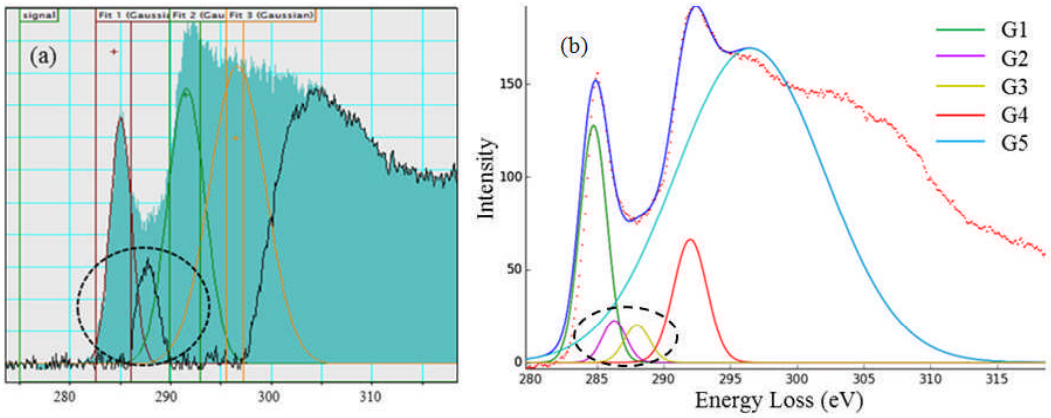

Figure 4.19: (a) Circled residual peak signal from a 3 Gaussian fit performed in Gatan Digital Micrograph, (b) circled residual peak signal from a 5 Gaussian fit performed in Hyperspy. The residual peak from (a) was deconvoluted into two separate peaks in (b).

the area of G1 to vary in order to accommodate the new components, which were then fitted using the following constraints:

- G2 centred at 286.5 eV (0.2 eV $\leq$ FHWM $\leq$ 1.5 eV)
- G3 centred at 288.5 eV (0.2 eV $\leq$ FHWM $\leq$ 1.5 eV).

The relative intensity under G1 is assumed to represent the proportion of planar sp^2 bonded carbon, as found in pristine graphite. In previous studies (Daniels *et al.*, 2007; Zhang *et al.*, 2011) this relative intensity has been normalised to reference materials, such as HOPG, in order to obtain absolute values. However for obtaining the change during beam damage, intensities have been normalised to the initial (t=0) spectrum (as in chapter 6), or for relative changes across an irradiated specimen, not normalised at all (as in chapter 9).

When performing such calculations, it is essential that the magic angle criterion is met (whereby specimen orientation does not affect the intensity of these peaks). A detailed discussion about the necessary operating conditions to satisfy this criterion can be found in section 5.2.

Non-planar sp^2 content

The spectral intensity around 287 eV gives information about hetero-atom content (deemed to be negligible in this case due to the high graphitization temperatures) and what is termed as non-planar sp^2 carbon (from non six-membered rings which induce curvature in the basal planes) (Daniels *et al.*, 2007; Mironov *et al.*, 2015; Zhang *et al.*, 2011). The signals from the G2 and G3 peaks in figure 4.19 were analysed to provide information regarding the non-planar sp^2 content of the specimen by measuring the ratio between the combined intensities under G2 and G3 (I_R) and normalising them to $I_{\pi^*+\sigma^*}$ as detailed in equation 4.10.

For obtaining the change in non-planar sp^2 bonded carbon during beam damage, I_R was normalised to the t=0 value for (sp^2 + non-planar sp^2) (as in chapter 6), or for relative changes across an irradiated specimen, not normalised at all (as in chapter 9).

$$Non - planar sp^2 \propto \frac{I_R}{I_{\pi^*+\sigma^*}} \tag{4.10}$$

Multiple scattering resonance

The MSR peak, occurring at an energy loss of around 330 eV is associated with the scattering shells located within the basal plane. When a $1s$ electron is excited in a carbon atom, this can be thought of as spherically radiating wave (figure 4.20). When this wave reaches the three nearest carbon atoms in the first shell, of radius 1.42 Å, it may reflect back to the excited atom or continue to the second nearest neighbour atoms, of which there are six in the second shell of radius 2.46 Å. The reflection of the wave from the second shell creates a standing wave whose energy (E_{MSR}) is inversely proportional to the square of the radius of the second shell (R_{MSR}) by

$$E_{MSR} = \frac{K_{MSR}}{{R_{MSR}}^2} \tag{4.11}$$

where K_{MSR} is a constant (Daniels *et al.*, 2007; Scott *et al.*, 2001). The value of K_{MSR} can be calculated by measuring E_{MSR} from a spectrum of HOPG where the nearest neighbour bond length can be assumed to be 0.142 nm (and so the next-nearest neighbour to be 0.246 nm) and then using equation 4.11 to calculate the

constant K_{MSR} to be 1980.89 eV Å^2. As the structure of the specimen becomes more ordered, the energy of the wave will become more defined, resulting in a sharper MSR peak. The radius of the second shell can then be determined by measuring E_{MSR} from a spectrum and using equation 4.11, leading to a value of the carbon-carbon bond length.

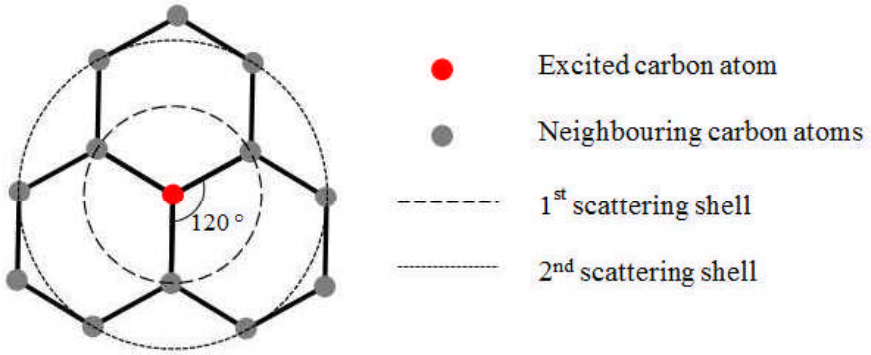

Figure 4.20: Schematic of the scattering shells within a graphite plane

4.3.3 Energy filtered TEM

In conventional TEM regions of darker contrast in a BF image might refer to either thicker material or material of a higher crystallinity. To distinguish between the two, energy filtered TEM (EFTEM) images can be acquired and plasmon ratio maps calculated. For graphite samples, two filters are used: one at 27 eV and one at 22 eV. In electron energy loss spectroscopy, the 27 eV plasmon peak is related to the electron density of crystalline graphite and hence its atomic order; a shift in this plasmon peak (towards 22 eV, which is a value typical of amorphous carbon) suggests a reduction in the density/atomic order so that a ratio between the two will provide a quantitative measure of graphitic content, and will simultaneously remove thickness and diffraction contrast observed in the BF image. In this Ph.D, EFTEM was used to assess the nature of material found within microcracks in irradiated graphite. More details of this study can be found in chapter 9.

4.4 Determining the electron dose

To determine the dose, D, experienced by a material in a transmission electron microscope, the electron current, I, must first be calculated by

$$I = \frac{1.875 \times 10^{15} \times b \times \varepsilon}{t_e \times C} \tag{4.12}$$

where b is a constant (1.3 at 200 kV), ε is the emulsion setting (set to 2 during TEM operation), t_e is the exposure time measured by the exposure meter on the TEM phosphor screen, and C is the screen size correction factor ($\equiv$1). The equation was sourced from FEI (FEI, 1986) (appendix C). To convert this to an electron flux, J, equation 4.12 must be divided by the electronic charge (e) and the beam area, A_b,

$$J = \frac{I}{A_b \times e} \tag{4.13}$$

Since the electron charge is in Coulombs, and the current is in Amps, this becomes a number of electrons per unit area per second. The dose is then calculated using equation 4.14 where σ_d is the displacement cross section.

$$D = J \times \sigma_d \tag{4.14}$$

The displacement cross section varies with electron energy and displacement threshold energy, E_{dt}. Referring to Figure 18 in Oen (1965) (appendix D) a displacement cross section of 16.25 barns was measured assuming an electron energy of 200 kV and a displacement threshold energy of 20 eV (Krasheninnikov & Nordlund, 2010). The value of E_{dt} has not yet been agreed upon within the literature with values ranging from 15 to 30 eV which results in a variation in σ_d so that D will vary by a factor of up to 7 (Banhart, 1999; Egerton, 2009; Karthik *et al.*, 2011; Krasheninnikov & Nordlund, 2010). When comparing electron irradiation experiments from the literature, where fluences are quotes in electrons per unit area or by dose in 'displacements per atom' (dpa), care has been taken to convert all dpa values according to the same value for σ_d. Assuming an operating voltage of 200 kV and a displacement cross section of 16.25 barns, the following electron

fluxes and doses can be determined for a variety of magnifications and beam sizes, examples of which are displayed in table 4.2.

Magnification	Beam area m^2	Electron flux $e^- m^{-2} s^{-1}$	Dose $dpas^{-1}$
5,000	2.32×10^{-10}	4.37×10^{20}	7.00×10^{-7}
10,000	5.81×10^{-11}	1.75×10^{21}	2.80×10^{-6}
36,000	4.48×10^{-12}	2.27×10^{22}	3.63×10^{-5}
280,000	7.41×10^{-14}	1.37×10^{24}	2.19×10^{-3}

Table 4.2: Examples of typical electron fluxes and doses at a variety of magnifications and beam sizes.

The change in beam size was recorded for varying the second condenser lens (C2) current in the CM200 and for varying beam intensity in the Tecnai. As there is a linear relationship (see figure 4.21) the data can be extrapolated to determine the radius of the beam (as measured on the screen, see appendix B) for large C2 currents/beam intensities during the collection of low loss spectra, for example.

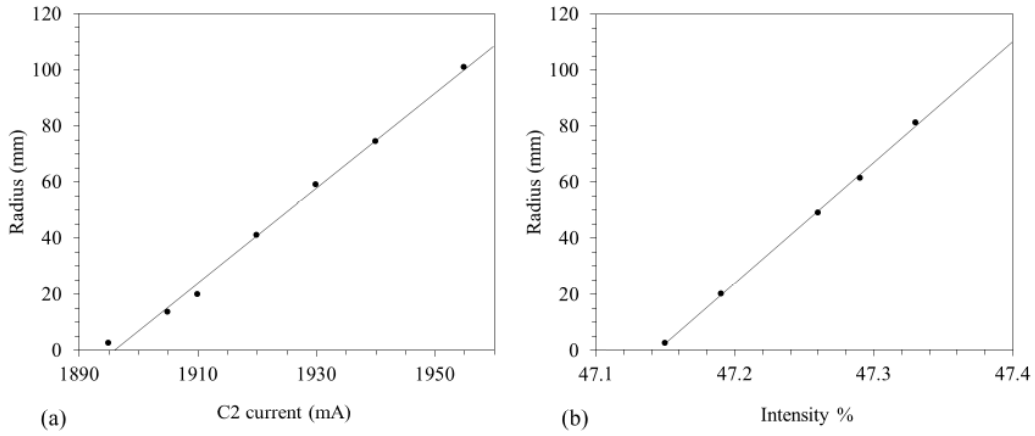

Figure 4.21: Change in (on screen) beam radius with respect to (a) C2 current at 36,000 magnification in the CM200 TEM and (b) beam intensity at 280,000 magnifications in the Tecnai TEM. (See appendix B for beam sizes.)

4.5 Source of samples

Virgin samples of nuclear PCIB, PCEA, and PGA and neutron irradiated samples of British Experimental Pile '0' (BEPO) and (Oldbury) PGA were provided by Abbie Jones at the University of Manchester. Neutron irradiated samples of PCEA and PCIB were provided by Will Windes of Idaho National Laboratory.

To investigate virgin material in the TEM, specimens were typically crushed using an agate pestle and mortar and mixed with acetone before being dispersed onto a holey carbon-coated copper TEM grid (3 mm diameter). To avoid the creation of airborne dust during radioactive sample preparation, a small amount of material was removed from a bulk block using file paper wetted with acetone, more acetone was then applied to suspend the particles in liquid which was then dispensed onto a holey carbon-coated copper TEM grid.

For in situ heating experiments, holey carbon-coated gold TEM grids were used to avoid sputtering effects. In general, the graphite platelets lie with the basal planes perpendicular to the electron beam. In order to view parallel to the basal planes it is necessary to find an area where the graphite platelet has a curled edge as illustrated in figure 4.22. Although this superficially gives a high contrast image of the graphite planes, it cannot be certain that the atoms are arranged in vertical columns as desired. It is likely that the atoms within the curved edge twist and curl in the third dimension to interfere with the image. This can be prevented with advanced sample preparation techniques such as precision ion polishing or focused ion beam to produce platelets in cross-section.

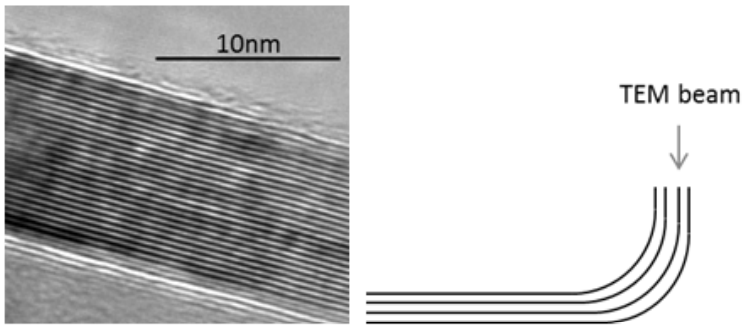

Figure 4.22: An area "looking down" the basal planes (left), and an illustration of curved plane edges (right).

.

The use of a precision ion polishing system (PIPS) was tested for its ability to create self-supported specimens and for use on neutron irradiated samples where the creation of airborne radioactive dust must be avoided. Due to the sensitivity of graphite, a low angle, low voltage approach was adopted. 3 mm disc specimens were exposed to a 3.5 keV ion beam at 3° for 8 hours. Achieving the required sample thickness proved to be difficult with this technique, and specimens were prone ot breaking.

Another approach for sample production was using a focused ion beam (FIB). This allows for specific regions of interest in the bulk to be selected for investigation within the TEM. The specimens prepared using this technique were made at Leeds by John Harrington (for the specimens investigated in chapter 8) and by Mike Ward (for the specimens investigated in chapter 9). An FEI Nova200 dual beam SEM focused ion beam (FIB) fitted with a Kleindiek micromanipulator for in situ lift out was used.

The as-received irradiated PCEA and PCIB specimens were ∼6 mm × 12 mm cylinders. PCEA contains medium sized round and needle grains (360 μm - 800 μm) and is manufactured via extrusion, and PCIB contains ultra-fine grains and is manufactured via iso-moulding (Kane *et al.*, 2011). Both use a petroleum coke source and are being considered for use in the IVth generation of graphite moderated nuclear reactors.

Oldbury graphite is PGA grade and was irradiated in the UK's Oldbury Magnox reactor. BEPO graphite is an extruded coke-based grade containing elongated needle filler particles (similar to those found in PGA) within a porous binder phase where the binder and crystallites do not have preferential alignment. The filler particles are fairly consistent in size, of order 1 mm × 0.5 mm (Huntingdon *et al.*, 2002). Three samples of neutron irradiated BEPO with different received doses were sourced from the same trepanned column. BEPO1 was farthest from the reactor core and received a dose of 0.4 dpa (∼3.1 × 10^{20} n cm^{-2}), BEPO16 was in the middle of the channel and received a dose of 1.27 dpa (∼9.8 × 10^{20} n cm^{-2}), whilst BEPO20 was closest to the core and received a dose of 1.44 dpa (∼1.1 × 10^{21} n cm^{-2}). The irradiation temperature during operation (in air) was between 20°C and 120°C, which is lower than the usual advanced gas cooled reactor operating temperature of ∼350°C. During the last 5 years the air was

recirculated and temperatures were increased up to ∼180°C to achieve a higher thermal output. The reactor was also annealed twice to ∼230°C, once during operation and once after to release the 200°C Wigner peak (Bell *et al.*, 1962). The BEPO reactor was in operation from 1948−1968 at Harwell in the UK and used natural or low-enriched uranium fuel and a graphite moderator to demonstrate the design for the Windscale Piles and to provide a facility for materials testing and radioisotope production (Wise, 2001).

To study the effects of neutron irradiation in a TEM, PCIB, PCEA, and BEPO specimens were prepared using an FEI Nova200 dual beam SEM/FIB fitted with a Kleindiek micromanipulator for in situ lift out. The analysed areas had varying thickness; but always below 150 nm. A gallium ion beam energy of 30 kV and beam currents between 5000 nA and 100nA were used, except for the final cleaning step where an energy of 5 kV and current of 29 pA were used in order to minimise the effects of beam damage and redeposition of sputtered material. The results from this work can be found in chapters 8 and 9.

Chapter 5

Preliminary Calibration Requirements

When studying structural changes at the atomic scale using TEM and EELS it is essential that the defects observed are a result of radiation damage and not imaging or spectral artefacts. This chapter will therefore detail the highly important preliminary experiments which were conducted to minimise artificial changes to spectra and micrographs. First, the microscope conditions and the reasons for selecting such conditions will be covered. The calibration procedure of the EELS equipment will then be detailed followed by a discussion of the calibration requirements for EFTEM image collection and interpretation. The issues associated with conventional TEM lattice image interpretation were discussed in section 4.2 and will therefore not be covered in this chapter.

5.1 Microscope conditions

TEM investigations were performed on two instruments at the University of Leeds unless otherwise stated. For electron irradiation experiments, Philips CM200 or FEI Tecnai TF20 field emission TEMs were operated at 200 kV with a tip extraction bias of 3.21 kV routinely providing an electron flux of 4×10^{18} electrons cm^{-2} s^{-1}. The CM200 was fitted with EELS and EFTEM equipment providing an EELS energy resolution of 0.7−0.8 eV. For EELS, the microscope was operated in diffraction mode with the smallest selected area aperture inserted, giving a circular projection on the specimen of diameter 150 nm, a collection semi angle

of 1.6 mrad, and a convergence semi angle of approximately 0.8 mrad, at a nominal camera length of 115 mm and a spectrometer entrance aperture of 0.6 mm diameter (corresponding to the magic or orientation independent angle (Daniels *et al.*, 2003)). Digital images and energy loss spectra were captured using a Gatan Imaging Filter (GIF) 200 with a 1 megapixel slow scan CCD array. Data from the array (i.e. images and spectra) were processed using Gatan's Digital Micrograph software.

When imaging neutron irradiated specimens it was essential that the effects of electron beam damage were minimized to avoid a discrepancy in results. As discussed in section 2.1.1 and shown in equation 2.2 the TEM operating voltage should be lower than 82 kV to prevent beam damage in neutron irradiated samples. To test this theory, HOPG specimens were subjected to an 80 kV TEM beam in the CM200 for several minutes. The images collected from these experiments are shown in figure 5.1. No significant damage was observed following 10 minutes of exposure to the electron beam. This operating voltage was therefore deemed appropriate for imaging neutron irradiated specimens.

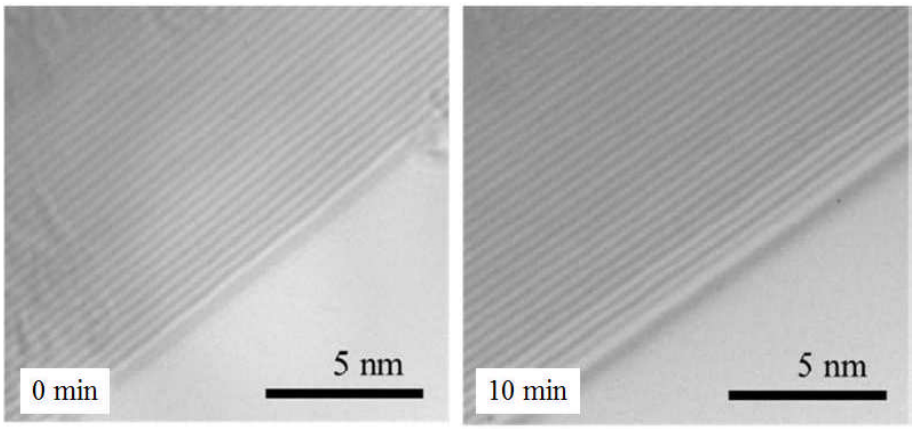

Figure 5.1: TEM micrographs of HOPG subjected to an 80 kV operating voltage for 10 minutes in the CM200 TEM.

Unless stated otherwise, all experiments were performed at room temperature where the localised heating effect from the electron beam was considered to be negligible due to the high thermal conductivity of graphite (Williams & Carter, 2009). In situ electron irradiation damage at higher temperatures was investigated using Gatan and DENS Solutions TEM heating holders.

Some of the data collected for this thesis were from external microscope facilities: high resolution HAADF STEM imaging and EELS spectrum imaging was performed at SuperSTEM, Daresbury, UK and some in situ heating experiments were performed at the University of York, UK. The specific operating conditions for this work will be detailed in the relevant results chapters alongside the data.

5.2 EELS calibration

Before collecting EELS spectra to investigate the chemical structure and graphitic nature of virgin, electron irradiated and neutron irradiated graphite, the operating conditions were fine-tuned and calibrated. This was performed by carrying out a number of experiments to assess the geometry of the electron beam and to determine the optimum angles at which to work.

5.2.1 Collection angle

In TEM diffraction mode, the collection semi angle, β, refers to the angle of the beam collected by a detector or aperture. It can be controlled by the aperture radius, r_A, and the camera length, L_{cam}, and is affected by the distances from the projector lens crossover to the viewing screen, h_1, and aperture, h_2, by equation 5.1 (Williams & Carter, 2009).

$$\beta = \frac{L_{cam}}{r_A} \times \frac{h_1}{h_2} \tag{5.1}$$

where the beam geometry for the above parameters is illustrated in figure 5.2. At the time this experiment was conducted, the Philips CM200 at the University of Leeds had a value of $h_1 = 389$ mm and $h_2 = 728$ mm.

At the magic collection semi angle β_m, the EEL spectra from an anisotropic sample are not affected by sample tilt, or orientation. For the acquisition of the carbon K-edge in graphite at an operating voltages of 200 kV, the magic angle is 1.7 mrad (Daniels *et al.*, 2003). The magic angle at 80 kV was theoretically calculated by Schattschneider *et al.* (2005) to be 4.63 mrad. The TEM must be operated such that the value of β is as close to the magic angle as possible.

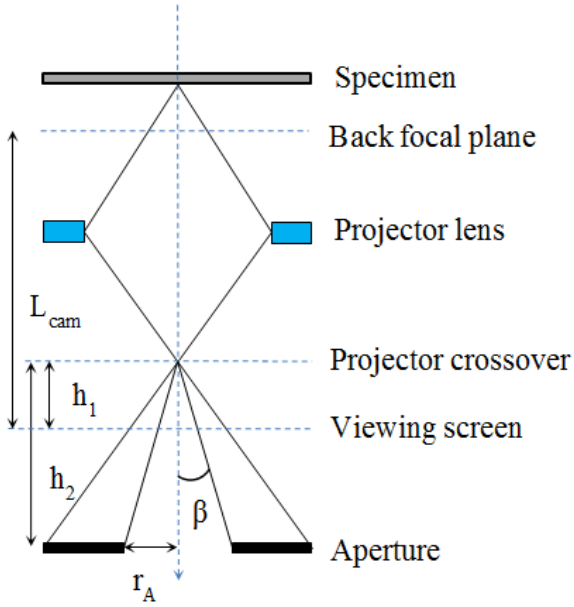

Figure 5.2: Beam geometry for the calculation of β adapted from figure 37.8 (Williams & Carter, 2009).

Using equation 5.1, a table can be drawn to see which camera length and aperture should be used at each operating voltage to meet the magic angle criterion.

L_{cam} (mm)	Calibrated L_{cam} (mm)	β (mrad) for varying aperture radii 0.3 mm	1 mm	1.5 mm
84	63	2.53	8.42	12.63
115	98	1.62	5.40	8.10
150	128	1.24	4.12	6.18
210	182	0.87	2.91	4.37
300	194	0.82	2.74	4.10

Table 5.1: Values of β for a series of camera lengths and aperture sizes in a Philips CM200 at 200 kV (equation 5.1).

Where the calibrated camera length is calculated by

$$L_c(screendown)^{actual} = \frac{L_c(screendown)^{quoted}}{L_c(screenup)^{quoted}} \times L_c(screenup)^{actual}. \tag{5.2}$$

From the above tables, a value of $\beta = \beta_m$ is not possible at the camera lengths and apertures available. At 200 kV the magic angle lies between camera lengths

L_{cam} (mm)	Calibrated L_{cam} (mm)	β (mrad) for varying aperture radii 0.3 mm	1 mm	1.5 mm
42	37	4.29	14.29	21.66
62	48	3.31	11.04	16.70
84	63	2.53	8.42	12.72
115	98	1.62	5.40	8.18
150	128	1.24	4.12	6.26

Table 5.2: Values of β for a series of camera lengths and aperture sizes in a Philips CM200 at 80 kV (equation 5.1).

of 84 mm and 115 mm with a 0.3 mm aperture and at 80 kV the magic angle lies between camera lengths of 115 mm and 150 mm, with a 1 mm aperture. When this is the case, the convergence semi angle and subsequent effective collection semi angle can be considered.

5.2.2 The effective collection semi angle and convergence semi angle

To acquire the optimum microscope conditions for EELS data collection, the magic angle must be used. However, the collection semi angle is not only influenced by this magic angle but also the convergence semi angle, α, also known as the angle of incidence, giving a new collection semi angle known as the 'effective collection semi angle', β_{eff}, where

$$\beta_{eff}^2 = \beta^2 + \alpha^2 \tag{5.3}$$

where the beam geometry for the above parameters is illustrated in figure 5.3.

For small values of α (i.e. a parallel beam), the effective collection semi angle is equivalent to the collection semi angle. However as α increases, its contribution to β_{eff} must be considered. In some cases, α can be used to increase the collection semi angle so that β_{eff} is closer to the magic angle. For example at 200 kV, referring to table 5.1, using a 0.3 mm aperture at a camera length of 84 mm, β is slightly larger than the required magic angle, however using the same aperture but at a camera length of 115 mm, β is slightly smaller than the required magic

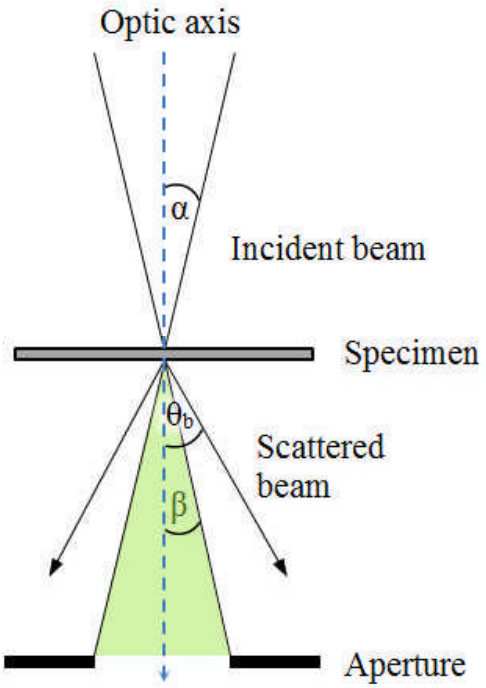

Figure 5.3: Beam geometry to define the convergence, collection, and Bragg semi angles.

angle. In the latter case, equation 5.3 can be used to calculate the required convergence angle to increase the value of β_{eff} so it is equal to the magic angle. Values of α have been calculated for a variety of camera lengths at both 200 kV (table 5.3) and 80 kV (table 5.4).

L_{cam} mm	Calibrated L_{cam}, mm	β (r_A = 0.3 mm) mrad	β_m (mrad) mrad	α, so β_{eff}=β_m mrad
84	63	2.53	1.7	-
115	98	1.62	1.7	0.38
150	128	1.24	1.7	1.12
210	182	0.87	1.7	1.43

Table 5.3: Required α to increase β_{eff} to β_m at 200 kV (equation 5.2)

When working at 200 kV, using a camera length of 115 mm and an aperture of 0.3 mm, a 0.38 mrad convergence angle would meet the magic angle criteria. At 80 kV, using a camera length of 150 mm and an aperture of 1 mm, a 2.11

L_{cam} mm	Calibrated L_{cam}, mm	β ($r_A = 1$ mm) mrad	β_m (mrad) mrad	α, so β_{eff}=β_m mrad
84	63	8.42	4.63	-
115	98	5.40	4.63	-
150	128	4.12	4.63	2.11

Table 5.4: Required α to increase β_{eff} to β_m at 80 kV (equation 5.2)

mrad convergence angle would meet the magic angle criteria.

5.2.3 Using the condenser current to determine the convergence semi angle

To check if the correct operating conditions are being used, the convergence angle can be measured by collecting diffraction patterns at a series of condenser (C2) currents. Extracting selected geometry from the diffraction patterns gives the convergence angle by

$$\alpha = \theta_b \frac{a}{b} \tag{5.4}$$

where θ_b is the Bragg angle (6.155 mrad for Au (assuming a (200) plane spacing of 2.04$\mathring{A}$) at a TEM operating voltage of 200 kV) and the measurements for a and b are illustrated in figure 5.4 (Williams & Carter, 2009).

A plot of convergence angle against C2 current can then be used to determine the optimum C2 current (which is more easily read from the microscope than the convergence angle) to meet the magic angle criteria. Data for the plot in figure 5.5 was collected on the University of Leeds' Philips CM200 using a spot size (C1 setting) of 1, with the selected area aperture in, at level 1. Some examples of the collected diffraction patterns are also presented. Using figures 5.5 and 5.6 the optimum operating conditions to satisfy the magic angle criteria can be deduced.

In practical terms, when operating the microscope in diffraction mode, it is preferable to work within a C2 range where the value for α is constant. The plateaus in figures 5.5 and 5.6 are at $\alpha \sim 0.8$ mrad for 200 kV and $\alpha \sim 1.2$ mrad for 80 kV.

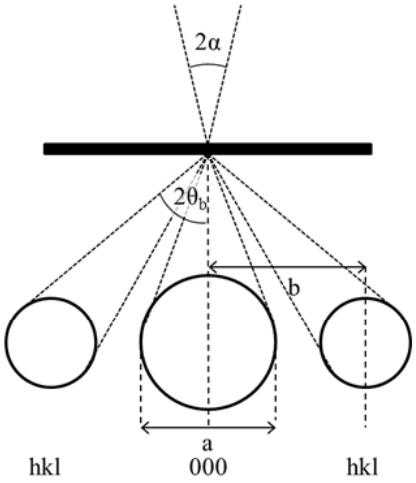

Figure 5.4: Illustration of electron microscope geometry to describe the parameters in equation 5.4 adapted from (Williams & Carter, 2009, figure 5.8).

Combining practical considerations for α values and referring back to the calculations for α values made in tables 5.3 and 5.4 it is possible to determine how close operating to the magic angle is possible. The results of this are displayed in table 5.5. Since the value of α is limited by the plateaus in figures 5.5 and 5.6, the best possible operating conditions for 200 kV are using a camera length of 115 mm and an aperture radius of 0.3 mm with the C2 current >1910 mA. This will make β_{eff} 1.81 mrad, an 8% error on the magic angle. At 80 kV, the best possible operating conditions met are using a camera length of 115 mm and an aperture radius of 1 mm with the C2 current >1128 mA. This will make β_{eff} 4.29 mrad, a 7% error on the magic angle.

Op. V	L_{cam}	β_m	β	α so β_{eff}=β_m	α plateau	β_{eff} for α plateau	Δ β_{eff}-β_m	Δ/β_m
kV	mm	mrad	mrad	mrad	mrad	mrad		
200	115	1.68	1.62	0.38	0.8	1.81	0.13	8%
80	115	4.63	4.12		1.2	4.29	0.34	7%
80	150	4.63	5.40	1.2	2.11	5.53	0.90	19%

Table 5.5: Practical vs. optimum operating conditions when collecting the carbon K−edge

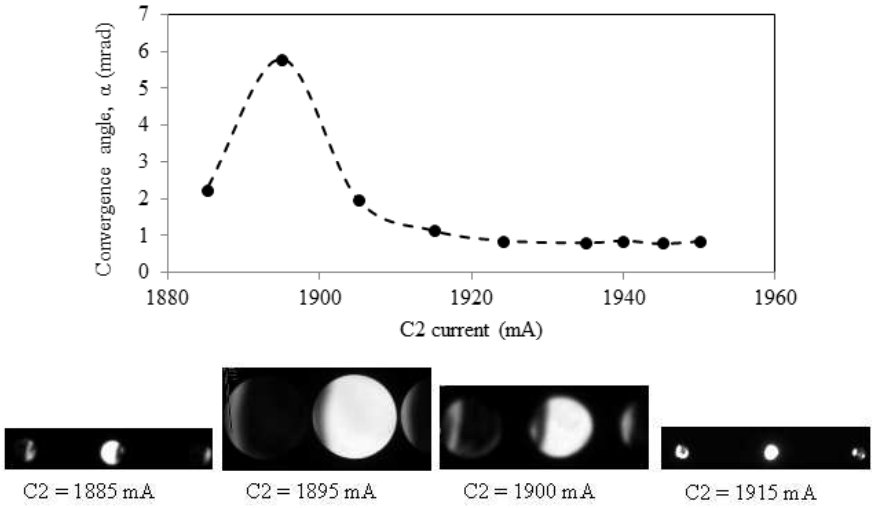

Figure 5.5: Change in convergence angle with C2 current at an operating voltage of 200 kV. Bottom images show diffraction patterns of the crystalline Au calibration sample used to measure a and b to determine α at 200 kV (see equation 5.4).

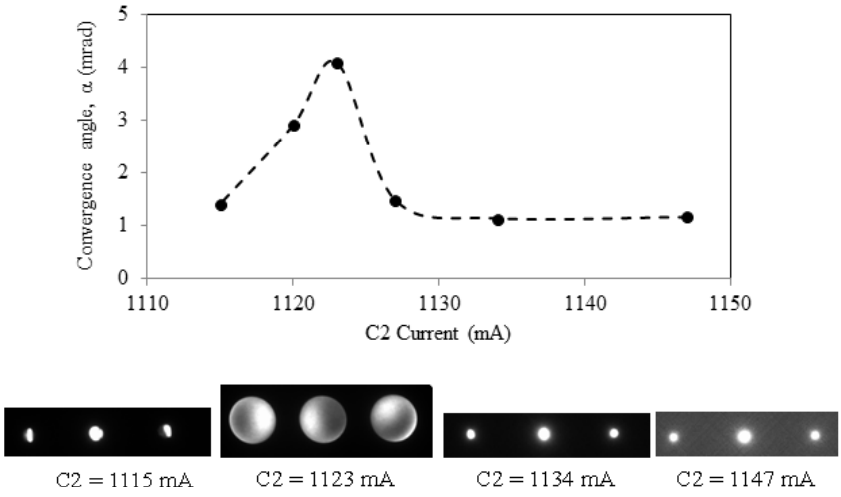

Figure 5.6: Change in convergence angle with C2 current at an operating voltage of 80 kV. Bottom images show diffraction patterns of the crystalline Au sample used to measure a and b to determine α at 80 kV (see equation 5.4).

5.3 Energy filtered TEM calibration

EFTEM image acquisition was performed with a window width of 3 eV (smallest available for plasmon mapping) and a collection semi angle defined by the objective aperture of 10.9 mrad. As discussed in section 4.3.3 the collection of plasmon ratio maps to assess a change in density across a graphite specimen requires the acquisition of two EFTEM images; one at 27 eV and one at 22 eV. It is important that the plasmon peak position is consistent, where any changes are a direct result of varying density and not sample orientation. Figure 5.7 clearly shows how the $(\pi + \sigma)$ plasmon peak position changes with collection semi angle (controlled by changing the camera length in diffraction mode). Above ~5 mrad, the plasmon peak position is constant at 26.5 eV where more electrons of high-energy loss contribute to the spectrum . When measuring the plasmon peak energy at constant collection semi angle (5.40 mrad) there is no significant variation with sample orientation (Figure 5.8). Since the $(\pi + \sigma)$ plasmon does not involve an interband or core-band transition this is to be expected, and has also been observed in graphitic material by Daniels *et al.* (2003). Therefore, operating at a collection semi angle of >5 mrad at 80 kV ensured a consistency in plasmon peak position, where any changes were a direct result of varying density. The objective aperture used in the EFTEM plasmon ratio imaging gave a collection angle of 10.9 mrad and therefore satisfied the above condition.

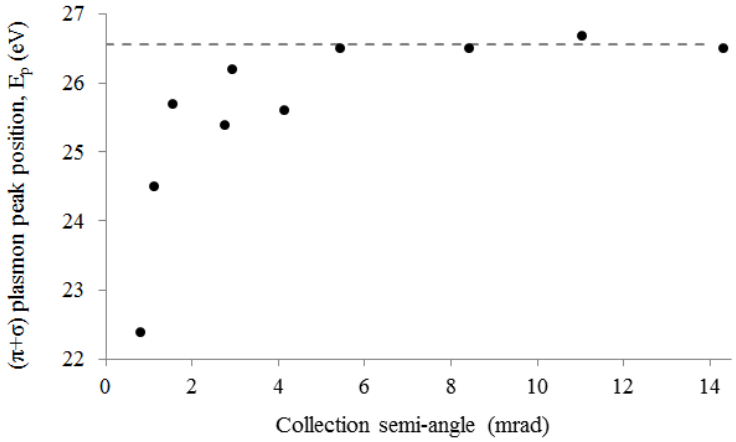

Figure 5.7: Change in $(\pi + \sigma)$ plasmon peak position with collection semi angle for an operating voltage of 80 kV.

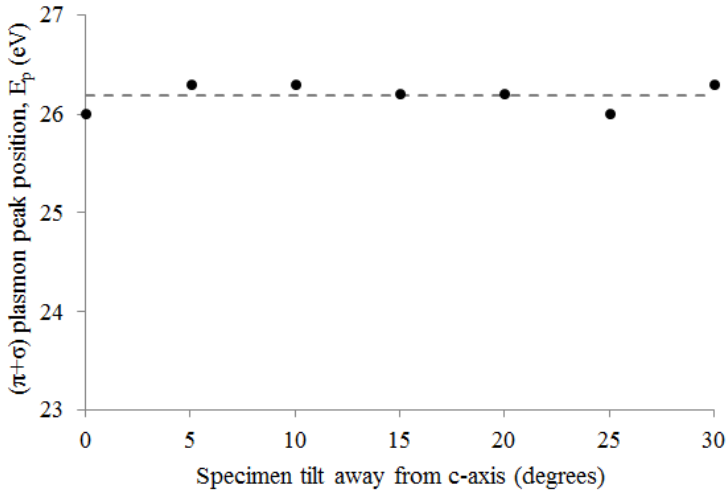

Figure 5.8: Change in $(\pi + \sigma)$ plasmon peak position with (β = 5.40 mrad) for an operating voltage of 80 kV.

To demonstrate the removal of mass thickness and diffraction contrast, this method was applied to a HOPG specimen of varying thickness (figure 5.9). Ratio maps were calibrated to $0.8 < I_{27eV}/I_{22eV} < 1.8$ following measurements by Daniels *et al.* (2003) so that high intensity reflects graphitic material and low intensity non-graphitic material. Significant thickness contrast in the unfiltered TEM image of HOPG translates to even contrast in the I_{27eV}/I_{22eV} plasmon map; whilst the amorphous carbon support film appears much darker due to the lack of graphitic character. In figure 5.9 (b) the plasmon ratio intensity drops from 1.4 to 0.6 at the HOPG surface indicating a presence of amorphous carbon. The degree of success in thickness contrast removal is dependent on the symmetry of the $(\pi + \sigma)$ plasmon; according to Daniels *et al.* (2003) significant asymmetry which might affect the plasmon maps occurs for sample thicknesses over ~200 nm. The thickness of each area was therefore determined (using EELS) to ensure this criterion was satisfied.

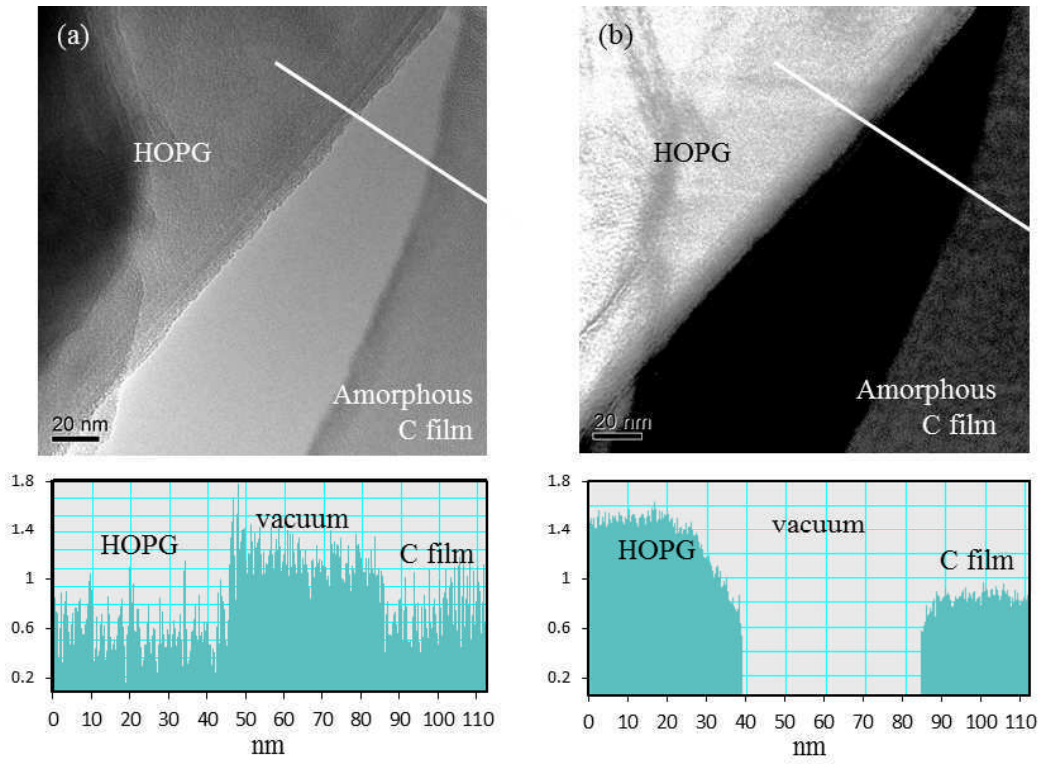

Figure 5.9: (a) TEM image of HOPG and amorphous carbon film (as labelled) showing thickness contrast on the left hand side of the region of HOPG. (b) EFTEM I_{27eV}/I_{22eV} plasmon map showing a removal of significant thickness contrast. Intensity profiles of each image are shown below to illustrate the change in contrast (following the white intersections in the micrographs).

Chapter 6

Quantitative Analysis of TEM Micrographs and EEL Spectra During Electron Irradiation

This chapter investigates the effect of electron irradiation on nuclear grade graphites within a TEM in an attempt to understand the fundamental processes involved in radiation damage. Virgin PGA graphite was chosen for inspection. PGA is a medium to coarse grain anisotropic nuclear graphite of typical density 1.74 g cm^{-3}. The anisotropy of this particular graphite comes from the tendency of the needle-like grain particles in the filler to align in the extrusion direction during the manufacturing process (detailed in section 1.2). TEM and EELS investigations were performed on an FEI CM200 TEM operated at 200 kV to induce specimen damage. The magic angle criterion detailed in section 5.2 was satisfied.

6.1 TEM results

Four areas of thin (<50 nm) PGA graphite were subjected to an average electron flux of 4.2×10^{18} electrons cm^{-2} s^{-1} (2.4×10^{-4} dpa s^{-1}, assuming a displacement cross section of 5 barns and a displacement threshold energy of 30 eV). Images of the basal planes and electron energy loss spectra were recorded periodically throughout. The micrographs and their corresponding selected area electron diffraction (SAED) patterns shown in figure 6.1 are typical of the damage produced by a 200 kV electron beam. In particular, the tortuosity (or curvature)

of the (002) lattice fringes can be seen to increase, the d-spacing increases, and the lattice fringe length decreases. These results suggest the breakup of the graphitic structure into nanocrystalline regions with increasing dose. These micrographs are comparable to those obtained by Karthik *et al.* (2011) and Takeuchi *et al.* (1999) who also investigated the effects of electron irradiation in nuclear graphite, HOPG, and highly graphitized carbon fibres. It must be noted that while these descriptions provide qualitative analysis, understanding the exact mechanisms of defect creation remains an area for investigation. A contrast change in a phase contrast TEM micrograph may not necessarily relate to a change in atomic position but may instead be due to a change in thickness or defocus (as a result of knock on damage and sputtering). Whilst every effort was made to ensure that images were acquired at Scherzer defocus, awareness of the issues associated with contrast reversal is highly important when analysing these disordered structures (Scherzer, 1949).

Diffraction patterns were also recorded at regular intervals during electron beam exposure and the spacing of (002) spots were measured using intensity profiles in Digital Micrograph. Figure 6.2 shows an increase in (002) inter-planar spacing of 10% following electron irradiation of 0.31 dpa, as measured from the diffraction patterns. The arcing of the diffraction spots was also measured using the GAAP software to assess the misalignment of layers induced during electron irradiation. Full details of this technique can be found in chapter 4. The data are presented in figure 6.3 and show a 40° increase in arcing of (002) diffraction spots following 0.86 dpa of electron irradiation.

TEM micrographs were also analysed, using software provided by the PyroMaN research group, to quantify the change in atomic arrangement following electron irradiation (Raynal *et al.*, 2010). Full details of this technique can be found in chapter 4. Application of the software to ordered and (electron irradiation induced) disordered areas is displayed in figure 6.4 with the extracted data presented in figures 6.5, 6.6, and 6.7. The lack of fringe detection (outlined in white over a filtered micrograph) for ordered structures is emphasized in figure 6.4(c) where only a third of the planes are detected. The orientation maps of these micrographs (figure 6.4(d) and (h)) show localised changes in the orientation of neighbouring planes where red indicates no relative change, yellow/green

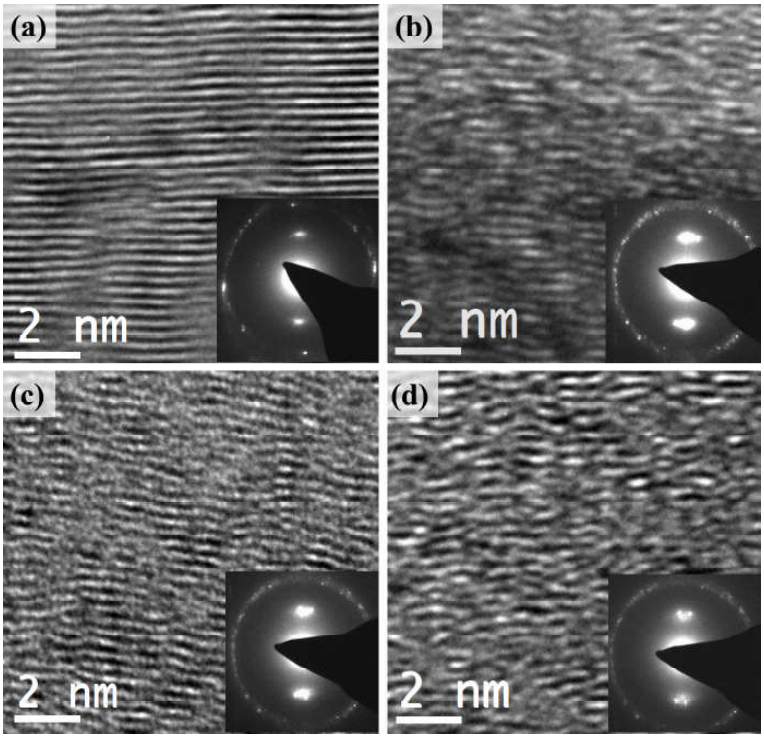

Figure 6.1: (a) - (d) Electron micrographs of PGA graphite with their corresponding SAED patterns during electron beam exposure at 200 keV and room temperature, receiving 4.2 x 10^{18} electrons cm^{-2} s^{-1} (2.4 x 10^{-4} dpa s^{-1} $\pm$ 6.4%). (a) D = 0.01 dpa, (b) D = 0.1 dpa, (c) D = 0.2 dpa, (d) D = 0.3 dpa.

.

indicates a clockwise misorientation and purple/blue indicates an anticlockwise misorientation (as illustrated in the chart next to figure 6.4(h)).

Data extracted from the fringe detection algorithm illustrated in figure 6.4(c) and (g) include fringe length (L2) and tortuosity (τ) (the latter defined as the ratio of the total length of a fringe to its direct end-to-end length). Figure 6.5, shows that for low doses (∼0.09 dpa), the tortuosity of each detected fringe is relatively low, with over 75% having a tortuosity of 1 to 1.03 and a fringe length which is relatively high, extending to 8.9 nm. However when the structure becomes disordered following electron irradiation (∼0.45 dpa), the tortuosity increases significantly, with highs of nearly 1.14, and the (002) lattice fringes break up into shorter lengths, 98% of which are below 1 nm in length.

A second-order statistical analysis of the orientation maps provided information about the relative orientation of neighbouring fringes. Referring to the

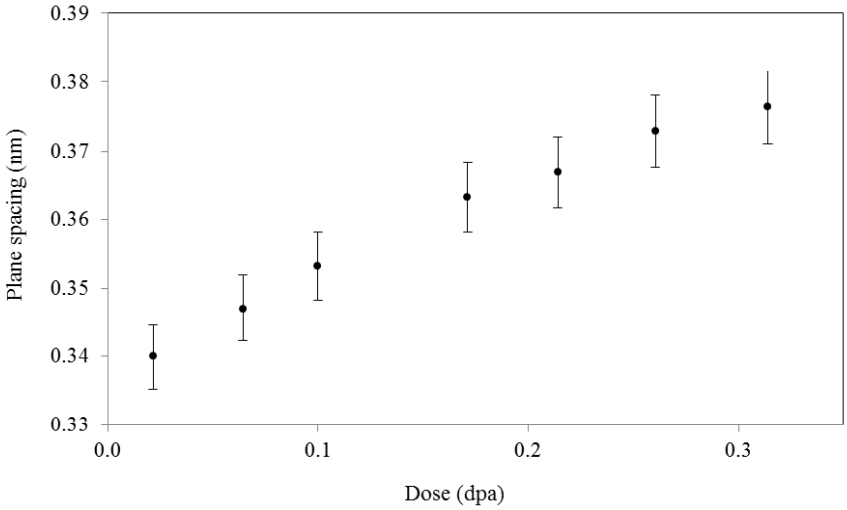

Figure 6.2: Change in interplanar spacing with respect to electron dose as measured from the spacing of (002) spot in a series of SAED patterns. Error bars represent analytical error following the analysis of three damage series. Dose error = ± 6.4%

.

schematic in figure 6.6, the angles of planes to the vertical axis (ϕ_1) were measured every 0.033 nm (pixel resolution) from the origin for a set of radii (r) up to a maximum of 4 nm. Data at each angle (θ) were then plotted on a graph of mean orientation difference ($\Delta\phi$) versus distance to determine the average opening angle for the 4 nm domain as shown in figure 6.6. The mean misorientation of the fringes corresponds to the plateau of the plots (Laffont *et al.*, 2002a). For example, the plot taken at 0.7 dpa plateaus at $\Delta\phi_{max} = 8.7°$ for both $= 0°$ and 90° (the two extremes of θ). The plateau is reached by the $\theta = 0°$ data before the $\theta = 90°$ data implying there is a quicker loss of orientation in the a-axis ($\theta = 0°$) (suggesting the fragmentation of basal planes) and domains are wider in the c-axis ($\theta = 90°$) (suggesting a retention of the layered structure). This automated procedure was performed on all micrographs acquired during electron beam exposure to produce a series of orientation maps and a plot of orientation angle against electron dose (figure 6.7). As expected it suggests that the relative orientation of planes increases with electron irradiation, but appears to plateau at high doses, suggesting there is a misorientation limit, potentially associated with the unstable transition from strained sp^2 intralayer bonding to sp^3 interlayer bonding. Although both data sets plateau at different values of $\Delta\phi$, they exhibit

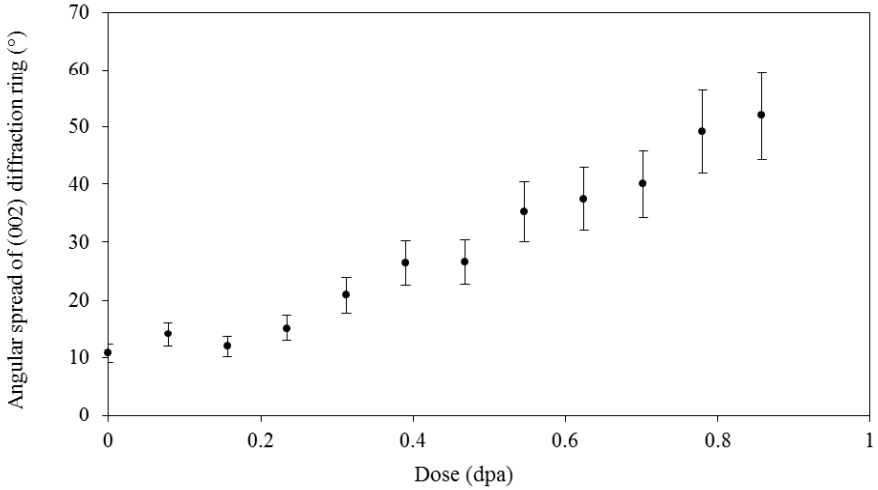

Figure 6.3: Change in the angular spread of the (002) spot with respect to electron dose. Data are extracted from SAED pattern analysis by measuring the FWHM of the intensity of (002) arcs. Error bars represent analytical error following the analysis of four damage series. Dose error = ± 6.4%

.

a similar trend suggesting there is a degree of short range homogeneity.

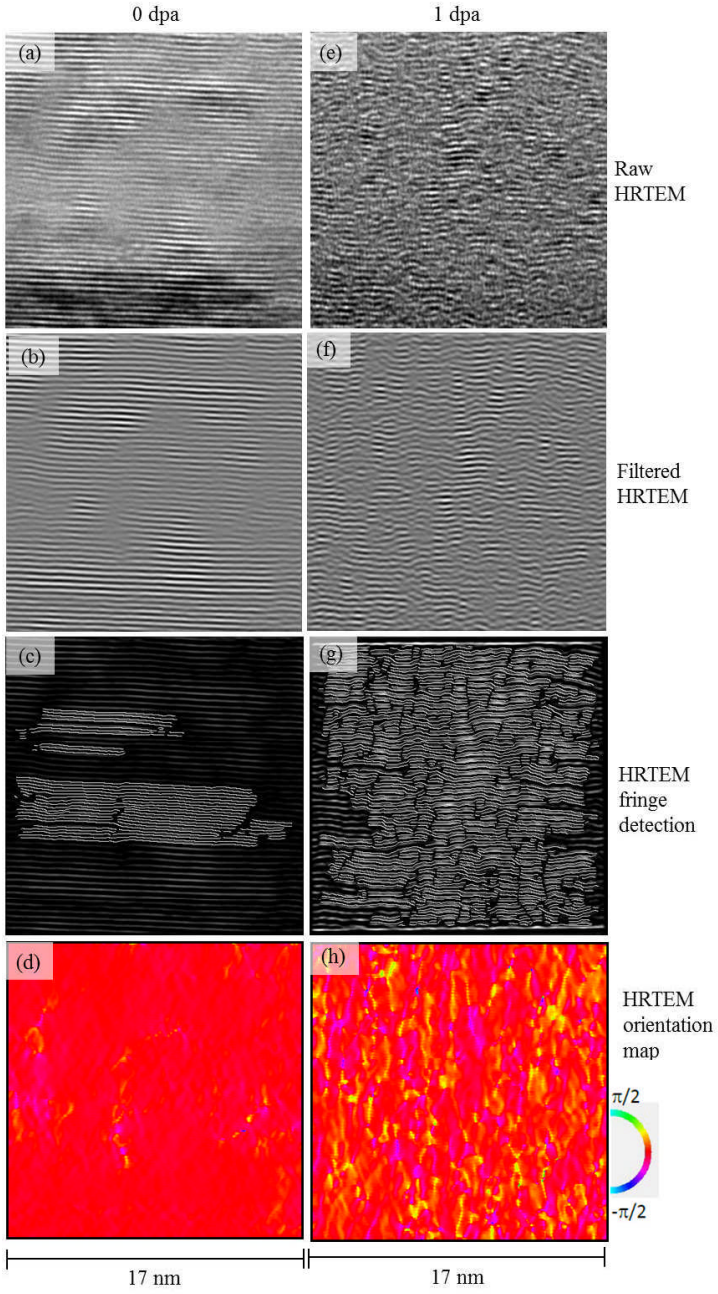

Figure 6.4: HRTEM images before (a-d) and after (e-h) 200 kV electron beam exposure for 5 minutes with electron flux 4.2 $\times$ 10^{18} electrons cm^{-2} s^{-1} (2.4 $\times$ 10^{-4} dpa s^{-1} $\pm$ 6.4%) (equating to 1 dpa). Images (a) and (e) show the raw HRTEM images, (b) and (f) the filtered HRTEM images, (c) and (g) illustrate the detection of (002) fringes within the HTREM, and (d) and (h) are orientation maps of the original HRTEM images.

.

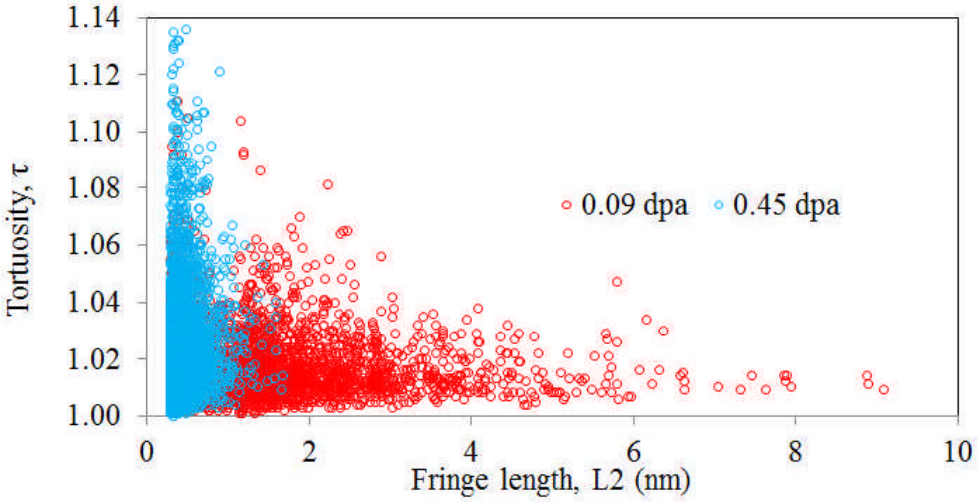

Figure 6.5: Comparison of fringe length and tortuosity data for the same region of interest having received low (0.09 dpa, red) and high (0.45 dpa, blue) electron irradiation doses.

.

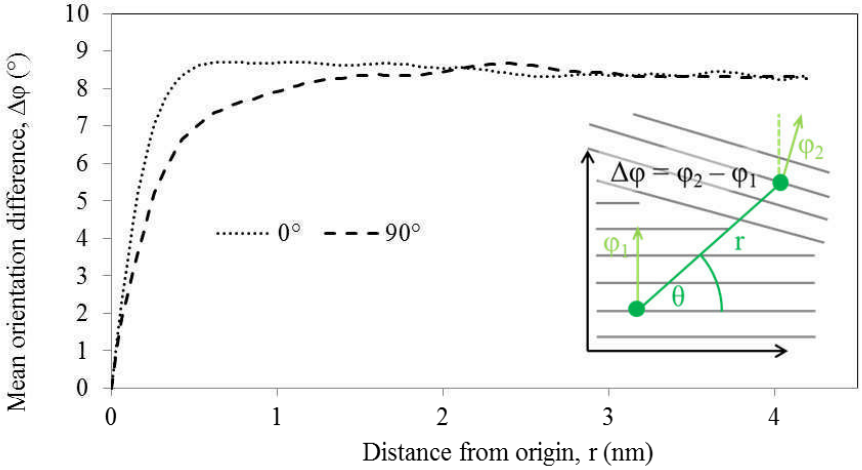

Figure 6.6: Change in mean orientation difference with distance from origin (r) at $\theta = 0°$ and $\theta = 90°$ following an electron dose of 0.7 dpa ± 6.4 %. The coherence lengths can be defined as the distance at which 90% of the value of the plateau is reached for the diagrams at 0° and 90° (DaCosta *et al.*, 2014).

.

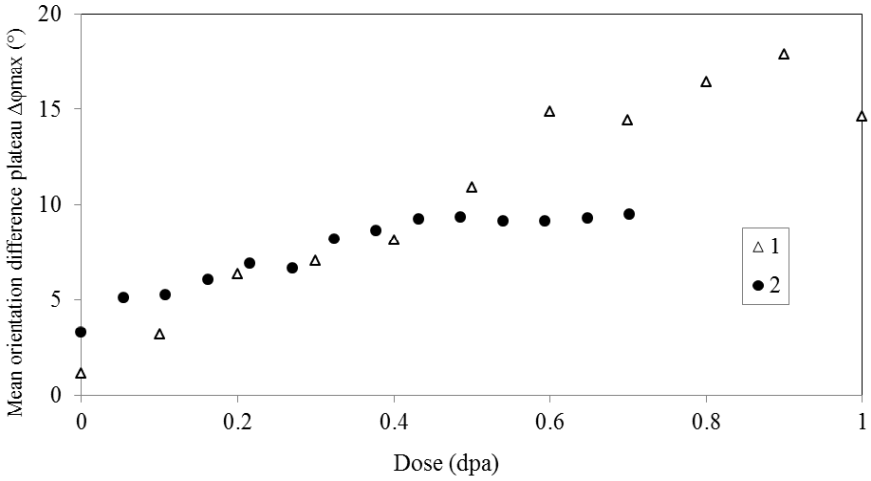

Figure 6.7: Change in mean orientation difference plateau, $\Delta\phi_{max}$, with electron irradiation for two irradiation data sets. Dose error = ± 6.4%.

6.2 EELS results

The bulk ($\pi+\sigma$) valence plasmon peak in the low loss region of the spectrum was analysed; the position of the peak being determined by taking the first derivative of the spectrum. The widely agreed value for the bulk plasmon peak position of HOPG in the literature is 27 eV (Egerton, 2009; Gass *et al.*, 2008; Henrard *et al.*, 1999; Laffont *et al.*, 2002a) (for comparison, the corresponding value for amorphous carbon is 23 eV). As illustrated in figure 6.8, the plasmon peak energy for PGA graphite is consistently lower than that of HOPG. This may be due to the misorientation of the specimen's *c*-axis relative to the normal of the incident beam (Marinopoulos *et al.*, 2002), in combination with the choice of the spectrometer collection angle (Brydson, 2001; Egerton, 2011). It may also be a result of the intrinsically lower density of this graphite grade (1.74 g cm^{-3}), compared to perfect graphite (2.2 g cm^{-3}) or the influence of crystallite boundaries. During the experiments the position of the plasmon peak appears unchanged, or perhaps slightly decreases, as a function of dose to within experimental error.

A representative set of EELS carbon K-edge spectra as a function of electron irradiation is presented in figure 6.9 (a)-(d). The π^* peak maximum of all spectra was calibrated to 285 eV, and carbon K-edge spectra were acquired every 90 to 100 seconds along with the corresponding low loss peak which was used to deconvolute

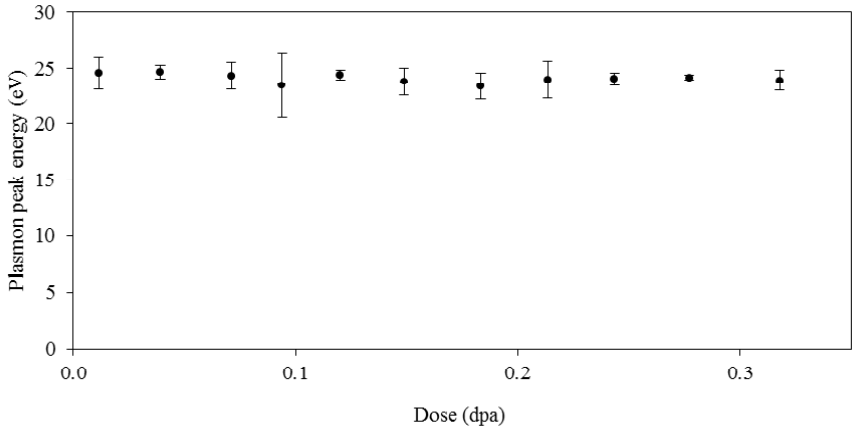

Figure 6.8: Change in plasmon peak position with electron dose. Data are averaged over two regions of electron transparent (002) oriented PGA graphite. The error bars reflect the experimental variance. Dose error = ± 6.4%.

each K-edge spectra to remove plural scattering. The data extracted from the spectrum acquired at t=0 were used to normalise subsequent sp^2 content data. Note that even after extensive electron irradiation damage, and even though the σ^* component appears to undergo considerable change with a reduction in fine structure indicative of a decrease in graphitic order (figures 6.2-6.7), the presence of the π^* peak indicates that the structure retains a distinct sp^2 character.

Five Gaussians were fitted using the constraints detailed on page 83. The variation of planar sp^2 content was calculated by comparing the ratio of the π^* intensity (G1) with the total carbon K-edge intensity (over a 20 eV window of onset 282.5 eV), the latter is proportional to the total number of carbon atoms present in the probed volume.

As can be seen in figure 6.10 the sp^2 content changed approximately linearly with respect to electron dose. The sp^2 content dropped to 76% following an exposure of 0.32 dpa, a value consistent with the typical value of 75% sp^2 carbon derived from an amorphous carbon film using this fitting method. These changes provide evidence for the introduction of atomic disorder as a result of electron beam exposure. The errors shown in figure 6.10 reflect an analytical error of 6% (determined by making slight changes to the energy windows to account for subjective discrepancy) and the variation in data between four separate experiments.

The signals from the G2 and G3 peaks were also analysed to provide informa-

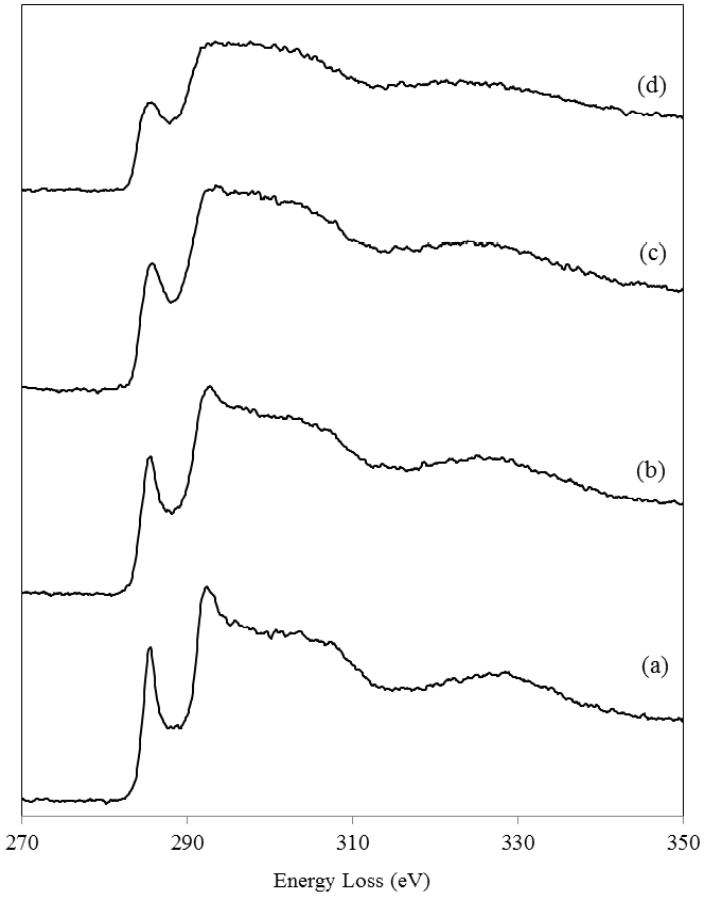

Figure 6.9: Change in EEL spectra with electron dose (D): (a) D = 0 dpa; (b) D = 0.113 dpa; (c) D = 0.209 dpa; (d) D = 0.267 dpa ± 6.4%.

tion regarding the non-planar sp^2 carbon content of the specimen by measuring the ratio between the combined intensities under G2 and G3 (I_R) and the combined intensities under the G1, G2 and G3 peaks (I_{R+sp^2}), as detailed in section 4.3.2 on page 85. This ratio is proportional to the fraction of sp^2 bonded carbon atoms which are bonded in a non-planar fashion and the increase in this quantity with increasing electron dose is plotted in figure 6.11. Note the non-zero value of this quantity at zero-extrapolated dose is due to the inherent intensity in this spectral region (even in a pure planar sp^2 carbon based material) as well as any non-planar sp^2 carbon atoms located at crystallite grain boundaries within the analysed volume. Comparing the data in figure 6.10 and 6.11, it appears as though the loss of planar sp^2 bonding (very roughly a 20% decrease) is predomi-

nantly accounted for by an increase in non-planar sp^2 bonded carbon.

Taking the first derivative of the carbon K-edge spectrum to analyse the change in the MSR peak position (at $\sim$ 330 eV) during the electron beam damage series, we observe a slight decrease in energy relating to an increase in C-C bond length (figure 6.12). The error associated with these data increases for higher doses where the MSR peak becomes wider leading to a degree of uncertainty in absolute peak position; the error bars in figure 6.12 represent experimental variation. Results obtained by Daniels *et al.* (2007) following a series of graphitization experiments are analogous, whereby the graphite began as a highly disordered material with an average bond length of 1.435 Å and through annealing became a near-perfect structure with a corresponding bond length of 1.420 Å. In Daniels' case, the decrease in bond length during graphitization was attributed to a decrease in sp^3 bonding (bond length = 1.54 Å) and the removal of heteroatoms and aliphatic molecules (bond length > 1.42 Å). In the present case however, no heteroatoms and aliphatic molecules are introduced to the system and the high energy barrier between graphite and diamond phases makes sp^2 to sp^3 transformation unlikely unless at very high temperature ($\sim$725°C) (Banhart, 2002). However, it has been established that the electron irradiation induces nanocrystallinity with atomic disorder at crystallite grain boundaries, (figures 6.1 and 6.6), and it is this disorder that reduces the packing efficiency of carbon atoms which is thought to increase the average bond length (e.g. for the most extreme case of amorphous carbon, the bond length increases to 1.44 Å(Magnuson *et al.*, 2012)). It is thus suggested that introduction of dislocations and defects along with a bending of planes (the introduction of non-six-membered rings of carbon atoms (Karthik *et al.*, 2011)) following electron irradiation increases the average C-C bond length. One might expect that an increase in bond length would lead to a reduction in valence electron density (and thus the possible slight reduction in plasmon energy with increasing dose as shown in figure 6.8).

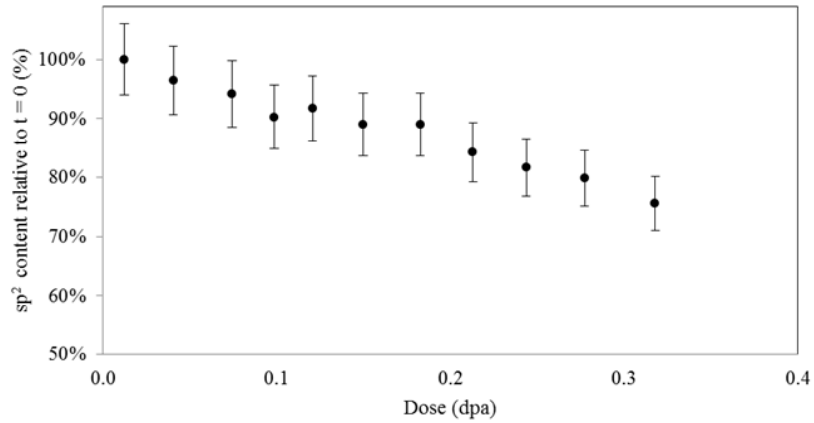

Figure 6.10: Change in sp^2 content with electron dose. Data were analysed using the 5 Gaussian fitting method and averaged over four regions of electron transparent (002) oriented PGA graphite. The error bars reflect the experimental variance and analytical error. Dose error = ± 6.4%.

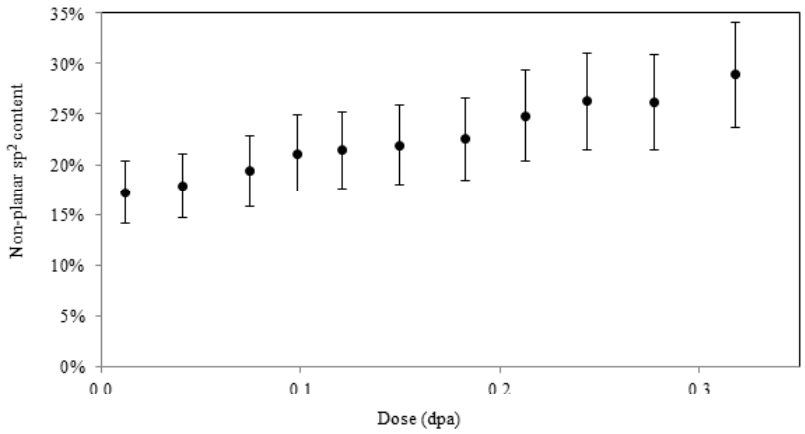

Figure 6.11: Change in non-planar sp^2 content with electron dose over two regions of electron transparent (002) oriented PGA graphite. Error bars reflect experimental variance and analytical error. Dose error = ± 6.4%.

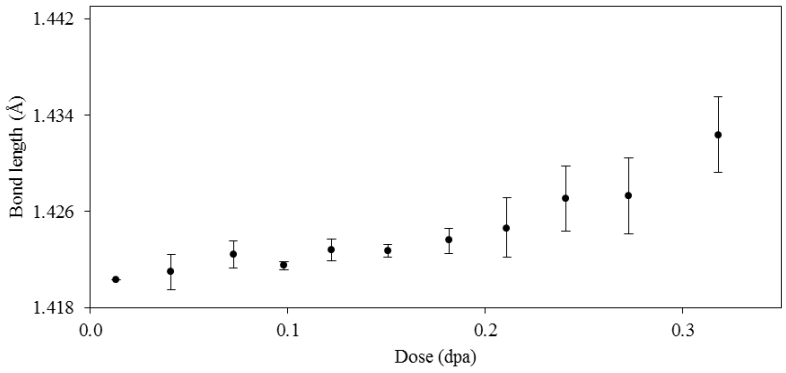

Figure 6.12: Change in MSR peak position with electron dose over two regions of electron transparent (002) oriented PGA graphite. Error bars reflect experimental variance and analytical error. Dose error = ± 6.4%.

6.3 3D atomistic modelling

In collaboration with Jean-Marc Leyssale, micrographs from these electron irradiated series were subject to the IGAR technique discussed in section 4.2.2. The data extracted from the simulation is compared to the experimental TEM and EELS data presented in this chapter. The atoms are labelled C1 to C6. C1, C2, C4 are carbon atoms with 1, 2 or 4 neighbours, and C3 are defect 3-fold carbon atoms. C6 are hexagonal 3-fold atoms whose nearest neighbours are sp^2 atoms (i.e. C6 (planar sp^2) or C3 (non-planar sp^2)).

Figure 6.13 shows the raw TEM images, the 3D models calculated through the IGAR technique, and the corresponding simulated TEM images during electron irradiation. TEM images of the 3D models are simulated using the multislice simulation approach as implemented in the NCEMSS software package (Kilaas, 1987). Comparing the simulated and experimental images, there are clear similarities in the degree of fringe fragmentation and the development of a tortuous nanotexture during electron irradiation. To properly assess the accuracy of the simulated TEM images, they are subjected to the 2D PyroMaN image analysis; figure 6.14 shows that the L2 values for experimental and simulated TEM lattice images are comparable, verifying that the 3D models contain much of the nanotextural information shown in the experimental TEM images. Information about the atomic bonding can also be extracted from the 3D IGAR models. Experimental and IGAR data for planar and non planar sp^2 bonded carbon atoms

are shown in figure 6.15. There is a close correlation between the two data sources for both parameters providing further evidence for the accuracy of the IGAR reconstruction.

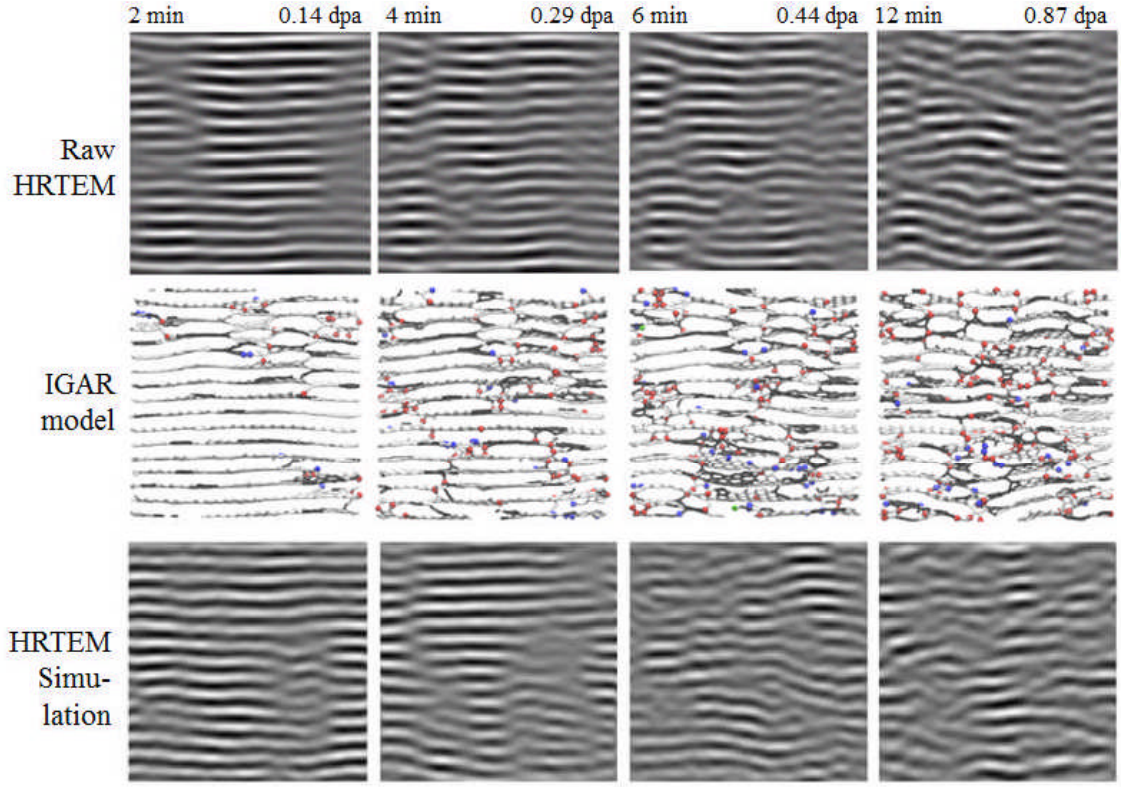

Figure 6.13: Application of the IGAR technique to micrographs of electron irradiated PGA graphite. The top row shows raw HRTEM images acquired at 200 kV. The middle row shows the 3D atomistic reconstruction of these images. The bottom row shows simulated HRTEM images of the 3D reconstructions using the multislice method.

This technique can be applied to a range of disordered graphite TEM images to better understand features of interest in a micrograph. Identifying defect structures in the 3D model and then identifying them in the simulated TEM image allows experimental lattice images to be better understood. It also allows the atomic models proposed in the literature by Banhart *et al.* (2011); Ewels *et al.* (2003); Heggie *et al.* (2011); Latham *et al.* (2008); Trevethan *et al.* (2013) to be assessed based on experimental results. Once the accuracy of the technique is verified, additional physico-chemical properties of the irradiated material can be extracted from the IGAR results such as mechanical and thermal properties.

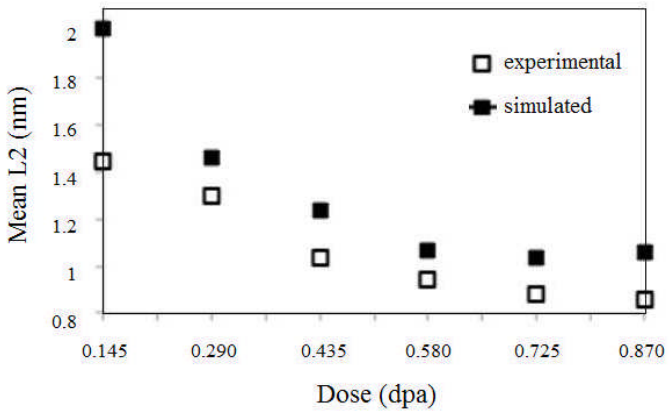

Figure 6.14: Application of the PyroMaN image analysis software to raw and simulated TEM images of IGAR 3D reconstructions to validate simulation and reconstruction statistics.

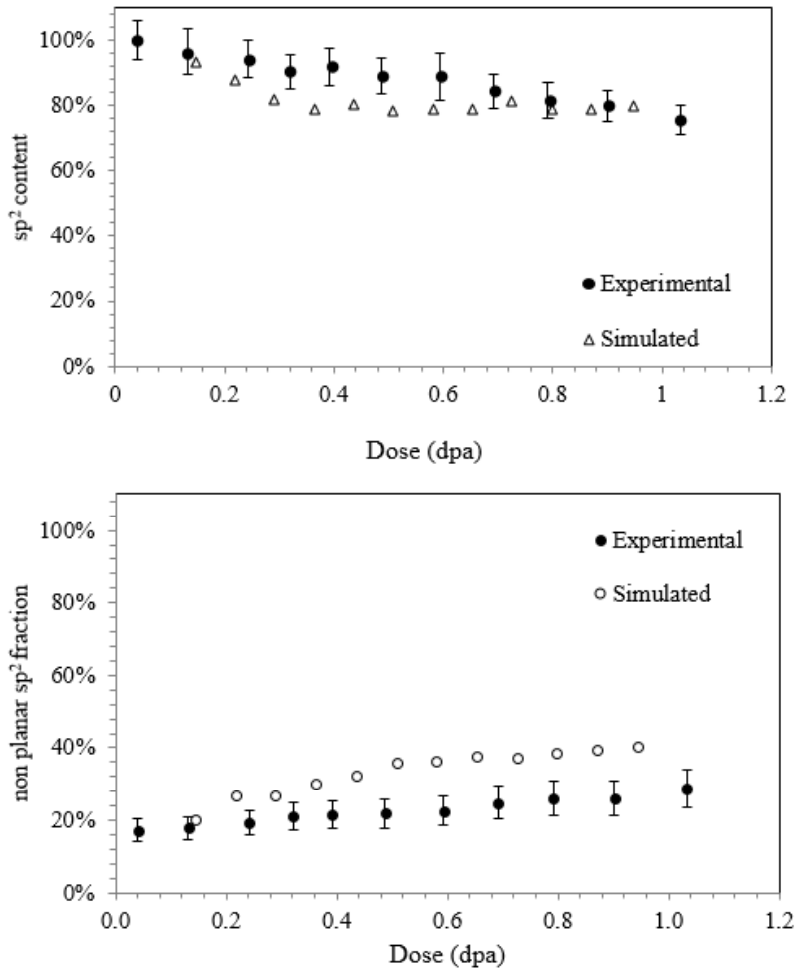

Figure 6.15: Comparison of experimental EELS and IGAR calculations for (a) planar sp^2 and (b) non planar sp^2 bonded carbon.

6.4 Discussion

This chapter has presented a new methodology to quantitatively analyse TEM micrographs of irradiation damaged graphite. Following electron irradiation at 200 keV, a decrease in the graphite (002) fringe length and an increase in tortuosity and relative misorientation was observed indicating a reduction in the alignment of basal planes. Analysis of the low and core loss of several EEL spectral series indicated little or no change in valence electron density, a decrease in planar sp^2 content (to levels similar to amorphous carbon at the highest doses), an increase in non-planar sp^2 content (to seemingly replace the loss of planar sp^2), and an increase in C-C bond length, all reflecting an increased tortuosity of (002) lattice fringes and the fragmentation of crystallites following electron radiation exposure. The application of the IGAR technique showed similar results to experimental data (L2, planar, and non-planar sp^2), and provided 3D models of 2D micrographs to enable a better visualisation of irradiated graphite, and a better understanding of how electron radiation induced defect structures are displayed in a TEM lattice image.

Considering the results presented in this chapter in parallel with the findings of the studies reviewed in chapter 3, several stages of radiation damage induced structural changes can be described. The Marsh-Griffith model describes four main structural stages during graphitization. Oberlin (1984) defined these stages as beginning with a semi coke material containing randomly distributed and randomly oriented "basic structural units", which organise into distorted columns following ~1000°C of heat-treatment. Adjacent columns then coalesce into distorted wrinkled layers (after ~1500°C), which eventually stiffen to become flat and perfect in the last stage (following ~2000°C heat-treatment) (figure 6.16(a)). In the case of radiation damage, a reversal of this process is observed with a few variations. Niwase & Tanabe (1993) proposed a three stage radiation induced structural degradation process, beginning with the creation of in-plane defects in the originally perfect structure which are able to annihilate with mobile interstitials. This then leads to turbulence in, and fragmentation of, basal planes, which eventually results in amorphization (figure 6.16(b)).

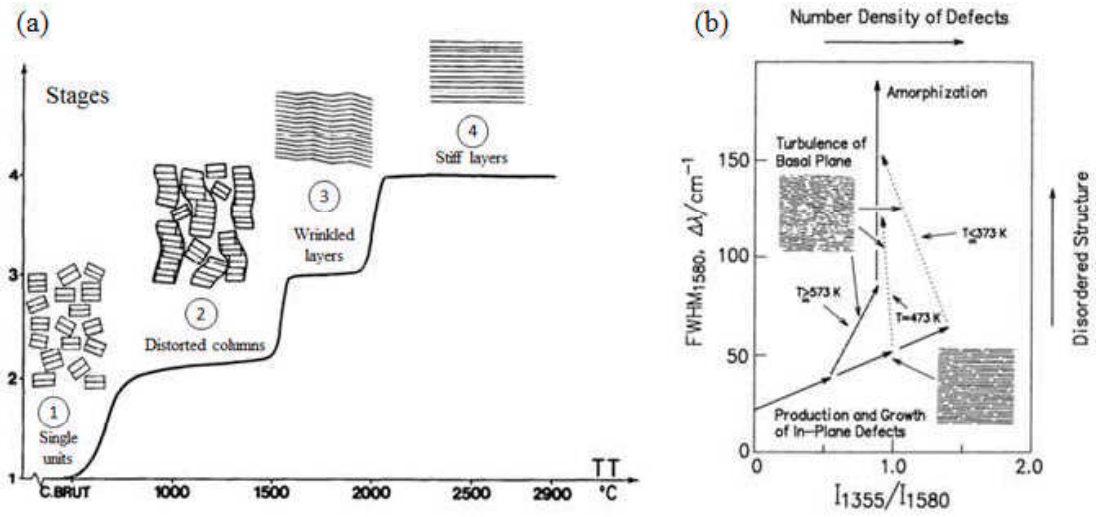

Figure 6.16: Proposed stages of structural change in (a) the graphitization process, based on TEM observations (Oberlin, 1984) and (b) radiation exposure, based on Raman experiments (Niwase & Tanabe, 1993).

It has been established in this chapter that virgin nuclear graphite which has undergone graphitization in the manufacturing process exhibits a high planar sp^2 content with relatively large crystallites containing flat and evenly spaced basal planes. This work has shown that exposure to electron radiation changes d-spacing, the concentration of hexagonal rings, the length and tortuosity of basal planes, the size of crystallites, and the composition of sp^2 carbon bonding. The typical increase in d-spacing is ~10% following electron radiation (0.5 - 0.7 dpa in the studies cited, and depending on TEM operating voltage, flux, and pre-irradiated graphitic structure) (Karthik *et al.*, 2011; Muto & Tanabe, 1997; Takeuchi *et al.*, 1999). This work showed the d-spacing to increase by 10% after 0.31 dpa of 200 kV electron radiation. XRD studies have shown that neutron radiation exposure also induces crystallite fragmentation, where both L_a and L_c are reduced by more than 50% (Gallego *et al.*, 2013; Mironov, 2015). The EELS results in this chapter and the work of Kane *et al.* (2011) and Takeuchi *et al.* (1999) show a retention of the π^* peak providing evidence for the retention of a layered structure and not the introduction of a completely amorphized material, despite crystal fragmentation and the introduction of complex defect structures as observed in the 3D IGAR model. The value for sp^2 in irradiated graphite,

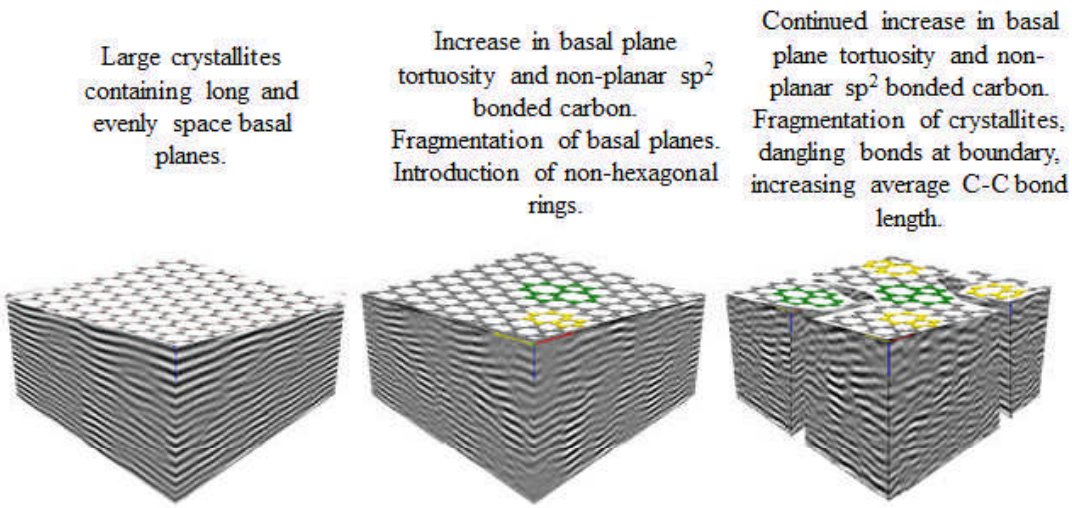

Figure 6.17: Proposed model for radiation damage showing three stages: pre radiation, low radiation exposure, and high radiation exposure.

as determined from core loss analysis in this chapter ($\sim$ 75%), is also higher than sp^2 content in amorphous pre heat-treated carbons ($\sim$ 55%) which might contain heteroatoms and nano-pores, further providing evidence for incomplete amorphization following electron irradiation (Daniels *et al.*, 2007; Powles *et al.*, 2009). There has been no quantitative analysis of the core loss spectra for electron irradiated graphites in the literature so comparisons can only be made to graphitized/pre-graphitized material.

Based on this information and the results in this chapter, a new nanoscale model describing the stages of radiation damage is proposed in figure 6.17 (pre-turnaround). Initially, large crystallites with a d-spacing of 0.335 nm are ordered, consisting of a majority of hexagonal rings. Following low radiation doses atomic defects are thought to distort the planar structure through the creation of non-hexagonal rings and an increase in d-spacing as shown in figures 6.2 and 6.13. The increase in d-spacing is thought to be a result of new basal planes forming between existing basal planes by the positive climb of dislocation dipoles (Karthik *et al.*, 2011; Kelly, 1971; Niwase, 2012). Accumulation of these defects increases the tortuosity of basal planes, as shown in figures 6.1 and 6.13. This increase in tortuosity is linked to the introduction of non-planar sp^2 as observed in 6.11 and 6.15(b) and a consequent reduction in planar sp^2 bonded carbon. At higher doses,

the fragmentation of crystallites occurs, resulting in an increase in the average C-C bond length due to an increase in peripheral dangling bonds at crystallite boundaries. The final structure exhibits a high proportion of non-hexagonal rings (possibly created via Jahn-Teller distortion around a single vacancy, as discussed on page 17, or through the creation of a Stone-Wales defect as discussed on page 19) and a reduced density, whilst maintaining a layered structure.

Chapter 7

Electron Irradiation of Specimens Heated In Situ

Graphite moderated nuclear reactors operate at temperatures around 350°C to reduce the degree of irradiation damage through continual thermal annealing. The temperature at which annealing occurs is dependent on the irradiation temperature. Post irradiation heat treatment of nuclear graphite can reverse some of the effects of irradiation damage; heat treatment up to 1000°C can return the Young's modulus to pre-irradiation levels and above 1250°C large interstitial loops are annealed, however heat treatment over 2700°C can result in residual damage where large interstitial loops collapse, increasing the basal plane contraction (Kelly *et al.*, 1966b; Reynolds, 1968).

When investigating new defect structures in graphite, it is common to calculate defect formation, migration, and activation energies using accurate modelling techniques such as density functional theory (Latham *et al.*, 2008, 2013; Li *et al.*, 2005; Trevethan *et al.*, 2013; Zhang *et al.*, 2010). The activation energy can be translated to a temperature, at which defect movement occurs, through the Arrhenius formula (equation 7.1),

$$\upsilon(T) = A(T)e^{-(E_a/k_BT)} \tag{7.1}$$

where $\upsilon(T)$ is the migration frequency, $A(T)$ is the vibrational frequency of the defect, and the exponential function describes the defect annealing rate (dependent on activation energy E_a, temperature T, and Boltzmann's constant k_B). Applying the Arrhenius formula (equation 7.1) to the calculated activation

energies of vacancies (1.1 eV (Latham *et al.*, 2013)) allows one to estimate the temperature where vacancy migration is significant. For a Debye frequency (A) of order 10^{14} Hz, the vacancy occurrence rates (υ) for different temperatures are displayed in table 7.1. For an atomic configuration to be created/annealed the value of υ must be >1. the point at which this occurs is between 100°C and 200°C.

Temperature (°C)	Vacancy occurrence rates (υ) (s^{-1})
20	1.2×10^{-5}
100	1.4×10^{-1}
200	1.9×10^{2}
300	2.2×10^{4}
400	5.8×10^{5}

Table 7.1: Variations in vacancy occurrence rate for a range of temperatures, based on the Arrhenius formula, assuming a Debye frequency of 10^{14} Hz and activation energy of 1.1 eV (Latham *et al.*, 2013).

To further explore the net damage temperature threshold and activation energies of defects, in situ electron irradiation experiments at a variety of temperatures have been completed. Collecting lattice images during 200 kV beam exposure has provided evidence for a damage temperature threshold. Since irradiation-induced, small interstitial loops (radius <100 $\mathring{A}$) have been seen to form below 650°C and are expected to migrate/coalesce above 1000°C (Telling & Heggie, 2007), it was expected that the effects of thermal annealing would reduce the damage rate, and that a temperature threshold could be deduced through a lack of electron beam damage beyond a certain temperature (Nakai *et al.*, 1991; Reynolds, 1968).

To decide on a suitable temperature range to perform electron irradiation studies, the migration energies of single interstitials and vacancies were considered. The migration energy of a single interstitial has been calculated to be $\sim$ 1.5 eV (Li *et al.*, 2005), but experimental results show a much smaller value of <0.4 eV (Thrower & Mayer, 1978). Converting these energies to a temperature through the Arrhenius formula (equation 7.1) gives a large temperature range of -130°C to 270°C (assuming $\upsilon(T) = 1$ migration per second and $A(T) = 10^{14}$ Hz (Li *et al.*, 2005; Telling & Heggie, 2007)). The single vacancy has been calculated

to have a migration energy of 1.1 eV, corresponding to a temperature of 125°C (El-Barbary *et al.*, 2003; Latham *et al.*, 2013; Trevethan *et al.*, 2013; Zhang *et al.*, 2010). Furthermore, typical reactor operating temperatures are around 350°C. Experiments were therefore conducted at -190°C, 20°C, 100°C, 150°C, 200°C, 300°C, and 400°C.

7.1 Experimental considerations

Behaviour of TEM grids and support films at high temperatures

When performing heating experiments in the TEM an appropriate grid and support film must be used. For conventional room temperature TEM investigations, 3 mm copper grids with an amorphous holey carbon support film are used; however at high temperatures the copper grids redeposit nano particles onto the carbon film which can contaminate the specimen. To assess the degree of nano particle redeposition following heating of copper grids, ex situ heating was performed, the results of which are displayed in figure 7.1. When heated, the carbon film itself can also tear and curl back on itself, providing little support for the specimen. Since the copper grid was deemed unsuitable, a literature search was carried out to select a more suitable grid (Luo *et al.*, 2011; Sharma, 2012; Zhang & Su, 2009). It was concluded that a gold grid with a holey carbon film would suffice up to temperatures of 850°C.

Preliminary results

Initial heating experiments were performed on the University's FEI Tecnai TEM at an operating voltage of 200 kV providing an electron flux of approximately 10^{19} electrons cm^{-2} s^{-1}. The heating holder initially used was a Gatan Smartset Hot Stage Controller (Model 901) which uses a Hexring® specimen clamp for thermal contact between the specimen and the R-type thermocouple.

The ramp rate was 200°C per minute and the specimen was left at the elevated temperature for 1 hour to achieve thermal stability. Despite these precautions a sufficient level of stability was not achieved and the micrographs exhibited thermal drift due to the unavoidable high frequency vibrations from the holder

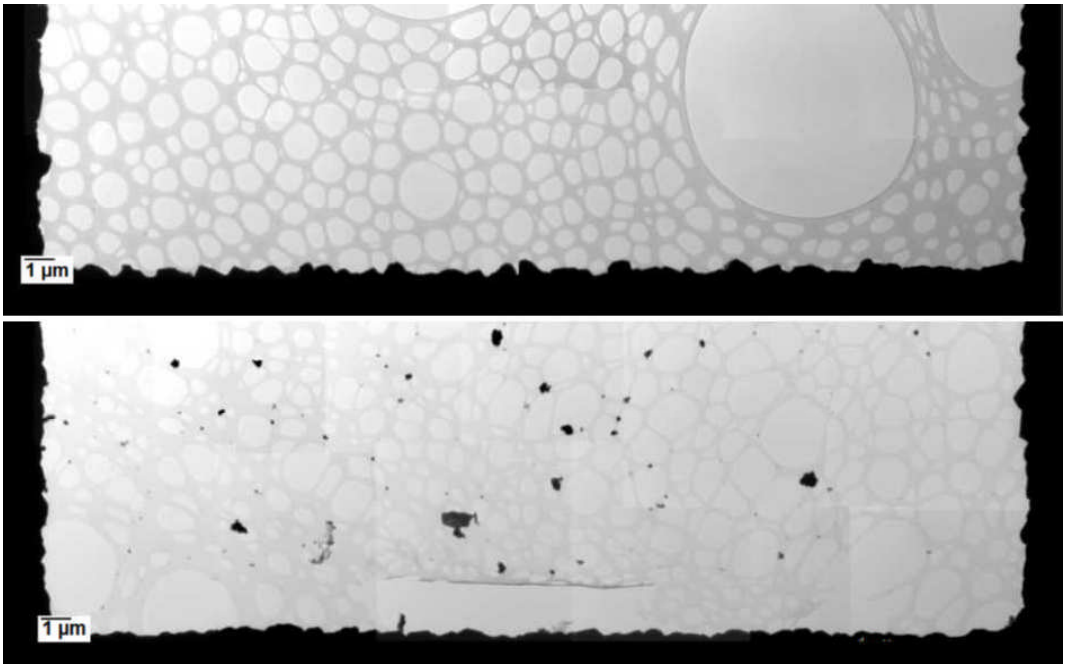

Figure 7.1: Amorphous carbon film and copper grid before (top) and after (bottom) ex situ heating to 650°C.

(figure 7.2). It was also not possible to image an area at room temperature and follow it during increases in temperature, again due to high levels of thermal drift. Nevertheless, the results from these experiments showed a reduction in damage rate with increasing temperature. However due to the slightly unstable imaging conditions, interpretation of the micrographs was difficult. Qualitative analysis showed that at 100°C the micrographs exhibit similar features to those from room temperature beam exposure. However at 400°C the degree of beam damage appears to be reduced. To make more quantitative assessments of this effect, additional experiments were performed with different heating holders.

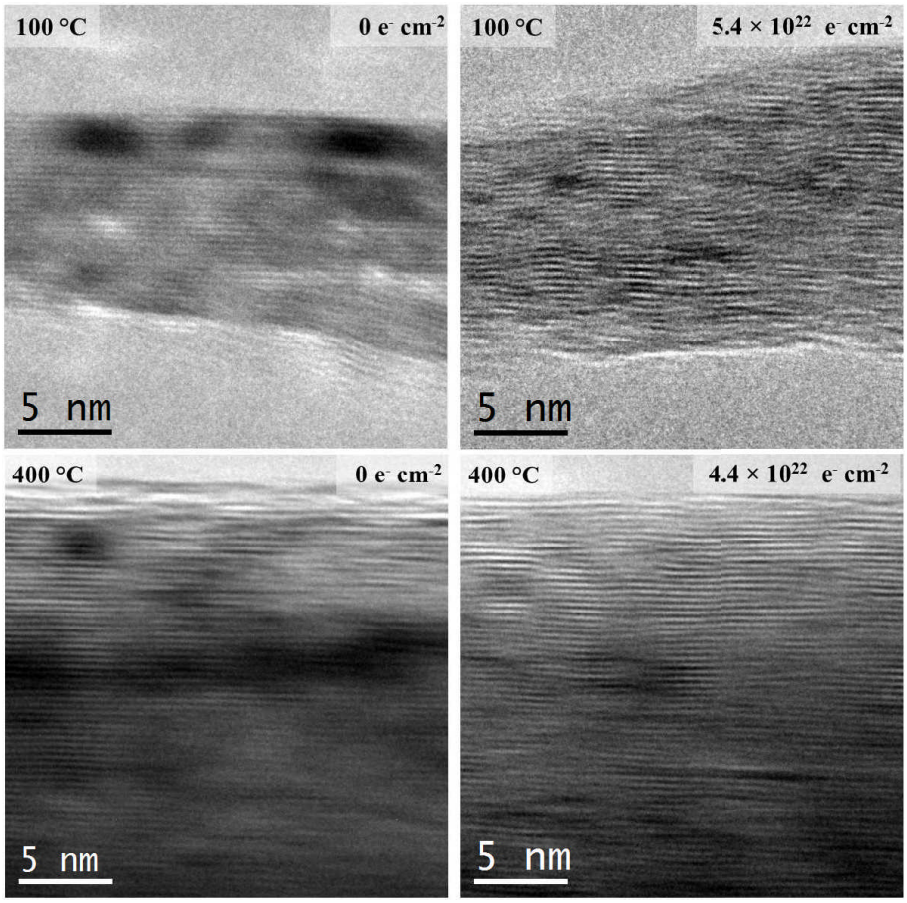

Figure 7.2: TEM micrographs before and after 200 kV electron beam exposure at 100°C and 400°C using the Gatan heating holder (Model 901).

7.2 In situ heating results (1)

To collect better quality images and to have a higher confidence in temperature calibration further experiments were carried out at the University of York. Their 1 $\mathring{A}$ double aberration corrected in situ JEOL 2200 FS TEM/STEM uses a Gatan single tilt heating holder (Model 628). Although drift occurs with this system during temperature changes, it is small enough to be able to follow regions of interest, and thermal stability is achieved within 20 minutes. Due to the different microscope configuration and operating procedure the electron flux was calculated slightly differently. The microscope provided a figure for the current density in the form of pA cm^{-2}; this was multiplied by the operating magnification (500,000 for all images presented) and divided by the electron charge (1.6×10^{-19}C). The electron flux for all experiments was of the order 10^{19} electrons cm^{-2} s^{-1}. A selection of images acquired during in situ heating experiments at 100°C, 300°C, and 400°C are presented in figures 7.3 and 7.5. As can be seen from the Fourier transforms, there seems to be a slight deviation from annularity. This most likely due to a slight astigmatism from the objective lens and from thermal drift during imaging.

For experiments at 100°C (figure 7.3) slight changes in the structure were observed following a fluence of 3.2×10^{22} electrons cm^{-2}. A decrease in fringe length and increase in d-spacing is observed as for experiments at room temperature, however the rate at which they occur is reduced (figure 7.4).

Electron irradiation experiments conducted at 200°C showed little damage (figure 7.5a), which was expected as the vacancy occurrence rate is >1 (as calculated by equation 7.1 to be 190 s^{-1}). The retention of a relatively ordered structure during electron beam exposure means that the micrographs are not suitable for PyroMaN software analysis (for reasons outlined in section 6.1). Intensity profiles across the micrographs and Fourier transforms however can be analysed; both show a slight increase in d-spacing (of ∼3%) from 0.334 nm to 0.344 nm (which is within error margins) suggesting material is becoming turbostratic (Laffont *et al.*, 2002b).

Electron irradiation at 400°C appears to show no net structural damage. TEM micrographs, Fourier transforms, and intensity plots (presented in figure 7.5(b))

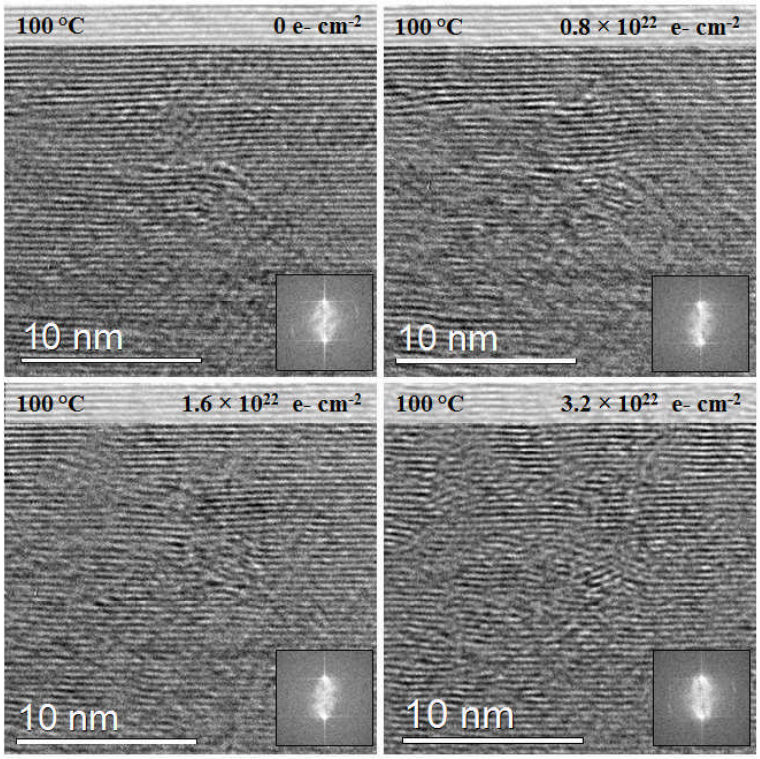

Figure 7.3: TEM micrographs and corresponding Fourier transforms during 200 kV electron beam exposure at 100°C using the Gatan heating holder at the University of York.

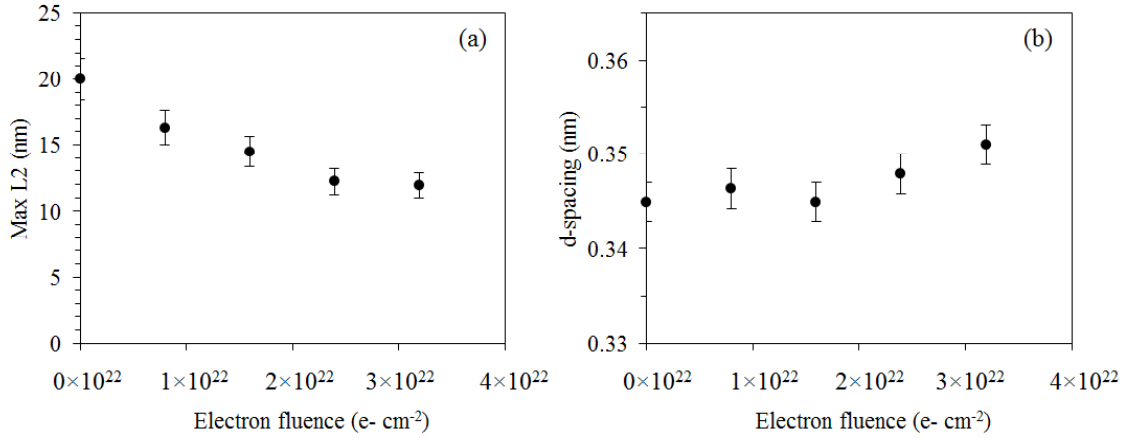

Figure 7.4: Change in fringe length (a) and d-spacing (b) with electron fluence during 200 kV electron beam exposure at 100°C using the Gatan heating holder at the University of York.

show no significant differences before and after a fluence of 3.2×10^{22} electrons cm^{-2} and the spacing of planes remains constant at 0.334 nm. At 400°C the high vacancy occurrence rate (10^5, see table 7.1) means that the energetic atomic structure is constantly making and breaking bonds, whilst always returning to the energetically favourable ordered graphitic structure.

The effects of thermal annealing following room temperature electron radiation were also investigated. Specimens were exposed to 2.7×10^{19} electrons $cm^{-2}s^{-1}$ for 20 minutes at 20°C before undergoing in situ heating to 400°C. To allow for the system to stabilize at 400°C, images were collected after 30 minutes under the same electron flux. A selection of TEM images collected during this experiment are shown in figure 7.6 along with their corresponding Fourier transforms. The results extracted are presented in figure 7.7 (using the same data analysis technique as outlined in chapter 6). From both figures, the effects of post irradiation thermal annealing are apparent. Initially, at 20°C, the structure decays in the expected manner, towards a highly tortuous nanotexture with short fringe lengths. After in situ thermal treatment at 400°C the structural changes appear to recover slightly so that the nanotexture is more ordered than that expected at the same fluence at 20°C, showing signs of thermal annealing. Data extracted from these micrographs and Fourier transforms agree with this observation. At room temperature the length of fringes decrease by ∼3 nm per 10^{22} electrons cm^{-2}, then following thermal treatment they increase at a slower rate of ∼2 nm per 10^{22} electrons cm^{-2}. A similar pattern is observed with d-spacing; at room temperature d-spacing increases by 0.01 nm per 10^{22} electrons cm^{-2}, then at 400°C decreases by 0.006 nm per 10^{22} electrons cm^{-2}. For both cases, the annealing rate is two thirds of the irradiation damage rate. The evidence for annealing suggests there are some electron irradiation induced atomic configurations present whose activation energy is $\leq$ 1.87 eV (based on the input of T = 400°C (673K), into equation 7.1 assuming $\upsilon = 1$ migration per second and $A = 10^{14}$ Hz). Any configurations with an activation energy higher than this will not be annealed at this temperature, therefore it is unlikely that the structure will return to its original state. For comparison, graphitization temperatures of ∼3000°C would be able to anneal structures with an activation energy up to 9.1 eV.

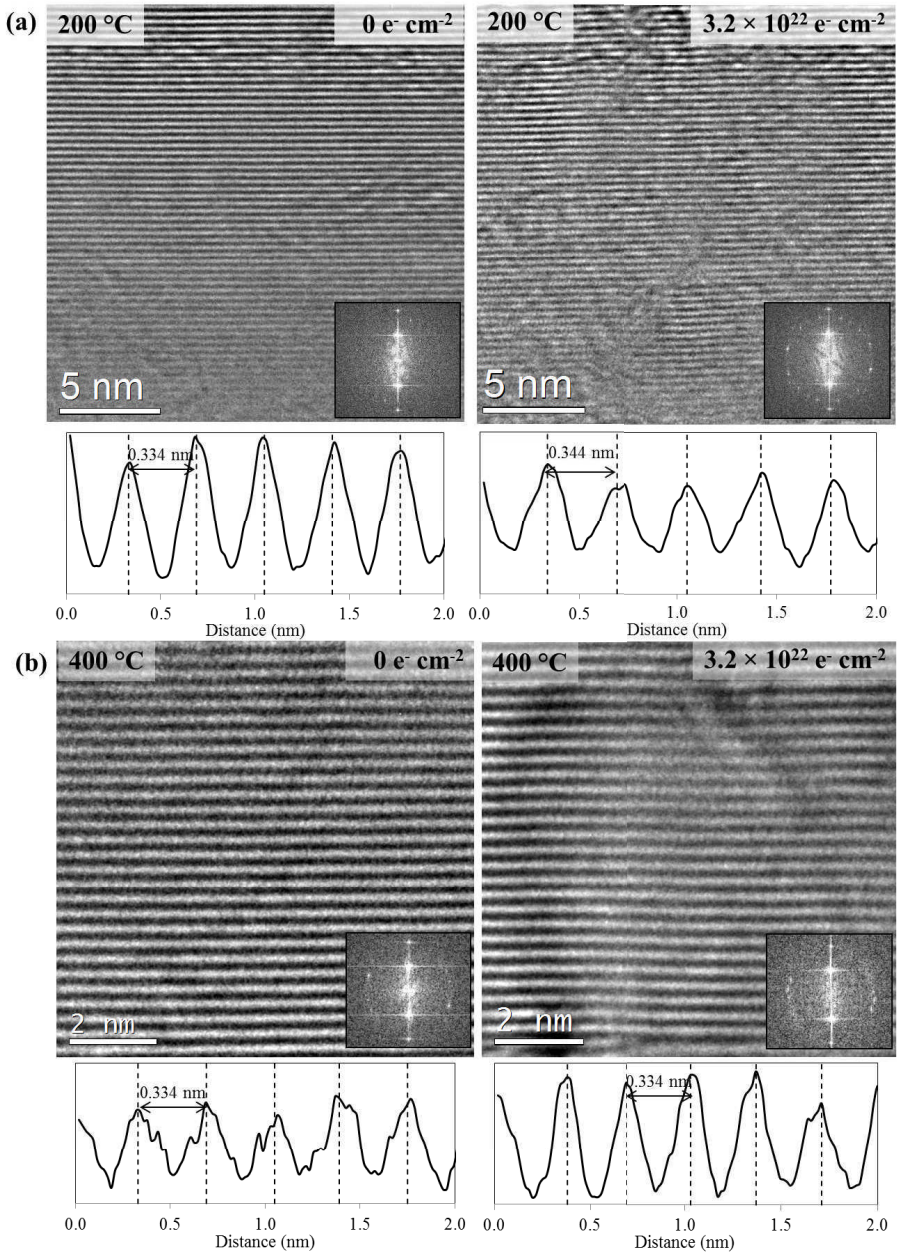

Figure 7.5: TEM micrographs and Fourier transforms during 200 kV electron beam exposure at (a) 200°C and (b) 400°C using the Gatan heating holder at the University of York. Below each micrograph is an intensity profile showing the spacing of (002) planes.

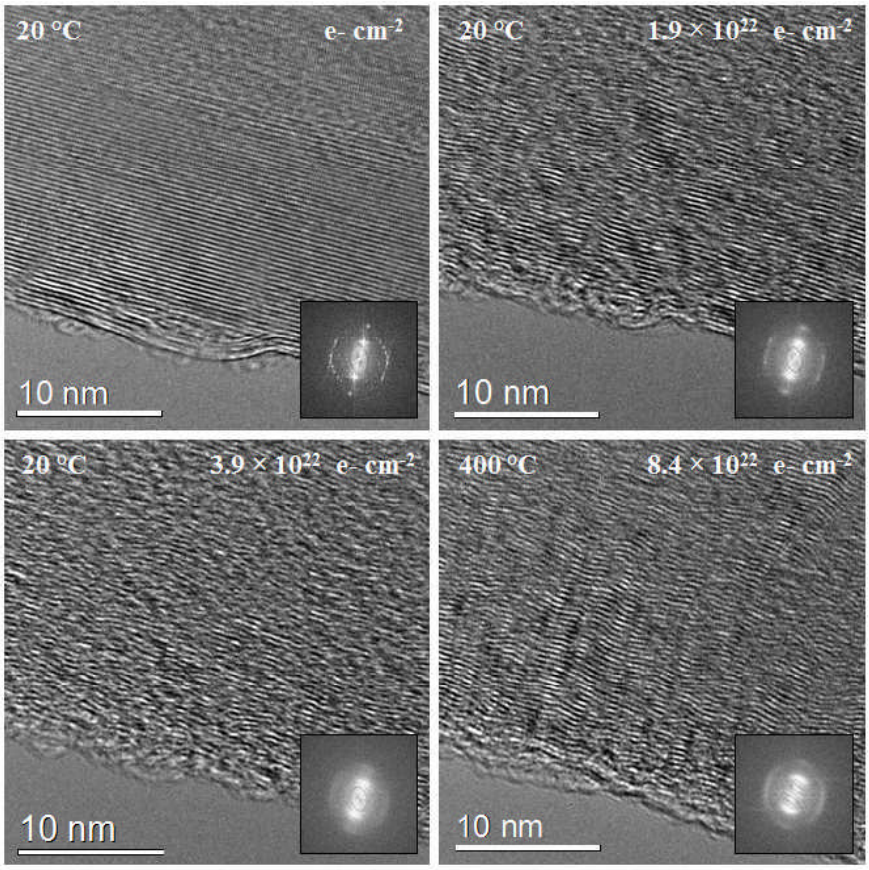

Figure 7.6: TEM micrographs and corresponding Fourier transforms during 200 kV electron beam exposure at 20°C then undergoing an in situ temperature increase to 400°C using the Gatan heating holder at the University of York (model 628).

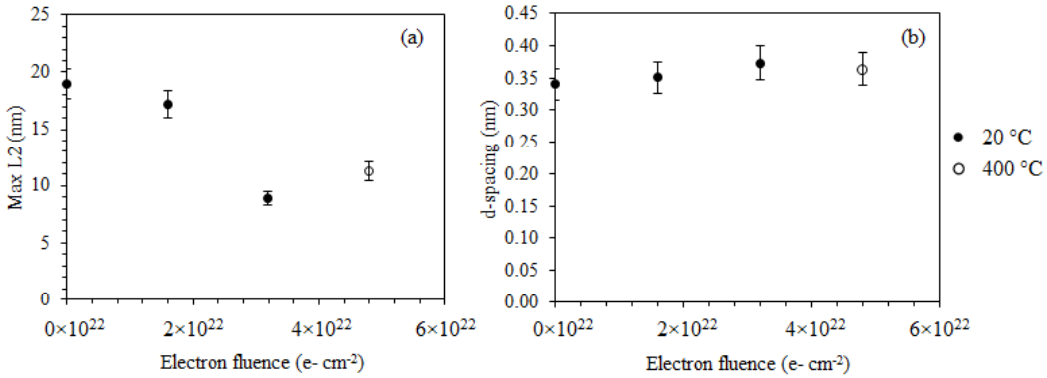

Figure 7.7: Change in fringe length (a); and d-spacing (b) with electron fluence during 200 kV electron beam exposure at 20°C then undergoing an in situ temperature increase to 400°C using the Gatan heating holder (model 628).

7.3 In situ heating results (2)

The most successful in situ heating experiments were performed using a DENS Solutions in situ TEM holder on the FEI Tecnai TEM at the University of Leeds. For this setup, the specimen does not require a conventional grid and support film as 'micro electro mechanical system' (MEMS) chips are used. The specimen is placed directly onto the chip which is then placed in the DENS holder and inserted into the microscope as with standard TEM holders. The chips are ~1 cm in length with a spiralled micro-hotplate (300 μm × 300 μm) at the centre using four point resistive temperature feedback (figure 7.8). This makes for accurate temperature readings (<± 5%), temperature stability (± 3 mK) and offers a ramp rate capability of 200°C per millisecond.

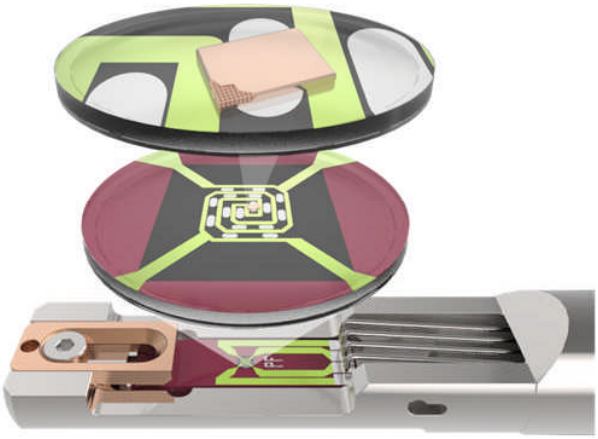

Figure 7.8: DENS Solutions chip within the TEM holder. Magnified images show the micro-hotplate and a specimen particle over a hole in the hotplate (DENS Solutions, 2015).

Crushed PGA graphite in acetone was dispersed onto the chip and in situ experiments were performed at 100°C, 150°C, and 200°C. The imaging conditions were exceptionally stable and drift was minimal, allowing the same area to be studied before and after temperature treatment. To investigate the large range in calculated and experimental migration energies of a single interstitial (~ 1.5 eV (Li *et al.*, 2005) theoretical, <0.4 eV experimental (Thrower & Mayer, 1978)) and the associated large range in temperatures (-130°C to 270°C) in situ cooling

experiments were also carried out. For this, a Gatan 636 double tilt cooling holder was used with the same operating conditions as for the heating experiments. Ground PGA graphite in acetone was dispersed onto 3 mm copper TEM grids coated with holey amorphous carbon film.

The results of these experiments are shown in figures 7.9, 7.10, and 7.11; at each temperature TEM images before and after electron radiation are shown (figure 7.9) along with plots of the progressive change in d-spacing (as measured from the Fourier transform of the micrograph) (figure 7.10), and fringe length (figure 7.11) and tortuosity (measured using the PyroMaN software discussed in Chapter 6).

In figure 7.10 the change in d-spacing with electron fluence is shown for -190°C, 20°C, 100°C, 150°C, and 200°C. At -190°C and 20°C the d-spacing begins to increase as soon as it is exposed to the electron beam. At 100°C and 150°C the d-spacing stays constant initially until a threshold fluence where it begins to increase at a rate of ∼0.3 nm per 10^{22} electrons cm^{-2}. This delayed structural change is in agreement with the findings of Kelly *et al.* (1966a) who exposed pyrolytic graphite to neutron irradiation at different temperatures. At 200°C the d-spacing does not significantly change, fluctuating between 0.343 and 0.352 nm.

The PyroMaN analysis technique to quantify a change in fringe length and tortuosity was applied to the micrographs collected at 100°C and 150°C. At 200°C and above, the basal planes largely extend beyond the image boundaries limiting the accuracy of the extractable data from the PyroMaN software. For both analysed data sets, the length of fringes decrease by ∼60% and the levels of tortuosity increase to >1.14 (figure 7.11). This provides evidence that at temperatures of 150°C and below, irradiation-induced structural damage occurs.

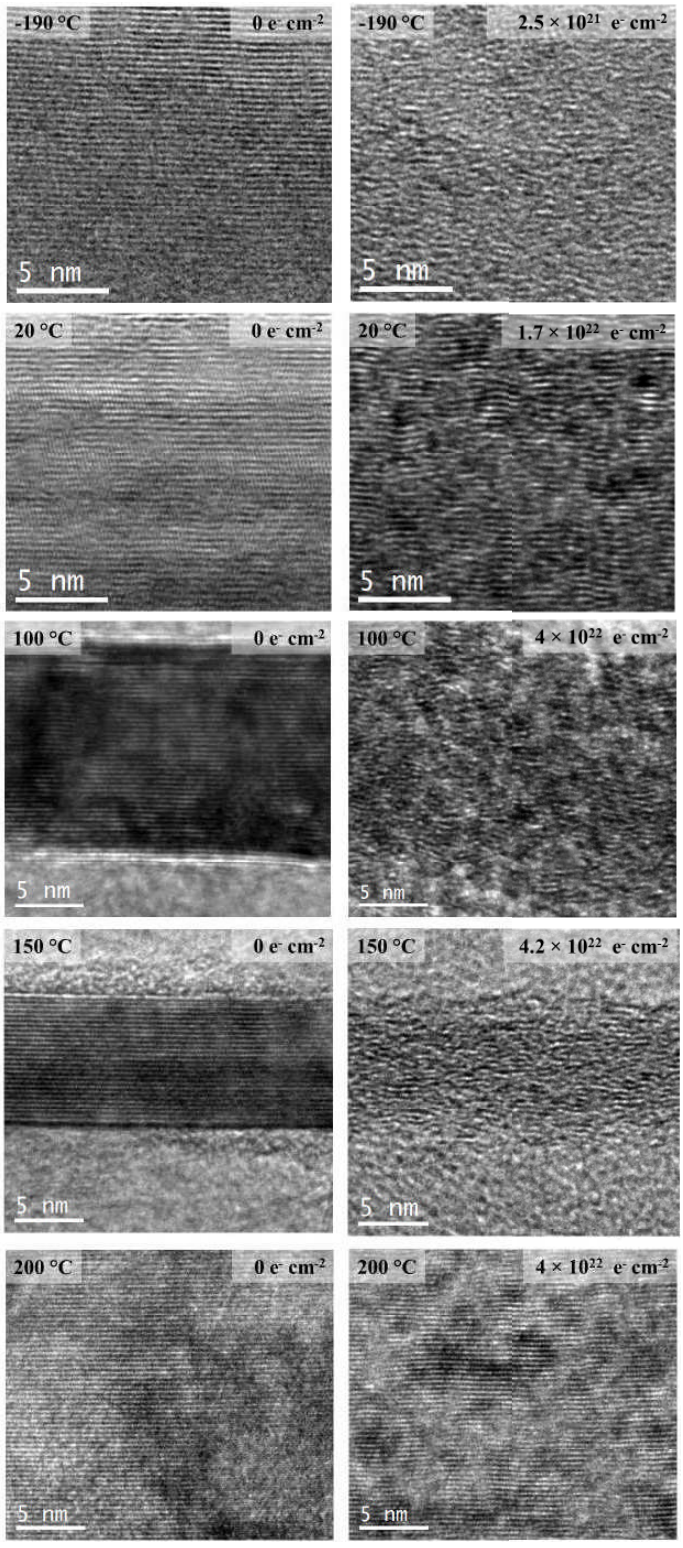

Figure 7.9: TEM micrographs before and after 200 kV electron beam exposure at -190°C, 20°C, 100°C, 150°C, and 200°C using the DENS Solutions in situ holder.

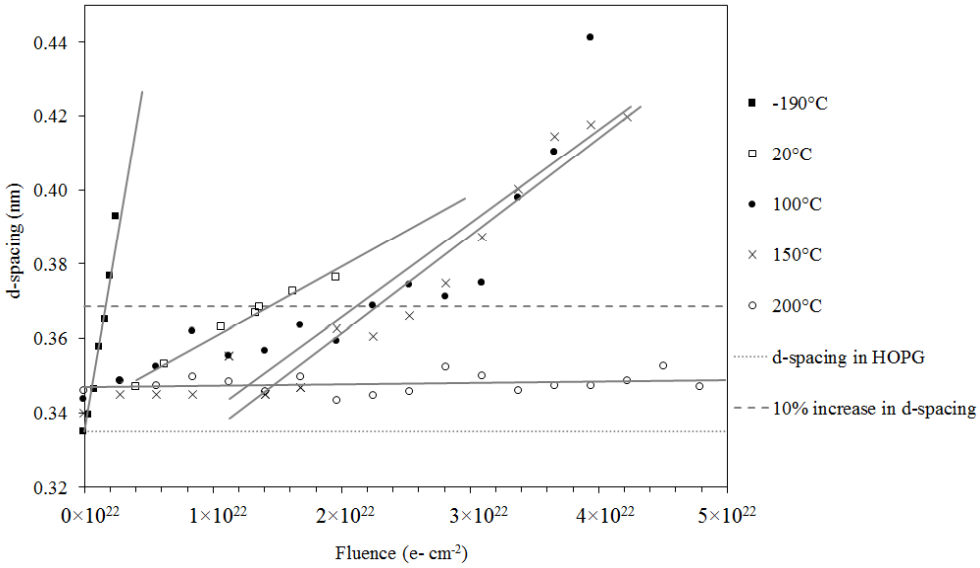

Figure 7.10: Change in d-spacing with electron fluence at 200 kV electron beam exposure at -190°C, 20°C, 100°C, 150°C, and 200°C.

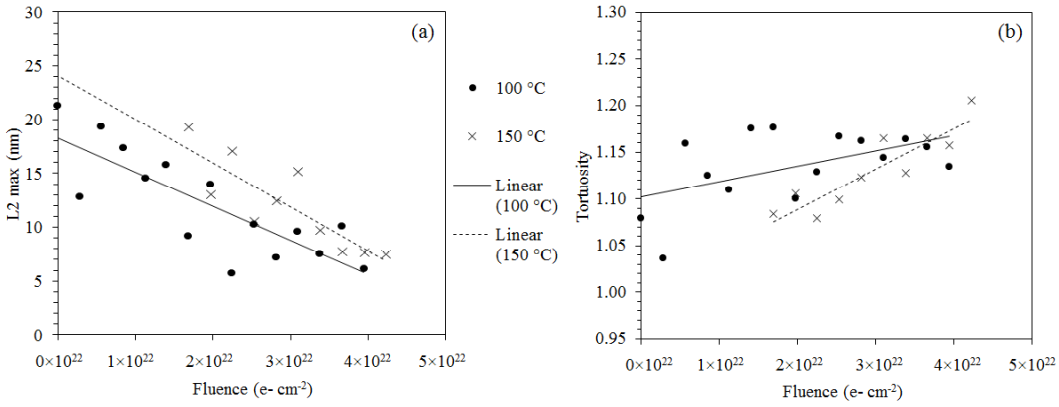

Figure 7.11: Change in fringe length (a) and tortuosity (b) with electron fluence at 200 kV electron beam exposure at 100°C and 150°C.

7.4 Discussion

To interpret a temperature threshold for irradiation damage from these results, a critical fluence at each temperature was determined. The critical fluence was defined as the fluence at which the d-spacing increased by 10%. Due to the low damage rates at 200°C, this data set was extrapolated (from figure 7.10) to predict the fluence at which a 10% change in d-spacing would occur. Muto & Tanabe (1999) performed a similar analysis based on [001] diffraction patterns collected for different temperature in situ electron irradiation experiments. In their study, the fluence was measured in terms of dpa and was therefore referred to as a dose. The critical dose was defined as the dose at which the [001] diffraction pattern turned into diffuse rings. To compare the two sets of data, the fluence thresholds determined in this chapter were converted to doses, in dpa, according to the conversion outlined on page 87 (equation 4.14). The data plotted in figure 7.12 are from data presented by Muto & Tanabe (1999) and from data presented in this chapter, at -190°C, 100°C, 150°C, and 200°C and from data at room temperature in chapter 6. In both data sets there is a clear point where the gradient changes. This turning point indicates there is a change in the annealing/radiation damage process at a certain temperature. For the data in this thesis and from Muto & Tanabe (1999), that point is ∼150°C and ∼125°C respectively. The difference in these values may be a result of different critical dose definitions, different specimens, and the slightly different electron fluxes used. Both data sets have been extrapolated to show the critical dose at a standard reactor operating temperature, 350°C ($1.6 \times 10^{-3} K^{-1}$).

The temperature threshold of ∼150°C determined from figure 7.12 reflects the density functional theory calculations of Latham *et al.* (2013) and indicates that above ∼150°C the hexagonal structure within basal planes is maintained and overall largely unchanged by radiation. The observation of the fragmentation and curvature of basal planes in TEM micrographs collected during electron irradiation below ∼150°C, along with an increase in d-spacing from SAED patterns, provides evidence that any annealing effects are outweighed by radiation damage at these lower temperatures.

To better understand the thresholds derived from figure 7.12 and those discussed in the literature, the migration energies of various defect configurations can be considered. Experiments measuring the electrical resistance and lattice parameters of a variety of low temperature, radiation exposed graphite grades have resulted in a range for the single interstitial migration energy (0.02 - 0.4 eV) (Goggin & Reynolds, 1963; Thrower & Mayer, 1978). However, theoretical calculations for such energies are consistently higher (∼1.2 - 2 eV) (El-Barbary *et al.*, 2003; Heggie *et al.*, 2011; Li *et al.*, 2005). It has been proposed that these discrepancies are due to experimental calculations not accounting for the effect of shear on migration energy (Li *et al.*, 2005; Niwase, 2002).

Since the curves in figure 7.12 follow an Arrhenius law (equation 7.1) the gradient from each of the two distinct sections can be determined to give the thermal annealing activation energy (E_a) in each temperature range. The activation energies above and below the threshold temperature for the data in this thesis were calculated to be 0.021 eV and 0.52 - 1.03 eV respectively. The latter data range reflects the values from different extrapolations of the T = 200°C data; one for a fixed interception of 0.335nm (0.52 eV), and one for a trend line with no fixed

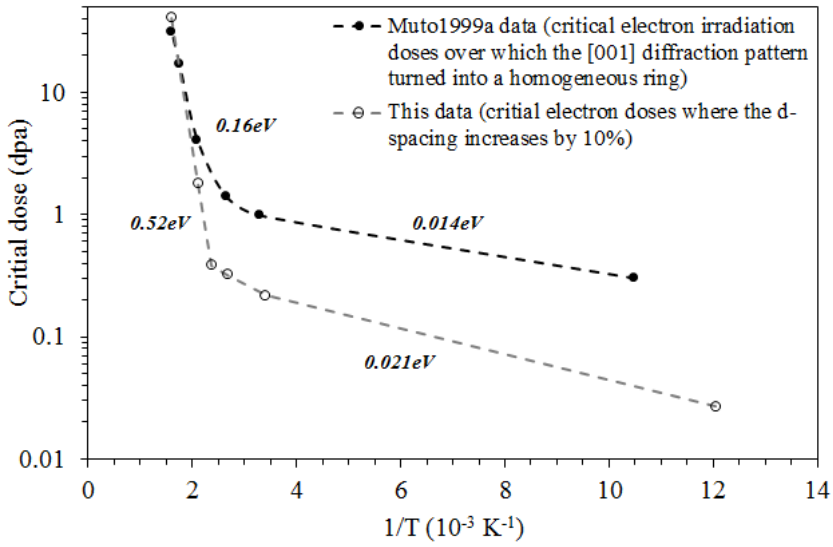

Figure 7.12: Arrhenius plot of the critical dose for different temperatures, with corresponding activation energies labelled. Data is plotted from this thesis and from that presented in Muto & Tanabe (1999). Data sets have been extrapolated to show the critical dose at 350°C ($1.6 \times 10^{-3} K^{-1}$).

interception point (1.03 eV). For the data extracted from Muto & Tanabe (1999) these values are 0.016 eV and 0.32 eV. Due to a lack of data points, the errors on these calculations are reasonably high; nevertheless, the values from both data sets are of a similar magnitude.

As discussed, it is expected that at temperatures below the ∼150°C threshold, the effects of radiation damage dominate so that the net effect is relatively fast structural damage. The low thermal annealing activation energy (0.014 - 0.021 eV) supports this theory. The calculations for activation energy can allow us to determine which defect structures are mobile and therefore aid recovery of radiation damage in each temperature range. Based on the migration energies cited in the literature, the annealing of structural changes induced by low temperature irradiation (<150°C) may be a result of surface diffusion of interstitial atoms. Radiation exposure can result in the diffusion of surface atoms even if energies below the displacement threshold are transferred (Banhart, 1999). Surface sputtering is also possible for energy transfers below the threshold for permanent displacements in the bulk (Cherns *et al.*, 1976). Sputtering occurs when a surface atom is knocked out of its position by a highly energetic incident particle, whose incident angle effects the probability of an atom being sputtered. The reported radiation-induced fragmentation of crystallites (Gallego *et al.*, 2013; Muto & Tanabe, 1999; Takeuchi *et al.*, 1997) would increase the net internal surface area therefore increasing the possibility of atomic mobility through diffusion and sputtering. Such surface atoms would be able to fill vacant sites on surfaces, but not in between planes (which would require higher energies). Above the ∼150°C threshold the effects of thermal annealing become more prevalent which is reflected through reduced damage and an increased thermal annealing migration energy (0.32 - 1.03 eV). The mobility of single interstitials in this temperature range would allow the structure to recover in between planes; in addition to surface migration, interstitials would be able to migrate through the lattice and fill vacancy sites.

The high operating temperatures of graphite moderated nuclear reactors (350°C) therefore reduces damage rates, however the long duration radiation exposures means that structural damage is still expected to occur. The extrapolation of data in figure 7.12 show the critical dose at 350°C ($1.6 \times 10^{-3} K^{-1}$) is 30 - 40

dpa. Assuming the dose rate in a graphite moderated nuclear reactor is 10^{-7} dpa s^{-1} (Karthik *et al.*, 2011), such a dose would occur after ∼12 years. Similarly, a reactor operating temperature of 450°C would increase this critical dose limit to 32 years. However, it must be noted that graphite moderated nuclear reactors are operated for around 7 years then undergo a 6 month down time period before being operated at full power. The lifetime usually quoted for reactors does not usually take this into account, meaning the full power lifetime is smaller. Furthermore, the c-axis expansion is expected to plateau and not increase indefinitely (Kelly *et al.*, 1966a). Therefore it is likely that effects of the critical dose (i.e. a 10% increase in d-spacing) will be experienced beyond the times quoted. Chapters 8 and 9 will investigate structural changes in specimens from materials test reactors and civil nuclear reactors following neutron radiation at a range of temperatures.

Chapter 8

Characterisation of Neutron Irradiated Graphites

Having established non-damaging TEM beam conditions and a quantitative image analysis technique for radiation damage through controlled electron irradiation, a variety of neutron irradiated specimens were investigated; two PGA graphites, BEPO and Oldbury, and two new graphite grades, PCEA and PCIB. The information about the irradiation temperatures and received doses for these specimens is displayed in table 8.1 and more information about the specimens themselves can be found in section 4.5. FIB sections were collected from filler unless specified, allowing for a fair comparison between specimens.

Grade	Specimen name	Dose (dpa)	Irradiation temperature (°C)
BEPO	BEPO1	0.40	100
BEPO	BEPO16	1.27	100
BEPO	BEPO20	1.44	100
PGA	Oldbury	5.00	325
PCEA	B25	1.50	350
PCEA	B17	6.80	670
PCIB	C03	1.50	350
PCIB	B02	4.00	535
PCIB	B05	6.80	655

Table 8.1: Received dose and irradiation temperature of neutron irradiated specimens.

8.1 TEM lattice images and SAED patterns

For TEM inspection, all specimens were prepared by grinding/crushing and FIB, and imaged at 80 kV on the CM200 and Tecnai microscopes at the University of Leeds. All micrographs were subject to the PyroMaN image analysis technique detailed in chapter 6. Since there is a limit in the measurement of fringe length to the width of the micrograph, images were cropped to be the same size, with the

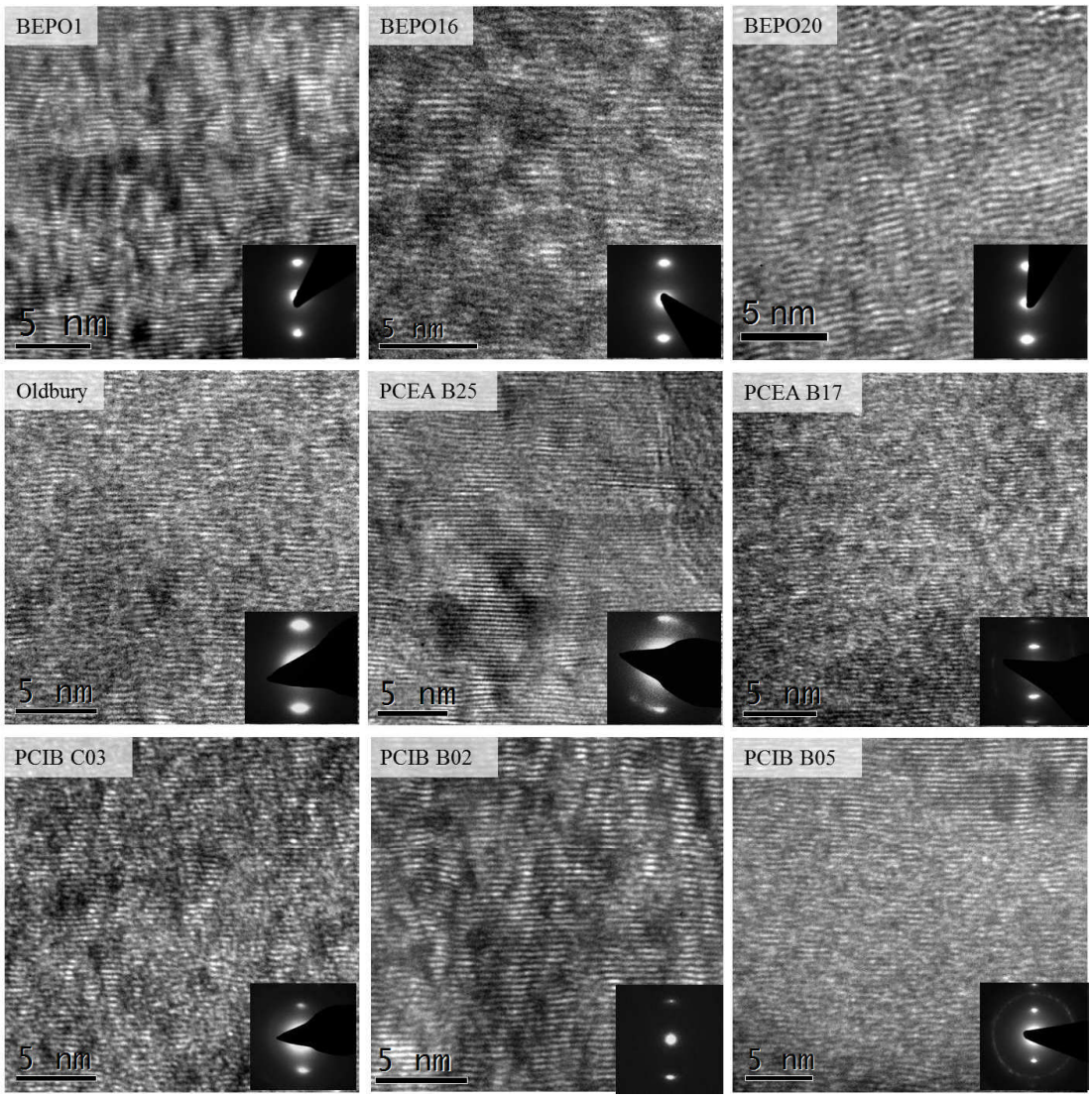

Figure 8.1: Representative micrographs and corresponding SAED patterns of the specimens detailed in table 8.1, as labelled.

same resolution to ensure a fair comparison between fringe length values for all specimens. Representative micrographs and SAED patterns from each specimen are shown in figure 8.1.

The d-spacing of basal planes was measured from the spacing of (002) diffraction spots in SAED patterns. At least five SAED patterns were collected for each specimen and the results from this analysis are shown in figure 8.2. Due to the relatively large aperture required for SAED pattern collection, the quoted values for d-spacing are an average over a specimen area of $\sim 10^5$ nm^2. PCIB and PCEA appear to maintain their d-spacing the most out of all specimens examined. PCIB B02 (4 dpa) shows a reduction in d-spacing compared to its lower and higher dose neighbours. This may indicate a point at which the annealing effects (at 535°C) become more prominent, despite the higher dose (4 dpa). PCIB B05 exhibits a higher d-spacing than PCIB B02 suggesting that the higher dose (6.8 dpa) has more influence on the structure, despite the increased contribution of thermal annealing at a higher temperature (655°C). The high dose high temperature PCEA B17 also shows a slightly lower value for d-spacing than the low dose low temperature PCEA B25. The BEPO specimens show a gradual increase in d-spacing with dose. This is to be expected as specimens were irradiated at the same temperature, which was below the annealing threshold estimated in chapter 7. The d-spacing of Oldbury (5 dpa) is comparable to BEPO1 (0.4 dpa). Since

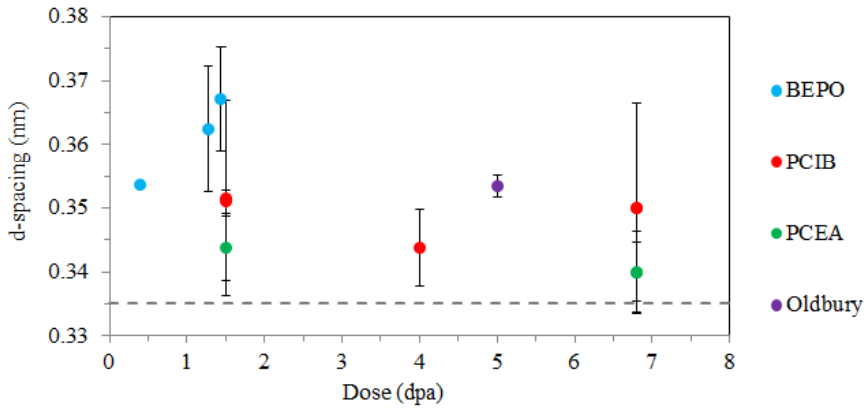

Figure 8.2: Plot of neutron dose and d-spacing as measured from SAED patterns for neutron irradiated graphites. The dotted line represents the d-spacing of HOPG. Error bars represent the standard deviation of each data set.

these graphites are of the same grade, direct comparisons can be made; it is likely that the retention of d-spacing is a result of the increased operating temperature for the Oldbury sample (325°C), allowing for continual thermal annealing. These results highlight the significance operating temperature has on structural change.

The data extracted for fringe length (L2) is displayed in figure 8.3. At least ten micrographs were analysed for each specimen. Figure 8.3(a) shows the raw data for maximum fringe length, and figure 8.3(b) shows how these lengths compare to the width of the micrograph (to avoid misinterpretation of results from slightly different sized micrographs). In general there is no significant trend between fringe length and received dose, micrographs were highly variable across all specimens, reflected through the large error bars in figure 8.3. Some speculative

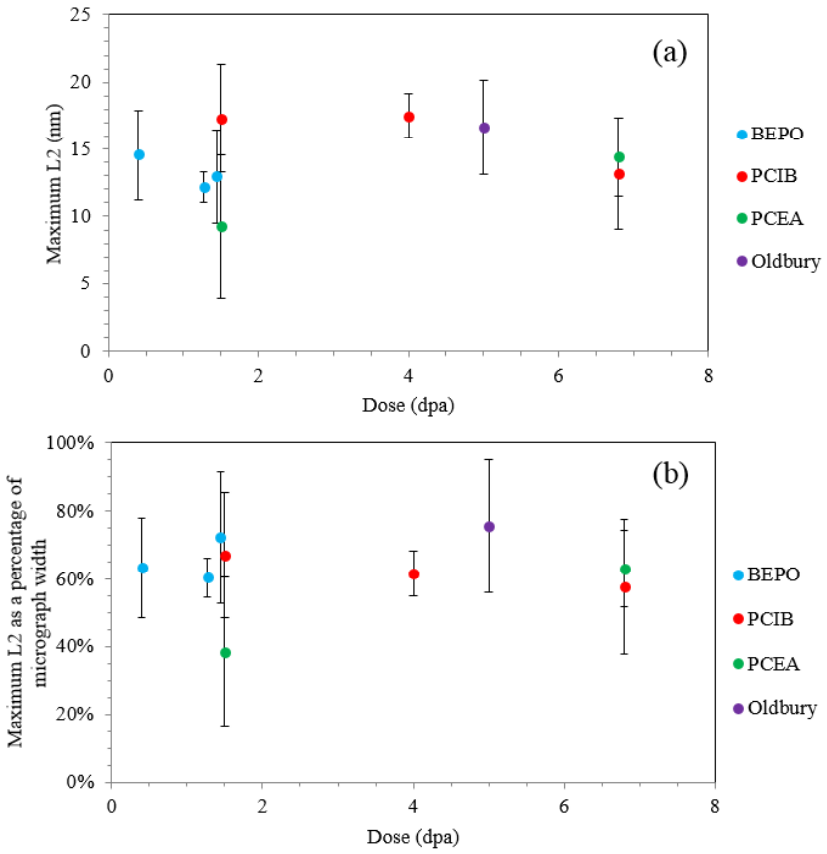

Figure 8.3: Plot of neutron dose and fringe length for neutron irradiated graphites. (a) shows raw data, (b) shows data as a percentage of the width of the micrograph. Error bars represent the standard deviation of each data set.

interpretations can be made however. The Oldbury specimen appears to retain fringe length the most out of all the specimens with an average fringe length of ~75% of the micrograph width, despite receiving 5 dpa of neutron irradiation. This is most likely due to the irradiation temperature (325°C) being above the threshold discussed in chapter 7 so that thermal annealing allows the structure to recover, reducing the effects of neutron radiation damage (e.g. the breaking of planes). BEPO and PCIB show signs of reduced fringe length with increasing dose, however the opposite is observed for PCEA.

The data extracted for tortuosity and orientation are shown in figure 8.4. Again, there are no obvious trends for either parameters. The extent of damage

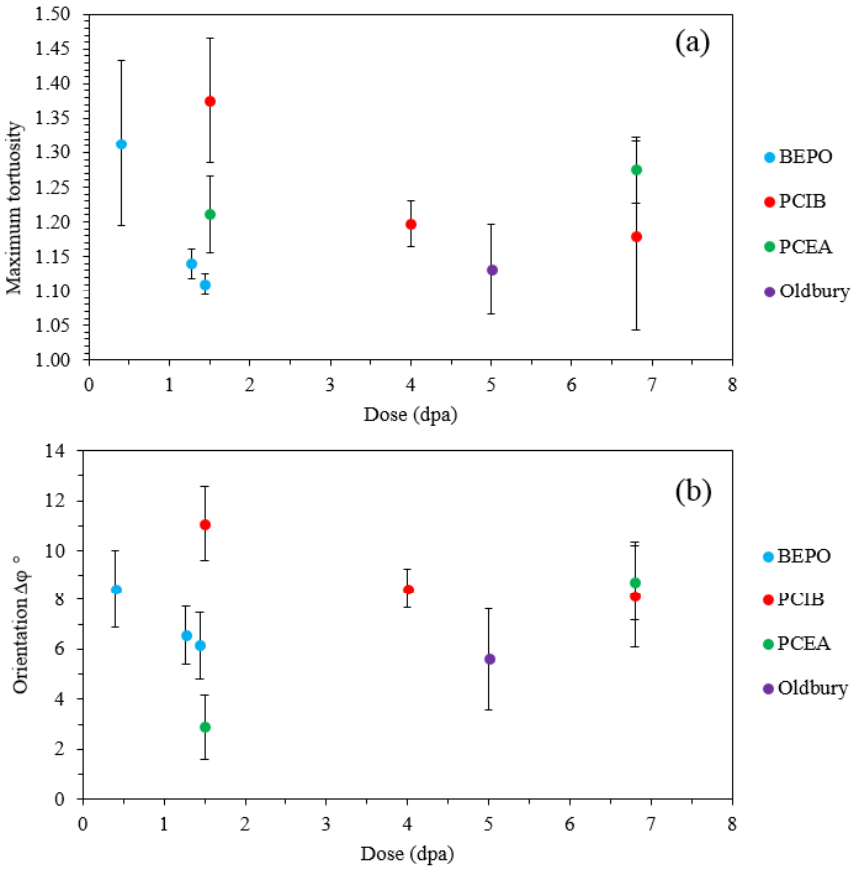

Figure 8.4: Plot of neutron dose against (a) tortuosity and (b) orientation for neutron irradiated graphites. Error bars represent the standard deviation of each data set.

appears to be highly variable throughout each specimen (reflected through the large error bars) and is extremely site specific across the specimen due to the anisotropic nature of nuclear graphite. In some cases the opposite of what is expected is observed; the tortuosity and orientation decreases with dose for BEPO and PCIB. Again, the Oldbury specimen appears to retain its structure the most out of all specimens. This has been observed for all TEM/SAED data analysis. Using the PyroMaN software to extract information about fringe length, tortuosity, and orientation is very sensitive to image conditions. Although every effort was made to allow for a fair comparison (consistency in TEM imaging conditions, image size, and resolution) it appears that the combination of the sensitivity of the software and variability in specimen thickness, the orientation of planes, and the anisotropy of nuclear graphite makes for highly variable data which must be interpreted with caution.

8.2 EELS

EELS was also performed on graphite grades PCIB and PCEA to assess changes in sp^2 content and density in the bulk material. All EEL spectra were collected at 80 kV at the magic angle conditions detailed in chapter 5. Representative core loss carbon K-edge spectra from PCEA and PCIB are shown in figure 8.5. The π^* and σ^* peaks were analysed following the method described in chapter 5 and data was normalised to sp^2 for HOPG. Using this method, virgin PCIB and PCEA exhibited $\sim$90% sp^2.

As seen in figure 8.6(a), little change in sp^2 was observed following neutron irradiation in both graphite grades. As with TEM results, the data was highly variable between different areas within each specimen, shown through relatively large error bars. The high dose high temperature specimens show evidence of structural recovery where sp^2 values are slightly higher than, or close to, values associated with low dose low temperature specimens. It is thought this is due to the high irradiation temperatures allowing for continual thermal annealing. In general, the sp^2 values have not reduced as much as for those from the room temperature electron irradiation discussed in chapter 6.

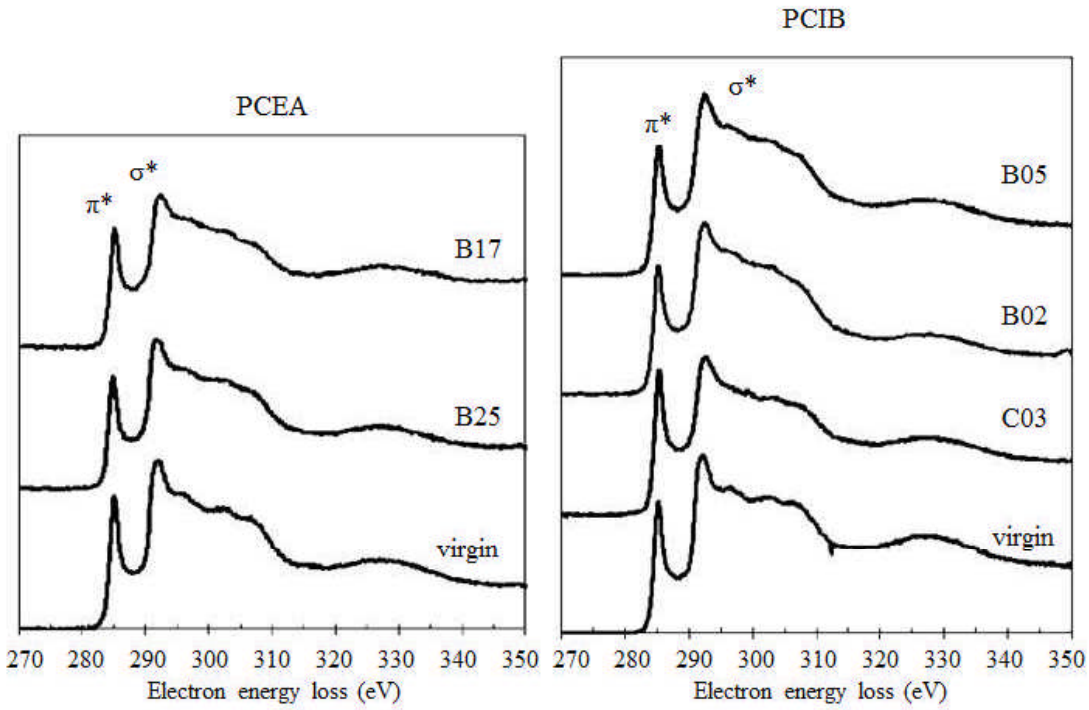

Figure 8.5: Representative core loss EEL spectra for virgin and irradiated PCEA and PCIB. Details of received dose and irradiation temperature are displayed in table 8.1.

Analysis of the (π^*+σ^*) plasmon peak in the low loss spectra showed a slight difference between virgin and irradiated specimens (figure 8.6(b)): for both graphite grades, the average position of the peak decreased by ~1 eV (4%). This implied a slight reduction in density following neutron irradiation. The data was also highly variable over different areas (in the most extreme cases, the (π^*+σ^*) plasmon peak position varied by 3 eV within the same specimen). Unlike the sp^2 data, this data shows little evidence for the thermal recovery of high dose high temperature specimens, possibly due to the introduction of irradiation induced microcracks. Due to the high variability in data further analysis of more samples is required to improve the confidence of this interpretation.

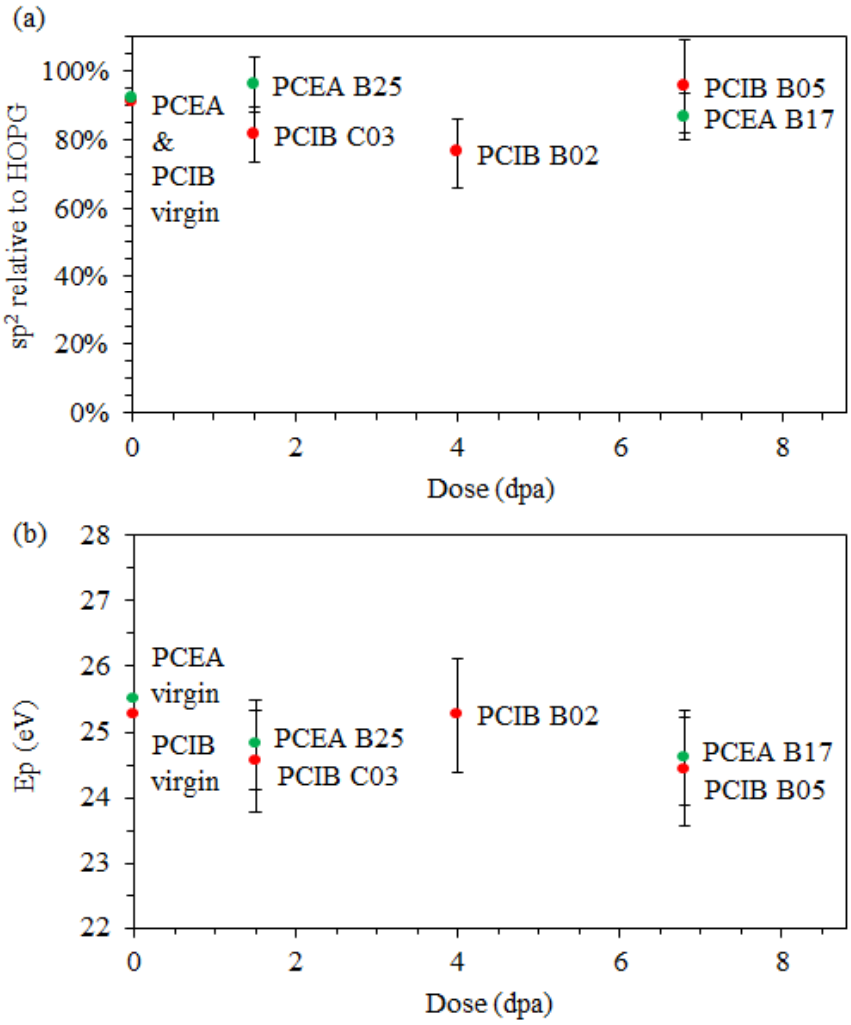

Figure 8.6: Averaged EELS data ((a) carbon sp^2 content (b) plasmon energy) extracted from ~30 spectra per specimen for virgin and irradiated PCEA and PCIB.

8.3 Previous experiments: XRD and Raman

XRD and Raman data on these samples has been reported by Mironov (2015). Some representative XRD patterns of virgin and irradiated PCIB and PCEA are shown in figure 8.7 and the data extracted from them is shown in table 8.2. Many peaks appear to broaden (e.g. (002) and (004)) or disappear (e.g. (103) and (006)) with irradiation dose while some (e.g. (100)) change in peak position. The positions of the (100), (110), and (112) reflections are associated

with a-spacing and the (002), (004), and (006) reflections are associated with c-spacing (i.e. (002) inter-planar spacing, referred to as d-spacing elsewhere). The FWHM of the (100) (or (110)) and (002) peaks and corresponds to the coherence lengths in the a-direction (L_a) and c-direction (L_c) respectively. Although XRD for both grades showed no significant changes in c-spacing compared to virgin specimens, the crystallite sizes were calculated to reduce by 35% (for both L_a and L_c) for low dose, low temperature exposures and by 50% (for both L_a and L_c) for high dose, high temperature exposures (compared to virgin specimens of the same grade). These results agree with the findings of Gallego *et al.* (2013). The data acquired for inter-planar spacing through XRD show consistently lower values compared to SAED results. This is potentially due to the larger volumes analysed by XRD, differences in specimen preparation (e.g. strain relief in thin specimens), or through a systematic error. A discrepancy in measured d-spacing from different techniques was also found by Muto & Tanabe (1997) whose results from FFT analysis were larger than those from SAED analysis.

Some representative first-order[1] Raman spectra of virgin and irradiated PCIB

[1]The name first order comes from the number of scattering events which involve only one phonon emission

Specimen	Dose (dpa)	Temp. (°C)	c-spacing (002) ($\mathring{A}$)	a-spacing (100) ($\mathring{A}$)	L_c ($\mathring{A}$)	L_a(100) ($\mathring{A}$)	L_a(110) ($\mathring{A}$)
PCEA virgin	-	-	3.370	2.455	229	399	647
PCEA B25	1.5	350	3.381	2.444	151	259	273
PCEA B17	6.8	670	3.382	2.448	120	309	353
PCIB virgin	-	-	3.375	2.454	226	374	619
PCIB C03	1.5	350	3.378	2.441	149	252	264
PCIB B02	4.0	535	3.372	2.454	149	306	662
PCIB B05	6.8	655	3.365	2.434	112	203	312

Table 8.2: Averaged data extracted from XRD patterns of specimens of virgin and irradiated PCEA and PCIB (Mironov, 2015). Errors for a and c-spacing is <3% and <6% for L_a and L_c.

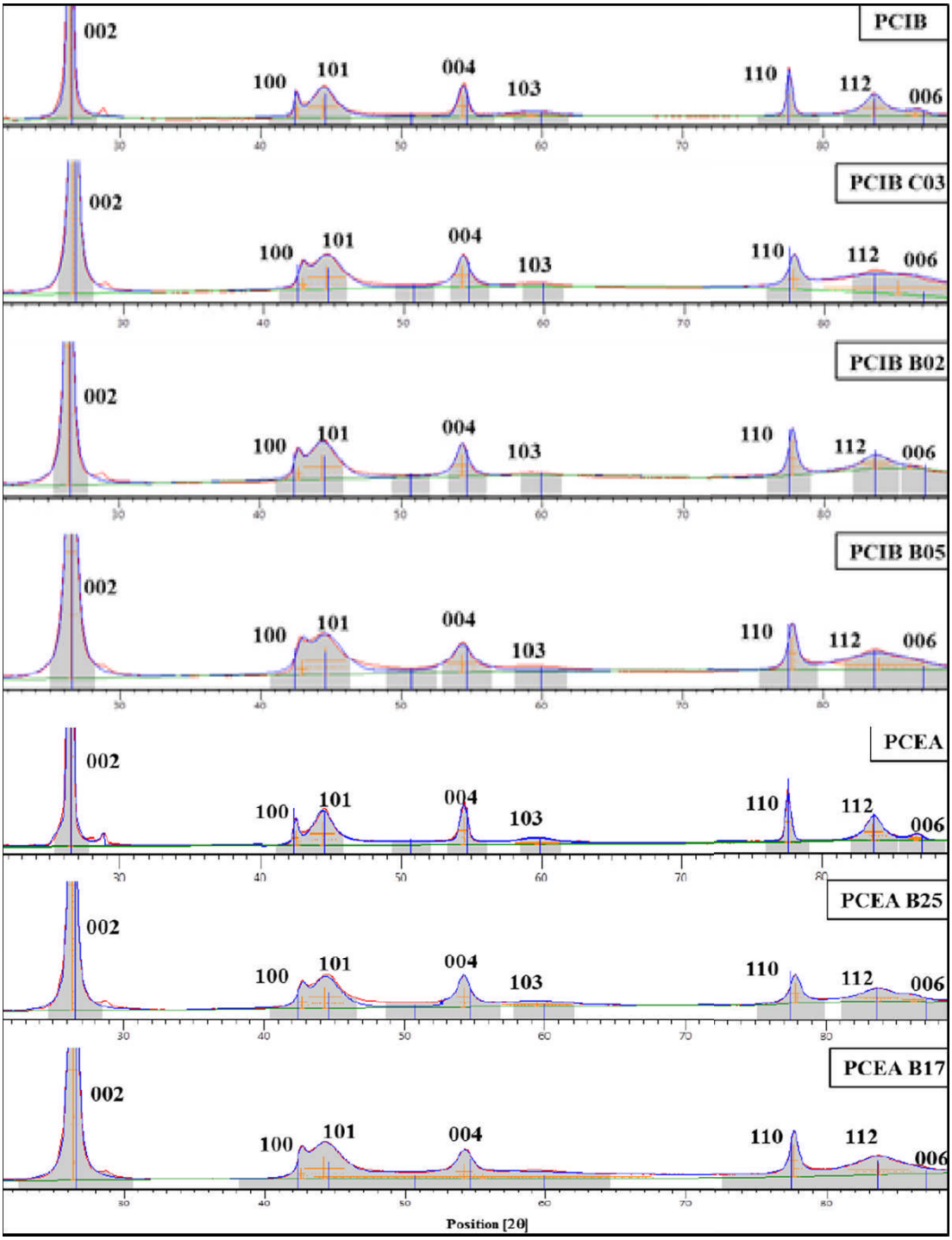

Figure 8.7: Representative XRD patterns of virgin and irradiated PCIB and PCEA (Mironov, 2015).

and PCEA are shown in figures 8.8 and 8.9 and the data extracted from them by peak fitting is shown in table 8.3. The physical meaning of each peak is discussed in section 3.2. The position of the G peak in the spectra of irradiated specimens it is higher than for the virgin specimen's spectrum, implying the fragmentation of crystallites following neutron irradiation in agreement with XRD. The spectra of irradiated specimens also show an increase in the FWHM of the G peak by 2-5 fold and the I_D/I_G ratio increases by up to ∼4 fold relative to the virgin specimen. The most significant changes are observed in the spectrum of specimens subject to low dose (1.5 dpa) and low temperature (350°C) (PCIB C03 and PCEA B25). With increasing dose and irradiation temperature, recovery is evident through the narrowing of peaks, reduction in I_D/I_G ratio and reduction in G peak position, suggesting that the higher irradiation temperature (655°C) allows defects to anneal. These results are in line with the findings of Gallego *et al.* (2013); Kane *et al.* (2011); Muto & Tanabe (1999); Muto *et al.* (1999) and the data presented in chapters 6 and 7.

Specimen	Dose (dpa)	Temp. (°C)	I_D/I_G	G FWHM (cm^{-1})	G peak (cm^{-1})	D peak (cm^{-1})
PCEA virgin	-	-	0.1-0.3	20	1581.8	1354.3
PCEA B25	1.5	350	0.6-0.8	90	1593.1	1364.8
PCEA B17	6.8	670	0.5-0.9	50	1587.2	1361.6
PCIB virgin	-	-	0.1-0.3	20	1582.4	1354.2
PCIB C03	1.5	350	0.7-1.1	70	1590.0	1362.3
PCIB B02	4.0	535	0.6-1.0	50	1587.3	1358.8
PCIB B05	6.8	655	0.6-1.0	50	1586.5	1358.4

Table 8.3: Averaged data extracted from over 40 Raman spectra per specimen of virgin and irradiated PCEA and PCIB (Mironov, 2015).

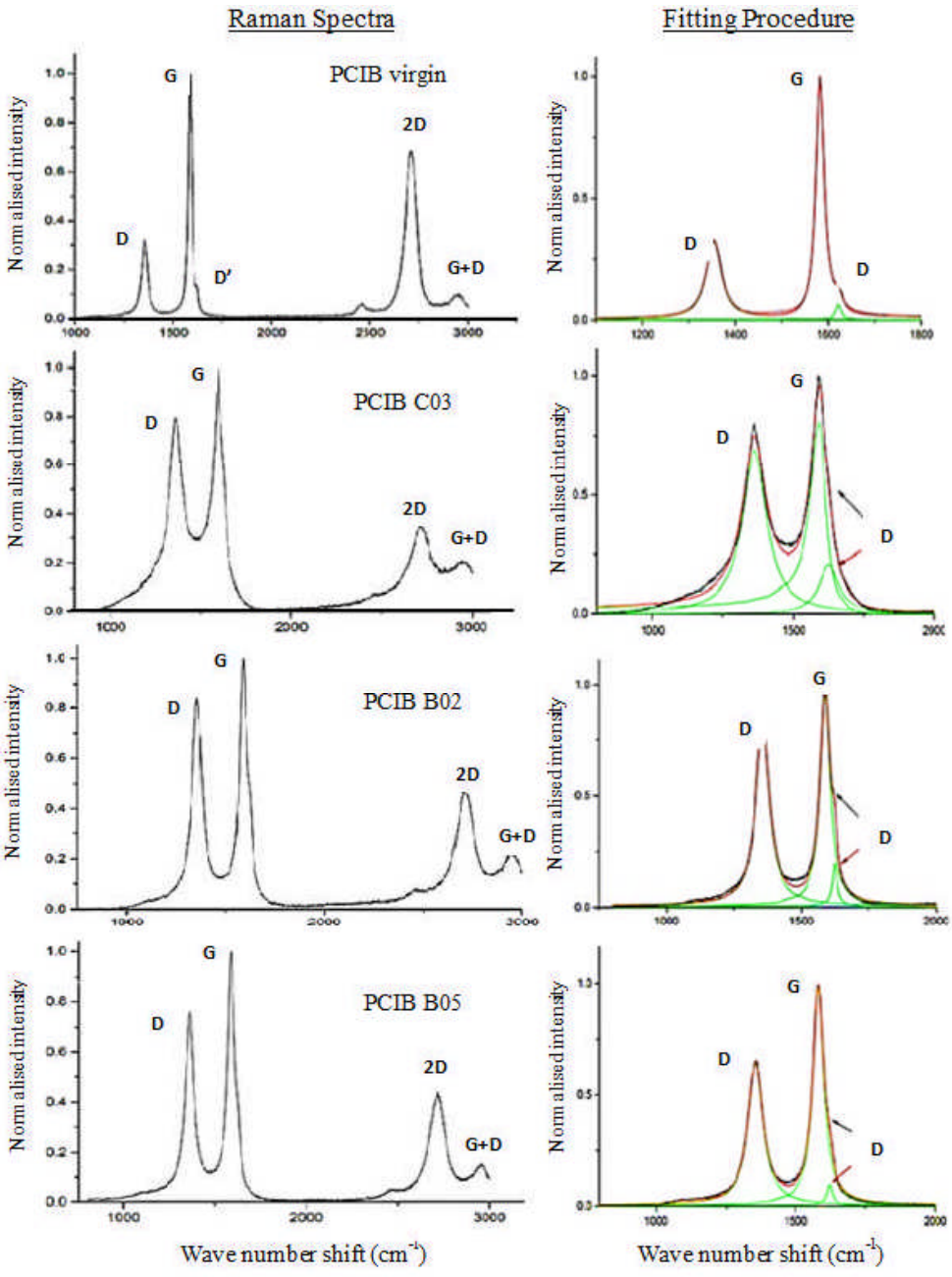

Figure 8.8: Representative first-order Raman spectra of virgin and irradiated PCIB (Mironov, 2015).

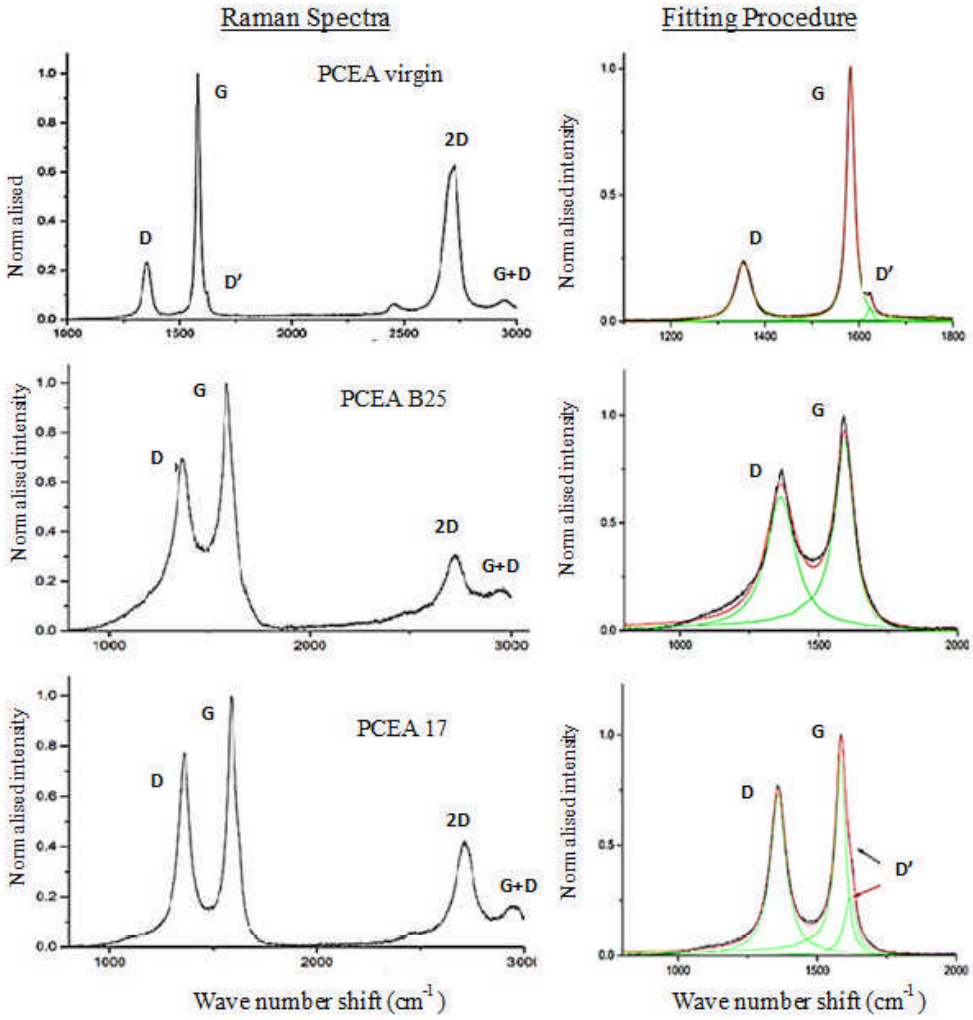

Figure 8.9: Representative first-order Raman spectra of virgin and irradiated PCEA (Mironov, 2015).

8.4 Conclusion

This chapter has shown that neutron irradiation induces basal plane and crystallite fragmentation, and has highlighted the effect temperature has on irradiation induced structural damage. Data from TEM, SAED, EELS, XRD, and Raman showed that low dose low temperature specimens tended to exhibit higher structural damage (such as lower sp^2 content, higher d-spacing, and reduced crystallite size) than high dose high temperature specimens. The retention of structure in the medium dose medium temperature Oldbury specimens suggested that there was an optimum point at which the temperature can have significant annealing effects, given that the dose is not too high (i.e. there is a balancing of forward and reverse reaction rates). In the case of Oldbury PGA graphite, this point is at 5 dpa and 325°C.

Chapter 9

Characterisation of Microcrack Material

Microcracks in neutron irradiated nuclear grade BEPO graphite were examined using TEM, EELS, Energy Dispersive X-ray (EDX), and EFTEM. Three irradiated specimens were investigated with received doses ranging from 0.4 to 1.44 dpa and an irradiation temperature range of 20−120°C. This new combined characterization technique has never before been applied to cracks in nuclear graphite. It has shown that disordered carbon material is present in a range of microcracks (of varying size and shape) in all irradiated specimens. EFTEM and EELS data showed that these cracks contained carbon material of lower density and graphitic character than that of the surrounding bulk graphite. The presence of partially filled microcracks has potentially significant implications for the development of microstructural models to allow the understanding and prediction of radiation-induced dimensional and property changes in nuclear graphite.

9.1 Experimental procedure and sample preparation

The nuclear graphite grade examined was BEPO; BEPO1 which received a dose of 0.4 dpa ($\sim 3.1 \times 10^{20}$ n cm^{-2}), BEPO16 which received a dose of 1.27 dpa ($\sim 9.8 \times 10^{20}$ n cm^{-2}), and BEPO20 which received a dose of 1.44 dpa ($\sim 1.1 \times 10^{21}$ n cm^{-2}). Specimens were prepared by FIB, with areas of filler region specifically selected. More details about these specimens can be found in section 4.5.

General TEM observations were carried out on an FEI Tecnai TF20 operated at 200 kV. The details of this equipment are discussed in chapter 5. EELS data was collected at SuperSTEM (the UK national facility for aberration corrected scanning TEM) using a Nion UltraSTEM100 equipped with a Gatan Enfina Spectrometer, operated at an acceleration voltage 60 kV to minimize beam induced irradiation damage. The energy resolution was 0.45 eV and the convergence semi-angle was ∼30 mrad. It must be noted that while these conditions do not satisfy the magic angle criterion (discussed in section 5.2) there is only a small variation in plasmon position within a limited tilt range. Assuming there is no significant change in local orientation in the graphitic planes surrounding the cracks, any effect on the low loss spectrum should be negligible. In order to measure and compare the density and graphitic nature of material within a microcrack to those of the bulk, EEL spectra were collected from several regions: within a microcrack, on the edge of a microcrack and in the neighbouring graphite bulk.

9.2 Data analysis

Figure 9.1 shows TEM images of the FIB sections from filler regions in all three irradiated BEPO specimens. Image J was used to analyse the cracks to calculate their dimensions and two dimensional percentage area (Rasband, 2014). BEPO1 has few cracks (periodicity 0.21 cracks/μm, percentage area 0.7%) which are relatively narrow (∼50-300 nm), BEPO16 has a slightly higher proportion of cracks (periodicity 0.56 cracks/μm, percentage area 4.36%) which are considerably wider, and BEPO20 has a high concentration of cracks (periodicity 1.70 cracks/μm, percentage area 9.6%) which are a mix of long thin lenticular cracks and larger wide cracks. This apparent increase in the proportion of cracks within the material reflects the fragmentation of the graphite microstructure with increasing neutron irradiation as has been observed in (Gallego *et al.*, 2013; Mironov *et al.*, 2015; Muto & Tanabe, 2000). However it must be noted that nuclear graphite is an incredibly inhomogeneous material and a statistical analysis of multiple areas through either multiple FIBed specimens or through SEM or light microscopy of larger areas is required to truly understand the relationship between dose and the number and size of crack. Radiation or temperature

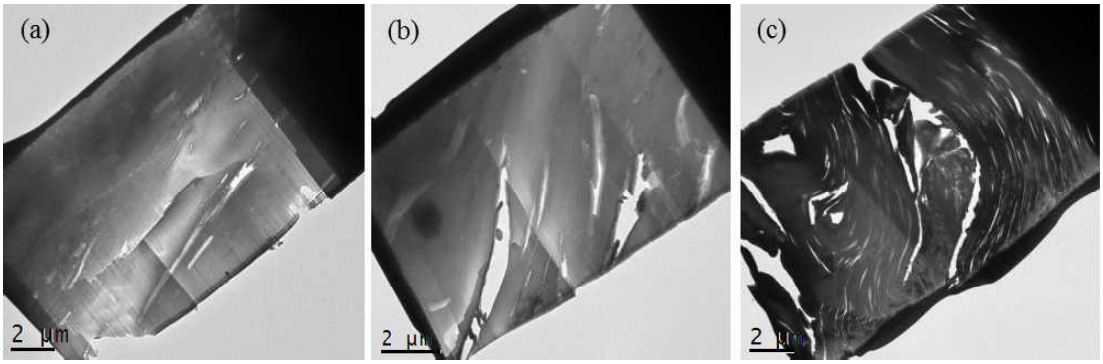

Figure 9.1: TEM images of a FIB section of filler from each sample: (a) BEPO1, (b) BEPO16, and (c) BEPO20.

induced crack closure in these specimens is not expected due to the low received dose and low irradiation temperature. A discussion of observed crack closure in the literature can be found on page 55.

In figure 9.2, TEM images of higher magnification show a range of microcracks (labelled A-D). In the TEM bright field micrograph in figure 9.2(b) regions of darker contrast might refer to either thicker material or material of a higher graphitic content. To distinguish between the two, EFTEM images were also collected and plasmon ratio maps were produced, the results of which will be discussed later in this section. High magnification TEM imaging and electron diffraction provides information about the crystallographic orientation of the cracks and from figure 9.2(b) and (c) it is clear to see that the basal planes and cracks are aligned suggesting that these are intra-granular cracks within the same crystallite.

To first establish that the material observed within a microcrack does not contain redeposited material from the FIB sputtering process or material amorphized by (Ga) ion beam implantation, EDX measurements were collected and quantified in terms of their gallium and platinum content (figure 9.3). EDX spectra showing microcracks with Ga content >0.2% and Pt content >0.15% were considered to contain FIB-induced damaged and/or redeposited material and all associated datasets were disregarded. The presence of a Cu peak in all spectra is due to the Cu TEM grid used, and the Pt peak which appears together with Ga is associated with FIB sputtering (from a protective Pt strap layer on top of the

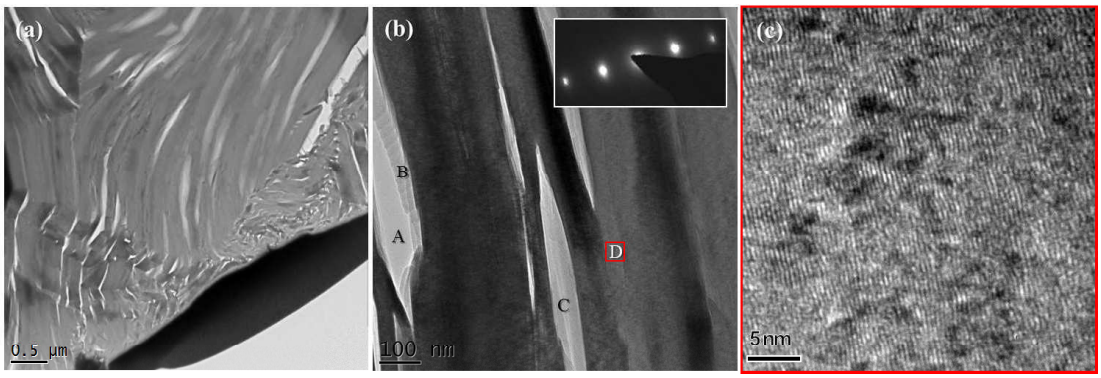

Figure 9.2: (a) relatively low magnification and (b) medium magnification TEM images of intra-granular microcracks within the FIB section of specimen BEPO20. Labels in (b): A - no material within the crack; B - material at the crack interface; C - a completely filled crack; D - graphitic bulk material. Electron diffraction pattern of the area shown in micrograph (b) is presented in the top right corner. (c) shows a high magnification TEM image of region D to verify the basal plane orientation is parallel to cracks.

specimen) and redeposition. The small levels of Ga visible in figure 9.3 (a) are most likely due to an unavoidable Ga implantation outer layer associated with all FIB prepared samples (Schaffer *et al.*, 2012).

EFTEM images were also used to assess the graphitic nature of the material within a microcrack. Following the procedure outlined in Daniels *et al.* (2003) and the EFTEM calibration detailed in section 5.3, two energy loss filtered images were used to produce an I_{27eV}/I_{22eV} plasmon ratio map to remove diffraction contrast and thickness effects; a 3 eV window centered at 27 eV representing the position of the plasmon peak for graphite, and a 3 eV window centered at 22 eV representing the position of the plasmon peak for non-graphitized material. Ratio maps were calibrated to $0.8 \leq I_{27eV}/I_{22eV} \leq 1.8$ following measurements by Daniels *et al.* (2003) so that high intensity reflects graphitic material and low intensity non-graphitic material.

The results of the EFTEM measurements on neutron irradiated BEPO specimens are shown in figure 9.4 where the removal of thickness contrast is apparent when comparing the intensities in the zero loss, 22 eV, and 27 eV filtered TEM images to the I_{27eV}/I_{22eV} plasmon ratio map. Figure 9.4 shows a series of EFTEM images from a FIB section of BEPO20. Four to six regions were analysed per

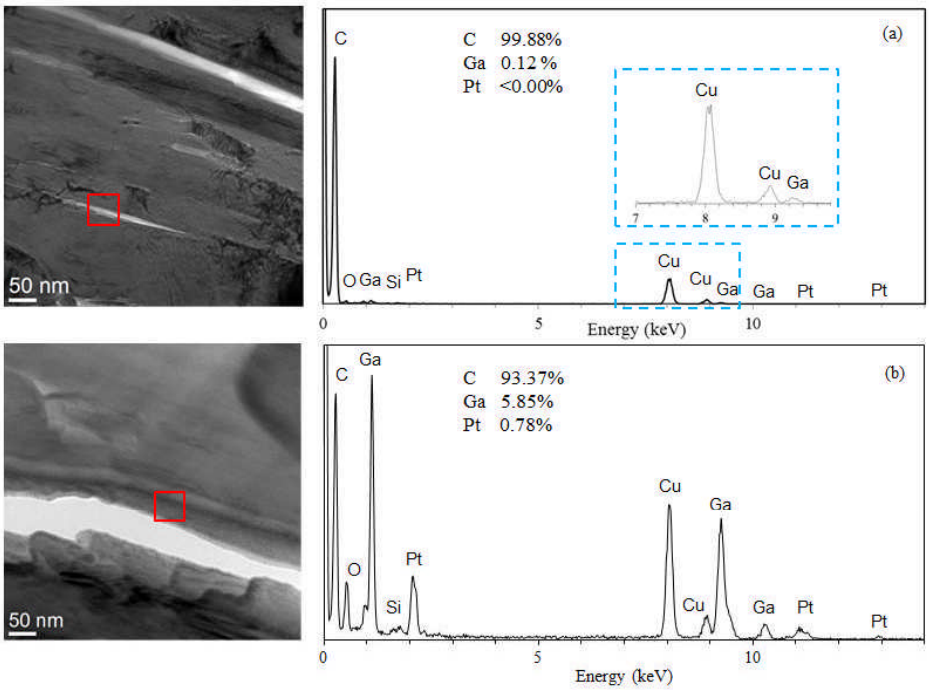

Figure 9.3: Examples of EDX spectra over a crack in BEPO1 showing (a) negligible Ga content (0.12%) and (b) significant Ga content (5.85%). Both spectra were normalised to the carbon peak at 0.2774 keV.

BEPO specimen, the results shown in figure 9.4 being representative. Four regions of interest have been identified: three different areas within cracks (A-C) and part of the bulk between cracks (D).

In figure 9.4(a) the dark features in the zero loss EFTEM image represent thicker material whereas the inverse is the case for the 22 eV and 27 eV filtered images in (b) and (c). However in the plasmon ratio map (figure 9.4(d)), the removal of thickness contrast means that bright features now represent regions of high graphitic character (27 eV) and dark features reflect either a hole or a region of low graphitic character (22 eV). Intensity profiles can be used to quantify interpretations (figure 9.5). When comparing the zero loss EFTEM image (figure 9.4(a)) to the plasmon ratio map (figure 9.4(d)), regions A, B, and C clearly differ. In the zero loss EFTEM, the crack at region A shows a high intensity. This is mirrored in the plasmon ratio map, where a relatively low intensity is recorded ($\sim$1.35 calibrated intensity units or 25.5 eV). For region B in the same crack, the

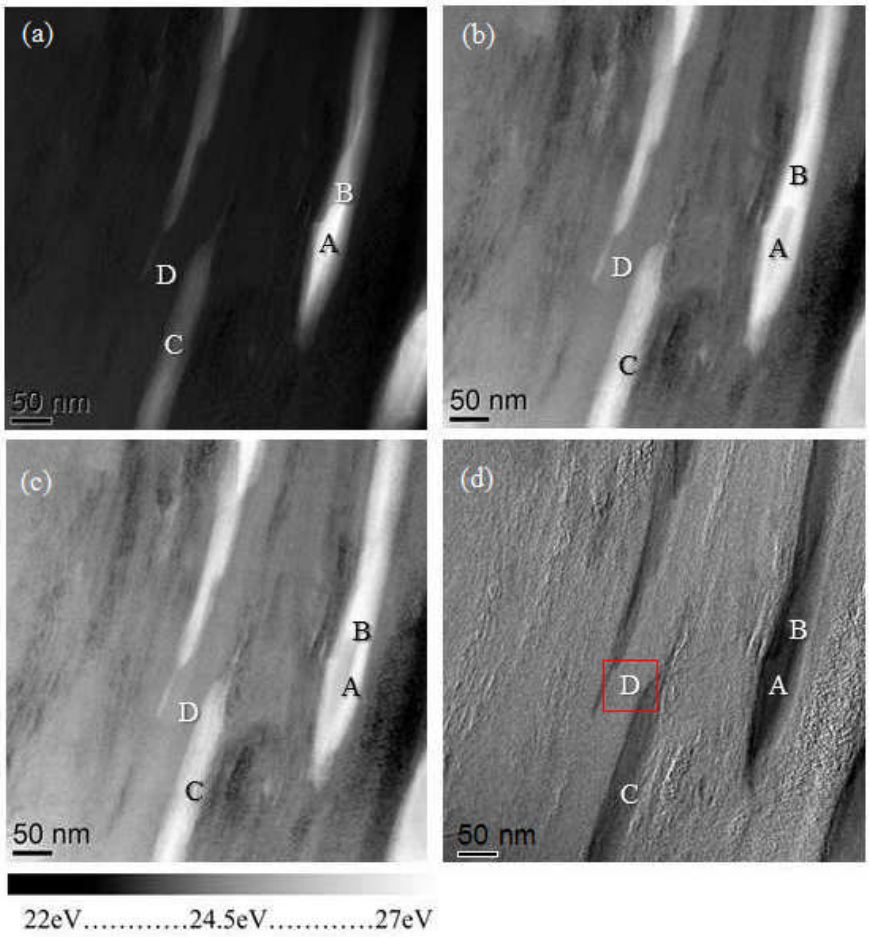

Figure 9.4: Representative EFTEM images for microcracks (A,B,C) in BEPO20. (a) zero loss filtered EFTEM, (b) 22 eV filtered EFTEM, (c) 27eV filtered EFTEM, and (d) I_{27eV}/I_{22eV} plasmon ratio map with calibrated intensity scale below.

zero loss EFTEM image shows a slightly lower intensity which is matched with a higher intensity in the plasmon ratio map (∼1.45 calibrated intensity units or 26.3 eV). The differences in plasmon ratio map intensities are shown in more detail in figure 9.5 and particularly highlight the effects of thickness contrast. In the zero loss image, one might assume region A was a hole however upon closer inspection in the plasmon ratio map, both regions A and B contain low density graphitic material. The intensity and corresponding plasmon energy over different cracks in all EFTEM plasmon ratio maps were measured. The average plasmon intensity was 25.4 eV; the lowest value was found over a crack in BEPO20 measuring 23.7

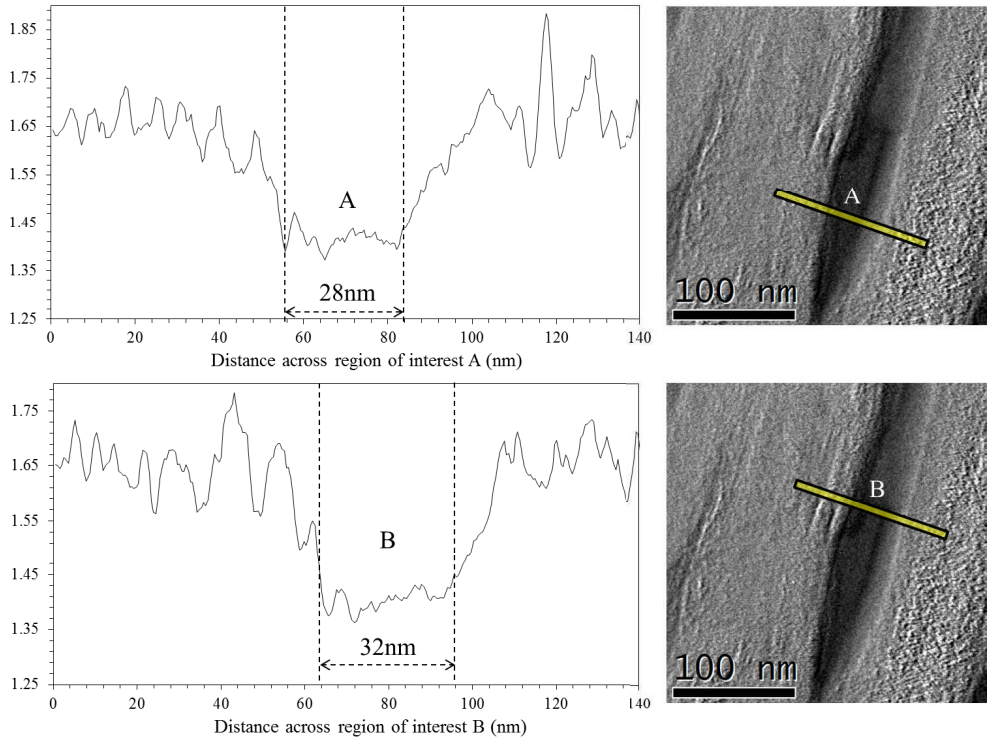

Figure 9.5: Intensity profiles across regions A and B from figure 9.4(d) plasmon ratio map to highlight differences in graphitic nature.

eV and the highest over a crack in BEPO1 measuring 26.7 eV.

On examination of the higher intensity regions in figure 9.5, particularly that on the left of region B, a fluctuation in intensity with a periodicity of approximately 8 nm suggests bands of material with different graphitic character are present; a result which is representative of all samples (with a slight variation of a few nm in periodicity). The change in intensity of these bands is reasonably significant with troughs as low as ∼1.55 and peaks as high as ∼1.75. These fluctuations are not a result of noise, the frequency of which is much higher. It is possible that these bands show the beginnings of crack formation where a trough (in the plasmon ratio map) will deepen and widen to form a crack containing disordered carbon. Damage accumulation and interstitial surface diffusion perhaps result in regions of localised disordered material which can act as sinks for further damage and eventually expand into cracks. A detailed discussion of the mechanisms for defect diffusion in graphite can be found in Gulans *et al.*

(2011); Thrower & Mayer (1978); Trevethan *et al.* (2013); Zhang *et al.* (2010). In general, diffusion along the basal plane is more common due to anisotropic atomic binding. It must be noted that the BEPO reactor operating temperature (20-120°C) is below the usual graphite moderated reactor operating temperature (>350°C) which may have hindered defect mobility. Furthermore, the irradiation temperature for these specimens is just below the temperature threshold of ∼150°C determined in chapter 7. This means the fragmentation of basal planes and crystallites is likely (Muto & Tanabe (1999)), increasing the proportion of grain boundaries. However, as discussed in chapter 7 the reported migration energies of single vacancies and interstitials vary considerably; experimental work has provided a widely accepted range (0.04 - 0.4 eV) for the single interstitial migration energy (Thrower & Mayer, 1978), whereas theoretical calculations range from 0.3 - 2 eV . Gulans *et al.* (2011); Trevethan *et al.* (2013). The low basal surface energy barrier (1.06 meV $\mathring{A}^{-2}$ (Telling *et al.*, 2003)) and the increase in nano-crystallinity following irradiation may create more possibilities for surface and grain boundary diffusion which would be expected to be able to occur at temperatures below the thresholds discussed in chapter 7.

Having established stable EEL spectra collection conditions, the variation in plasmon energy within, and on the edge of, a microcrack, and in the neighbouring graphite bulk was measured using STEM/EELS spectrum imaging, as shown in figure 9.6. For each area investigated high and medium angular annular dark field (HAADF/MAADF) images were acquired and then HAADF, MAADF, and EELS spectrum images were collected from a specific region of interest. 0.68-6.2 nm wide line scans of the EELS spectrum image were used to measure the energy position of the $(\pi + \sigma)$ plasmon, π plasmon peak, and the intensity of the π plasmon. Hyperspy was used to fit Gaussians to the two plasmon peaks and extract the required information (more information about this procedure can be found in section 4.3.2).

Six areas were examined in BEPO16 and BEPO20. In the bulk, the $(\pi + \sigma)$ plasmon energy was measured to be between 26.2 eV and 27.7 eV which is characteristic of near-perfect graphite (Chu & Li, 2006; Daniels *et al.*, 2003; Fink *et al.*, 1984). This is also consistent with the findings in chapter 6 where a significant change in $(\pi + \sigma)$ plasmon energy in the bulk due to irradiation was

not observed. The energy of the $(\pi + \sigma)$ plasmon peak decreased over all cracks but to differing degrees. The most extreme case was seen in BEPO20 where the plasmon energy was measured to be 21.5 eV at the crack centre; on average the plasmon energy over a microcrack decreased to ~23.8 eV. For comparison the value for amorphous carbon is ~22 eV (Chu & Li, 2006; Prawer & Rossouw, 1988). These results show slightly lower values for $(\pi + \sigma)$ plasmon energy than those found from EFTEM data, which could be due to the differing collection

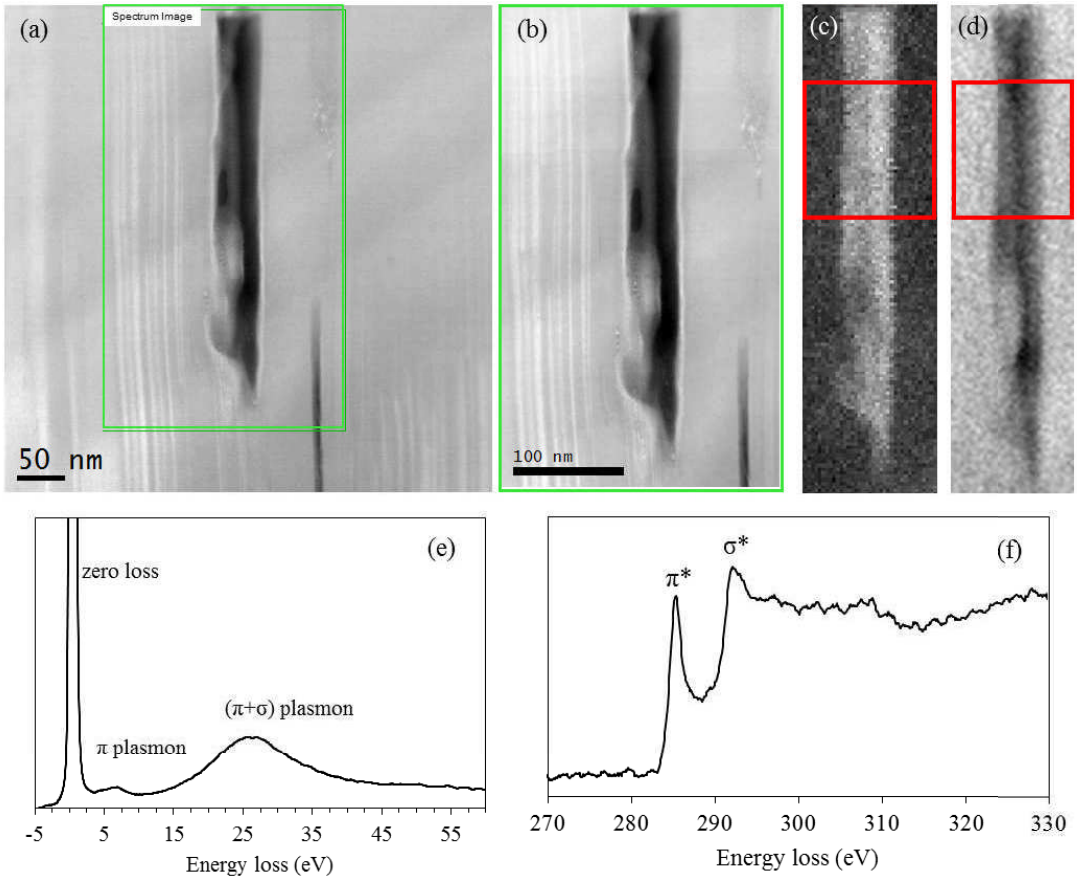

Figure 9.6: HAADF and EELS spectrum images in BEPO16 with extracted low and core loss EELS. This particular microcrack has a width of ~55 nm. (a) HAADF image showing the area overview. (b) HAADF spectrum image of the region of interest outlined by the green rectangle in (a). (c) and (d) show low loss and core loss EELS spectrum images respectively, showing the area in which EELS data was analysed in red. Vertically integrating the spectrum image of bulk material in (c) and (d) is plotted in (e) for low loss and in (f) for core loss respectively.

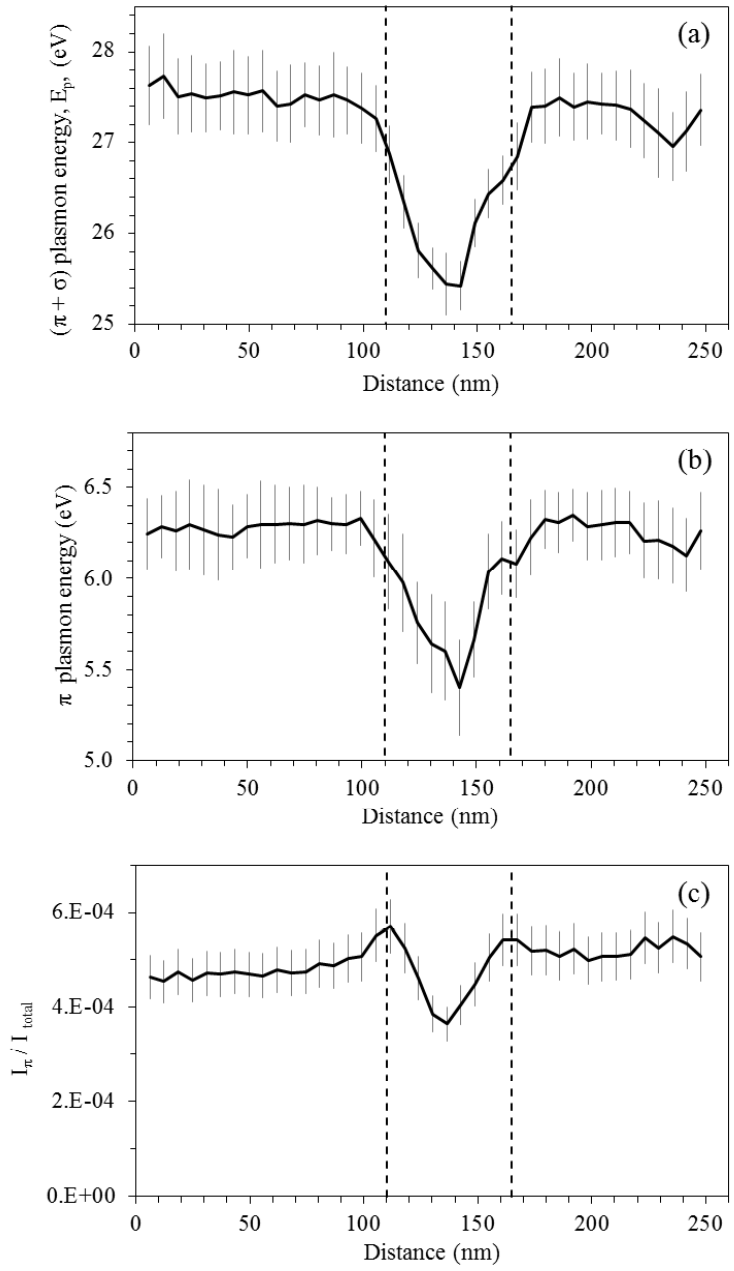

Figure 9.7: Extracted data from the low loss EEL spectra from the region of interest outlined in red in figure 9.6(c). (a) Change in $(\pi+\sigma)$ plasmon energy with distance across crack; (b) change in π plasmon energy with distance across crack; (c) change in π plasmon intensity with distance across crack, normalised to total low loss (inc. elastic peak). The vertical dotted lines represent the crack boundaries. Error bars represent the standard deviations of the vertically integrated horizontal line scans.

angles, however the trends are the same. The $(\pi + \sigma)$ plasmon energy is related to density so that the observed reduction in $(\pi + \sigma)$ plasmon energy across a crack represents a reduced density of material within the cracks. This reduction in density is not seen in the bulk irradiated graphite which implies that the cracks contents are a result of atomic diffusion into the crack and not the remains of an ordered graphite structure.

The π plasmon peak energy also reduced in value across the crack in all areas examined. In the bulk, the π plasmon energy was measured to be between 6.0 eV and 6.3 eV which is again characteristic of near-perfect graphite (Chu & Li, 2006; Fink *et al.*, 1984). In all cases, the reduction in π plasmon energy was to $\sim 5 \pm 0.5$ eV suggesting a reduction in crystallinity and density possibly due to sub 10 nm crystallite sizes (Hashimoto *et al.*, 1999). The normalised intensity of the π plasmon peak was also measured; a π plasmon window from 4.5 eV to 8 eV and total intensity window from -3 eV to 50 eV were used. The intensity was found to reduce by an average of 40% relative to the bulk, which indicates a reduction in the degree of π bonding. These results are in line with those from polycrystalline graphite in the work of Hashimoto *et al.* (1999) where a correlation between π plasmon energy and relative intensity was also found; and with results from a graphitization series by Daniels *et al.* (2007) where EELS spectra from pre-graphitized material show a π plasmon intensity of $\sim$50% of that in the graphitized product.

In the core loss region, the π^* and σ^* peaks, and the Gaussian associated with changes in intensity of the high energy shoulder of the π^* peak (at $\sim$287 eV) were analysed using HyperSpy (de la Peña *et al.*, 2015). Both these measured fitted peak intensities were normalised to the total carbon K-edge ($\sim$20 eV window). All five core loss Gaussians were fitted using the constraints detailed in section 4.3.2. The relative change in Gaussian peak areas as the STEM probe traverses the region of interest, from bulk to crack, is presented in figure 9.8. There appears to be a direct replacement of planar sp^2 bonding by non-planar sp^2 in the disordered graphitic material found within a crack. This is demonstrated by the fact that across all regions examined for both BEPO16 and BEPO20, within the crack the planar sp^2 content decreased by an average of $\sim$33% ($\sigma_x = 18\%$) while the

non-planar sp^2 content increased by an average of ∼30% (σ_x = 15%) relative to the surrounding bulk material.

9.3 Discussion

For the regions investigated, all microcracks of width <100 nm were either fully or partially filled with low density material in agreement with the study of Wen

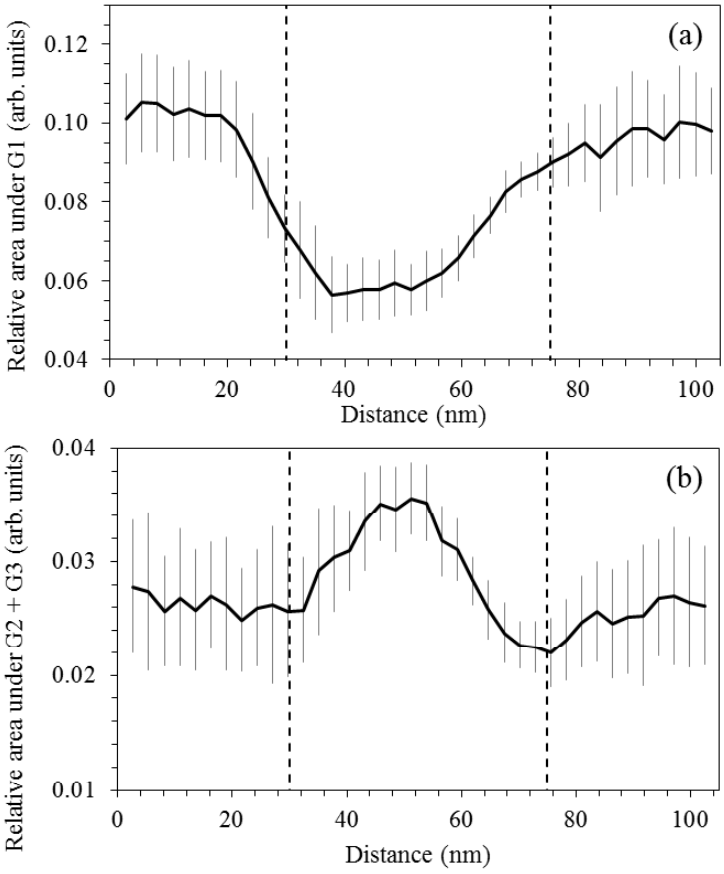

Figure 9.8: Extracted data from the core loss EEL spectra from the region of interest outlined in red in figure 9.6(d). (a) Change in relative area under G1 (associated with planar sp^2 content) with distance across crack. (b) Change in relative area under G2 + G3 (associated with non-planar sp^2 content) with distance across crack. The vertical dotted lines represent the crack boundaries. Error bars represent the standard deviations of the vertically integrated horizontal line scans.

et al. (2008) and Karthik *et al.* (2015) on similar virgin and irradiated nuclear graphite grades. From EELS and EDX measurements it it was found this material was composed of low density carbon of reduced graphitic character. Comparing the surrounding bulk material to the material within the cracks, EELS revealed a reduction in the volume plasmon energy within the microcracks consistent with a lower density material, together with a 30% reduction in planar sp^2 bonded carbon which was replaced by non-planar sp^2 bonded carbon. In material surrounding the microcracks, EFTEM measurements revealed a ∼8 nm periodic change in graphitic character which was tentatively assigned to the beginnings of microcrack formation, where a region of low graphitic character will widen to form a microcrack containing disordered carbon.

The presence of disordered material within microcracks before irradiation has implications for the evolution of the material within microcracks and the mechanisms behind dimensional change around microcracks during irradiation. The current consensus is that the migration energy of a single vacancy is such that they only become mobile above an irradiation temperature of 100°C, and this is even higher for a single interstitial defect. This initially suggests that the disordered material observed within the cracks does not accumulate as a direct result of irradiation-induced migration. However, the low basal surface energy barrier and the irradiation-induced fragmentation of the microstructure create increased possibilities for low energy diffusion surface pathways via grain boundaries. It is therefore proposed that the pre-irradiation filled microcracks arising from the manufacturing process act as sinks for surface and grain boundary diffusing atoms via fast diffusing pathways. Further detailed analysis of the in-crack material within virgin specimens and irradiated specimens at a range of temperatures would increase the understanding of this theory. In-crack material behaviour and structural changes following high temperature (>2000°C) annealing is also of interest. The presence of low density material within microcracks has implications for the understanding of radiation-induced dimensional change and the associated changes in properties of nuclear graphite during service life. The characterisation technique can be extended beyond nuclear graphite and applied to a wide range of carbons.

Chapter 10

Final Discussion and Further Work

Four key research questions were stated at the beginning of this thesis (section 1.3). This final chapter will address each question based on the literature review and experiments carried out. Any remaining related questions will be highlighted along with the necessary work required to answer them.

1. How does (electron and neutron) radiation affect graphite at the nanoscale, what role does flux and temperature play, and how can theoretical calculations be used to better understand these phenomena?
2. What is the best way to measure these changes?

A combination of TEM, SAED, EELS, EFTEM, XRD, and Raman spectroscopy provided a variety of information about structural changes induced by electron and neutron radiation.

Quantitative analysis of TEM lattice images using the PyroMaN software has provided information about the length and curvature of basal planes and their relative orientation. However, such analysis is sensitive to differences in TEM imaging conditions, image size and resolution, and degree of structural disorder. In addition, the significant anisotropy of nuclear graphite makes for highly variable data which must be interpreted with caution. This was particularly evident in analysing neutron irradiated specimens where there was a large range in extracted data. Despite these limitations, electron and neutron radiation clearly

resulted in the fragmentation of basal planes and induced a tortuous nanostructure.

Collecting SAED patterns provided to be highly useful in understanding the c-axis dimensional change through measuring the spacing of (002) diffraction spots. It was found that electron and neutron irradiation resulted in an increase in d-spacing. For the doses considered in this thesis an increase of $\sim$10% (compared to HOPG) was commonly experienced. This was in agreement with similar studies in the literature (Iwata, 1985; Kelly, 1981; Muto & Tanabe, 1997). Using SAED patterns from in situ electron radiation experiments at temperatures of -190°C to 200°C critical doses and an associated temperature threshold for irradiation damage was determined. Plotting the critical dose against 1/T gave a temperature threshold of $\sim$150°C indicating that above this temperature, the hexagonal structure within basal planes is maintained and overall largely unchanged by radiation. The Arrhenius law allowed for thermal annealing activation energies to be calculated; below the temperature threshold, this energy was calculated to be of the order 10^{-2} eV and above the temperature threshold, this energy was calculated to be of the order 10^{0} eV.

Analysis of the low and core loss spectra from EELS experiments provided information about specimen bonding and density. Measuring the position of the $(\pi + \sigma)$ plasmon peak gave information about valence electron density, which is directly related to the total density. Electron and neutron irradiation showed this peak to slightly reduce in energy implying a reduction in density. It was proposed that this was a result of the increase in dangling bonds at crystalline boundaries following the radiation-induced fragmentation of crystallites, and the introduction of microcracks. Further analysis of the $(\pi + \sigma)$ plasmon peak could involve measuring the FWHM following radiation damage to assess the degree of plasmon damping, providing further information about local bonding. The retention of the π plasmon peak during radiation damage indicated that a layered structure was largely retained despite severe structural damage. In the core loss region, a five Gaussian fitting methodology was developed to extract information about sp^2 bonding; the relative intensities of the π^* and σ^* peaks were analysed to calculate the planar sp^2 content of the specimen, and the residual Gaussian in the trough

between the π^* and σ^* peaks was used to calculate non-planar sp^2 content. Electron irradiation showed a clear reduction in planar sp^2 content to ~70% of the unirradiated specimen which was replaced by non-planar sp^2 bonded carbon. Virgin nuclear graphites (PCEA and PCIB) exhibited a planar sp^2 content of ~90% (compared to HOPG), which reduced by ~10% in neutron irradiated specimens of the same grade. The high dose high temperature specimens show evidence of structural recovery where sp^2 values were slightly higher than, or close to, values associated with low dose low temperature specimens. It is thought this was due to the high irradiation temperatures allowing for continual thermal annealing. The position of the multiple scattering resonance (MSR) peak in the core loss spectra was used to calculate in-plane bond lengths. The position of this peak decreased with radiation, implying an increase in average C-C bond length. As with the reduction in density, it is expected that this is due to the increase in dangling bonds at crystalline boundaries following the radiation-induced fragmentation of crystallites.

EFTEM experiments enabled the change in graphitic character across neutron irradiated specimens to be quantified. A fluctuation of intensity (of periodicity ~8 nm) across a line profile in the bulk, suggested bands of material with different graphitic character were present. It was suggested that these bands show the beginnings of crack formation where a trough (in the plasmon ratio map) would deepen and widen to form a crack containing disordered carbon. Damage accumulation and interstitial surface diffusion could result in regions of localised disordered material which would act as sinks for further damage and eventually expand into cracks.

Although XRD and Raman experiments were not carried out for this thesis, Mironov (2015) analysed the same PCEA and PCIB specimens with these techniques. These findings complemented the results from the aforementioned techniques strengthening confidence in data interpretation. In particular, XRD analysis showed crystallite sizes to reduce with neutron irradiation (in agreement with the work of Gallego *et al.* (2013)), and the results from Raman studies provided evidence for the fragmentation of crystallites following neutron irradiation and a significant reduction in structural disorder. The most significant changes were observed in specimens subject to low dose (1.5 dpa) and low temperature

(350°C) (PCIB C03 and PCEA B25). With increasing dose and irradiation temperature, recovery was evident suggesting that the higher irradiation temperature (655°C) allows defects to anneal.

Suggested further work to complement the results discussed would be to examine the material at a crystallite boundary. Using BF and DF TEM imaging of a FIBed specimen, a boundary can be selected and subjected to a similar analysis methodology as that described in chapter 9. It would be of interest to understand how the bonding and density changes over these areas, as compared to the bulk.

Due to the high variability in data from neutron irradiated specimens, it is proposed that further analysis of more samples (of differing grades and having received different doses at different temperatures) is required to improve the confidence of data interpretation. In particular, it would be useful to have only one variable when comparing neutron irradiated specimens, i.e. constant received dose for varying temperature and conversely constant temperature for varying received dose.

It is also proposed that this collection of characterisation techniques is extended beyond nuclear graphite and applied to a wide range of carbons.

3. Is it possible to simulate a reactor environment within a TEM?

The considerations required to simulate a reactor environment within a TEM were discussed in section 2.1.1. In short, it is widely accepted that the higher dose rate of electrons in a TEM to neutrons in a nuclear reactor (by about 10^4) and the reduced cascade damage from electrons due to their lower mass (by about 10^{-4}) make for a comparable, but not identical environment. Electron irradiation at room temperature was found to induce a more damaged structure that those observed in neutron irradiated specimens. However this series of experiments was essential in providing a controlled environment to develop the methodology for quantitatively analysing radiation damage with TEM, SAED, and EELS. In situ electron irradiation at reactor operating temperatures showed little structural change due to the low fluences. To achieve fluences comparable to those in a reactor, the specimen would have to be exposed for much longer or at a higher flux.

An extrapolation of the critical dose vs. 1/T plot (figure 7.12) discussed above and in chapter 7 allowed critical doses to be predicted for the operational temperature ranges commonly used in civil nuclear reactors; at 350°C the critical dose would occur after 12 years, at 450°C the critical dose would occur after 32 years of full power.

4. Does the material behave uniformly; are there structural differences between the behaviour of material in the bulk, within cracks, and at grain boundaries?

Disordered carbon material was observed in a range of microcracks (of varying size and shape) in BEPO irradiated specimens. The presence of partially filled microcracks has potentially significant implications for the development of microstructural models to improve the understanding and prediction of radiation-induced dimensional and property changes in nuclear graphite. EFTEM and EELS data showed that these cracks contained carbon material of lower density and graphitic character than that of the surrounding bulk graphite. Comparing the surrounding bulk material to the material within the cracks, EELS revealed a reduction in the $(\pi + \sigma)$ plasmon energy within the microcracks consistent with a lower density material, together with a 30% reduction in planar sp^2 bonded carbon which was replaced by non-planar sp^2 bonded carbon. It was proposed that the pre-irradiation filled microcracks arising from the manufacturing process act as sinks for surface and grain boundary diffusing atoms via fast diffusing pathways. To better understand this theory, a detailed analysis of the in-crack material within virgin specimens and irradiated specimens at a range of temperatures is required. Investigating the behaviour of in-crack material following high temperature (>2000°C) annealing was also suggested. Data collected in chapter 8 showed that the highly anisotropic structure of nuclear graphite means that the effects of radiation damage are site specific (for example, depending on how close it is to a pore, crack, or grain boundary).

A new methodology for quantitatively analysing the nanostructure of irradiated graphite has been developed. Existing techniques have been improved (e.g. EELS fitting) and the application of new techniques have been demonstrated (e.g. 2D and 3D micrograph analysis). The determination of a temperature threshold

through in situ TEM experiments complements the theoretical calculations of migration energies for interstitials and vacancies, and enables a better understanding of the behaviour of graphite under irradiation at a range of temperatures. Significant and novel findings regarding the characterisation of material within cracks will have an influence the development of nano/microstructure models which predict the response of a polycrystalline graphite to irradiation and temperature.

Appendix A

Publications, conferences, and awards

Publications

- Mironov, B.E., Freeman, H.M., Brown, A.P., Hage, F.S., Scott, A.J., Westwood, A.V.K., Da Costa, J.-P., Weisbecker, P., Brydson, R.M.D. (2015). Electron irradiation of nuclear graphite studied by transmission electron microscopy and electron energy loss spectroscopy. *Carbon*, **83**, 106117. doi:10.1016/j.carbon.2014.11.019

- Mironov, B.E., H M Freeman, H.M., Brydson, R.M.D ., Westwood, A.V.K ., and Scott, A.J. (2014). Simulating Neutron Radiation Damage of Graphite by In-situ Electron Irradiation. *Journal of Physics: Conference Series*, **522**. IP Address: 129.11.132.6

- Freeman, H.M., Jones, A.N., Ward, M.B., Hage, F. S., Tzelepi, N., Ramasse, Q.M., Scott, A.J., Brydson, R.M.D., (2016). On the nature of cracks and voids in nuclear graphite. *Carbon*, 103, 45-55. doi:10.1016/j.carbon.2016.03.011

- Freeman, H.M., Brydson, R.M.D., Electron Irradiation of Specimens Heated In Situ. In preparation.

- Farbos B., Freeman H.M., Hardcastle T., da Costa J-P., Brydson R.M.D., Scott A.J., Germain C., Vignoles G.L., Leyssale J-M., Property prediction in heavily irradiated graphite via an integrated experimental and atomistic modelling approach. In preparation.

Attended conferences and meetings

Date	Conference/Meeting	Contribution
August 2012	NanoteC, Brighton, UK	Poster
September 2012	European Microscopy Congress, Manchester, UK	Poster
December 2012	PyroMaN research consortium meeting, Bordeaux, France	Attendee
April 2013	Universities Nuclear Technology Forum, London, UK	Presentation
September 2013	Electron Microscopy and Analysis Group, York, UK	Poster
September 2013	International Nuclear Graphite Specialist Meeting, Seattle, USA	Presentation
February 2014	PyroMaN research consortium meeting, Bordeaux, France	Presentation
April 2014	Sustainable Nuclear Energy Conference, Manchester, UK	Poster
July 2014	Microscience Microscopy Congress, Manchester, UK	Presentation
September 2014	International Microscopy Conference, Prague, Czech Republic	Presentation
September 2014	International Nuclear Graphite Specialist Meeting, Hangzhou, China	Presentation
March 2015	Institute of Physics Nuclear Industry Group Evening Lecture	Presentation
April 2015	EdF Annual Graphite Meeting, Manchester, UK	Attendee
July 2015	Microscience Microscopy Congress, Manchester, UK	Presentation
September 2015	International Nuclear Graphite Specialist Meeting, Nottingham, UK	Presentation

Awards

Date	Award	Amount
July 2014	Institute of Physics research student conference fund	£250
July 2014	Institute of Materials, Minerals and Mining Andrew Carnegie Fund	£250

July 2014	Armourers & Brasiers Gauntlet Trust research student travel grant	£500
April 2015	Leeds University Institute for Materials Research Best Student Paper Award	£300

Appendix B

TEM beam size

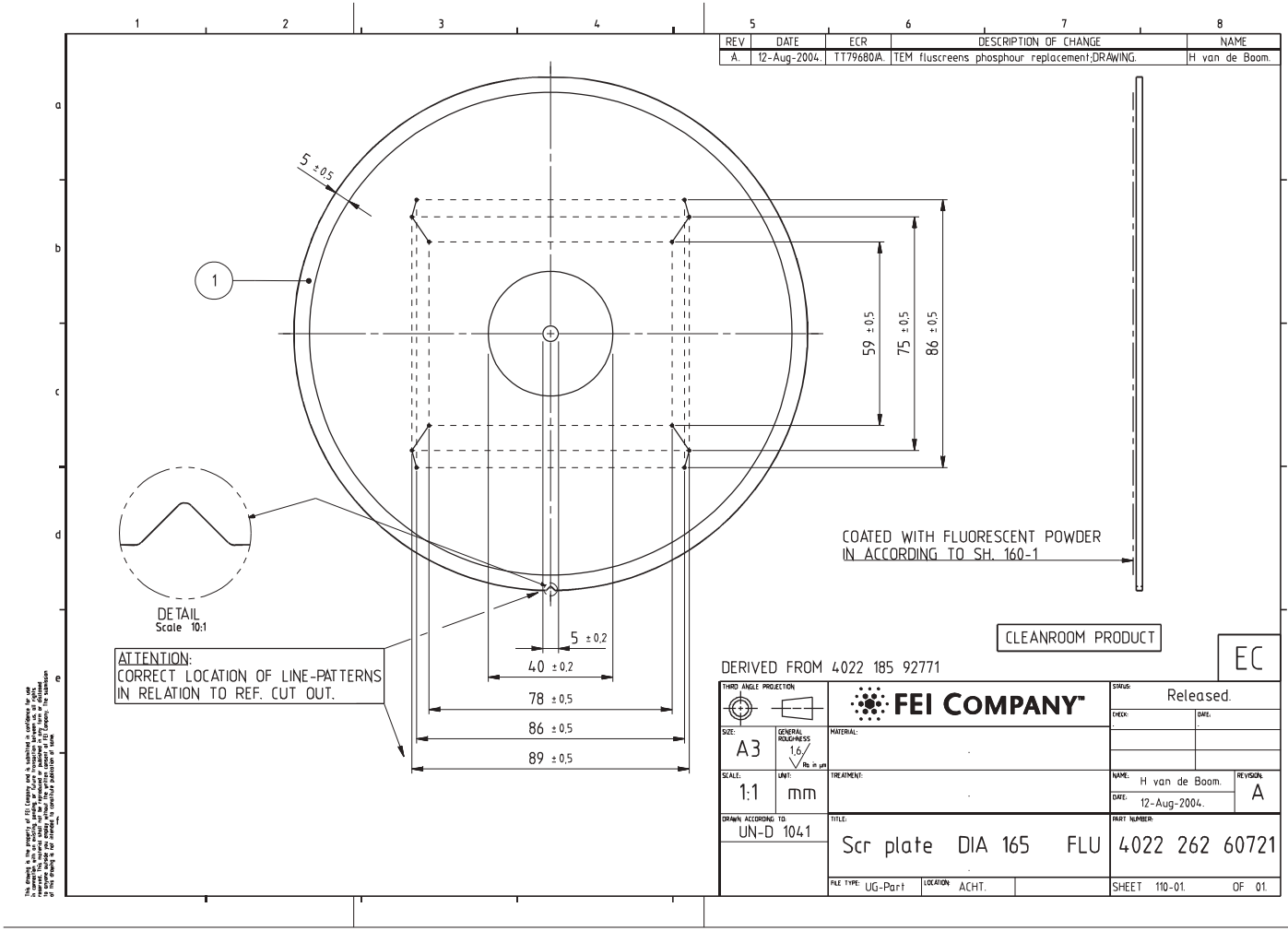
REV | DATE | ECR | DESCRIPTION OF CHANGE | NAME
A. | 12-Aug-2004. | TT79680IA. | TEM fluscreens phosphour replacement;DRAWING. | H van de Boom.
5 ±0,5
1
59 ±0,5
75 ±0,5
86 ±0,5
COATED WITH FLUORESCENT POWDER
IN ACCORDING TO SH. 160-1
DETAIL
Scale 10:1
ATTENTION:
CORRECT LOCATION OF LINE-PATTERNS
IN RELATION TO REF. CUT OUT.
5 ±0,2
40 ±0,2
78 ±0,5
86 ±0,5
89 ±0,5
CLEANROOM PRODUCT
EC
DERIVED FROM 4022 185 92771
THIRD ANGLE PROJECTION
FEI COMPANY
STATUS: Released.
SIZE: A3
GENERAL ROUGHNESS 1,6 Ra in µm
MATERIAL:
SCALE: 1:1
UNIT: mm
TREATMENT:
NAME: H van de Boom.
DATE: 12-Aug-2004.
REVISION: A
DRAWN ACCORDING TO: UN-D 1041
TITLE: Scr plate DIA 165 FLU
PART NUMBER: 4022 262 60721
FILE TYPE: UG-Part
LOCATION: ACHT.
SHEET 110-01. OF 01.

Appendix C

TEM beam current calculation

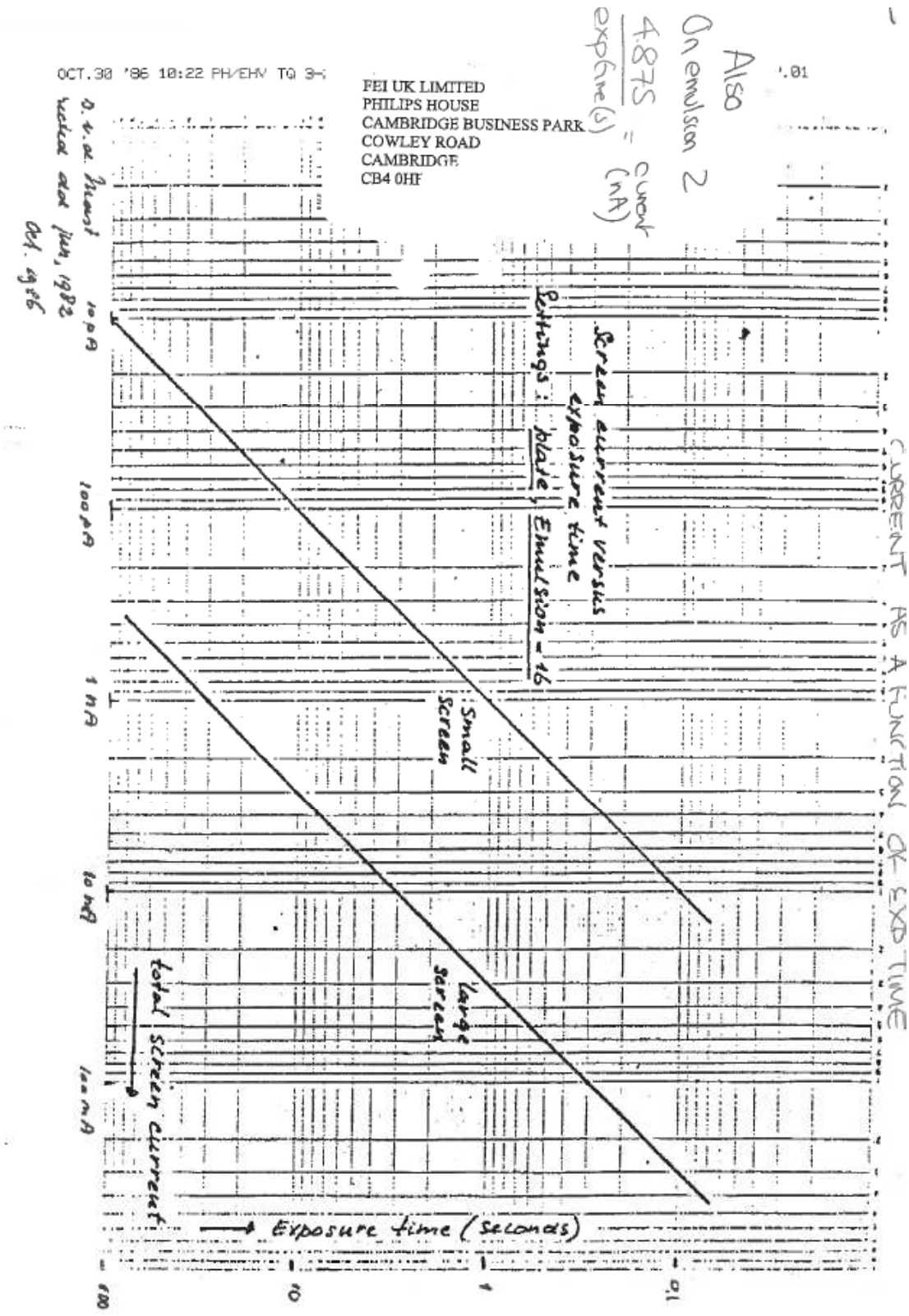

Figure C.1: Beam current as a function of exposure time (FEI, 1986).

Appendix D

Determining the displacement cross section

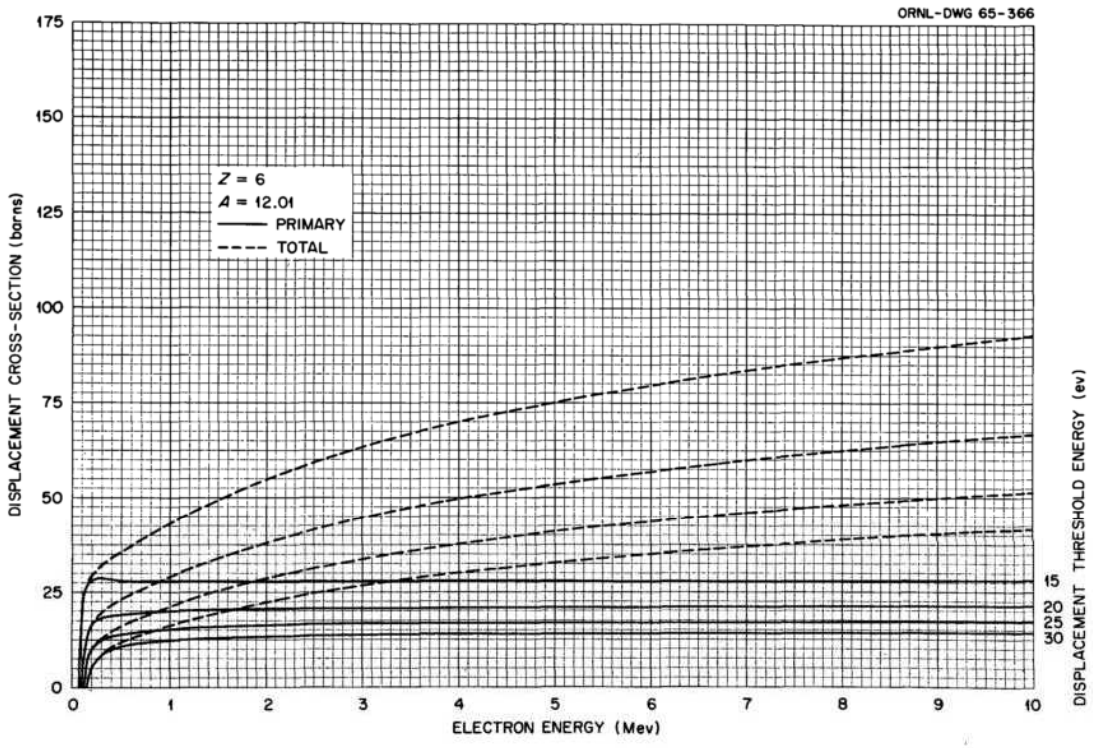

Figure D.1: Change in displacement cross section with operating voltage for displacement threshold energies of 15 eV - 30 eV (Oen, 1965)

References

Asthana, A., Matsui, Y., Yasuda, M., Kimoto, K., Iwata, T. & Ohshima, K.i. (2005). Investigations on the structural disordering of neutron-irradiated highly oriented pyrolytic graphite by X-ray diffraction and electron microscopy. *Journal of Applied Crystallography*, **38**, 361–367. 40

Bacon, G.E. & Warren, B.E. (1956). X-ray diffraction studies of neutron-irradiated graphite. *Acta Crystallographica*, **9**, 1029–1035. 49

Baker, C. & Kelly, A. (1965). No Title. *Ibid*, **11**, 729. 33

Baker, D.E. (1970). Graphite as a neutron moderator and reflector material. *Nuclear Engineering and Design*, **14**, 413–444. x, 2, 3, 4, 5, 9, 26, 27, 28, 29, 30, 31, 32

Banhart, F. (1999). Irradiation effects in carbon nanostructures. *Reports on Progress in Physics*, **62**, 1181–1221. 14, 87, 140

Banhart, F. (2002). The role of lattice defects in the formation of new carbon structures under electron irradiation. *Journal of Electron Microscopy*, **51**, 189–194. 114

Banhart, F., Kotakoski, J. & Krasheninnikov, A.V. (2011). Structural defects in graphene. *ACS nano*, **5**, 26–41. 13, 14, 17, 18, 20, 56, 57, 117

Batson, P. (1993). Carbon 1s near edge absorption fine structure in graphite. *Physical Review B*, **48**, 2608–2610. 76

Bell, J.C., Bridge, H., Cottrell, A.H., Greenough, G.B., Reynolds, W.N. & Simmons, J.H.W. (1962). Stored Energy in the Graphite of Power-Producing Reactors. *Philosophical Transactions of the Royal Society A: Mathematical, Physical and Engineering Sciences*, **254**, 361–395. 91

Berger, S.D., McKenzie, D.R. & Martin, P.J. (1988). EELS analysis of vacuum arc-deposited diamond-like films. *Philosophical Magazine Letters*, **57**, 285–290. 47, 58, 59

Bernier, N., Bocquet, F., Allouche, a., Saikaly, W., Brosset, C., Thibault, J. & Charaï, a. (2008). A methodology to optimize the quantification of sp2 carbon fraction from K edge EELS spectra. *Journal of Electron Spectroscopy and Related Phenomena*, **164**, 34–43. 47

Berre, C., Fok, S., Marsden, B., Babout, L., Hodgkins, a., Marrow, T. & Mummery, P. (2006). Numerical modelling of the effects of porosity changes on the mechanical properties of nuclear graphite. *Journal of Nuclear Materials*, **352**, 1–5. 52

Boehm, H.P. (1997). The first observation of carbon nanotubes. *Carbon*, **35**, 581–584. 6

Bollmann, W. & Hennig, G. (1964). Electron microscope observations of irradiated graphite single crystals. *Carbon*, **1**, 525–533. 6

Bruley, J., Williams, D.B., Cuomo, J. & Pappas, D. (1995). Quantitative near-edge structure analysis of diamond-like carbon in the electron microscope using a two-window method. *Journal of Microscopy*, **180**, 22–32. 47

Brydson, R. (1991). Interpretation of Near-Edge Structure in the Electron Energy Loss Spectrum. *EMSA Bulletin*, **21**, 57–67. 78, 80, 82

Brydson, R. (2001). *Electron Energy Loss Spectroscopy*. Royal Microscopical Society Microscopic Handbooks Volume 48. BIOS Scientific Publishers Ltd, Oxford, UK. 111

Brydson, R., Scott, A. & Brown, A. (2002). Some thoughts on source monochromation and the implications for electron energy loss spectroscopy. 80

Burchell, T., Clark, R., Eto, M., Haag, G., Hacker, P., Janev, R., Neighbour, G., Stephens, J. & Wickham, A. (2000). IAEA international database on irradiated nuclear graphite properties. Tech. Rep. February 2000, IAEA Nuclear Data Section. 26, 27, 31

Burden, A. & Hutchison, J. (1996). Real-time observation of fullerene generation in a modified electron microscope. *Journal of Crystal Growth*, **158**, 185–188. 37, 56

Campbell, A.a., Campbell, K.B. & Was, G.S. (2013). Anisotropy analysis of ultra-fine grain graphite and pyrolytic carbon. *Carbon*, **60**, 410–420. 41, 74

Cherns, D., Minter, F. & Nelson, R. (1976). Sputtering in the high voltage electron microscope. *Nuclear Instruments and Methods*, **132**, 369–376. 140

Chi, S.H. & Kim, G.C. (2008). Comparison of the oxidation rate and degree of graphitization of selected IG and NBG nuclear graphite grades. *Journal of Nuclear Materials*, **381**, 9–14. 56

Christie, H., Robinson, M., Roach, D., Ross, D., Suarez-Martinez, I. & Marks, N. (2015). Simulating radiation damage cascades in graphite. *Carbon*, **81**, 105–114. 10

Chu, P.K. & Li, L. (2006). Characterization of amorphous and nanocrystalline carbon films. *Materials Chemistry and Physics*, **96**, 253–277. 164

Crouse, B. (2011). Linear defects: dislocations. 21, 22

Cuesta, A., Dhamelincourt, P., Laureyns, J. & Mart, A. (1998). Comparative performance of X-ray diffraction and Raman microprobe techniques for the study of carbon materials . *Journal of Materials Chemistry*, **8**, 2875–2879. 51

DaCosta, J., Weisbecker, P., Farbos, B., Leyssale, J.M., Vignoles, G. & Germain, C. (2015). Investigating carbon materials nanostructure using image orientation statistics. *Carbon*, **84**, 160–173. 70

DaCosta, J.P., Germain, C. & Baylou, P. (2000). Level Curve Tracking Algorithm for Textural Feature Extraction. In S.Y. Sanfeliu A, Villanueva JJ, Vanrell M, Alquzar R, Crowley J, ed., *15th Intl. Conf. on Pattern Recognition*, 909–912, Los Alamitos, CA: IEEE, Barcelona. 43, 44, 70, 72

DaCosta, J.P., Weisbecker, P., Farbos, B., Leyssale, J. & Vignoles, G.L. (2014). Investigating carbon materials nanostructure using image orientation statistics. *Carbon*. 43, 110

Daniels, H., Brydson, R., Rand, B. & Brown, A. (2007). Investigating carbonization and graphitization using electron energy loss spectroscopy (EELS) in the transmission electron microscope (TEM). *Philosophical Magazine*, **87**, 4073–4092. 45, 47, 76, 78, 81, 83, 84, 85, 114, 166

Daniels, H.R., Brydson, R., Brown, A. & Rand, B. (2003). Quantitative valence plasmon mapping in the TEM: viewing physical properties at the nanoscale. *Ultramicroscopy*, **96**, 547–58. 93, 94, 101, 102, 159

de la Peña, F., Burdet, P., Ostasevicius, T., Sarahan, M., Nord, M., Fauske, V.T., Josh Taillon, Eljarrat, A., Mazzucco, S., Donval, G., Zagonel, L.F., Walls, M. & Iyengar, I. (2015). HyperSpy 0.8.1. 79, 166

Deacon, R.F. & Goodman, J.F. (1958). Lubrication by Lamellar Solids. *Proceedings of the Royal Society A: Mathematical, Physical and Engineering Sciences*, **243**, 464–482. 28

DECC (2014). Table of past and present nuclear reactors in the UK. Tech. rep., Department of Energy and Climate Change, London. 2

Delannay, L., Yan, P., Payne, J. & Tzelepi, A. (2014). Predictions of inter-granular cracking and dimensional changes of irradiated polycrystalline

graphite under plane strain. *Computational Materials Science*, **87**, 129–137. 6, 24, 53, 54, 56

DENS Solutions (2015). Nano-Chip Technology. xv, 134

Díaz, J., Anders, S., Zhou, X., Moler, E., Kellar, S. & Hussain, Z. (2001). Analysis of the π * and σ * bands of the x-ray absorption spectrum of amorphous carbon. *Physical Review B*, **64**, 125204. 47

Diaz, J., Monteiro, O. & Hussain, Z. (2007). Structure of amorphous carbon from near-edge and extended x-ray absorption spectroscopy. *Physical Review B*, **76**, 1–12. 82

Donahue, M.J. & Rokhlin, S.I. (1993). On the Use of Level Curves in Image Analysis. *CVGIP Image Understand ing*, **57**, 185–203. 43

Egerton, R.F. (2009). Electron energy-loss spectroscopy in the TEM. *Reports on Progress in Physics*, **72**, 016502. 45, 87, 111

Egerton, R.F. (2011). *Electron Energy-Loss Spectroscopy in the Electron Microscope*. Springer, 3rd edn. 75, 77, 111

El-Barbary, a., Telling, R., Ewels, C., Heggie, M. & Briddon, P. (2003). Structure and energetics of the vacancy in graphite. *Physical Review B*, **68**, 1–7. 56, 126, 139

El-Barbary, a.a., Trasobares, S., Ewels, C.P., Stephan, O., Okotrub, A.V., Bulusheva, L.G., Fall, C.J. & Heggie, M.I. (2006). Electron spectroscopy of carbon materials: experiment and theory. *Journal of Physics: Conference Series*, **26**, 149–152. 13

Ewels, C., Telling, R., El-Barbary, a., Heggie, M. & Briddon, P. (2003). Metastable Frenkel Pair Defect in Graphite: Source of Wigner Energy? *Physical Review Letters*, **91**, 1–4. 20, 117

Farbos, B., Weisbecker, P., Fischer, H., Da Costa, J.P., Lalanne, M., Chollon, G., Germain, C., Vignoles, G. & Leyssale, J.M. (2014).

Nanoscale structure and texture of highly anisotropic pyrocarbons revisited with transmission electron microscopy, image processing, neutron diffraction and atomistic modeling. *Carbon*, **80**, 472–489. 73

FEI (1986). Current as a function of exposure time. xvi, 87, 181

Ferrari, A.C. & Robertson, J. (2000). Interpretation of Raman spectra of disordered and amorphous carbon. *Physical Review B*, **61**, 14095–14107. xi, 51

Fink, J., Muller-Heinzerling, T., Pfluger, J., Bubenzer, A., Koidl, P. & Crecelius, G. (1983). Structure and bonding of hydrocarbon plasma generated carbon films: an electron energy loss study. *Solid State Communications*, **47**, 687–691. 48

Fink, J., Muller-Heinzerling, T., Pfluger, J. & Scheerer, B. (1984). Investigation of hydrocarbon-plasma-generated carbon films by electron-energy-loss spectroscopy. *Physical Review B*, **30**, 4713–4718. 48

Fitzgerald, S.P. & Yao, Z. (2009). Shape of prismatic dislocation loops in anisotropic α -Fe. *Philosophical Magazine Letters*, **89**, 581–588. 22

Gallego, N.C., Burchell, T.D. & Klett, J.W. (2006). Irradiation effects on graphite foam. *Carbon*, **44**, 618–628. 24

Gallego, N.C., Meisner, R.A. & Burchell, T.D. (2013). Annealing Studies of Irradiated HOPG using X-ray Measurements. In *Presentation at the International Nuclear Graphite Specialists Meeting*, Oak Ridge National Laboratory, Seattle. 24, 49, 121, 140, 150, 152, 157, 171

Gass, M.H., Bangert, U., Bleloch, A.L., Wang, P., Nair, R.R. & Geim, a.K. (2008). Free-standing graphene at atomic resolution. *Nature nanotechnology*, **3**, 676–81. x, 18, 19, 111

Geim, A.K. (2015). Graphene : Status and Prospects. *Science*, **324**, 1530–1534. 6

Goggin, P.R. & Reynolds, W.N. (1963). The annealing of thermal conductivity changes in electron-irradiated graphite. *Philosophical Magazine*, **8**, 265–272. 139

Gulans, A., Krasheninnikov, A., Puska, M. & Nieminen, R. (2011). Bound and free self-interstitial defects in graphite and bilayer graphene: A computational study. *Physical Review B*, **84**, 1–6. 16, 17, 162, 163

Haag, G. (2005). Properties of ATR-2E Graphite and Property Changes due to Fast Neutron Irradiation. Tech. rep., Institut für Sicherheitsforschung und Reaktortechnik Jül-4183. 2, 5, 10, 11, 19, 23, 26, 27, 29, 30, 31, 32

Hacker, P.J., Neighbour, G.B. & McEnaney, B. (2000). The coefficient of thermal expansion of nuclear graphite with increasing thermal oxidation. *J.Phys. D: Appl.Phys*, **33**, 991–998. 24, 25, 32, 53

Hagos, B., Jones, A.N., Marrow, T.J. & Marsden, B.J. (2010). Microstructural analysis of irradiated nuclear graphite waste. In *DIAMOND'10 Conference*, vol. 3. xii, 49, 52, 53, 55

Hall, G., Marsden, B. & Fok, S. (2006). The microstructural modelling of nuclear grade graphite. *Journal of Nuclear Materials*, **353**, 12–18. xi, 25, 28, 29, 31, 32

Harris, P.J.F. (1997). Structure of non-graphitising carbons. *International Materials Reviews*, **42**, 206–218. 6

Harris, P.J.F. (2012). Fullerene-like models for microporous carbon. *Journal of Materials Science*, **48**, 565–577. 6

Hashimoto, H., Nishiuma, S., Takada, K., Nakamura, K., Ueno, R. & Den, T. (1999). Crystallite Size Dependence of Plasmon Energies in Polycrystalline Graphite Observed by Reflected Electron Energy Loss Spectroscopy. *Japanese Journal of Applied Physics*, **38**, 4136–4141. 166

Heggie, M.I., Suarez-martinez, I., Davidson, C. & Haffenden, G. (2011). Buckle , ruck and tuck : A proposed new model for the response of graphite to neutron irradiation. *Journal of Nuclear Materials*, **413**, 150–155. 6, 23, 30, 117, 139

Hennig, G. (1962). Vacancies and dislocation loops in graphite. *Applied Physics Letters*, **1**, 55. 6

Henrard, L., Stephan, . & Colliex, C. (1999). Electron energy loss study of plasmon network excitations in curved carbon network. *Synthetic Metals*, **103**, 2502–2503. 76, 111

Hinks, J., Haigh, S., Greaves, G., Sweeney, F., Pan, C., Young, R. & Donnelly, S. (2014). Dynamic microstructural evolution of graphite under displacing irradiation. *Carbon*, **68**, 273–284. 40, 56

Hinks, J.A., Jones, A.N., Theodosiou, A., van den Berg, J.A. & Donnelly, S.E. (2012). Transmission Electron Microscopy Study of Graphite under in situ Ion Irradiation. *Journal of Physics: Conference Series*, **371**, 012046. 53, 55, 56

Holland, M., Klein, C. & Straub, W. (1966). The lorenz number of graphite at very low temperatures. *Journal of Physics and Chemistry of Solids*, **27**, 903–906. 26

Hull, D. & Bacon, D. (2011). *Introduction to dislocations*. Elsevier Ltd., 5th edn. 17, 21

Huntingdon, S., Ormerod, P. & Mowles, S. (2002). Characterisation of Oxidised and Irradiated Magnox Core Graphite. Tech. rep., BNFL Commercial. 90

Ishiyama, S., Burchell, T.D. & Eto, M. (2008). The effect of high fluence neutron irradiation on the properties of a fine-grained isotropic nuclear graphite. *Journal of Nuclear Materials*, **230**, 1–7. xi, 26, 29, 30

Iwata, T. (1985). Fine structure of Wigner energy release spectrum in neutron irradiated graphite. *Journal of Nuclear Materials*, **133-134**, 361–364. 35, 170

Jouffrey, B., Schattschneider, P. & Hébert, C. (2004). The magic angle: a solved mystery. *Ultramicroscopy*, **102**, 61–6. 61

Kane, J., Karthik, C., Butt, D., Windes, W. & Ubic, R. (2011). Microstructural characterization and pore structure analysis of nuclear graphite. *Journal of Nuclear Materials*, **415**, 189–197. 53, 56, 90, 121, 152

Karthik, C., Kane, J., Butt, D., Windes, W. & Ubic, R. (2011). In situ transmission electron microscopy of electron-beam induced damage process in nuclear grade graphite. *Journal of Nuclear Materials*, **412**, 321–326. xi, 13, 19, 38, 39, 41, 45, 46, 56, 87, 105, 114, 121, 122, 141

Karthik, C., Kane, J., Butt, D.P., Windes, W.E. & Ubic, R. (2015). Neutron irradiation induced microstructural changes in NBG-18 and IG-110 nuclear graphites. *Carbon*, **86**, 124–131. xi, 38, 39, 55, 56, 168

Kelly, B., Marsden, B., Hall, K., Martin, D., Harper, A. & Blanchard, A. (2000). Irradiation Damage in Graphite due to Fast Neutrons in Fission and Fusion Systems. Tech. rep., International Atomic Energy Agency, Vienna. 22

Kelly, B.T. (1971). A Simple Model of the Effect of Interstitial Atoms on the Interlayer Properties of a Graphite Crystal. *Carbon*, **9**, 627–631. x, 14, 15, 122

Kelly, B.T. (1981). Graphite - The Most Fascinating Nuclear Material. 15, 35, 170

Kelly, B.T., Martin, W.H. & Nettley, P.T. (1966a). Dimensional Changes in Pyrolytic Graphite under Fast-Neutron Irradiation. *Philos. Trans. Royal Society London A*, **260**, 37. 32, 135, 141

Kelly, B.T., Price, M. & Dolby, P. (1966b). The Annealing of Irradiation Damage in Graphite. *Journal of Nuclear Materials*, **20**, 195–209. 124

Kennedy, C. (1990). DOE/ORNL Report DOE-HTGR- 88511. Tech. rep., Oak Ridge National Laboratory. 29

Kilaas, R. (1987). Interactive software for simulation of high resolution TEM images. In R.H. Geiss, ed., *22nd MAS*, 293–300, Kona, Hawaii. 72, 116

Klemens, P. & Pedraza, D. (1994). Thermal conductivity of graphite in the basal plane. *Carbon*, **32**, 735–741. 26

Knight, D.S. & White, W.B. (1989). Characterization of diamond films by Raman spectroscopy. *Journal of Materials Research*, **4**, 385–393. 51

Koike, D.F. & Pedraza, J. (1992). Structural change of graphite during electron irradiation. In *Materials Research Society*, 67–72. 13, 56

Krasheninnikov, a.V. & Nordlund, K. (2010). Ion and electron irradiation-induced effects in nanostructured materials. *Journal of Applied Physics*, **107**, 071301. 11, 12, 13, 20, 87

Kushita, K.N. & Hojou, K. (1991). In situ EELS observation of graphite structure modification due to hydrogen ion irradiation. *ULtramicroscopy*, **35**, 289–293. 35

Kwiecinska, B., Suárez-Ruiz, I., Paluszkiewicz, C. & Rodriques, S. (2010). Raman spectroscopy of selected carbonaceous samples. *International Journal of Coal Geology*, **84**, 206–212. 51

Laffont, L., Monthioux, M. & Serin, V. (2002a). Plasmon as a tool for in situ evaluation of physical properties for carbon materials. *Carbon*, **40**, 767–780. 107, 111

Laffont, L., Monthioux, M. & Serin, V. (2002b). Plasmon as a tool for in situ evaluation of physical properties for carbon materials. *Carbon*, **40**, 767–780. 129

Lamarsh, J.R. & Baratta, A.J. (2001). *Introduction ot Nuclear Engineering*. Prentice Hall, third edit edn. 2

Latham, C.D., Heggie, M.I., Gámez, J.a., Suárez-Martínez, I., Ewels, C.P. & Briddon, P.R. (2008). The di-interstitial in graphite. *Journal of Physics: Condensed Matter*, **20**, 395220. 14, 16, 17, 20, 117, 124

Latham, C.D., Heggie, M.I., Alatalo, M., Oberg, S. & Briddon, P.R. (2013). The contribution made by lattice vacancies to the Wigner effect in radiation-damaged graphite. *Journal of physics. Condensed matter : an Institute of Physics journal*, **25**, 135403. xviii, 56, 124, 125, 126, 138

Leder, L.B. & Suddeth, J.a. (1960). Characteristic Energy Losses of Electrons in Carbon. *Journal of Applied Physics*, **31**, 1422. 48, 79

Lewis, E.E. (2008). *Fundamentals of Nuclear Reactor Physics*. Elsevier/Academic Press. 2, 26

Leyssale, J.M., Da Costa, J.P., Germain, C., Weisbecker, P. & Vignoles, G.L. (2009). An image-guided atomistic reconstruction of pyrolytic carbons. *Applied Physics Letters*, **95**, 231912. 44, 72, 73

Leyssale, J.M., Da Costa, J.P., Germain, C., Weisbecker, P. & Vignoles, G. (2012). Structural features of pyrocarbon atomistic models constructed from transmission electron microscopy images. *Carbon*, **50**, 4388–4400. 44, 45, 73

Li, L., Reich, S. & Robertson, J. (2005). Defect energies of graphite: Density-functional calculations. *Physical Review B*, **72**, 1–10. 14, 16, 17, 56, 124, 125, 134, 139

Luo, Z., Oki, A., Carson, L., Adams, L., Neelgund, G., Soboyejo, N., Regisford, G., Stewart, M., Hibbert, K., Beharie, G., Kelly-Brown, C. & Traisawatwong, P. (2011). Thermal stability of functionalized carbon nanotubes studied by in-situ transmission electron microscopy. *Chemical physics letters*, **513**, 88–93. 126

Ma, Y. (2007). Simulation of interstitial diffucsion in graphite. *Physical Review B*, **76**. 16, 17

Maeta, H., Iwata, T. & Okuda, S. (1975). c -Axis Spacing Changes in Pyrolytic Graphite after Neutron Irradiation at 5 K. *Journal of the Physical Society of Japan*, **39**, 1558–1565. 35

Magnuson, M., Andersson, M., Lu, J., Hultman, L. & Jansson, U. (2012). Electronic structure and chemical bonding of amorphous chromium carbide thin films. *Journal of physics. Condensed matter : an Institute of Physics journal*, **24**, 225004. 114

Marinopoulos, a., Reining, L., Olevano, V., Rubio, A., Pichler, T., Liu, X., Knupfer, M. & Fink, J. (2002). Anisotropy and Interplane Interactions in the Dielectric Response of Graphite. *Physical Review Letters*, **89**, 076402. 111

Maruyama, T. & Harayama, M. (1992). Neutron irradiation effect on the thermal conductivity and dimensional change of graphite materials. *Journal of Nuclear Materials*, **195**, 44–50. 26

Matsuo, H. (1980). The effect of porosity on the thermal conductivity of nuclear graphite. *Journal of Nuclear Materials*, **89**, 9–12. 26, 52

Metcalfe, M.P. & Payne, J.F.B. (2008). The effects of thermal annealing on the mechanical properties of PGA graphite. Tech. rep., RSC, Gloucestershire. 15

Mindell, J.a. & Grigorieff, N. (2003). Accurate determination of local defocus and specimen tilt in electron microscopy. *Journal of Structural Biology*, **142**, 334–347. 66, 67

Mironov, B. (2015). *Nuclear Graphite: Structural Characterisation and the Effects of Irradiation (Ph.D Thesis)*. Phd thesis, University of Leeds. xvi, xviii, 24, 50, 121, 149, 150, 151, 152, 153, 154, 171

Mironov, B., Freeman, H., Brown, A., Hage, F., Scott, A., Westwood, A., Da Costa, J.P., Weisbecker, P. & Brydson, R. (2015).

Electron irradiation of nuclear graphite studied by transmission electron microscopy and electron energy loss spectroscopy. *Carbon*, **83**, 106–117. 45, 85, 157

Mitchell, E.W.J. & Taylor, M.R. (1965). Mechanism of stored-energy release at 200C in electron irradiated graphite. *Nature*, **208**, 638–641. 17

Monthioux, M. & Kuznetsov, V.L. (2006). Who should be given the credit for the discovery of carbon nanotubes? *Carbon*, **44**, 1621–1623. 6

Mrozowski, S. (1954). Mechanical Strength, Thermal Expansion and Structure of Cokes and Carbons. *Proceedings of the Conferences of Carbon*, 31. 6, 24, 25, 31, 53

Muto, S. & Tanabe, T. (1997). Damage process in electron-irradiated graphite studied by transmission electron microscopy. I. High-resolution observation of highly graphitized carbon fibre. *Philosophical Magazine A*, **76**, 679–690. 33, 34, 35, 36, 38, 40, 41, 42, 56, 121, 150, 170

Muto, S. & Tanabe, T. (1999). Fragmentation of graphite crystals by electron irradiation at elevated temperatures. *Journal of Electron Microscopy*, **48**, 519–523. xi, xv, 37, 138, 139, 140

Muto, S. & Tanabe, T. (2000). Temperature effect of electron-irradiation-induced structural modification in graphite. *Journal of Nuclear Materials*, **283-287**, 917–921. 157

Nakai, K., Kinoshita, C. & Matsunaga, A. (1991). A study of amorphization and microstructural evolution of graphite under electron or ion irradiation. *Ultramicroscopy*, **39**, 361–368. xi, 37, 38, 56, 125

Neighbour, G.B. & Hacker, P.J. (2005). An analysis of irradiation induced creep in nuclear graphite. Tech. rep., British Energy. 32

Nightingale, R. (1962). *Nuclear Graphite*. Academic Press. 3, 6, 10, 31, 53

Niwase, K. (2002). Irradiation-induced amorphization of graphite: A dislocation accumulation model. *Philosophical Magazine Letters*, **82**, 401–408. 139

Niwase, K. (2012). Raman Spectroscopy for Quantitative Analysis of Point Defects and Defect Clusters in Irradiated Graphite. *International Journal of Spectroscopy*, **2012**, 1–14. 122

Niwase, K. & Tanabe, T. (1993). Defect Structure and Amorphization of Graphite Irradiated by D+ and He+. *Materials Transactions, JIM*, **34**, 1111–1121. 35, 52, 120, 121

Nordlund, K., Keinonen, J. & Mattila, T. (1996). Formation of Ion Irradiation Induced Small-Scale Defects on Graphite Surfaces. *Physical Review Letters*, **77**, 699–702. 10

Null, M., Lozier, W. & Moore, A. (1972). Thermal diffusivity and thermal conductivity of pyrolytic graphite above 1500K. *Carbon*, **10**, 352. 26

Oberlin, A. (1984). Carbonization and graphitization. *Carbon*, **22**, 521–541. 120, 121

Oen, O. (1965). Cross Sections for Atomic Displacements in Solids by Fast Electrons. Tech. rep., Oakridge National Lab. xvii, 87, 183

Ohr, S., Wolfenden, A. & Noggle, T. (1972). Electron displacement damage in graphite and aluminium. In G. Thomas, R.M. Fulrath & R.M. Fisher, eds., *Electron Microscopy and Microstructure of Materials*, 964, University of California Press. 9

Papworth, A.J., Kiely, C.J., Burden, A.P., Silva, S.R.P. & Amaratunga, G.A.J. (2000). Electron-energy-loss spectroscopy characterization of the sp 2 bonding fraction within carbon thin films. *Physical Review B*, **62**, 628–631. 76

Parent, P. & Zucker, S. (1989). Trace inference, curvature consistency and, curve detection. *IEEE Trans. Patt. Anal. Machine Intell.*, **11**, 823–839. 42

Pimenta, M.a., Dresselhaus, G., Dresselhaus, M.S., Cançado, L.G., Jorio, a. & Saito, R. (2007). Studying disorder in graphite-based systems by Raman spectroscopy. *Physical chemistry chemical physics : PCCP*, **9**, 1276–91. 51

Powles, R., Marks, N. & Lau, D. (2009). Self-assembly of sp2-bonded carbon nanostructures from amorphous precursors. *Physical Review B*, **79**, 1–11. 44, 47

Prawer, S. & Rossouw, C.J. (1988). Structural investigation of helium ion-beam-irradiated glassy carbon. *Journal of Applied Physics*, **63**, 4435–4439. 164

Rasband, W. (2014). Image J. 157

Raynal, P.I., Monthioux, M., DaCosta, J.P. & Dugne, O. (2010). Multi-scale quantitative analysis of carbon structure and texture: iii. Lattice fringe imaging analysis. In *Carbon conference*, 1–2. 70, 105

Reimer, L., Zepke, U., Moesch, J., Schulze-Hillert, S., Ross-Messemer, M., Probst, W. & Weimer, E. (1992). EELS Atlas. Tech. rep., Carl Zeiss. 78, 80, 81, 82

Reynolds, W.N. (1968). *Physical properties of graphite*. Elsevier Publishing Co. LTD. 124, 125

Reynolds, W.N.; Thrower, P. (1963). The Flux-Level Effect in Radiation Damage in Graphite. *Journal of Nuclear Materials*, **10**, 209–214. 6

Reynolds, W.N.; Thrower, P. (1965). The Nucleation of Radiation Damage in Graphite. *Phil. Mag*, **12**, 573–593. 34

Rowe, G. (1960). The friction and strength of clean graphite high temperatures. *Wear*, **3**, 454–462. 28

Schaffer, M., Schaffer, B. & Ramasse, Q. (2012). Sample preparation for atomic-resolution STEM at low voltages by FIB. *Ultramicroscopy*, **114**, 62–71. 159

Schattschneider, P., Hébert, C., Franco, H. & Jouffrey, B. (2005). Anisotropic relativistic cross sections for inelastic electron scattering, and the magic angle. *Physical Review B*, **72**, 045142. 94

Scherzer, O. (1949). The Theoretical Resolution Limit of the Electron Microscope. *Journal of Applied Physics*, **20**, 20. 65, 66, 68, 105

Scott, A., Brydson, R., MacKenzie, M. & Craven, A. (2001). Theoretical investigation of the ELNES of transition metal carbides for the extraction of structural and bonding information. *Physical Review B*, **63**, 245105. 85

Sharma, R. (2012). Experimental set up for in situ transmission electron microscopy observations of chemical processes. *Micron (Oxford, England : 1993)*, **43**, 1147–55. 126

Shtrombakh, Y., Gurovich, B., Platonov, P. & Alekseev, V. (1995). Radiation damage of graphite and carbon-graphite materials. *Journal of Nuclear Materials*, **225**, 273–301. 22, 29, 56

Simmons, J..H..W.. (1965). *Radiation damage in graphite*. Pergamon Press, Oxford. 32

Smith, M., Eash, D. & McKibbin, K. (1964). Longitudinal tensile properties of H4LM graphite in the temperature range -253 to 500C. *Carbon*, **1**, 181–183. 28

Smith, R. (1990). A Classical Dynamics Study of Carbon Bombardment of Graphite and Diamond. *Proceedings of the Royal Society A: Mathematical, Physical and Engineering Sciences*, **431**, 143–155. 10

Sun, K., Stroscio, M.a. & Dutta, M. (2009). Graphite C-axis thermal conductivity. *Superlattices and Microstructures*, **45**, 60–64. 26

Sutton, A. & Howard, V.C. (1962). The role of porosity in the accommodation of thermal expansion in graphite. *Journal of Nuclear Materials*, **1**, 58–71. 24, 25, 31, 32, 53

Takeuchi, M., Muto, S., Tanabe, T., Arai, S. & Kuroyanagi, T. (1997). Damage process in electron-irradiated graphite studied by transmission electron microscopy. II. Analysis of extended energy-loss fine structure of highly oriented pyrolytic graphite. *Philosophical Magazine A*, **76**, 691–700. 41, 45, 46, 140

Takeuchi, M., Muto, S., Tanabe, T., Kurata, H. & Hojou, K. (1999). Structural change in graphite under electron irradiation at low temperatures. *Journal of Nuclear Materials*, **271-272**, 280–284. 105, 121

Tanabe, T., Muto, S., Gotoh, Y. & Niwase, K. (1990). Reduction of the crystalline size of graphite by neutron irradiation. *Journal of Nuclear Materials*, **175**, 262–265. 56

Telling, R.H. & Heggie, M.I. (2007). Radiation defects in graphite. *Philosophical Magazine*, **87**, 4797–4846. 56, 125

Telling, R.H., Ewels, C.P., El-Barbary, A.A. & Heggie, M.I. (2003). Wigner defects bridge the graphite gap. *Nature materials*, **2**, 333–7. 6, 9, 16, 17, 20, 22, 30, 163

Teobaldi, G., Tanimura, K. & Shluger, a. (2010). Structure and properties of surface and subsurface defects in graphite accounting for van der Waals and spin-polarization effects. *Physical Review B*, **82**, 1–14. 16

Thrower, P. (1964). No Title. *British Journal of Applied Physics*, **15**, 1153. 34

Thrower, P.A. (1967). Interstitial Loops in Graphite, their Motion and their Effect on Elastic Modulus. *Philosophical Magazine*, **16**, 189–209. 34

Thrower, P.A. & Mayer, R.M. (1978). Point defects and self-diffusion in graphite. *Physica Status Solidi (a)*, **47**, 11–37. 12, 17, 56, 125, 134, 139, 163

Trevethan, T., Dyulgerova, P., Latham, C.D., Heggie, M.I., Seabourne, C.R., Scott, A.J., Briddon, P.R. & Rayson, M.J. (2013). Extended Interplanar Linking in Graphite Formed from Vacancy Aggregates. *Physical Review Letters*, **111**, 095501. 18, 19, 56, 117, 124, 126, 163

Tromp, R.M. & Schramm, S.M. (2013). Optimization and stability of the contrast transfer function in aberration-corrected electron microscopy. *Ultramicroscopy*, **125**, 72–80. 68

Tsai, S.C., Huang, E.W., Kai, J.J. & Chen, F.R. (2013). Microstructural evolution of nuclear grade graphite induced by ion irradiation at high temperature environment. *Journal of Nuclear Materials*, **434**, 17–23. 40, 56

Tuinstra, F. & Koenig, J.L. (1970). Raman Spectrum of Graphite. *The Journal of Chemical Physics*, **53**, 1126.

Wen, K., Marrow, J. & Marsden, B. (2008). Microcracks in nuclear graphite and highly oriented pyrolytic graphite (HOPG). *Journal of Nuclear Materials*, **381**, 199–203. 5, 25, 32, 53, 54, 55, 56, 167

Williams, D.B. & Carter, C.B. (1996). *Transmission Electron Microscopy: A Textbook for Materials Science*. Springer. 58, 59, 61, 65, 66, 75, 80, 82

Williams, D.B. & Carter, C.B. (2009). *Transmission Electron Microscopy; A Textbook for Materials Science*. Springer, 2nd edn. 79, 93, 94, 95, 98, 99

Wirth, B.D. (2007). Materials science. How does radiation damage materials? *Science*, **318**, 923–4. 21, 22

Wise, M. (2001). Management of UKAEA graphite liabilities. Tech. rep., UKAEA, Harwell, Didcot, Oxfordshire. 91

World Nuclear Association (2015). Nuclear Power Reactors. x, 3

Yan, P., Delannay, L., Payne, J.F.B. & Tzelepi, A. (2014). A Micromechanistic Crystal Plasticity Model for Graphite. In *The 4th EDF Energy Nuclear Graphite Symposium. Engineering Challenges Associated with the Life of Graphite Reactor Cores*, EMAS Publishing. 24

Young, H.D. & Freedman, R.A. (2007). *University Physics with Modern Physics*. Addison-Wesley, 12th edn. iv, v, 29

Zhang, H., Zhao, M., Yang, X., Xia, H., Liu, X. & Xia, Y. (2010). Diffusion and coalescence of vacancies and interstitials in graphite: A first-principles study. *Diamond and Related Materials*, **19**, 1240–1244. 17, 124, 126, 163

Zhang, Z. & Su, D. (2009). Behaviour of TEM metal grids during in-situ heating experiments. *Ultramicroscopy*, **109**, 766–74. 126

Zhang, Z.l., Brydson, R., Aslam, Z., Reddy, S., Brown, A., Westwood, A. & Rand, B. (2011). Investigating the structure of non-graphitising carbons using electron energy loss spectroscopy in the transmission electron microscope. *Carbon*, **49**, 5049–5063. 47, 59, 83, 84, 85

Zheng, G., Xu, P., Sridharan, K. & Allen, T. (2014). Characterization of structural defects in nuclear graphite IG-110 and NBG-18. *Journal of Nuclear Materials*, **446**, 193–199. 49

Zhou, Z., Bouwman, W., Schut, H. & Pappas, C. (2014). Interpretation of X-ray diffraction patterns of (nuclear) graphite. *Carbon*, **69**, 17–24. 24, 49